Biomolecules on micro/nano-structures

Thesis submitted in accordance with the requirements of the University of Liverpool for the degree of Doctor of Philosophy

By

Serban Dobroiu

August 2012

Acknowledgements

First and foremost, I would like to express my gratitude to my supervisor, professor Dan Nicolau, for giving me the chance to pursue this research. I would like to thank him not only for the financial support and professional guidance but, most importantly, for the friendly talks and (sometimes fatherly) advice.

I would also like to thank my family, my mom Ioana, dad Paul, and (twin) sister Ruxandra for their support. I also want to thank my girlfriend Alina for her care and understanding.

Finally, I want to acknowledge dr. Jenny Aveyard-Hanson for technical advice and fruitful discussions; I am also grateful for Jenny's knowledge of people that know people that know people.. I also thank dr. Falco van Delft from Philips Research Europe for the microfabrication work and helpful discussions.

Last but not least, want to thank friends and colleagues from the BioNano group, and from the EE&E department for their friendship.

Abstract

The aim of this thesis is to investigate the use of hybrid, patterned substrates, relying on standing wave induced fluorescence enhancement/suppression, in fluorescence detection based biorecognition devices e.g. microarrays. The thesis is structured into two parts. The first one covers the theoretical background of microarray technology and an introduction to microfabrication respectively. The research question is also introduced and the rationale behind the proposed solution is revealed. The second part is an account of the experimental work carried out on designing and testing new hybrid substrates for fluorescence-based bio-recognition devices.

Chapter I.1 introduces the basic principles of microarray construction. A brief history of microarrays, together with possible substrate materials are presented together with a wide variety of activation chemistries. Further, main probe printing methods are described. In chapter I.2, the motivation for this work is discussed, together with the proposed means. The literature concerning standing wave formation when placing a fluorophore in the vicinity of a reflecting surface is presented. The exploitation of interference based phenomena in the field of bio-assay devices, e.g. microarrays, by number of researchers in the last 10 years is also presented. Also, the use of microfabrication to address issues regarding spot morphology is presented. A brief introduction to the main steps and processes, together with advantages and limitations, of semiconductor fabrication are described in chapter I.3. A range of "non-classical" lithographical processes are highlighted as candidate techniques for low scale, research oriented applications. These still allow the interfacing of biomolecules with topographical and/or chemical patterns that approach the biomolecular dimensions.

The second section is an account of the practical undertaken from proving the principle proposed in chapter I.2 to the fabrication and use of prototype devices for DNA hybridization-based assays. In chapter II.1 the proof of principle is delivered using a simple procedure based on a fluorescent probe. The formation of standing waves and consequent amplification-suppression behaviour of fluorescence on axially nano-sized structures is demonstrated. Signal-to-noise, both as a critical performance metric in microarrays, and as a measure of local contrast as a result of spatially confined enhancement-suppression of fluorescence is discussed. The influence of constructive parameters of structure geometry is also discussed. Preliminary assessment of DNA hybridization based detection is carried out on the same type of substrates and a potential surface chemistry is proposed and tested in chapter II.2. Further, the effect of incorporating a titania adhesion layer in the pillar staructure on the fluorescence is examined. In chapter II.3, capitalising on previous work, two types of prototype slides are designed, fabricated and tested and their performance is compared to that of commercial slides. The slide design is discussed along with the motivation for its adoption. It is shown that the performance of the prototype slides is comparable to that of commercial slides. Finally, concluding remarks and a discussion on the future perspectives generated by the device architecture presented and tested here is available in the closing section.

Note: substrate design was carried out at the University of Liverpool while device fabrication was carried out at Philips Research Europe (The Netherlands).

Table of Contents

List of acronyms

AFM atomic force microscopy
APTES 3-aminopropyl triethoxysilane
BSA bovine serum albumin
cDNA cloned DNA
COC cyclic olefin copolymer
CVD chemical vapour deposition
DMSO di-methyl sulfoxide
DNA deoxyribonucleic acid
DNQ diazonaphtoquinone
DOD drop on demand
DPN dip pen nanolithography
DTT dithiothreitol
FLIC fluorescence interference contrast
FWHM full width at half height
GPTES 3-glycidoxypropyltrimethoxysilane
HMDS hexamethyldisilazane
HRP horseradish peroxidase
IUPAC International Union for Pure and Applied Chemistry
LSPR localized surface plasmon resonance
MBE molecular beam epithaxy
MEMS microelectromechanical system
MOCVD metal-organic chemical vapour deposition
NA numerical aperture
NHS N-hydroxy succinimide
NIL nano-imprint lithography
opl optical path length
PAA polyacrylamide
PAG photoacid generator
PBS phosphate buffered saline
PC polycarbonate
PDMS poly(di-methyl siloxane)
PEG poly(ethylene glycol)
PH pinhole
PHS poly(hydroxy styrene)
PMMA poly(methyl methacrylate)
PMT photomultiplier tube
PP polypropylene
PPy polypyrrole
PS polystyrene
PSD percent standard deviation
PSPD position sensitive photo detector
PTFE poly(tetra-fluoro ethylene)
PVD physical vapour deposition
RIE reactive ion etching
RMS root mean squared
RNA ribonucleic acid
RoI region of interest

S/N signal to noise ratio
SAM self assembled monolayer
SCIL surface conformal imprint lithography
SD standard deviation
SDS sodium dodecyl sulphate
SNR signal to noise ratio
SPDP N-Succinimidyl 3-[2-pyridyldithio]-propionate
SPM scanning probe microscopy
SPR surface plasmon resonance
SSC saline-sodium citrate
ssDNA single stranded DNA
SSIMS static SIMS
TMAOH tetramethylammonium hydroxide
TOF-SIMS time of flight-secondary ion mass spectrometry
Tris tris(hydroxymethyl)aminomethane
UV ultraviolet
μCP micro-contact printing

List of figures

List of tables

I. Part I: Theoretical background

I.1 Chapter 1: Microarrays

I.1.1 Introduction

Microarrays are a class of solid state devices that rely on probing the extent of bio-molecular recognition events to extract information e.g. gene expression levels, molecular diagnostics, protein/peptide-drug molecule interactions. Although these recognition events can be probed through various means, e.g. in solution, via blotting and so on, what makes the concept of microarrays attractive are the massive parallelization and miniaturization. Additionally, the ability to interface the microarray planar architecture with existing and proven detection methods, e.g. fluorescence, contributed to the wide adoption of such devices. The implications of miniaturization are mainly related to the experimental costs. Miniaturization drives down these costs by making possible the use of minute amounts of valuable (bio)reagents. Miniaturization also contributes to the parallelization which means hundreds to tens of thousands of experiments can be performed at the same time, in a parallel rather than sequential manner, which leads to economies of scale and time. Adding to these advantages, fluorescence is one of the established analytical techniques, being first proposed by (Stokes 1864). To sum up, it is probably enough to say that any type of assays that are based on a quantifiable molecular recognition reaction can be transposed into the microarray format.

I.1.1.1 Brief history

The history of microarray started at the end of the 1980's with the work done at the Affymax Research Institute under the direction of Stephen Fodor (Lenoir and Giannella 2006). His unpublished work prompted a team of researchers at Stanford University lead by Patrick Brown (as Mark Schena admits in the introduction to his book, Microarray Analysis) to adopt a similar strategy using cloned DNA (cDNA) while the team at Caltech, led by Leroy Hood, opted for a different printing method inspired from ink-jet printers (Blanchard et al. 1996). However, the idea of carrying out biorecognition reactions on solid substrates was not necessarily new, it was rather the way in which these teams of scientists were able to capitalise on existing technologies. Before giving a brief look into the history of microarrays devices, it is

probably necessary to know what the constraints of the pre-microarray technologies were.

I.1.1.1.1 Before microarrays

Research and diagnostics techniques based on molecular recognition or on the simple presence of an analyte were first carried out on solid porous substrates like nitrocellulose membranes. A technique was proposed by GE Southern in 1975 (Southern 1975) that enabled the analysis of DNA fragments through hybridization to RNA. Radiometric (using radioactive isotope labelling) or fluorographic (using a fluorophore to enhance the ionizing radiation readout) hybridization detection was used. This resulted in the advent of the eponymous technique. Soon, other similar procedures emerged: northern blotting dealing with RNA detection in 1977 (Alwine et al. 1977); western blotting, dealing with the detection of proteins using antibodies, was developed in 1979 (Towbin et al. 1979) (an account of the discovery is given by one of the inventors in). Although applied to different classes of bio-analytes, these methods involve the transfer of the fractionated analyte from the electrophoretic medium to a porous solid medium called membrane (nitrocellulose, nylon) and their presence needs to be detected and quantified. The detection was initially radiometric although colorimetric and chemiluminescent methods are available now. Radiometric detection is still a costly procedure that requires the use of specialized reagents and equipment; this problem has been however alleviated by the emergence of non-isotopic labels and new detection routines. There are however fields of research where the limitations of these techniques become apparent and insurmountable. This is the case for research in domains like drug discovery, genomics and proteomics, where the amount of data to be analyzed is so large that it requires the use of massively parallel methods rather than sequential ones. It is easy to see then how any non-parallel technique would simply become time- and cost-inefficient in such circumstances.

I.1.1.2 Microarrays

The idea behind microarrays is a perfect example of a technology that was developed by capitalizing on progresses in various unrelated fields. The original concept was first brought forward when, at the Affymax Research Institute, the possibility of creating new drug discovery devices capable of screening large libraries of chemical compounds was proposed. The technologies that would enable the development

were, according to (Lenoir and Giannella 2006) the solid state peptide synthesis proposed by Merrifield (Merrifield 1963). These are based on the advances in combinatorial chemistry[1]. Combinatorial chemistry involves synthesis and evaluation of the (medicinal, catalytic and so on) activity of large libraries of compounds This was coupled with advances in semiconductor device industry, particularly the ability to modify the chemistry of polymeric layers at specific locations using only light (photolithography). The proposed approach was to synthesize arrays of peptides on a solid support to be used as drug-testing devices. This materialized into the first array of in-situ synthesized peptides (Fodor et al. 1991). In this approach, surface bound peptides are synthesized from amino acids derivatized with photolabile groups. The photo-removal of the protecting group can be achieved locally by exposing the substrate to light through a mask. The researchers also proved the feasibility of the concept by exposing the synthesized peptides to a fluorescently labelled antibody and observing the sequence-dependant florescence at each site which they could correlate to the binding affinity. In the same paper, oligonucleotide array synthesis was also proposed. Using a similar photochemical approach, three years later, (Pease et al. 1994) demonstrated hybridization based discrimination between sequences differing by one base. An important aspect of light directed synthesis was the overall efficiency which was determined by the efficiency of the individual deprotection steps (85 to 95% for the peptides and over 95% for oligonucleotides) which in turn determines the maximum length of a correctly synthesized sequence. A similar array based approach was reported by (Southern et al. 1992) who proposed the synthesis of oligonucleotide arrays on glass by means of a physical mask.

Around the same time, two other research groups were proposing different approaches. The group at Stanford University, inspired by the unpublished work at Affymax (Schena 2003e), proposed the use of cDNA, reverse transcribed from RNA. Moreover, the cDNA was deposited onto a glass surface using spotting pins (Schena et al. 1995), which were essentially open capillaries, either micro-machined steel or tweezers (Shalon 1995). A different technology, closer to Southern's approach (Southern et al. 1994), proposed the in situ synthesis of oligonucleotides by delivering reagents to "surface tension wells", where the synthesis of the probes

[1] A concept defined by the International Union for Pure and Applied Chemistry (IUPAC) as "using a combinatorial process to prepare sets of compounds from sets of building blocks"(Maclean et al. 1999)

would take place, by means of ink-jet printing (Blanchard et al. 1996), an existing technology that the authors identified as capable, in terms of throughput, to efficiently be used in oligonucleotide arrays. The further development of the technology was exponential, with hybridization-based array techniques becoming the norm for genomic research (Ewis et al. 2005). The technology was also expanded to protein, carbohydrate, cell and tissue arrays (Martel et al. 2005).

I.1.2 Microarray technology – principles

In the following, a brief overview of the basic technological and operational basic principles of microarray technology is presented. Microarray fabrication can be classified by the way in which the probe molecule is synthesized into two categories: offline synthesis (printed microarrays) and online synthesis (*in-situ* photolithographic synthesis) The discussion will focus on printed DNA microarrays as *in-situ* synthesis is currently applied by few commercial suppliers and in-house printing is still the preferred method for bio-medical research. An emphasis will be made on detection methods, with focus on fluorescence detection. Also, quality metrics affecting the detection and quantification process will be discussed.

I.1.2.1 Substrates

Biomolecule are arrayed onto solid supports whose properties follow some general guidelines defined by a number of authors (Carrillo et al. 2005; Dufva 2009; Schena 2003d). The microarray substrates have to be solid, i.e. non-flexible, flat and planar, i.e. the surface topography needs to be even over a certain range and to display a general undistorted geometry. Chemical inertness, durability and ease of chemical derivatization are also required. Another important requirement for the microarray substrate is not to interfere in the detection process, whether this takes place via fluorescence or some other detection scheme. For example, when fluorescence is used, one identifies the amount of auto-fluorescence as a primary quality metric. It is however difficult to divide substrates into defined categories as some comprise of a solid that acts as mechanical support for certain coatings and substrate types are generally linked to a specific surface chemistry.

Glass is one of the few materials that can meet all the requirements highlighted in the previous paragraph with relative ease. Indeed, the vast majority of microarrays are printed on standard microscope slide sized pieces of glass. Commercial products that

are printed on high quality, extremely flat and of low autofluorescence glass substrates include: Arrayit, Thermo Scientific, Schott, Inanovate, Imgenex, Agilent, Corning and so on. For in situ synthesized oligonucleotide arrays, e.g. the GeneChip from Affymetrix, silicon is the material of choice due to the ease of interfacing with photolithography tools. Glass can be used to provide the chemically active surface or just as a support for less rigid layers like polymers or gels. Other substrate materials are less common but nevertheless used. Plastics are a good candidate for microarray substrates due to their low cost, flatness and ease of chemical activation that can be done via oxidative UV or plasma treatments. But they do suffer from disadvantages like high auto-fluorescence and water absorption. One reason for choosing polymer substrates is better integration into microfluidic devices (Sun et al. 2011; Zhao et al. 2008). Poly(methyl methacrylate) (PMMA) is commonly used for biologic applications due to its good optical properties and ease of chemical surface activation (Fixe 2004). A biocompatible surface chemical activation route relying on grafting of a biocompatible, phospholipid copolymer onto a cyclic olefin copolymer slide (COC) with similar optical properties to PMMA, was shown to out-perform functionalized glass in terms of thermal stability (Kinoshita et al. 2006). Gels can also be used for arraying purpose, taking advantage of their 3D network which allows a higher immobilization capacity than flat, non-porous solids do. Gels however need a solid support which is usually glass. Polyacrylamide gel (PAA) are commonly used as the nucleic acids can be modified and copolymerized with the 3D matrix (Tang and Xiao 2009). An alternative to PAG is represented by polyethylene glycol (PEG) hydrogels which, due to their structure, allow higher water content and consequently better biorecognition kinetics (Kim et al. 2008; Kivlehan et al. 2012).

I.1.2.2 Substrate activation strategies

The attachment chemistry is first determined by the nature of the substrate material if the molecules of interest are attached directly to it, or, in the case of polymers, metals or gels, by the surface chemistry of the binding layer. There are a few chemistries that are common and they will be discussed briefly in the following paragraphs. General requirements for successful attachment chemistry include fast reaction kinetics with a few steps as possible and free of harsh derivatization conditions (temperature, pH). The surface derivatization should exhibit a good yield and be stable over time. Also, it should be immune from side-reactions occurring

concurrently or competitively with the attachment. Also, autofluorescence due to the surface chemistry needs to be minimized.

I.1.2.2.1 Glass chemistry and similar surface chemistries

Glass is probably the most used substrate for biomolecule immobilization. Glass is readily available, robust, both physically and chemically and transparent. However, this is not to say that microarray glass is cheap. Microarray grade glass is highly pure to ensure minimal autofluorescence and it is also flat in order to eliminate illumination and focus related artefacts. One of the most important advantages of glass is that virtually any surface functionality can be introduced by the use of a class of organic derivatives called silanes. These reagents generally comprise of a silane molecule that has three alkoxy substituents, most commonly methoxy or ethoxy, while the fourth substituent carries the required surface functionality. The use of silane reagents is determined by the presence of hydroxyl groups on the surface of glass on the one hand, and the ability of alkoxy silane molecules to polymerize and then form hydrogen bonds with the surface. The same is valid for other types of surfaces, provided that an oxide layer exists: silicon oxide, metals.

The three main chemical groups that are commonly used in microarray probe attachment are amine, aldehyde and epoxy groups and they can all be introduced on the surface via silanization.

I.1.2.2.1.1 Amine

Amine functionality (introduced via silanization or through polylysine coating) is generally used for electrostatic binding rather than covalent binding. Amine groups are charged at neutral and acidic pH values and can therefore interact with negatively charged groups on both nucleic acids (negatively charged phosphate backbone) and proteins. Unfortunately, this type of interaction is not specific so the orientation of the adsorbed molecule can lead to steric hindrance effects leading to lower biomolecular recognition yields. Due to the lack of unsaturated bonds, autofluorescence is not a major problem with these surface chemistries.

Aminated surfaces however are not limited to electrostatic adsorption of biomolecules. First of all, amines react with aldehyde groups to yield imine bonds so attachment of biomolecules with incorporated aldehyde groups can be achieved (discussed further with regards to the aldehyde surfaces). Another way to achieve

covalent binding is to use amine-reactive crosslinkers: coupling with carboxylic acids is mediated by carbodiimide derivatives while coupling with thiols is achieved via maleimide or disulfide chemistry.

I.1.2.2.1.2 Aldehyde chemistry

Aldehyde groups are generally used in conjunction with free amine containing biomolecules, whether naturally (in the form of free lysine or arginine amino acid residues in proteins) or purposely derivatized (oligonucleotides). These groups are grafted onto a glass surface via silanization and their reaction with amine groups yields imine bonds (Schiff bases). The Schiff base formation is favoured by low water content as the reaction proceeds with the elimination of a water molecule. Apart from the availability of amine groups for coupling, another reason that recommends the use of aldehyde chemistry is related to the printing quality in that spreading is limited onto the hydrophobic aldehyde surface. Unfortunately, the imine bond is susceptible to acid hydrolysis so a stable linkage can be obtained if the imine is reduced to secondary amine via the use of a reducing agent ($NaBH_4$). This has the extra advantage that it reduces the un-coupled aldehyde groups as well to hydroxyl groups that, due to their negative charge, will help in reducing non-specific binding (by repelling the negatively charged phosphate groups or the usually negatively charged fluorescent dyes). Other coupling chemistries rely on crosslinkers that have aldehyde reactive groups like hydrazides and alkoxyamines, especially useful when fabricating carbohydrate microarrays due to their existing aldehyde groups (Gudmundsdottir et al. 2009).

I.1.2.2.1.3 Epoxide chemistry

Epoxide chemistry is probably the most versatile chemistry available for biomolecule covalent attachment. Epoxides (oxiranes) are functional groups consisting of three member rings, two carbon atoms and one oxygen atom. The reactivity of epoxides is due to the strained nature of the ring, the reactions leading to the breaking of this ring being named ring opening reactions. Ring opening can be achieved with various reagents. Chemical functionalities relevant in the realm of biomolecules can take part in ring opening reactions and their reactivity in these conditions is pH-modulated ((Hermanson 1996)). Free surface epoxides can then be inactivated towards non-specific binding using amino-alcohols.

I.1.2.2.2 Silicon

Although the use of silicon as a substrate for microarrays is centred on exploiting the silicon oxide chemistry, i.e. surface hydroxyl groups discussed previously, oxide free silicon can be derivatized for biomolecule attachment. The growth of a native oxide layer is a spontaneous process when a clean silicon surface is exposed to air and humidity in the atmosphere. This oxide layer can however be removed by treatment with hydrofluoric acid, leaving a clean silicon surface with Si-H exposed. Under UV radiation, this surface will react with alkenes to yield a Si-C bond, as illustrated by (Strother et al. 2000), when an amine functionality is introduced via a tert-butoxycarbonyl-protected 1-amino 10-decene as illustrated in **Figure I.1.1**.

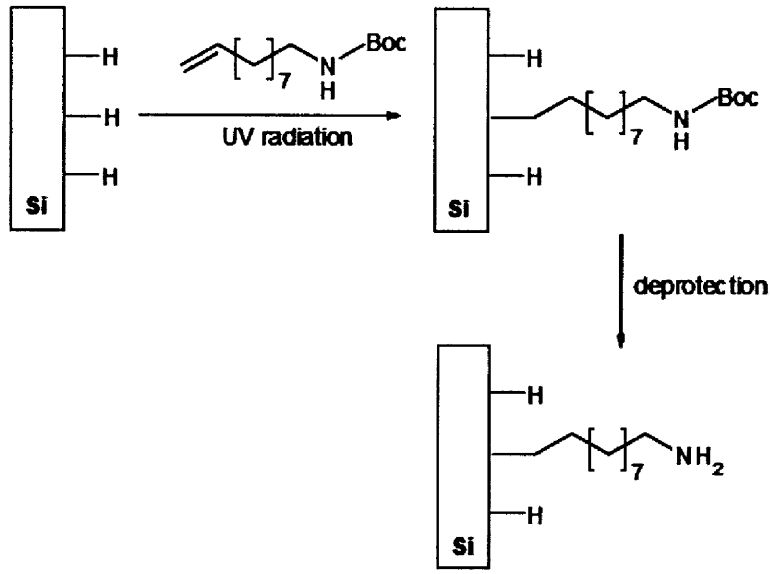

Figure I.1.1. Chemical activation of clean silicon and introduction of amine surface groups. The oxide layer can be removed from the silicon surface using HF resulting in a hydrogen-passivated surface which can then be derivatized using alkenes and UV light. Adapted with permission from (Strother et al. 2000). Copyright (2000) Oxford University Press.

I.1.2.2.3 Gold

The most widely used technique for chemical attachment of biomolecules to gold surfaces involves the formation of thiol self assembled monolayers (SAMs). The affinity of gold for transitional metals is the driving force of thiol SAMs formation on gold. The ease of their preparation has become a routine. The mechanism involves two stages, a fast one consisting of the chemisorption of the molecules followed by a slower process during which the molecules organize themselves into an ordered monolayer (Ulman 1996). The two steps are governed by different effects: the first one is related to the surface-head group interaction (Widrig et al. 1991), in terms of

electron density and the second process is influenced by the nature of the carbon chain (van der Waals forces and hydrogen bonding between the adsorbate molecules) (Offord et al. 1994), the length of the carbon chain (Rappe 2002), the bulkiness and chemical nature of the termination (Loiacono 1990). The crystallographic phase Au(111) is known to lead to the highest packing density and order degree. Deposition time and solvent used (Bensebaa et al. 1997; Pool et al. 2007) are also influencing the characteristics/quality of the monolayer.

Many examples of different end groups are available in literature, ranging from simple ones like carboxyl, hydroxyl, methyl, and amine to more complex ones like coordination complexes (Viana et al. 2005) , ethylene-glycol (Valiokas et al. 1999) , pyridine and phenol in the form of thiophenol and thiopyridine (Jin et al. 1999). Minimizing the nonspecific binding of the target biomolecules to the surface can be achieved by building multicomponent SAMs.

As a substrate for biomolecule attachment, gold is preponderantly used in label-free surface plasmon resonance based techniques (SPR, LSPR, and surface plasmon enhanced fluorescence) (Bombera et al. 2012; Chen et al. 2012b; Dettin et al. 2011; Kwon et al. 2012).

I.1.2.2.4 Polymers

As mentioned previously, polymers are not the main choice in terms of substrate materials but they can be used in the form of a surface coating that can then be chemically endowed by various means, generally UV or plasma but also wet chemical and copolymerization with functional monomers. The advantage is that polymer films can be easily applied onto solid surfaces via spin-coating. Another option is surface induced polymerization. The table below synthesizes some functionalization procedures applied to common polymers.

Table I-1. Functionalization of polymers for bio-molecule attachment

Polymer	Method	Surface chemistry
Polystyrene (PS)	oxidation with $KMnO_4/H_2SO_4$ followed by carbodiimide mediated coupling with amine (Zammatteo et al. 1996)	carboxylic acid, amine
	plasma immersion ion implantation (MacDonald et al. 2008)	ketone
Poly(tetrafluoroethylene) (PTFE)	oxygen plasma (Vandencasteele et al. 2008)	all oxygen-containing functionalities, hydrophobicity modulated by plasma power
Polypropylene (PP)	ammonia plasma (Matson et al. 1995; Matson et al. 1994)	amine
Poly(methyl methacrylate) (PMMA)	basic hydrolysis followed by amide formation (Fixe et al. 2004)	carboxylic acid, amide
	wet reduction with $LiAlH_4$ (Cheng et al. 2004)	hydroxyl
	sulphur dioxide plasma (Hiratsuka et al. 2008)	sulfonic acid
Polycarbonate (PC)	UV-ozone (Li et al. 2007)	carboxylic acid, hydroxyl
	wet chemical treatment involving alkylation, or amination of the aromatic rings followed by coupling with glutaraldehyde or thioundecanoic acid (Banuls et al. 2008)	amine, thiol, aldehyde, chloroalkyl
Cyclic olefin copolymer (COC)	plasma treatment (Hwang et al. 2008)	all oxygenated functionalities
	photografting polyethylene glycol methacrylate (Stachowiak et al. 2007)	polyethylene glicol
Polypyrrole (PPy)	polymerization or copolymerization with carboxypyrrole (Hwang et al. 2008; Lee et al. 2006; Peng et al. 2005) or an an NHS-ester activated monomer (Tlili et al. 2008)	nitrile, carboxylic acid, amine-reactive NHS-ester

Another way to activate polymer surfaces makes use of lasers. These are able to break down chemical bonds inside the polymer exposing various chemical groups, most of them oxygenated. Medium to high resolution patterning on large areas is an advantage. Laser treatment of polymers followed by biomolecule attachment has been demonstrated by (Douvas et al. 2005; Sarantopoulou et al. 2011). For protein adsorption, where biomolecular surface is combinatorial in terms of hydrophobicity

and charge, the creation of hydrophobicity gradients along linear domains using polymer-metal stacks was demonstrated (Dobroiu et al. 2010; Nicolau et al. 2010)

I.1.2.2.5 Gels

Gels are colloidal systems comprising a liquid that is trapped within a solid three dimensional network. Gels are routinely used as separation media for electrophoretic applications and also as blotting media. They are used as covalent immobilization media for biomolecules, owing their high density of binding sites to the their three dimensional topology. It is also argued that the gels provide a friendlier surrounding for proteins which mitigates to some extent denaturation (Tanase et al. 2011). The downside is that higher amounts of biomolecules are needed (del Campo and Bruce 2005). Attachment takes place by polymerizing the gel precursor with the acryl modified oligonucleotides (Brueggemeier et al. 2005; Huang et al. 2009; Pan et al. 2008) and proteins (Brueggemeier et al. 2004; Brueggemeier et al. 2009; Marsden et al. 2009) and aptamers (Srinivas et al. 2011) polyacrylamide gels. Activation of gels with reactive groups is also possible, as illustrated by the use of NHS-ester derivatized PEG-acrylamide gels and amine-modified oligonucleotides (Kivlehan et al. 2012). It has also been demonstrated that hydrogels can be patterned through spatially directed selective polymerization via dip-pen nanolithography (Rakickas et al. 2011) or heat (Pan et al. 2008).

I.1.2.2.5.1 Dendrimers

Dendrimers and dendrons are branched compounds related to polymers. While polymers have a generally linear topology, dendrimers and dendrons are branched molecules where branching is ordered, as opposed to randomly branched polymers (Caminade et al. 2008). The difference between dendrimers and dendrons lies in the nature of the core. For dendrimers the stepwise growth has a radial nature while the growth of dendrons is directed, leading to the formation of a so called chemically addressable focal point. Because of the branched ordered nature and the molecular weight and structural control, they have been used in microarray applications (Caminade et al. 2006) as high capacity linkers for biomolecules (Park et al. 2008b; Trevisiol et al. 2003; Zhang and Zhou 2011; Zhu et al. 2010) but also as amplified fluorescent labels. Dendrons have also been used to provide optimal spacing between surface immobilized oligonucleotides to improve hybridization kinetics (Hong et al. 2005).

I.1.2.3 Specific interaction

Immobilization of biomolecules by exploiting specific interactions like the avidin-biotin one does not, technically speaking, fit with the techniques discussed so far but it is worth mentioning briefly. The selectivity and strength of the avidin-biotin recognition is illustrated by the extremely small dissociation constant of the avidin-biotin complex (in the order of 10^{-14}- 10^{-16} M^{-1} for both avidin and streptavidin respectively and biotin (Holmberg et al. 2005; Laitinen et al. 2006)). This can be exploited in biomolecule attachment procedures by attaching avidin to a solid surface and then exposing it to biotin-derivatized (biotinylated) molecules. Although it is not commonly used in DNA arrays, biotin can be used as a label for oligonucleotides with chemiluminescent detection occurring via molecular recognition by horseradish peroxidase (HRP)-conjugated avidin (Rubtsova et al. 2010).

I.1.3 Probe delivery

The probe molecules (capture probes) need to be delivered to the surface of the substrate in a manner that ensures accuracy and reproducibility or precision in terms of position, spatial distribution, and geometry; a probe dispensing system must also ensure economical reagent use. The implications of these parameters are deep as they will affect downstream microarray data analysis, starting with the actual detection of features and finishing with the extraction of meaningful information from the experiment. The process of probe delivery will be referred to as "printing" hereafter. There are many printing systems in place and they can be categorized into contact, non-contact, microfluidic-based and photolithographic printing methods. Biomolecule array printing can take place either by delivery of the biomolecules to specific areas or delivering the precursors for *in situ* synthesis (in situ synthesis methods are reviewed by (Gao et al. 2004)).

I.1.3.1 Contact printing

Contact printing defines a printing technology where the printing element makes contact with the substrate surface. The most used contact printing method makes use of capillarity and surface tension, and solid or split pins, the so called quill pins, that are used to transfer solutions containing the probe molecule (Clark et al. 2008). They work by dipping them in a solution containing the specie to be attached and, due to capillary forces, the reservoirs are loaded while deposition takes place when they are

brought into contact with the substrate surface through surface tension. Their use has been reviewed elsewhere (Austin and Holway 2011; George 2006).

Micro-contact printing (μCP) is another way to deliver biomolecules to a surface in a controlled, spatially accurate manner. μCP is a member of the soft lithography family that enables the sub-micron chemical patterning of surfaces by using a polymer stamp, usually made of a formulation of poly(dimethyl siloxane) – PDMS, that is loaded with the species to be printed. The time the stamp is pressed onto the substrate and the pressure can modulate the size of the printed features. μCP has been applied to carbohydrate arrays (Michel and Ravoo 2008; Wendeln et al. 2010), protein (Qin et al. 2007; Renault et al. 2002) and DNA arrays (Rahman et al. 2006; Wang et al. 2009) and to *in situ* synthesized DNA arrays (Xiao et al. 2002).

Dip-pen Nanolithography (DPN) is a chemical patterning technique derived from scanning probe microscopy. It relies on the transfer of molecules to be patterned from a scanning probe to a surface through the water meniscus that forms between the two objects. It has been proposed as a method to pattern biomolecules on surfaces for arraying purposes in a parallelized manner (Irvine et al. 2011; Martinez-Otero et al. 2011; Thompson et al. 2011) since a limiting factor of DPN is the printing rate (Nyamjav and Holz 2010).

I.1.3.2 Non-contact printing

Non-contact printing was proposed in the early days of microarraying as an alternative to *in situ* photolithographic and pin printing and it relies on a pre-existing technology used in printers (Blanchard et al. 1996) also known as ink-jetting. Ink-jetting type printing can be used for both delivery of biomolecules or their *in situ* synthesis by delivering the synthetic precursors (Kwon et al. 2006) sequentially. Its advantage over pin printing is that, since there is no contact between the substrate and printing element, substrate damage and pin contamination (Tsai et al. 2006) are eliminated. The printing devices operate by ejecting a droplet by piezoelectric (Nagaraj et al. 2008) or thermal means but the minimum spot size is in the 10 – 20 μm (Park et al. 2008a). Other droplet expulsion methods are currently being considered acoustic (Wong and Diamond 2009), pneumatic (Xu et al. 2006), laser assisted (Barron et al. 2005; Dinca et al. 2008), liquid bridge transfer (Hartmann et

al. 2008). An overview of these technologies coming under the umbrella term of drop-on-demand (DOD) can be found in (Zaugg and Wagner 2003).

I.1.3.3 Microfluidic printing

Microfluidic devices are architectures that comprise miniaturized structures allowing for the handling of minute volumes of liquids. Thus, the species to be arrayed can be transported in solution to defined locations on the substrate or, in the case of oligonucleotide arrays, they can be synthesized in situ from precursors that were transported using the same methods. The need for dedicated channels for each biomolecule remains a challenge for high throughput applications but where high probe density is not critical, microfluidic systems "do the job" (Geissler et al. 2009). Circumventing the need for dedicated channels has been demonstrated by careful control of flow parameters allowing the pattern multiplexing in one channel, as shown by (Didar et al. 2012). The delivery of oligonucleotide precursors to specific sites and their activation, following Southern's original contribution (Southern et al. 1994), is also possible (Moorcroft et al. 2005; Saaem et al. 2010; Srivannavit et al. 2009).

I.1.3.4 Photolithography

Photolithographic synthesis of biomolecule arrays, specifically peptide and oligonucleotide was first proposed by (Fodor et al. 1991; Pease et al. 1994) at the dawn of microarray technology. The solid phase synthesis of peptides had already been demonstrated by Merrifield 30 years before (Merrifield 1963) while solid phase oligonucleotide synthesis via phosphoramidite chemistry was demonstrated by (Matteucci and Caruthers 1981) only ten years before. In the semiconductor industry, photolithography made use of clever and complex ways of using light to push the limits of resolution. The synthetic method towards oligonucleotide arrays proposed by the researchers at Affymetrix was based on the phosphoramidite chemistry demonstrated by (Matteucci and Caruthers 1981) but adapted for photo-induced rather than acid-induced deprotection (Pease et al. 1994) as illustrated in **Figure I.1.2**. Briefly, a synthetic cycle can be carried out to obtain arbitrary sequence oligonucleotide sequences starting from protected nucleosides. The novelty introduced by the researchers at Affymax was the use of a photo-labile protecting group, illustrated by the yellow sphere in **Figure I.1.2**, enabling thus the activation of the 5'reaction sites using light. The use of photomasks allowed selective exposure of

well-defined areas on the substrate thus making possible the custom extension of the oligonucleotide sequence and the printing of extremely high density arrays, on the order of $10^4 - 10^6$ features per cm^2 (Seo and Hoffman 2006). The process requires however expensive fabrication infrastructure and manufacturing a custom set of masks for each chip. Moreover, the length of the oligonucleotide is limited to around 100 bases (Dufva 2005) since, over the whole (stepwise) process, incomplete yield in each step accumulates and leads to decreased overall yield with increasing number of bases. Despite this, in 2001, Affymetrix' GeneChip held 90% of the market share (Robertson 2001). An improvement with regards to the costly usage of masks came in the form of mirror arrays which act as a continuously customizable mask (Singh-Gasson et al. 1999).

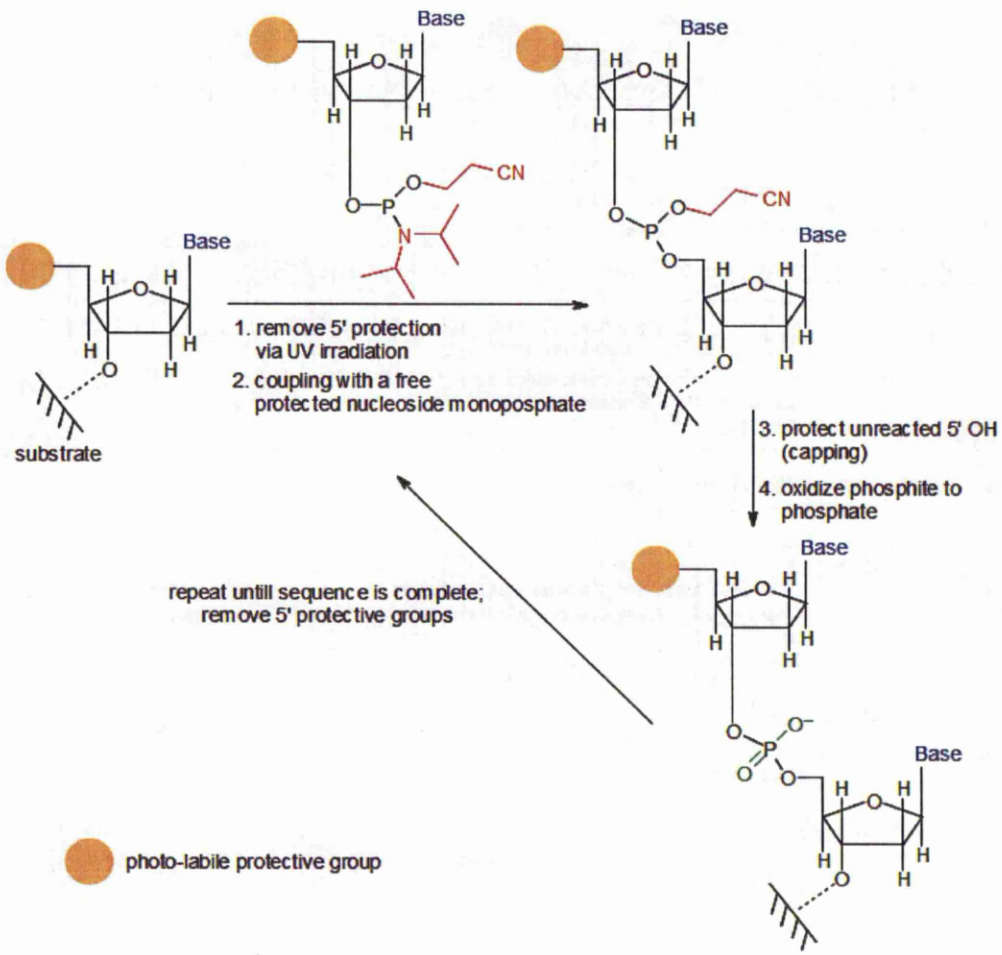

Figure I.1.2. In situ light-directed synthesis of oligonucleotides used in Affymetrix chips. Adapted with permission from (Eritja 2007). Copyright (2007) Kluwer Academic Publishers

Despite the obvious advantages of the GeneChip i.e. high density of the printed features with high feature fidelity, the so called "home-brewed" arrays are the

common choice for research and diagnostics fields due to their lower costs (for low to medium density chips, the GeneChip is more expensive per feature printed but at high density, its cost becomes advantageous; thus, for applications where a high feature density is not critical, e.g. molecular diagnostics, it is more economical to work with less dense arrays) and the ability to work with cDNA rather than with length-limited oligonucleotides. These home-brewed arrays are being printed using the methods outlined above, with cDNA strands or off-line synthesized oligonucleotides. The printing process has deep implications on the downstream data analysis and interpretation and this will be discussed below. For now, it is important to note that printing solutions, whether for contact or non-contact printing, contain additives to control the spot morphology through spreading and evaporation control. During the printing, humidity control needs to be tightly controlled as well. The importance of spot morphology and, in general, the influence of spot geometrical parameters on data quality will be outlined in the subsection dealing with spot quality.

After printing, the unbound probe molecules are washed off and, generally, the surface that has not been printed is rendered inactive to chemisorption and physisorption of target molecules. Substrates are then exposed to buffered solutions containing the target material and the recognition process is allowed to proceed. The extent of this is then quantified most commonly through optical means, e.g. fluorescence, and the data resulted is analysed.

I.1.4 Detection

The microarray platform allows for a multiplexed monitoring for further quantification of specific interactions between surface-bound entities, the probes, and the target molecules. There are many ways in which this task can be carried out with the most common way employing fluorescently labelled targets. Nevertheless, other detection schemes have been proposed: quantum dots (reviewed here (Zajac et al. 2007)); nanoparticles and hybrid nanoparticles (Enrichi et al. 2011; Richards et al. 2008; Zhang et al. 2011); surface plasmon resonance (Kwon et al. 2012; Tabakman et al. 2011), impedance (Cho et al. 2010; Fernandez-Sanchez et al. 2011; Park et al. 2008b); electrochemical (Elsholz et al. 2009); SEM (Wang et al. 2002); chemiluminescence (Corgier et al. 2007).

Fluorescence detection was one of the elements that made microarray technology so attractive. It had been proposed as a tool for both qualitative and quantitative measurements since the middle of the nineteenth century and it was used extensively in various fields or research: analytical chemistry, physical chemistry, biology. On the other hand, fluorescence imaging was routinely used so the instrumentation was readily available (laser scanning confocal microscopy was patented in the 1960's (Minsky 1961)). In a sense, from this endpoint, as with the fabrication of oligonucleotide arrays, the stage was already set for the use of fluorescence as the best available technology. Apart from this, fluorescence imaging is fast and its resolution is only limited by light diffraction (even nanometre resolution is now possible with high resolution microscopy tools); a broad range of fluorescent dyes, covering the entire visible spectrum (and going into the near infrared), is available and progress in optoelectronics has led to higher sensitivity detectors.

Fluorescence is a phenomenon that takes place when light absorbed by a molecule, also referred to as excitation, induces the promotion of an electron from the ground state, i.e. from the lowest energy state, to a higher energy state and subsequently leads to emission of light as the electron returns to the ground level. Fluorescence is, along with phosphorescence, a form of photo-luminescence, that is, light emission induced by light absorption. The process is illustrated schematically in **Figure I.1.3** using a Jablonsky diagram[2]. There are two clarifications that need to be made: one is related to the loss of energy of the electron in the excited state and the second one refers to the difference between fluorescence and phosphorescence.

[2] "[...]state diagrams in which molecular electronic states, represented by horizontal lines displaced vertically to indicate relative energies, are grouped according to multiplicity into horizontally displaced columns" from (McNaught et al. 1997)

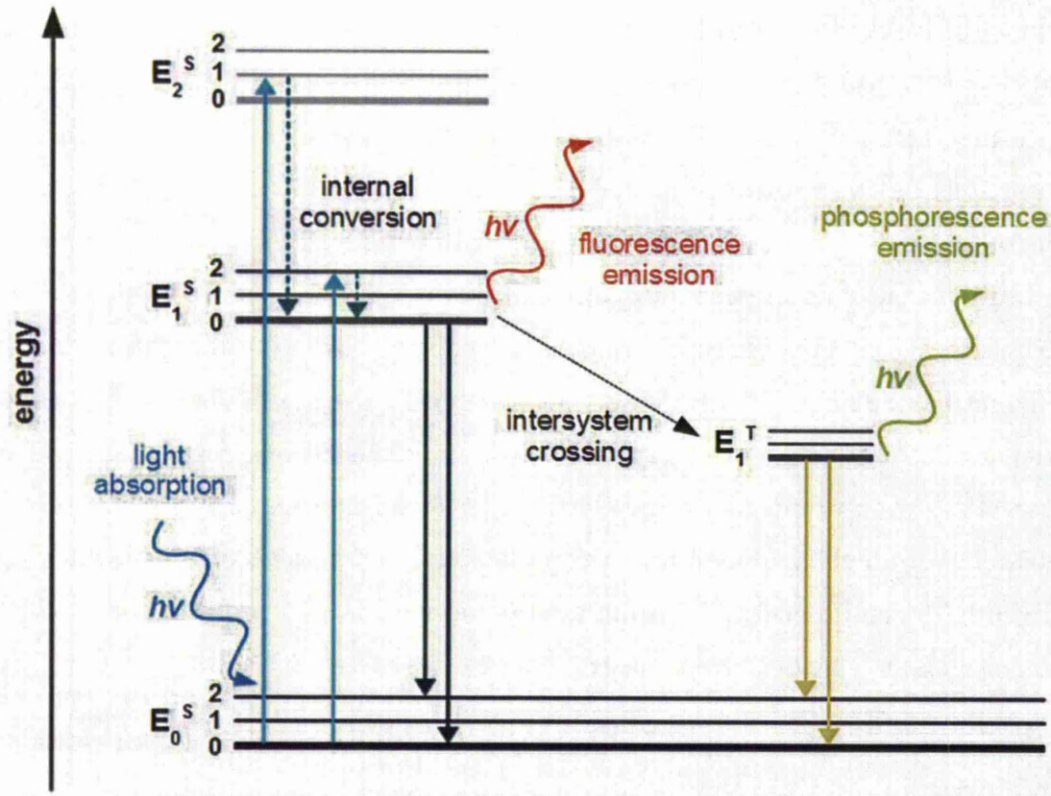

Figure I.1.3. Schematic representation of a photoemission process. Edited from (Lakowicz 2006b)

Once the electron absorbs a light quanta (represented by *hv* in **Figure I.1.3**) it will be rapidly promoted to a higher energy level (for instance from E_0 to E_1). Note that, within the same electronic level there are different vibronic levels (denoted by 0, 1 and 2 in **Figure I.1.3**). If promotion to a higher electronic energy level is accompanied by a gain in vibronic level, a return to the ground vibronic level of the excited state takes precedence. If the electron is promoted to an excited state which is not the lowest one (E_2), then energy is lost through a radiationless process known as *internal conversion* (Hof 2003). From the excited energy state, the process or returning to the ground state can take place through difference mechanisms. If the process takes place with preservation of the electronic spin state (singlet state, the excited electron is still paired with the second electron on the ground level so the total spin number is zero, represented in **Figure I.1.3** by the superscript *S*) then one photon will be emitted. Because some energy is lost as heat, the wavelength of the emitted photon will be higher than that of the excitation photon (because energy is inversely proportional to wavelength). This process is called fluorescence emission. The difference between the excitation and the emission wavelengths is called Stokes shift. The electron can also suffer a change its spin state from singlet to triplet (total

spin number 1, marked with the superscript T in Figure I.1.3) in a process called *intersystem crossing* (Hof 2003). Light emission as a result of the electron returning from the E_1^T state to the E_0^S state is called phosphorescence. Because the spin transition is forbidden, phosphorescence emission is less likely to happen (the rate of phosphorescence emission is much smaller than that of fluorescence emission (Lakowicz 2006b)). and it this thus less. Energy can also be lost through non-radiative routes, both intra-molecular and inter-molecular which do not lead to photo-emission (fluorescence quenching) (Lakowicz 2006a).

Another important aspect is related to the broad band character of the excitation and emission wavelengths (or photon energies). The rules of energy quantization state that absorption of a photon is only allowed when the energy of that photon is equal to the difference in energy between a ground and an excited electronic level. This in turn would mean that the excitation spectrum should be a narrow line while it actually has a band-like appearance. This does not mean that Planck's law does not hold but that a range of photon energies (i.e. photon wavelengths) can trigger various transitions with various probabilities. The almost mirror-like shape of the emission and excitation spectrum of a Cy5 dye shown in **Figure I.1.4** mimics these excitation probabilities as emission probabilities. Also related to the shape of the excitation-emission spectra is the fact that, since emission is preceded by a transition from the excited state higher than the lowest excited state to this lowest excited state, then emission will be induced by photons with any energy from the range of energies that are absorbed.

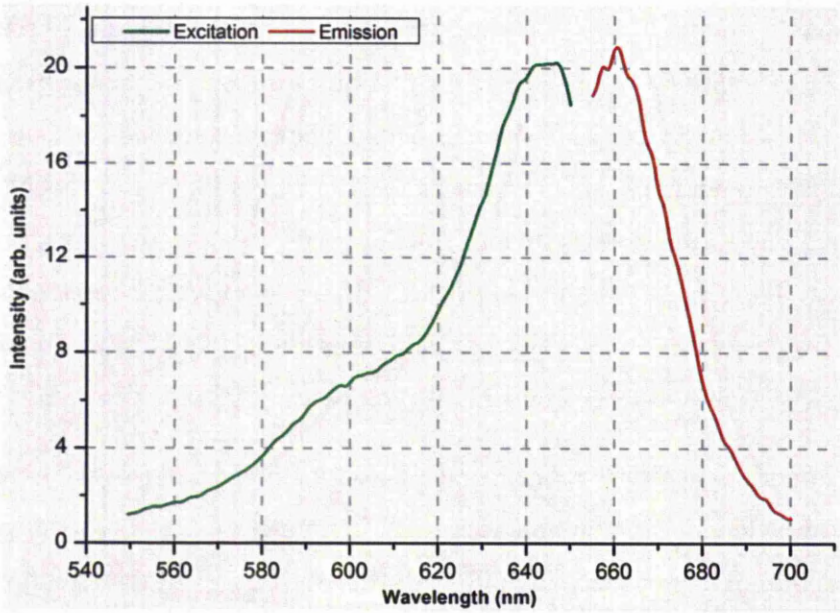

Figure I.1.4. Excitation (green) and emission (red) spectra for a Cy5-labelled oligonucleotide (spectra acquired in-house using a Perkin Elmer LB50 spectrofluorimeter)

Molecules that undergo fluorescence emission are called fluorophores and commonly referred to in the field or microarrays as fluorescent labels, dyes or tags because they can be attached to biomolecules of interest, usually the target molecule and their emission intensity can be correlated to the relative amount of target. A fluorophore can be characterized by its quantum yield, which is a measure of the efficiency with which absorbed photons are transformed into emitted photons. For reasons related to the instrumentation, the Stokes shift of the dye is also important. Briefly, the excitation light needs to be filtered from the emission light, as the intensity of latter is a few orders of magnitude lower than the former and it would thus lead to poor contrast. The Stokes shift is the difference between the excitation and emission maxima and it is easy to see that the further apart these values are, the less chance there is for the emission light to be contaminated by (reflected) excitation light.

Instrumentation for fluorescence detection generally consists of a (confocal) laser scanner. In a microarray scanner, the microarray slide is first illuminated with a laser source which supplies the excitation light. The most commonly used dyes are Cy3 and Cy5 or dyes with similar excitation and emission wavelengths. This means that the laser output wavelength needs to match only the two excitation wavelengths corresponding to these two dyes. A laser is used for sample illumination because the laser light is highly monochromatic and collimated, that is the emission wavelength

is confined to a very narrow spectral range and the beam angular spread is very small (can be focused to a very small spot). Illumination of the entire substrate is achieved by either scanning the objective over a fixed substrate or scanning the substrate under a fixed objective. Light is collected through the lens system and passed through a dichroic mirror that only allows the emission light through to the detector while excitation light, reflected by the substrate is not allowed through. This is important since fluorescence intensity is typically a few orders of magnitude lower than that of the excitation light. The performance of the dichroic mirror needs to be high so that good discrimination between excitation and emission wavelengths is achieved. Light reaching the detector will be transformed into an electric signal with the intensity proportional to the emission intensity and digitized.

Some microarray scanners are confocal. The principle of operation in confocal microscopy sketched in **Figure I.1.5**. Briefly, an imaging system like a microscope will collect light reflected by an object. But light arising from above and below the focal plane will contaminate the image. This light can be eliminated by intercalating an optical element after the lens that filters away light coming from other planes than the focal one. This element is called a pinhole aperture and serves to eliminate light coming from different planes of focus. Using a confocal scanner is not mandatory and whether it actually provides benefits outweighing the drawbacks is a matter of debate (a comparison between confocal and non-confocal systems is available here (McGovern and Fayek 2002)). The advantage of using a confocal scanner is that light coming from planes below and above the focal plane is filtered, to a certain extent, leading to better noise suppression. On the other hand, because the focal plane is actually a three dimensional domain in space rather than a two dimensional object, it will possess a physical thickness which depends on the pinhole diameter, light wavelength and lens NA (numerical aperture). The suppression of background contribution refers therefore to light arising from the depth of the substrate rather than its surface. Disadvantages of confocal scanners include higher costs (acquisition and cost of ownership) and tight focus control.

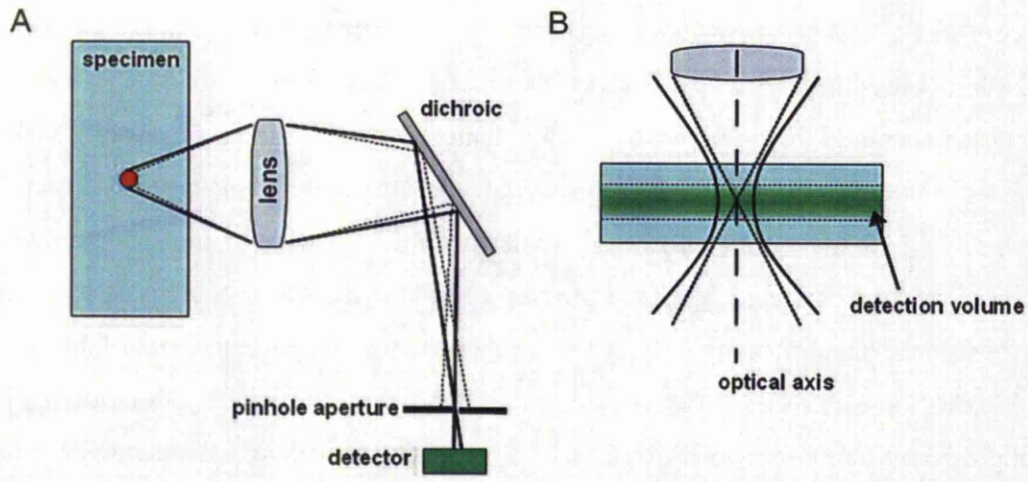

Figure I.1.5. Simplified optical path diagram of a confocal imaging system (A, excitation optical path is omitted) adapted with permission from (Wilson 2011). Copyright (2011) Blackwell Publishing. Gaussian beam profile through the specimen (B).

There is also a trade-off between sectioning capacity and light-collection ability The relationship between optical slice thickness, a measure of discrimination along the vertical (optical) axis, and imaging parameters such as wavelength of the emitted light, the refraction index of the medium that the light passes through, the numerical aperture of the lens (*NA)* and the pinhole diameter (*PH)* is discussed extensively in (Wilson 2011). An analytical formula that describes this relationship is also given in the same contribution. It is enough to say that, for a given lens and emission wavelength, it the axial resolution increases as the pinhole diameter is reduced for pinhole diameters larger than 1AU while for pinhole diameters smaller than 1AU, the effect is negligible (Wilson 2011). This decrease leads however to a decrease in the amount of light that is collected by the lens, that is, to a lower sensitivity of the system. Also, the depth discrimination capability is enhanced when using objectives with a high NA (Carlsson and Aslund 1987).

There are however some aspects that make classical fluorescence detection schemes in microarray assays sub-optimal: photo-bleaching, auto-fluorescence, difficult absolute quantification, quenching.

Photo-bleaching occurs when the fluorophores no longer respond to the incoming radiation after a certain illumination period. The effect of this is that, generally speaking, the fluorescence will decrease with increased illumination time. How fast this happens depends on the fluorophore but it is accepted that repeated imaging leads to a decrease in emission output.

Auto-fluorescence is a phenomenon that describes an emission that does not arise from the presence of the fluorophore but from outside factors, most commonly, the substrate. The substrate can be an important source of auto-fluorescence, with polymeric substrates generally exhibiting a stronger emission than glass does. Nevertheless, glass can fluoresce as a result of impurities and this is why specialty glass is used for microarraying applications. The surface chemistry of the substrates can be another source of fluorescence but depends on the chemical structure and complexity of the surface groups; however, even a simple compound like APTES displays a small amount of auto-fluorescence.

Quenching is a process involving loss of energy through a process other than by photo-emission. Although this phenomenon is the basis for a number of techniques, a problem arises when its occurrence is unwanted. An interesting example is highlighted by (Gruber et al. 2000) showing that the labelling degree can be either detrimental or advantageous depending on the dye used.

Absolute quantification is the ability to correlate the observed fluorescence intensity to the number of molecules present in a certain area. This is the reason why microarray experiments are carried out using controls, multicolour arrays, and the results are reported as relative to the controls. Theoretical models that relate fluorescence to a quantifiable biorecognition process using adsorption models (for instance Langmuir adsorption or competitive hybridization models (Gharaibeh et al. 2010)) have been proposed but none have been generally adopted or accepted. The reason is the complexity and the wealth of parameters affecting the biorecognition process resulting in more or less accurate estimated values that can be improved via calibration (Hekstra et al. 2003).

I.1.5 Spot quality metrics

There are many sources of variation that can affect the subsequent processing of microarray data, as identified by (Dufva 2005; Wu et al. 2001). The focus of this discussion will be however on sources related to the printing step: spot shape and position. A printing system should be able to deliver a defined amount of probe solution to the surface of the substrate in a reproducible and economical way. The control and reproducibility of these tasks is not only related to the volume of probe solution but also to the position relative to the neighbouring spots. After the reagent

droplet has been deposited, other factors require precise control: the spreading of the probe droplet, the evaporation of the liquid and the shape of the printed feature.

The ideal printed spot should be consistent throughout the microarray: the spots should have the same size and shape and the spacing should be maintained. This would lead to an improvement in the data quality and reduce statistical uncertainty of the extracted data (McQuain et al. 2003). Moreover, the same authors point out that complex data processing steps such as data normalization could be minimized if not eliminated altogether with better quality spots. To understand this, a closer look at both the spot identification process and spot quality metrics is needed.

The microarray architecture's principal advantage is that it offers the possibility to simultaneously interrogate a large number of biorecognition processes. This is called multiplexing. At the same time, multiplexing is only a true advantage if, apart from interrogation, the answers can be collected in the same quick manner. That is, once the experiment is ended, the data extraction needs to take place at a high rate and this can only be done using computers and automation. Otherwise, as the process rate would be limited by its slowest step, multiplexing would not be a real advantage. It is obvious that, for this goal to be reached, automated and unsupervised processing of microarray results, in the form of images, is a prerequisite. An automated procedure involves the automated pattern recognition and this is not a trivial task since the order degree and geometrical similarity to a predetermined shape of these patterns is loosely controlled. According to (Drăghici 2003), there are five spot quality descriptors: spot signal area to spot area ratio, shape regularity, spot area to perimeter ratio, displacement and spot uniformity. These descriptors are used to asses the certainty with which data acquired from a spot characterized by these metrics reflects a real behaviour. In other words, these metrics have the role of weights and the better the metric, the higher the weight of the measured behaviour. Further, a brief discussion about the spot displacement and spot shape and how these characteristics affect the measurement process will be made.

The first step in the processing of microarray results is the identification of the neighbourhood where each printed spot is located. This process is called gridding and it divides the surface of the substrate into small grid cells, each containing one feature. This can be achieved either manually, placing a template grid over the

substrate image, or in an automated manner, requiring at least some prior knowledge about the position and size of the spot (Bajcsy 2004). Normally, the gridding process should result in a collection of geometrical domains containing the spot at their centre. When deviations from this are registered, a first quality descriptor is employed – the spot displacement. This relates the real spot position inside the grid cell to the ideal position, which is at the centre of the grid cell. As displacement errors can have a number of causes: substrate related (non-uniform chemistry or topography changes), printing device imprecision, substrate movement (Schena 2003c), the minimization of spot position irregularities is required. The following spot quality metrics arise from the spot identification process, a process that divides the content of a grid cell into foreground, i.e. the spot or the signal containing area, and the background, i.e. the vicinity of the spot which does not contain any specific signal.

The process that separates the signal-containing area from the surroundings, within a grid cell, is at the foundation of microarray data analysis. This is because the correctness of process of attributing pixels to the foreground and background can affect the outcome of the analysis. The quality metrics involved after this stage are the shape regularity and spot area to perimeter ratio. They are both related to the shape of the spot, or the extent to which a predetermined geometrical shape, most commonly a circle, can approximate the shape of the spot. The difference between these two metrics is that while the spot area to perimeter ratio is only a measure of the similarity of the spot to the geometrical shape, circularity in most of the cases, the shape regularity gives a more complete picture of spot quality by taking into account the rejected pixels that belong to the predicted spot area. In other words, if the spot finding algorithm predicts that the spot should be located within a circular area of a certain size, this metric tells the analyst how many non-signal pixels are contained within that perimeter. As mentioned before, these metrics play the role of weights so any printing error leading to doughnut shaped spots or half-moon shaped spots will render the information extracted from that spot less credible. From this, the importance of controlling the spot morphology, that is its size and shape becomes clear. Unfortunately, current technologies do not offer tight control of these parameters relying on the inclusion of additives in the printing buffers and resting the weight of spot geometry control on the printing equipment. The use of additives in

the printing solutions is related to both the spreading and the rate of evaporation of the droplets, a process whose implications will be discussed shortly. A different approach to this is proposed in this contribution. This will be detailed in the following paragraphs.

In the processing sequence, the shape related quality descriptors only come into play after the actual detection and identification of foreground and background pixels. The working principles behind algorithms that this process relies on are discussed in depth in the experimental section. For now, a brief presentation in a tabular form is available in **Table I-2** below aggregated from (Bajcsy 2006; Bozinov and Rahnenfuhrer 2002; Petrov et al. 2002). A general idea that can be extracted is that most of these algorithms are heavily relying on assumptions about the spot position, size and shape which make these algorithms susceptible to failure (shortcomings of each algorithm are shown in column three of **Table I-2**). From this standpoint, it becomes obvious that additional knowledge would be beneficial to the entire process.

Table I-2. Main methods used for feature identification and the way in which they can be affected by uncertainty in position and morphology

Method				Principle	Weak points (concerning shape, size and position of the spot)
spatial				two concentric circles are applied on the spot; pixels outside the larger circle are assigned to the background while pixels inside the small circle are assigned to the foreground	exact position of spot is not known; shape variations might lead to inclusion of background pixels in the spot (or the opposite); spot radius variation might lead to errors
intensity	segmentation	seeding		seeds are planted inside spot area; the region is extended by adding pixels with similar intensity values to form a contiguous area	the seeds are planted in the centre of the spot assuming the spot is located at the centre at the grid cell
		watershed		uses morphological operators to filter out pixel groups that deviate from a pre-defined shape and size	a certain spot shape and size is assumed; valid spots might be discarded
	clustering			arrange pixel intensities in a descending order and assign the top brightest fraction (numerically equal to the fraction of spot pixels in the total number of pixels) to the foreground	fraction is calculated based on a theoretical spot size and position in the grid cell; real position and size might deviate from the expected
hybrid (different variants combining the spatial and intensity based algorithms)				a predefined shape is fitted on a contiguous area supplied by a segmentation method is fitted; if fitting is poor, the spot is discarded	the choice of fitting shape and size is based on ideal spot descriptors
				Mann-Whitney test is applied to two populations drawn from the background and foreground; the pixels passing the median test are assigned to the foreground	the choice of background and foreground is dictated by the theoretical spot descriptors

As stated earlier, control over spot position and morphology is critical for the quality of the extracted data (Sobek et al. 2007). An important factor is the spot morphology that can be influenced by the printing conditions, i.e. printing equipment, environment, printing solution composition and surface properties. The first step of the printing process is the transfer of liquid via contact or ejection to the substrate. For pin printing, which is the most commonly used (Wu et al. 2012), the adhesive force between the liquid and the substrate plus the mass of the droplet need to be higher than the adhesive force between the liquid and the pin. This condition tends to be more difficult to achieve when hydrophobic substrates are used. Printing technology aside, the evolution of the droplet after being deposited on the substrate can be affected by two factors: evaporation and spreading. These two processes can lead to changes in the spot morphology and size. Concerning the spreading, this is a process by which the droplet stabilizes itself by balancing the surface energy of the

three phases involved. It is easy then to see that properties of the substrate (hydrophilicity/hydrophobicity, roughness), probe solution (surface tension, viscosity) and gas phase (humidity) affect the spreading of the droplet. For instance, surface chemical and physical inhomogeneity lead to non-circular spots (McHale 2007). This also means that the spreading can be modulated by these parameters but the variability introduced by such complex interdependencies means that printing must be optimized for different surfaces and printed material (Dawson et al. 2005). Unfortunately, the optimization process is mostly a trial-and-error process. Spreading can be mitigated by proper choice of the liquid composition or the surface properties (SuperPVDF slides from Arrayit or UltraGAPS from Corning are hydrophobic, leading to reduced spreading). Droplet evaporation is closely linked to droplet spreading and is a major factor affecting the spot morphology by modifying the intra-spot probe distribution.

A liquid droplet tends to minimize its free surface energy by taking a spherical shape. Minimization of the surface free energy when the droplet is placed on a flat substrate is more complex because now, instead of one free energy term describing the free energy at the liquid-vapour interface, γ_{LV}, surface free energy at the solid-liquid interface, γ_{SL}, and solid-vapour interface, γ_{SV}, need to be taken into account. Depending on the surface free energy balance, a liquid droplet can either spread into a film or remain a droplet (McHale 2007).

$$S = (\gamma_{SL} + \gamma_{LV}) - \gamma_{SV}$$

where S denotes the total free surface energy. If $S > 0$, the droplet will spread into a film. If $S < 0$, the droplet will maintain a hemi-spherical shape with a liquid-solid contact angle θ. Generally, it is said that a liquid wets a surface if the liquid contact angle smaller than 90° and conversely, a liquid does not wet a surface if the liquid contact angle is higher than 90° as illustrated in **Figure I.1.6**.

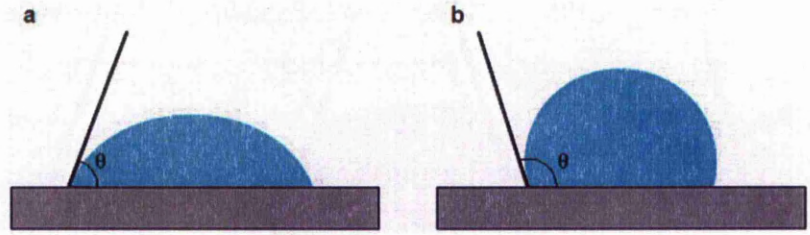

Figure I.1.6. Surface wettability by liquids as determined by the contact angle (water droplet in blue on a solid surface in grey)

The contact angle relates the surface free energy at the three interfaces through Young's law:

$$\cos\theta = \frac{\gamma_{SV} + \gamma_{SL}}{\gamma_{LV}}$$

It follows that he equilibrium between adhesive forces (the numerator) and cohesive forces (the denominator) is given by the cosine of the contact angle. The magnitude of the contact angle depends on the physico-chemical properties of the liquid and those of the solid material.

After deposition droplet evaporation has been extensively studied and theoretical models for the evaporation regime have been proposed: either the contact angle is preserved and the droplet contact area decreases or the contact area is preserved while the contact angle changes (Dugas et al. 2005) as shown in **Figure I.1.7**. When the contact area decreases, the solvated material is deposited at the centre of the spot while evaporation with decrease in contact angle can lead either to a uniform film or to the well known "coffee stain" pattern (Deegan et al. 1997). According to the same author, the requirements for this phenomenon are a pinned contact line, a non-zero contact angle and evaporation. The "coffee stain" pattern is due to capillary transport effects from the centre to the edges of the droplet, as evaporation decreases the height of the droplet. Subsequent contributions have shown however that the phenomenon is more complex. As opposed to Deegan's conclusion, that the behaviour is not solution composition dependant, (Hu and Larson 2006) show that a small amount of surfactant can reverse the behaviour, leading to central deposition of the material. In another study, (Deng et al. 2006) confirmed these results using Triton X-100 but, more importantly, showed that the surface chemistry must be optimized for high attachment yields. A downside to this is that surface specific optimization of printing solution composition, while improving spot morphology might adversely

affect spot quality in other ways (Rickman et al. 2003). Nevertheless, common additives to saline buffer printing solutions include DMSO, betaine and SDS while Triton X (Liu et al. 2009), sarkosyl (Dugas et al. 2005), glycerol and sucrose (Smith et al. 2002), trehalose (Preininger et al. 2005) were also tested. In the end, solving the problem of coffee-stain spots is not a trivial matter as pointed out by (McHale 2007), as increasing the surface hydrophilicity might have the unwanted effect of spot spreading and increasing the solute concentration might not be technically possible. The perpetuation of the problem, i.e. the impossibility to generate controlled geometry spots, and the inability of the proposed solutions to offer a general, substrate independent resolution lead to an increasing number of scientific papers proposing newer and more robust spot detection algorithms. The conclusion that can be drawn from this is that a substrate non-specific method offering reduced variability in terms of spot quality would be warranted.

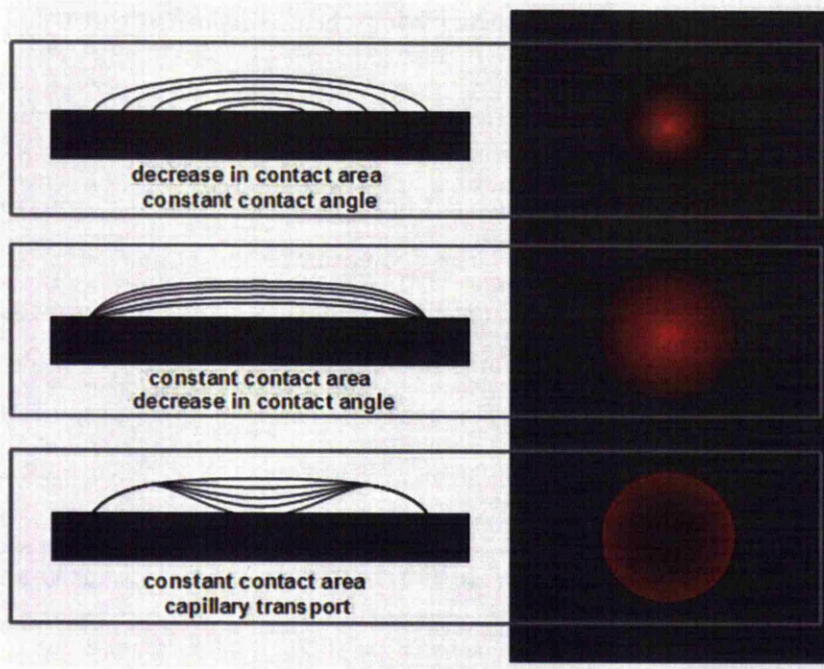

Figure I.1.7. Possible drying scenarios; top: concentration of material at the centre, middle: ideal drying with uniform evaporation and bottom: pinned contact line leading to mass transport to the edges (the images on the right illustrate the corresponding scenario)

The literature concerning substrate induced droplet confinement to achieve a pre-designed shape and size of the spot is quite scarce. Common patterning methods that impart a desired spatial distribution are limited in applicability by the accuracy and precision of the printing equipment. For instance, geometrical confinement through μCP or direct-write lithography is one possible option but its application to high

density arrays could be limited. Other methods are based on lithographical methods which are far from being accessible platforms.

Surfaces can be chemically patterned using research-level methods, e.g. μCP, DPN, direct write lithography. Apart from DPN (which is affected by the traditional limitations of scanning probe methods), these methods do offer the ability to chemically pattern relatively large areas with good resolution, reaching the sub-micron domain Furthermore, resolution requirements are not as critical in surface bio-assay techniques so as to cause technological limitations since the transition to nanoarrays poses specific difficulties (Dufva 2005). However, multiplexing does require liquid handling with micron-precision so the patterning should be complemented by an ability to deliver different biomolecules at different spatially addressable locations on the substrate with a reasonable accuracy that would eliminate or at least minimize errors due to misalignment. When liquid dispensing is concerned, as is the case for feature printing in most microarray applications, it has been shown that misalignment errors exist and they affect, indirectly, the outcome of the bio-assay. From this point of view, patterning methods like μCP could in principle work but with some limitations as highlighted in **Figure I.1.8**. Patterning areas with defined and tightly controlled geometrical properties (i.e. shape and size) is within the capabilities of such methods. However, such a system is far from being optimal due to contamination in the absence of a physical barrier (spill over to adjacent spots) illustrated in **Figure I.1.8 bottom left** or unwanted physisorption due to high local probe concentration as shown in **Figure I.1.8 bottom right.**

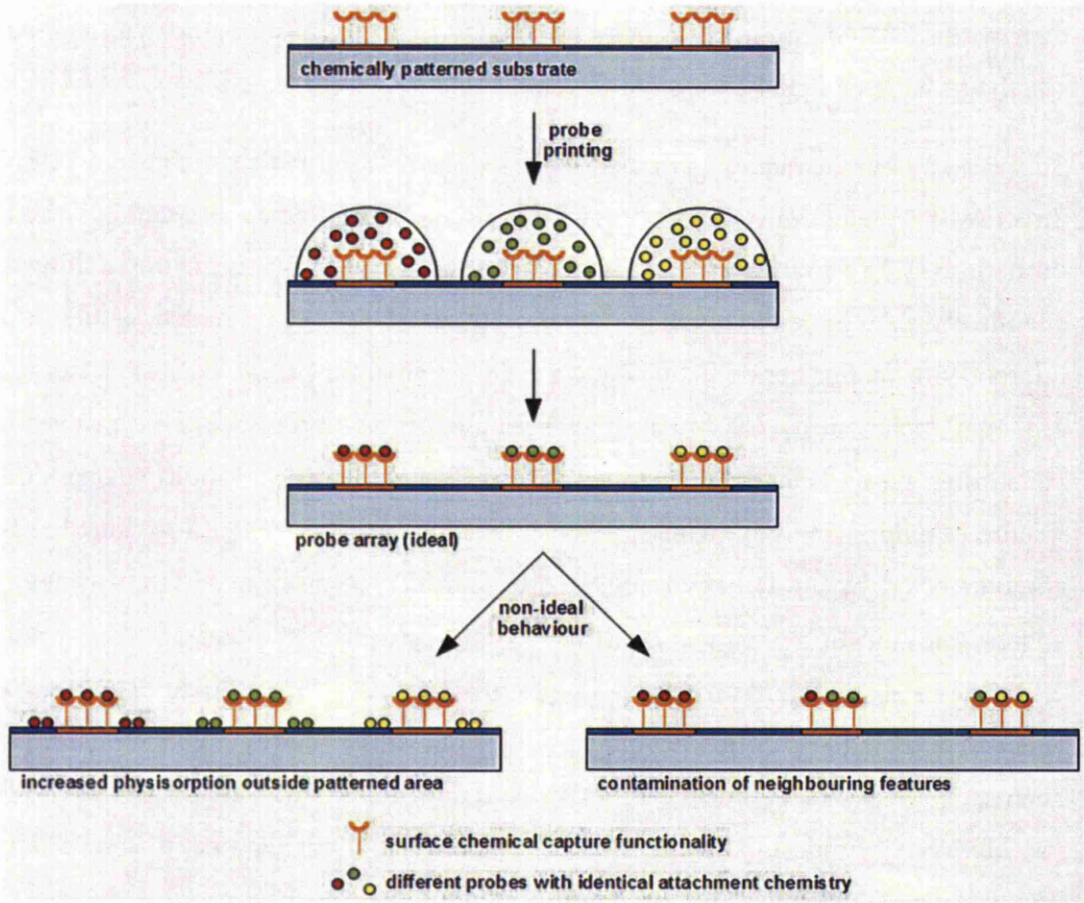

Figure I.1.8. Chemical patterning without a complementary topographical boundary can suffer from non-specific binding (bottom left) or cross-contamination (bottom right)

A recent contribution however proposes a different approach regarding the problems arising from uncertainties related to intra-spot and inter-spot variability (Moran-Mirabal et al. 2007) through the use of physical masks in the form of a hydrophobic polymeric template made of parylene (poly(p-xylene)). The authors identify the lack of research into improving spot quality metrics in microarrays by other means than printing solution composition changes. They also show that, due to the relative success of such strategies, the onus is on smart image processing algorithms. Briefly, openings with controlled size and shape are lithographically patterned into a parylene film. These openings or micro-wells are then used as a template for the printing of DNA capture probes. Following hybridization, the polymer layer is peeled off, a process shown in **Figure I.1.9 a**. The spot morphology resulting from the use of such templates (**Figure I.1.9 c, d**) is shown to be better than that of spots printed using the classic approach (**Figure I.1.9 b**).

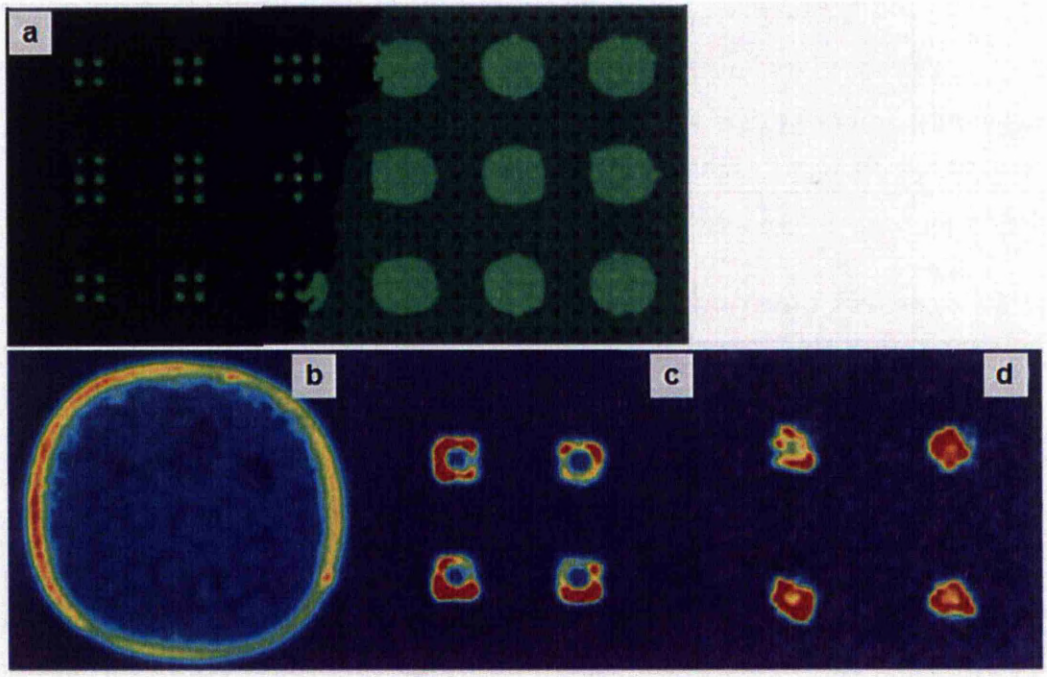

Figure I.1.9. The approach proposed by Lin et al. comprising lift-off parylene masks that can be used to confine the liquid to micro-wells. The authors show that this leads to improved spot uniformity, eliminating coffee-stain morphology. Reprinted with permission from Lin et al. 2007. Copyright (2007) American Chemical Society.

By using the percent ratio of intra-spot standard deviation to intra-spot mean intensity as a measure of intra-spot uniformity (PSD), they showed that the spots printed using the lift-off templates outperformed the ones printed classically. This improvement was attributed to the decrease in the propensity to coffee-stain formation but this didn't arise from a non-pinned contact line. Rather, the presence of parylene (and consequently, the presence of a hydrophilic-hydrophobic interface) was observed to modify the capillary flow inside the droplet from outward (on control slides) to inward (on the patterned slides). While the quality of the templated spots was shown to be better than that of the control ones, using the PSD measure, a visual assessment results in the identification of two problems: the intra-spot uniformity is improved but seems to be plagued by the same (admittedly lower) lack of control over the intra-spot variability. Secondly, the shape of the spot does not seem to be tightly controlled as the patterned material is a plastic. Nevertheless, this contribution serves to identify a new approach to solving the problem of non-uniform printing in microarrays.

I.2 Chapter 2: The Research Question. And One Possible Answer

Having offered a brief insight into the microarray technology and having brought forward the argument for adopting a new approach towards the tighter control of the size printed features, of their location and morphology, a novel technique, compatible with mainstream arrayed probe assay procedures will be discussed.

I.2.1 Research question

It has been shown that, although microarray technology has advanced rapidly and has been broadly accepted and adopted in the fields of genomic (and associated) research, drug discovery and molecular diagnostics, there are still areas that are perfectible. One such area identified by us is the necessity for a better control of feature printing. The implications of printed feature quality on the data extraction and aggregation have been discussed. Briefly, they range from difficulties in low level processing like actual spot finding and foreground-background separation to complex level data analysis and information extraction. Improving spot related parameters results in confidence level of the extracted information enhancement and possibly a reduction in the number of replicates needed and in the complexity of resource hungry computer algorithms used for data extraction and quantification. It is true that considerable effort has been put into improving the printing equipment and understanding that surface chemistry has on the quality of the printed features. However, little research has been put into making use of structured surfaces as a complementary alternative. To this end, what is proposed here is to use purposely engineered substrates, displaying a laterally micro-structured topography that can positively affect printed spot quality metrics.

I.2.2 One possible answer to the research question: structured, fluorescence interference-based substrates

As stated previously, a contribution to the topic has proposed polymer lift-off templates (Moran-Mirabal et al. 2007). Our approach is similar in objective but relies on manipulation of light through a smart geometry of the substrate achievable with standard microfabrication tools. These substrates aim at alleviating problems related to spot quality in a chemistry-independent manner comprising two directions:

- firstly, physical constraint of printed droplets to a geometrically defined, positionally controlled area and, secondly,

- manipulation of light so that fluorescent signal from areas outside the region of interest is suppressed while light coming from the region of interest is amplified[3].

The principle of the method is based on using substrates that have been endowed with z-axis nanostructures having xy ranges in the microns and tens of microns domains that are able to promote the formation of standing waves. These standing waves present axial planes where light is either suppressed or amplified, depending on the relationship between optical path length (the product between geometrical distance and refraction index) and light wavelength. A primary source of inspiration for the architecture needed to meet these attributes was a fluorescence microscopy technique called fluorescence interference contrast microscopy (FLIC microscopy).

The FLIC microscopy technique allows for very accurate distance measurement on the z-axis by relating the intensity of fluorescence emission from a fluorochrome to its distance from a reflective surface. When a fluorophore is placed in the vicinity, i.e., nanometres to micrometres away, of a reflecting surface part of the excitation light is reflected and interferes with the incoming wave. By varying the distance between the emitter, i.e., the fluorophore, and the reflector, i.e. reflecting surface, an amplification or suppression of the intensity of fluorescence can be achieved. The physical and mathematical framework of the process has been reported before (Brandstatter et al. 1988). Using a monolayer of fluorescent molecules on silicon oxide terraces it was demonstrated (Lambacher and Fromherz 1996) that the principles of classical optics explain the modulation of the intensity of fluorescent signals. Based on this observation, the authors proposed a microscopy technique, entitled FLuorescence Interference Contrast microscopy - FLIC, which is capable of accurately measuring nanometre-scale distances on the z-axis. In the original FLIC experiment, the intensity values of the fluorescence emission obtained using a substrate inducing interference effects, i.e. formation of standing waves, are fitted on a curve describing the relationship between the unknown effective optical paths, i.e., thickness of the substrate layer, and the excitation and emission wavelengths

[3] The meaning of the term "amplification" in this context is that of "enhancement". The optical set-up discussed and adopted in this work is passive rather than active (as, for instance, in laser cavities). Amplification would imply that the number of photons is increased which would violate the principle of energy conservation. Through interference, a redistribution of energy rather than an increase or decrease is obtained.

(Brandstatter et al. 1988). Provided that the refraction indices corresponding to the effective optical path segments are known, the distances can be accurately measured.

The mathematical treatment of the optical model of FLIC has been extensively described.(Parthasarathy and Groves 2004) The authors start from a model accounting for the formation of standing waves as direct and reflected excitation and emission light, respectively, interfere. Starting from this ideal model, a more realistic but rather complex model is built by considering the impact of (i) imperfect reflection, (ii) non-normal light incidence, (iii) fluorophore orientation, (iv) light polarization and (v) poly-chromatic emission light. In our study we used as a framework the model accounting for imperfect reflectivity only, since we found that this model describes well, for the first amplification cycle, the fluorescence intensity profile vs. the fluorophore-reflector distance. The basic model is described by **equation 1**, which relates the measured fluorescence to the excitation and emission wavelengths, and optical path length:

$$F_{exp} \propto sin^2\left(\frac{2\pi nh}{\lambda_{ex}}\right) sin^2\left(\frac{2\pi nh}{\lambda_{em}}\right) \quad (1)$$

where F_{exp} is the observed fluorescence intensity; λ_{ex} and λ_{em} are the excitation and emission wavelengths, respectively; n is the index of refraction of the medium that light passes through; h is the reflector-fluorophore distance. The practical application of the model will be discussed in depth in the experimental section. The shape of the curve described by **Eq. 1** is illustrated in **Figure I.2.1** below. The shape of the curve is characteristic of a two beam interference system rather than a multiple beam interference system (like a Fabry-Perot interferometer[4] where the curve is characterized by sharp spikes).

[4] A Fabry-Perot interferometer is a device that can be used as a very sensitive spectrometer consisting of a cavity enclosed by two highly reflective mirrors. The distance between the two reflecting elements can be varied. Inside the cavity, multiple reflections occur giving rise to multiple beam interference. (Totzeck 2012)

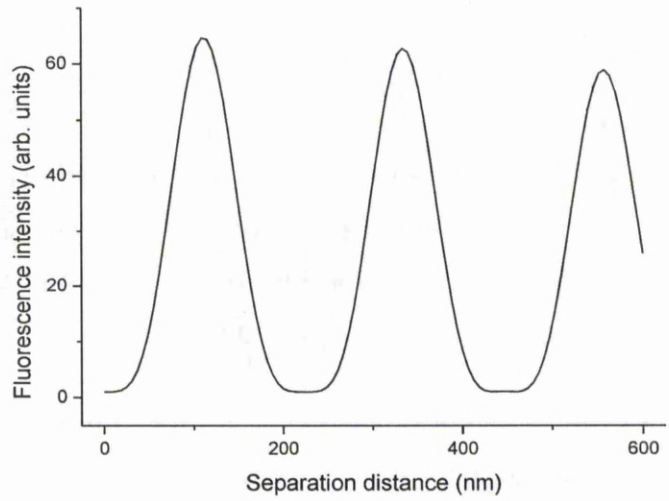

Figure I.2.1. Idealized shape of the curve described by eq. 1, relating the fluorescence intensity to the fluorophore - reflector separation distance

Within the same theoretical framework, but in a rather inverse fashion than the original FLIC experiments, by selecting the proper materials and fabricating structures with heights derived from theory, a fluorophore can be placed in a plane coinciding with interference peaks (points of maximum constructive interference) and as a result its emission will be amplified. Conversely, any extrinsic fluorescence source that needs to be suppressed can be placed in a plane characterized by maximum destructive interference. Indeed, while the original FLIC methodology aimed to use the variations of fluorescence intensity to measure distances with nanometre precision, our approach aims to use the heights of the nanostructures the fluorophore is placed upon to maximise, or minimise, its fluorescence. Moreover, the principle of intensity modulation by height can be applied, within certain limits, to minimise the background or noise.

Interference based phenomena has also been recently proposed as a way to improve signal-to-noise ratio in microarrays by a number of researchers. An architecture based on an optically reflective layer and an optically transparent dielectric was proposed for DNA arrays (Marino et al. 2008; Redkar et al. 2006) with good results; the same principles were later applied to protein microarrays (Cretich et al. 2009). The potential commercial benefits of the technology quickly became apparent, and materialized into patents (Fernandez 2009a; Schultz et al. 2011) and also commercial products (HiSens microarray slides from Schott). However, the novelty of the present approach is the structuring of the dielectric film leading to spatially confined

fluorescence. Additionally, the confinement is geometrically defined a priori using precisely microfabricated structures. This is similar to an extent to Lin's approach but possibly offers an additional advantage related to cost and time. While in the parylene lift off masks approach, once a slide has been printed, the masks needs to be removed and the substrate cannot be reused unless a new parylene layer is deposited and patterned, our proposed slide architecture can potentially be reused after a simple cleaning procedure as long as the structures are not affected (dry cleaning procedure like UV-ozone or plasma).

Having provided the theoretical background for the working principle of the proposed slide layout, it is now necessary to provide a short description of the new slides. Their general layout is illustrated in **Figure I.2.2**. The initial interference based approach relies, in its simplest form, on using a dielectric layer (SiO_2 here) as spacer between the fluorophore and the reflective surface (reflector, silicon - Si - or platinum - Pt). This is a continuous, homogeneous layer onto which features are printed. Excitation light will travel from the source to the fluorophore but some light will travel through the dielectric layer and reach the reflector, where it will be reflected back to the fluorophore. In this way, the relative phase difference between direct and reflected light will be determined by the optical path difference and the wavelength of the light. If the thickness of the dielectric is correctly chosen, the fluorophore will be placed in the plane corresponding to the position where constructive interference forms. The outcome is two-fold: firstly, this means that photoemission will be possible and secondly, since constructive interference results in amplification of light intensity, the photoemission will be amplified correspondingly. The same mechanism is valid for the emission light. It is important to note here that, because the film is homogeneous and continuous, emission from the surface, i.e. resulting from non-specific adsorption of fluorescently labelled target molecules, will also be amplified to a level similar to that of the captured targets. Contrary to this, we hypothesized that, using a structured dielectric film, i.e. an array of pillars and inverted pillars, can be used to "confine" fluorescence to certain areas (green), while suppressing it in other areas (orange) as illustrated in **Figure I.2.2**. To this end, silicon oxide pillars and inverted pillars were fabricated on silicon or platinum surfaces. The two reflectors, i.e. silicon and platinum were used because they have different reflectivity properties, with the metal outperforming the silicon

one. Also, there are two complementary architectures that can lead to the same effect: the pillars and the inverted pillars, which are essentially very shallow nano-wells. The test structures that will be used initially consist of small footprint pillars, between 1 and 25 μm^2, and imaging will be carried out using a confocal microscope. Because the final test of the principle required imaging in a microarray scanner, the resulting images being the ultimate proof, pattern dimensions will be modified to accommodate the resolution of the microarray scanner.

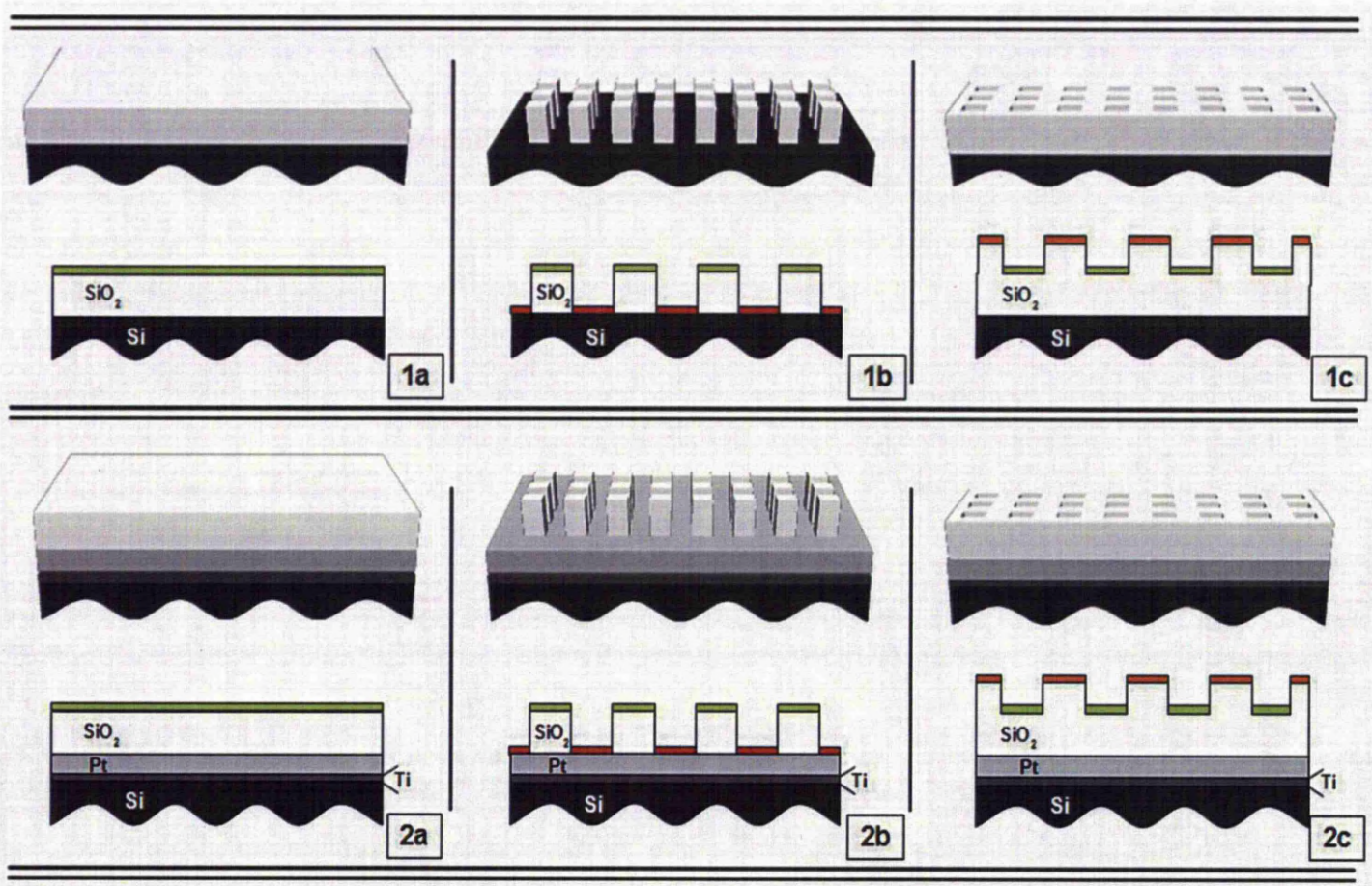

Figure I.2.2. Proposed new substrate architecture to improve fluorescence read-out in bio-molecular recognition-based devices. All designs are based on a multi-layered structure. From left to right, in the first column flat substrates are illustrated while in the middle and right columns, two types of structuring are shown. Each 3D representation is accompanied by a 2D cross-section. When the fluorophore is placed in the green region, its fluorescence is enhanced while when it is located in the red regions, its fluorescence is suppressed.

At this point, a short description of the figures of merit that will be used to asses the quality of the features printed on these new substrates is needed. The minimisation of the noise is critical for the detection and measurement reliability. As the signal of interest is buried in noise, for large levels of noise the signal relative to the background varies too much for a meaningful estimation. Conversely, any decrease of the noise translates in an increase of the sensitivity of the system. Consequently, important efforts by the manufacturers of readout equipment focused on the measurement system–related noise, but relatively less interest has been paid to the minimisation of the noise related to the substrate material. Meanwhile important research by microarray substrate companies and microarray users alike, focused on the minimisation of the noise due to non-specific binding, as well as on the maximisation of the signal of interest.

Indeed, a central quality metric that is commonly quoted by the manufacturers of microarray readout equipment and microarray slides, and their users, is the signal-to-noise ratio (SNR, also abbreviated S/N), or at times denominated as signal-to-background, S/B. Its importance stems from the fact that it is actually a measure of the certainty with which a signal in general, and in particular, the spot intensity, can be identified. As suggested by its definition, the SNR can be improved by amplification of the signal, decreasing the background fluorescence, or by increasing its uniformity. The detection limit and reliable quantification of analytes is of critical importance to biomedical microdevices, involving the mastery of various fields such as analytical chemistry, medical diagnostics, signal processing, and pattern recognition (Danzer 2007). Usually, and depending on the number of samples, a SNR value of 3 is sufficient for a detection event to be characterized by a confidence level of 0.01 (Janiga et al. 2008; Walter et al. 2010). In the case of microarrays, the SNR is usually defined as the background-corrected average intensity in the Region of Interest (RoI) divided by the dispersion of the background intensity measured by the standard deviation of the signal outside RoI. One important clarification needs to be made though: the calculation of the SNR is based on the assumption that the background intensity and standard deviation outside the spot, reflects the intra-spot intensity and SD in the absence of the biomolecular recognition reaction. Unfortunately, this is not always the case but the error associated to such an assumption does not weigh heavily in the final result (Ochs and Bidaut 2002).

Consequently, there are three, concurring, ways of increasing the SNR, i.e., (i) increasing the foreground signal; (ii) decreasing the background; and (iii) increasing the uniformity of the background. The methodology presented here can be used for both the amplification of the foreground signal through the formation of constructive interference as well as, separately, for minimisation of the background fluorescence by destructive interference. In our study, the SNR parameter will be used primarily as a figure of merit quantifying the ability of the proposed chip architecture to efficiently confine fluorescence and discriminate between the fluorescence arising from the two different planes. In other words, the magnitude of the relative suppression with respect to the fluorescence intensity measured where maximal constructive interference forms can be quantified using the SNR. Another reason for using the SNR is that, in the first instance, test structures were immersed in the fluorophore solution rather than spotted. Thus, a measure of uniformity seems less relevant.

A second figure of merit that will be used to asses the quality of the substrates will be the PSD proposed by (Moran-Mirabal et al. 2007) and co-workers. This will be suitable, in conjunction with the SNR, to substrates with printed features.

I.3 Chapter 3: Introduction to microfabrication

I.3.1 Introduction

The term fabrication in the context of semiconductor devices and, more recently, applied in fields associated to bio-medical research has a broad meaning encompassing the entire collection of processes and technologies associated with manufacturing micron and sub-micron range features on solid substrates that, together, form functional devices. The progress of fabrication technology is associated with the necessities imposed by an ever-growing demand for high performance and affordable electronic devices leading to an exponential development in performance and capabilities. This exponential growth has been predicted by Gordon E. Moore from Intel and is known as Moore's law; it is typically illustrated by plotting the number of transistors per chip versus time and which is doubling every 18 months (Moore 1995) (while the cost per transistor should be following a similar but decreasing trend). The future evolution and limits of the technologies in the context of Moore's law is a subject of ongoing debate. But the trend for miniaturization is not characteristic to semiconductor industry only, as technologies originally developed for silicon-based devices have successfully been employed in rapidly developing bio-chip fields (genomics, proteomics, lab-on-a-chip), among others.

The fabrication process can be divided, chronologically, into a number of steps; any number of them can be employed, depending on the particular features that are needed while other are mandatory (e.g. substrate preparation). The miniaturised structures are built on a solid, crystalline support, usually a silicon wafer but also glass or other materials. When silicon is used, high purity silicon is shaped into cylindrical chunks called ingots and sliced into wafers. The surface of the wafers needs to be pre-treated before usage to ensure cleanliness and, if needed, to change the properties of the material (e.g. implantation of impurities when electrical properties need to be changed). If the patterns need to be made into a material different from silicon, that layer, whether metal, semiconductor or dielectric can be deposited on the surface using a variety of methods. Next, patterning of the surface can be achieved, in a first step by applying a layer of a photosensitive material called photoresist; resists can also be sensitive to charged particles like electrons or ions. Other lithographical methods include (nano)imprint lithography, where the

photomask acts also as a mould or, more recently, colloidal lithography (hole–mask colloidal lithography where colloidal spheres, either metal or polymer are used as etch masks, or nanosphere lithography where self-assembly of micro-and nano-spheres are assembled on surfaces to form Fischer patterns and material is deposited in the voids). Also, scanning probe lithography is a good option for low research level testing and production. Once the resist has been exposed, the pattern can be transferred to the underlying layer via wet or dry etching. These steps can be repeated for as many times as needed, depending on the complexity of final product. For small series fabrication, other methods, falling under the umbrella of micromachining make use of lasers or charged particle beams to directly print a pattern or to create 3D structures. Obviously, some form of quality control needs to be implemented at the end of the process; apart from electrical and dopant concentration measurements, characteristic for the semiconductor industry, other forms of analysis like scanning probe and optical microscopy, electron microscopy, profilometry and the like can be employed as needed.

Other fields have taken advantage and built upon the foundations laid by the continuous developments in micro- and nanotechnology, resulting in small revolutions in photonics, telecommunications and bio-medical devices. Concerning the latter, it is now difficult to imagine the evolution of such devices like (bio)sensors of all kind, microfluidic platforms, various types of DNA and protein arrays, to quote just a few in the absence of micro-technology.

I.3.2 Thin film deposition

Films with the thickness on one axis very small compared to the dimension on the other axes generally fall in a special category of "thin films". They are used in semiconductor fabrication but are also common in optical applications, from mirrors and filters in microscopy to the optical coatings of glasses. Thin films can consist of metals, single or alloys, non-metals, semiconductor materials or compound materials like oxides, nitrides, silicides, carbides and so on. An important aspect of thin films is that many of the bulk properties of the material are not conserved in the case of thin films, giving rise to thickness dependant properties. For instance, the resistivity of thin metal films is higher than that of bulk materials, density of thin films is almost always lower than that of their bulk counterparts (Franssila 2004c), optical properties need to be determined experimentally as the deposition parameters can

affect them significantly (Bennett et al. 1989; Borgogno et al. 1984) and the list can continue. A complete list of properties that change with diminishing dimensions, and the direction of that change is available (Wasa et al. 2004a).

The properties of thin films are determined by the method used to create them. From this standpoint, we can distinguish gas phase physical and chemical methods, electrochemical methods and liquid coating (spin-, dip- and spray-coating). The physical and chemical methods take place in vacuum. The choice of the method is based on the compatibility with the material to be deposited, the compatibility with the substrate material, throughput and costs.

Physical deposition from gas phase is called physical vapour deposition (PVD) and is a method of depositing thin films by bringing the material to be deposited, the target material, to a gaseous state by various means and directing these vapours to the substrate, where they condense to form a (continuous) film. The transition from solid phase of the target material to gaseous phase can be accomplished through heating, ablation or sputtering. Thermal evaporation can be achieved by electrically heating a crucible containing the target material, heating a filament that radiatively or conductively heats the target, or using a filament coated in the target material to name but a few. Evaporation can also be achieved by heating the target material using an electron beam focused at the target, where the kinetic energy of the electrons is transformed to thermal energy upon electron bombardment. The formation of X-rays during the process has to be considered but e-beam evaporation has the advantage of high evaporation rates (Franssila 2004b). Evaporation can also be achieved by making use of light-matter interaction as is the case of laser induced deposition via ablation, a process of delivering energy to a material that is sufficiently high to break the bonds between the atomic or molecular species and remove them through evaporation (Wasa et al. 2004c). Some advantages of laser evaporation are the high power density leading to high heating rates; and for some target materials, the composition of the films can follow that of the target, an advantage over conventional thermal deposition (Manova et al. 2010). A particular case of thermal evaporation deposition is molecular beam epitaxy, whose particularity stems not from the heating technique but from the design of the target

material holder. The "Knudsen cell"[5] is an enclosure with a very small aperture that, upon heating, favours the formation and sustention of solid phase - gas phase equilibrium. The size of the aperture is chosen so that this equilibrium is not disturbed. In this way, the flow of material from the target to the substrate is uniform and free of sudden variations. Molecular beam epitaxy allows for the growth of crystalline (as opposed to polycrystalline or amorphous in the case of open source techniques) thin films that replicate the crystalline lattice of the substrate (provided that there is good matching between the two). Probably the most commonly used method for metal deposition is sputtering. This involves bombardment of the target with noble gas ions, almost exclusively Ar^+, resulting in the displacement of target atoms from the target as a result of momentum transfer. Because of this, the energy of the sputtered particles can be quite high, even though, since the pressure at which sputtering deposition is done is high, these particles are slowed down by collisions with gas molecules. There are both beneficial effects to higher energy particles, such as increased adhesion due to displacement of loosely bound atoms or contaminating species on the substrate, but also negative effects such as film or substrate damage (Franssila 2004a; Rossnagel 2002).

The other gas-phase deposition method is chemical vapour deposition (CVD). In CVD, the precursors of the film are already in gas phase and they are flowed on top of the substrates, where they react to it. In CVD, as opposed to PVD, a chemical reaction takes place at the surface of the substrate. The surface reaction rate is temperature dependent but the mass transport of reactive species from the bulk to the surface and the desorption rate of spent reactants from that same surface need to be accounted for. The high temperature of the process is required to provide enough energy to start the chemical reaction (activation energy). Unfortunately, this means that not all substrates or combinations of substrate and film material can be accommodated. An enhancement of this method is using plasma to (partially) supply the necessary energy to the precursor molecules. This reduces the energy barrier that the reactant species need to cross and, consequently, a lower temperature can be employed.

[5] The Knudsen regime for a gas is attained when the mean free path of the components of the gas is larger than the size of the container that holds the gas; that is to say, collisions between gas phase components are less frequent than collisions between these species and the walls of the enclosure (Chorkendorff and Niemantsverdriet 2003)

Generally, regardless of the deposition method, the process can be described as a stepwise process. An overview of the process is described (Wasa et al. 2004b) (in depth treatment is available (SreeHarsha 2006)). First, the gas phase species are adsorbed on the surface of the substrate. These species are mobile and are able to move on the surface until, by meeting other identical species, the adsorbate forms clusters (atomic aggregates containing up to a few million atoms). The next step is either desorption or growth of the cluster via interaction and incorporation of other adsorbed aggregates. This growth renders the cluster thermodynamically stable. The number of clusters that can form on the surface is determined by complex factors, both material and process related. These clusters then coalesce on the surface and form islands which grow laterally until the entire surface is covered (other cluster formation events may take place meanwhile). The growth of the films is constantly monitored, both for thickness and also for quality markers. This can be done using techniques that allow for in situ and real time measurements: quartz crystal microbalance, ellipsometry for thickness measurements, low energy electron diffraction for crystalinity (in the case of MBE) and mass spectrometry and the like to monitor the gas phase species in the case of CVD.

Metal layers can also be deposited through electrochemical processes. For instance, the substrate can be immersed in an electrolyte solution containing the metal to be deposited and connected to the cathode electrode. When an electrical current is passed through the circuit thus formed, the metal in the electrolyte solution will be deposited on the wafer, the amount of deposited material being proportional to the current. Electroless deposition is also possible and consists of reducing a metal compound from an electrolyte solution on a surface that has previously treated with a catalyst (Balci et al. 2012).

Thin oxide layers can also be deposited starting from alkoxides, compounds with the formula $M(OR)_x$, where M can be a metal or non-metal (e.g. silicon). If deposition is carried out from the liquid phase, the method consists of using an alkoxide of the elements whose oxide needs to be deposited which, through hydrolysis and polymerization reactions, forms a porous network with liquid trapped inside the pores - the gel. Thermal treatment of this resulting gel yields an oxide (Klein 1991; Turova 2002). Deposition can be made through spin-coating, spray coating or dip-coating. The other option is to start from the vapours of the precursor alkoxide (other

types of precursors can also be used: borazane and borazine for boron nitride films (Kim et al. 2012), tetrakisdimethylamidotitanium and t-butylarsine for titanium arsenide films (Thomas et al. 2011), trimethylaminealuminium hydride for aluminum (Benson et al. 2012)), provided that the vapour pressure is reasonably high (metal-organic chemical vapour deposition - MOCVD) (Bradley 2001; Torres-Huerta et al. 2012).

I.3.3 Patterning

Surface patterning involves, in an initial step, the creation of an image onto a photosensitive layer called (photo)resist. In this initial stage, image formation can be achieved through various mechanisms, all of them being light induced/initiated. This complex process yields an organic polymeric layer of material with either the positive or negative image of the patterns which can be subsequently used as a mask to transfer the image to the layer underneath. Thus, the resist does not only provide the image to be transferred but also withstands the treatment involved in image transfer. The succession of steps involved in the creation of this organic polymeric mask fall under the term of lithography. A brief history of the development of resist materials is available in (Willson et al. 1997) while the evolution of photolithography from the 1960's until the 2000's is available in (Bruning 1997, 2007).The basic steps will be outlined below.

I.3.3.1 Surface treatment

Lithography can be performed on a variety of solid substrates but semiconductor fabrication takes place on silicon wafers and that is why we will refer to these substrates. A clean silicon surface will spontaneously develop an oxide film, a few nanometer in thickness, upon exposure to air. Water vapours from the atmosphere promote the formation of surface silanol groups, rendering the film hydrophilic. As will be seen later, resists are quite non-polar so adhesion between the resist and the substrate will be poor. It is therefore necessary to match the surface energy of the substrate with that of the resist and this can be achieved by modifying the surface chemistry of the oxide (priming), i.e. decreasing its hydrophilicity. Although this can be achieved with a variety of reagents, one commonly used chemical is hexamethyldisilazane (HMDS). The structure consists of two methyl tri-substituted silane molecules joined together through a secondary amine bridge. Upon exposure of the clean and dehydrated substrate to HMDS vapours at a temperature between

100 and 200°C, the amine bridge cleaves and the two silane radicals react to the surface silanol groups resulting in a surface that displays trimethylsilyl groups. The by-product of this reaction is ammonia (see **Figure I.3.1**). Although liquid priming can be done, the vapour phase correspondent is preferred due to better uniformity and lower reagent usage. Sub-optimal priming and over-priming are possible and can negative consequences on resist adhesion (Levinson 2005a).

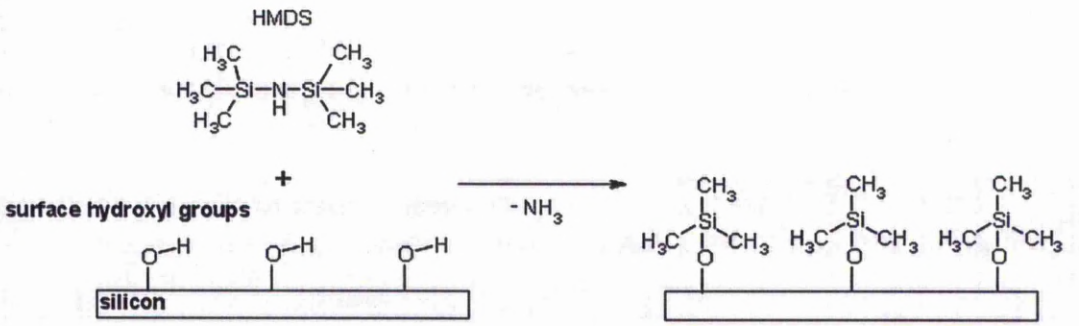

Figure I.3.1. Mechanism for HMDS surface priming.

Priming can also be applied on other materials with surfaces exposing OH groups like glass. Pre-cleaning of these surfaces is necessary before priming and it can be achieved using wet chemical (RCA[6] cleaning, piranha solution, hydrofluoric acid) or dry (oxygen plasma, UV-ozone) etching methods as these will oxidize organic contaminants (remove metal contaminants in the case of the RCA clean) and activate the surface, i.e. create OH groups. The dehydration step is achieved by baking the substrates at temperatures between 120 and 150°C to remove adsorbed water (extensive information on cleaning technology for the microelectronic industry is available (Reinhardt and Kern 2008)).

I.3.3.2 Application of the resist

Resist materials are supplied as solutions, the solid polymeric material and additives being dissolved in a solvent or a mixture of solvents. The resist can be applied through several methods, namely spin-coating, spray-coating and dip-coating. The most commonly used method is spin-coating because, although it is less economical than spray-coating, it gives better results in terms of film uniformity (Levinson 2005b).

---

[6] RCA clean was developed by Werner Kern while working for Radio Corporation of America (which the name of the procedure stands for) comprising a wash in a 1:1:5 NH_4OH:H_2O_2:water mixture and a second wash in a 1:1:6 HCl:H_2O_2:water mixture

Spin-coating is a procedure wherein a volume of resist is dispensed onto the substrate and the film is spread onto it by spinning the substrate at a controlled speed and acceleration, sometimes passing through different speed regimes. The resist can be applied while the substrate is at rest or is spinning. The purpose of spin-coating is to achieve a defect-free resist layer with controlled and uniform thickness over the entire substrate. In principle, the factor affecting the thickness of the film are spinning speed and resist viscosity (which, in turn, is determined by the nature of the solvent(s), the solid content and the molecular weight of the dissolved material) (Levinson 2005b); typically, layer thickness versus spinning speed plots are provided for each resist. However, the coating process is only optimal in certain speed ranges, depending on the size of the substrate. Resist thickness is also influenced by the rate at which the solvent evaporates and this in turn imposes the need for good temperature gas extraction control during the process to avoid film thickness non-uniformity. The thickness of the resist layer is also dictated by the other factors. Normally, best resolution is achieved with a thin layer of resist but this can only be decreased down to a limit determined by physical constraints. For instance, the patterned resist acts as an etch mask in the pattern transfer stage of the process but the etch selectivity is not absolute; that is to say that the resist film is affected by the etchant but, ideally, at a rate smaller than that with which the substrate is being etched. Another instance when the patterned resist acts like a mask is during ion implantation and, rather obviously, the masking performance (capacity to stop incoming ions) depends on the thickness of the resist layer. Consequently, the choice of a layer thickness is not a trivial matter. Moreover, the behaviour of very thin layers is very different from that of the bulk material because they are confined to very small dimensions in at least one direction. Thus, interfacial phenomena become important and film quality becomes more sensitive to substrate defects (Okoroanyanwu 2010c).

After the spin-coating, the resist layer still contains solvent that needs to be removed before the latent pattern can be created through exposure. This is achieved in the pre-baking (soft bake) stage, albeit not totally since the soft bake temperature is maintained below the solvent's boiling point. Soft baking is commonly carried out on hot-plates although convection ovens are also used. Controlled cooling down of the substrates after this stage is also as important as the heating.

I.3.3.3 Exposure

The pattern needs to be defined on the resist layer first by exposing it to the electromagnetic radiation of appropriate wavelength (energy) through a mask. The mask consists of a solid, transparent support, usually fused quartz (due to the material's good thermal properties, specifically its low coefficient of thermal expansion), on top of which the negative or positive image of the pattern to be transferred to the resist layer is patterned into a non-transparent layer. The non-transparent layer is either metallic chromium or chromium containing alloys due to the very good absorbance (low transmittance). The fabrication of masks involves depositing the opaque layer onto the quartz substrate and applying the resist followed by exposure using a direct-write technique like electron beam or laser patterning. Quality control is very tight in mask fabrication to virtually eliminate any defects since masks are used to replicate a certain pattern on thousands of wafers, making the masks themselves quite expensive (thousand to tens of thousands dollars per mask) and the process of mask making very laborious. In practice, masks can be copied and the high quality master is retained, and can be replicated in case damages are incurred by the copies. Since masks are fabricated for specific patterns, the only way to create a new mask is through direct write lithography, using electron beam or laser pattern generators. Direct writing thus enables the generation of any pattern but the fact that the exposure is carried out pixel by pixel (in a scanning fashion) is limited by time constraints and data constraints (volume of data that describes the geometry of a pattern – address of each pixel – and the data rate needed to transfer this data). After exposure, the pattern is developed in the appropriate solvent (mixture) and then the pattern is transferred to the opaque layer through wet chemical or plasma etching and then the resist can be stripped. The mask containing the required pattern is then used to expose a wafer onto which resist was previously spun. Originally, the mask was brought into contact with the resist or kept at a very small distance away from it. These masks covered the entire surface of the wafer and were transferring the pattern in a 1:1 manner, thus relying on homogeneous illumination intensity across the entire field. The advent of projection lithography, illustrated in **Figure I.3.2** along with contact and proximity printing for comparison, however, which relies on placing the mask at a distance from the wafer, imaging it and then using optical elements to scale this image down, eliminated the problems related to the frequent damaging of the mask through contact contamination or the lower resolution of proximity exposures

due to diffraction (Seisyan 2011). The idea behind projection lithography came from early mask making technology (Becker 2003) that involved the use of a photorepeater, in which patterns for circuits were repeatedly imaged onto the blank mask after being scaled down optically. Projection lithography is now carried out in rigs called "steppers". The operating principle in steppers relies on projecting the scaled down pattern from a photomask to the wafer. When the right dose of energy has been delivered to the surface, the wafer is moved relative to the position of the mask and the process is repeated. When this mode of operation is employed, the steppers are called "step-and-repeat". A hybrid advancement of this technology called "step-and-scan" which relies on exposing a fraction of the mask through a slit and scanning both the mask and the wafer stage, resulting in advantages related to the complexity of the lens and the efficient use of large fields.

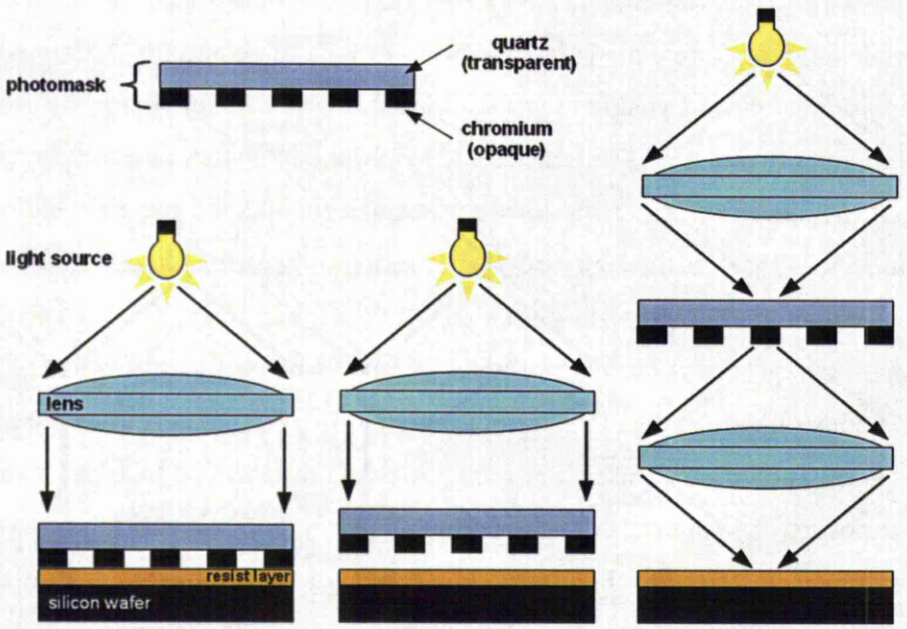

Figure I.3.2. Illustration of contact, proximity and projection printing (from left to right) respectively. Adapted with permission from (Seisyan 2011). Copyright (2011) American Institute of Physics

Generally, a resist formulation consists in a resin (of monomeric or polymeric nature), photosensitizer and additives, all dissolved in a certain solvent. Interaction of resists with the relevant electromagnetic radiation wavelength, or charged particle energy, results in a change that affects its solubility in the developer solution, relative to the unexposed areas. Resists are classified into negative and positive tone, depending on whether the resist looses or gains solubility as a result of exposure.

This is illustrated in **Figure I.3.3** where the patterning tonality for both positive and negative tone resist is shown. Thus, for

- negative resists: the part of the resist that is exposed to radiation loses solubility in the developer and for
- positive resists: the exposed area of the resist becomes soluble in the developer.

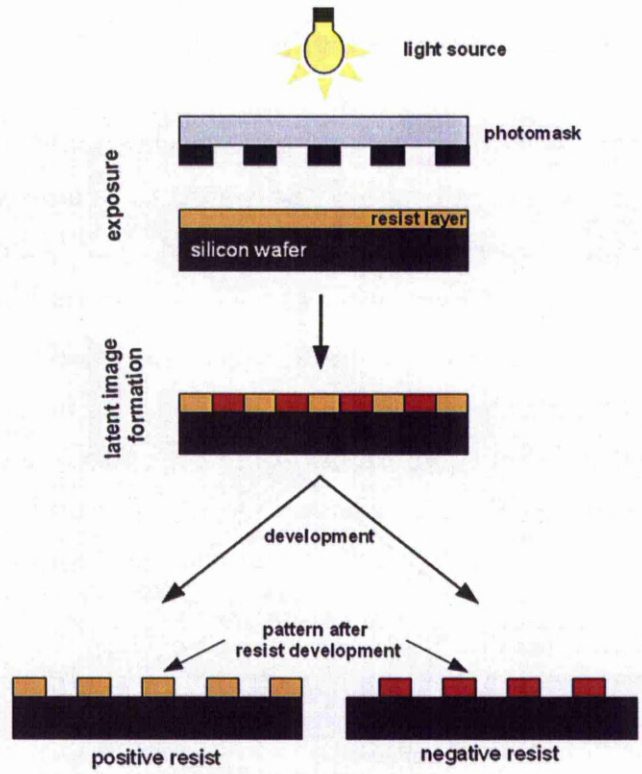

Figure I.3.3. Schematic depiction of positive (right) and negative (left) photoresists. With positive resists, the exposed areas are washed away and for negative resists, the resist is removed from the unexposed areas upon development

However, the choice of resist tonality is not trivial, as the images resulting from dark-field and bright-field masks are not complementary, and, depending on the pattern type, a certain tone is favoured over the other (De Simone et al. 2011).

Upon exposure of the resist, a latent image is said to form inside it; that is to say, the pattern from the mask is replicated inside the resist in the form of a chemical spatial distribution. In negative resists, this mechanism is generally based on crosslinking of the individual polymer strands, generating insoluble species; additionally, negative resists can work either through polymerization of monomers or polarity change. In the case of both crosslinking through radiation-generated species, and polarity

change, the sensitivity of the resist can be improved through chemical amplification, i.e. introduction of a chemical that, upon exposure to light, catalyses the changes that lead to solubility modification throughout the resist (Ito 2007). This has deep implications on the sensitivity of the resist in that one photon can fuel many reaction events, leading to a decrease in the amount of light – dose – needed to induce a change in the photosensitive layer and results in increased throughput. This is in opposition to a non-amplified resist where a photon is responsible for one reaction event only. The image formation in positive resists can take place through two mechanisms, main chain scission or polarity switch, both in either the chemically amplified or non-amplified form. Apart from the general mechanisms characterising image formation in the negative and positive resists, there are other characteristics that differentiate them. For instance, the non-exposed areas of a negative resist are developed using organic solvents; while the exposed, crosslinked resist is insoluble in these solvents, it will however take up solvent and swell. This is in opposition to positive resists, where the exposed resist is soluble in water whereas the non-exposed areas are not affected by the presence of water since they are hydrophobic. The swelling affects the achievable resolution and, although solvent can be removed through subsequent post-exposure baking steps, it has the potential to cause pattern irregularities. Nevertheless, negative resists are the resists of choice in lift-off processes. The lift-off process is a procedure for patterning metal or inorganic layers by depositing them on a patterned resist. Upon dissolution of the resist, the metal or inorganic resting on the resist will essentially lift leaving behind only the metal or inorganic resting on the substrate. The straight of negative undercut is characteristic of negative resists while positive undercut characterizes positive resists. It can be seen in **Figure I.3.4** that positive undercut can favour whisker formation upon resist dissolution.

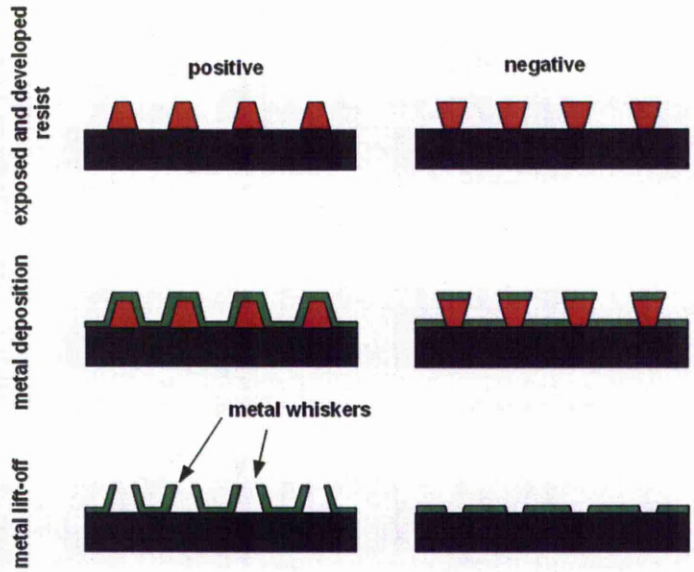

Figure I.3.4. Resist undercut can affect the outcome of metal patterning through lift-off. A straight or negative undercut characteristic for negative resists is beneficial while a positive undercut, characteristic of positive resists, can lead to the appearance of whiskers or even to the formation of a continuous metal layer, making lift-off impossible

Some commonly used photoresists and their corresponding image formation mechanisms are illustrated below:

I.3.3.3.1 Negative resists

A negative resist, commonly (if not exclusively) used in the creation of moulds for (bio)MEMS and microfluidic devices is SU-8. This resist comprises a resin containing 8 epoxy groups per monomer (hence the name) and a photoacid generator (PAG). Upon exposure, the PAG decomposes and provides the proton that, in the initiation step, will open the epoxide ring. Once the reaction is initialized, the polymerization of the monomer then propagates further by subsequent ring opening reactions. Initiation and propagation take place during the post-exposure bake (Teh et al. 2005). This process is shown schematically in **Figure I.3.5**.

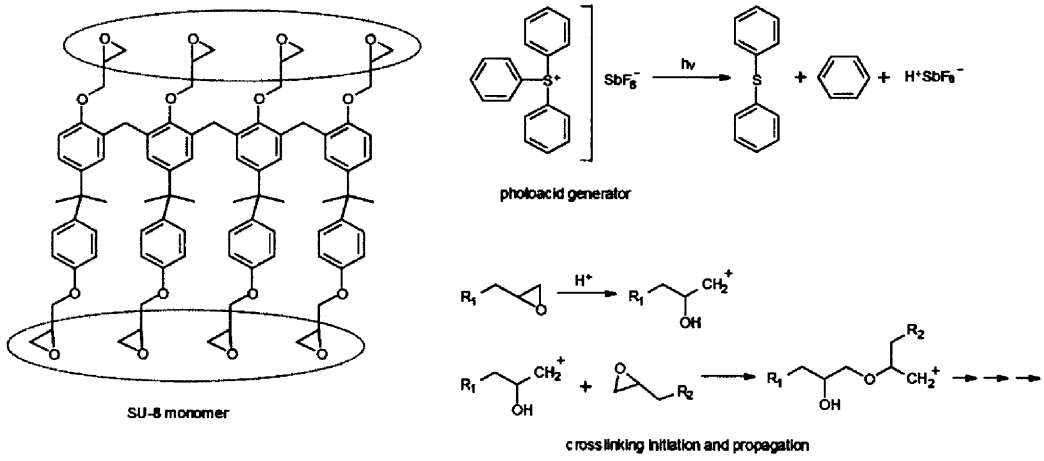

Figure I.3.5. The structure of SU-8 (left) and latent image formation mechanism (right). Upon light absorption, the PAG decomposes to form the acidic specie (antimonic acid, $HSbF_6$). Polymerization of the monomer is initiated through the acid (H^+) catalysed epoxide ring opening reaction resulting in radical[7] formation[8]. The process repeats itself through the propagation stage. Adapted with permission from (Teh et al. 2005). Copyright (2005) American Institute of Physics/American physical Society.

SU-8 is a chemically amplified resist valued mainly for its low absorbance which allows light to penetrate into the resist layer, down to the substrate. This means that very high aspect ratio structures can be fabricated. It is also notoriously difficult to strip from surfaces and that is why it is used in applications that rely on the presence of the crosslinked resist (mould making for imprint lithography, soft lithography).

I.3.3.3.2 Positive resists

Novolac/DNQ

According to (Reiser et al. 1996), in 1996, 98% of the integrated circuits fabricated worldwide used a Novolac/DNQ base photoresist, this system having been the workhorse of semiconductor fabrication since the 70's to the 90's. The photoresist is comprised of a water-soluble Novolac (originally spelled Novolak) polymer of the reaction product between phenol and formaldehyde, and an azide derivative of naphtoquinone acting as a dissolution inhibitor. Upon exposure to UV light, the photosensitive DNQ will decompose to an unstable intermediary which, in the presence of water transforms into a carboxylic acid which is soluble in the base aqueous developer.

[7] "A molecular entity [...]possessing an unpaired electron." from (McNaught et al. 1997)
[8] "A chain polymerization in which the kinetic-chain carriers are radicals." from (McNaught et al. 1997)

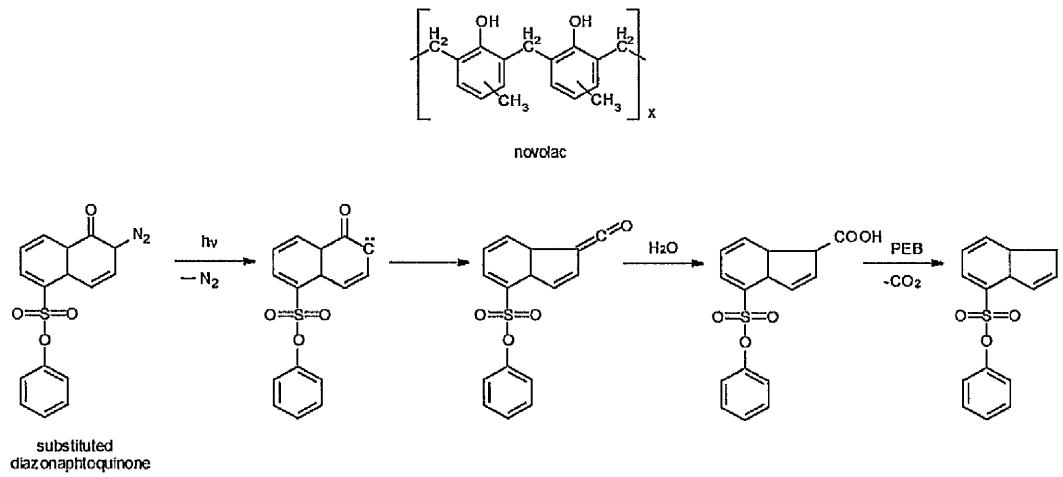

Figure I.3.6. Structure of Novolac (top) and DNQ (bottom) and its chemical transformation leading to solubility change of Novolac upon light exposure. The substituted DNQ looses molecular nitrogen as a result of light absorption to form an unstable intermediary (1) that rearranges to form a ketene (2). In the presence of water, the ketene is transformed into a indene-carboxylic acid (3) which undergoes heat induced decarboxylation (4). Adapted with permission from (Reiser et al. 2002). Copyright (2002) Elsevier.

The process outlined in **Figure I.3.6** above illustrates the ideal process pathway but side reactions with both negative and positive impact exist (Okoroanyanwu 2010b). The mechanism of dissolution inhibition was not fully understood in the beginning and it was assumed that the formation of the indenecarboxilic acid plays the main role. However, by assessing the solubility of the Novolac resin in the presence of unsubstituted DNQ, arenesulfonic acid and the substituted DNQ respectively, it was shown that the contribution of the unsubstituted DNQ has a marginal effect on the solubility of Novolac in aqueous basic media whereas the arenesulfonic acid ester of naphthalene has a pronounced effect. This lead to the proposition of a mechanism in which the heat evolved through the rearrangement of the radical species actually disrupts the hydrogen bond between the sulfonic acid and the hydroxyl groups of the resin, leading to the solubilisation of the Novolac (Reiser 1998; Reiser et al. 2000).

PHS

Another chemically amplified positive resist system is based on poly(hydroxystyrene) (PHS) and can be exposed at lower wavelengths than DNQ/Novolac based systems due to lower absorbance characteristics (Okoroanyanwu 2010a). As opposed to the latter, in PHS-based systems the dissolution inhibitor is bound to the polymer. Moreover, interestingly enough, PHS based systems can be used in both tones, depending on the solvent used for development (Ito 1997). The mechanism of image formation is based on latent image

formation through photoacid generation followed by heat-induced acid hydrolysis of the protecting group. The protective group further decomposes into gaseous compounds (Miyake et al. 2001). The process is outlined schematically in **Figure I.3.7**.

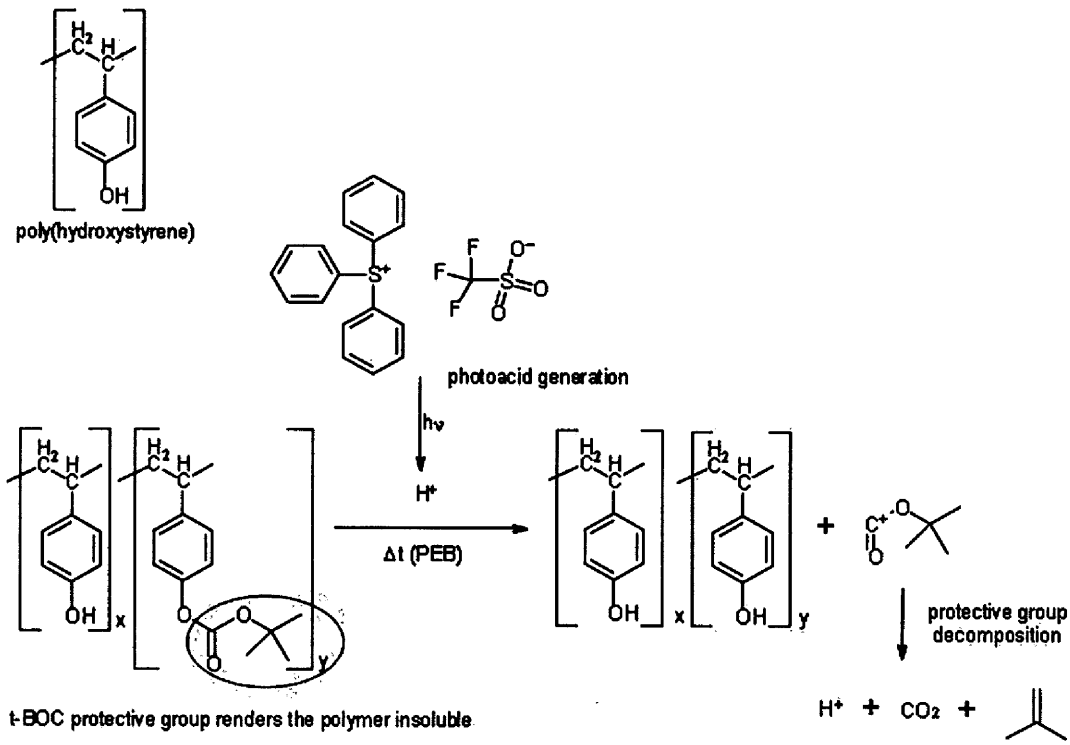

Figure I.3.7. Structure of PHS and the solubility change mechanism as a result of light exposure. Upon exposure to light, the PAG undergoes photolysis resulting in Lewis acid[9] formation (the triflate anion, $CF_3SO_3^-$). This acidic specie catalyses the thermal cleavage of the protective group (which decomposes further into carbon dioxide and isobutene with acid regeneration) and renders the resist soluble in aqueous media. Edited from (Ito 2007) and (Miyake et al. 2001)

I.3.3.4 Post-exposure bake

In the two illustrated cases of chemically amplified resists, an additional heat treatment step is necessary after the exposure. The need for this extra step can be imposed by several reasons. For chemically amplified resists (Rodriguez-Canto et al. 2011), again illustrated in the case of SU-8, the exposure generates the photoacid while the change in solubility is achieved via heating. Another aspect is related to the non-uniform axial distribution of the photoactive specie due to formation of standing

[9] "A molecular entity (and the corresponding chemical species) that is an electron-pair acceptor and therefore able to react with a Lewis base to form a Lewis adduct, by sharing the electron pair furnished by the Lewis base." from (McNaught et al. 1997)

waves. Standing waves form as a result of interference between direct light travelling downwards through the resist and light being reflected by the reflecting substrate at the bottom of the resist layer. In other words, the photoactive compound can receive different doses as a function of its axial position (along the z-axis of the resist, planes where constructive and destructive interference occurs alternatively). The photoactive species can be made to diffuse through the resist by heating. Needles to say that temperature and time control during this step is critical, as unwanted effects like excessive diffusion leading to blurring of the latent image and loss of resolution, and poor line edge roughness (Reynolds and Taylor 1999; Sha et al. 2009) can appear at non-optimal temperatures.

I.3.3.5 Resist development

The development step is the process of removing the portion of resist that is soluble in the development solvent. Essentially, the image that until this point existed as a distribution of chemical species, the latent image, is now created in topography by the removal of material through selective solvation. Because of this, development can be considered to be a critical step. Negative resists are developed from organic solvents while positive resists are developed from aqueous basic ones (TMAOH). For features with a high aspect ratio, additives in the form of surfactants are used with the developer to reduce the surface tension of the developer and mitigate the capillary effect (Yeh et al. 2011). After development is complete, drying is achieved via spinning.

I.3.4 Pattern transfer

The role of the resist is to define the pattern that will be transferred to the underlayer. For this reason, the resist has to be able to withstand the process of pattern transfer which is achieved by a form of etching (and hence, the name). Etching is a process to remove material (in a controlled manner) from a certain area. This process can be characterized by two parameters: the etch rate, which is the speed at which material, measured as depth, is removed (measured in length/depth units per time); and the etch selectivity, which is the ratio of the etch rates for two different materials (etch selectivity is expressed as a ratio for two given materials) (Campbell 2008a). Obviously, the etch rate needs to be fast but not fast enough to render the process difficult to control and etch selectivity needs to be high to ensure good discrimination between materials. Another characteristic of the etching process is its isotropy. This

is both substrate and technique dependent. Isotropy is determined by the advancement of the etch front: if it advances with the same rate in all directions, the process is said to be isotropic whereas if the advancement takes place on a preferred direction, it is called anisotropic (at a certain anisotropy degree). The difference between isotropic and anisotropic etching is illustrated in **Figure I.3.8**. Etching can be carried out using a liquid system (wet chemical etching) or in a gas phase, at medium to high vacuum.

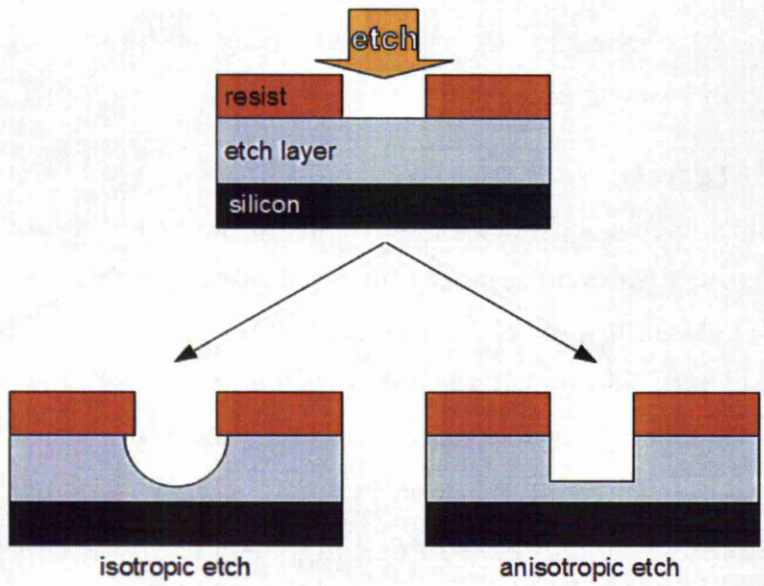

Figure I.3.8. Etch profile for an isotropic (left) and anisotropic (right) process

Wet chemical etching is performed in liquid solutions, usually corrosive ones, and the material removal process is based on the formation of soluble chemical compounds by reaction of the components in the etch solution with the substrate. The composition of these solutions depends on the nature of the material that needs to be removed and the material that acts as mask. The variety of wet chemical etch recipes is very vast, sources for these recipes being available (Williams et al. 2003; Williams and Muller 1996). Wet chemical etching has its drawbacks, generally related to the generation of liquid (toxic) waste, susceptibility to defects due to particulate contamination and less control of the process (Campbell 2008b; Nakata et al. 1980).

Non-wet etching methods are based on using gas phase, more or less energetic, reactive species (plasmas) that attack the surface and dislodge surface atoms in the form of gaseous compounds. Depending on the pressure at which the process takes place, one can identify high pressure plasma etching, reactive ion etching, high

density plasma etching and ion milling (Campbell 2008b). A plasma etching process operating at lower pressures is high density plasma etching. Because the plasma is operated at high vacuum, the mean free path of the reactive species is longer, meaning that the energy needed to accelerate them can be maintained at lower levels. This translates into lower surface damage and better etch selectivity. Operating at lower pressures, in reactive ion etching, the dislocation of surface volatiles formed as a result of reaction between plasma generated reactive species and the surface is enhanced by bombardment with heavier ions. The RIE can achieve high anisotropy because the ions movement is given by the direction of the electric field, which is perpendicular to the substrate (therefore, parallel to the walls of the feature)(Oehrlein 1986). Formation of protective coatings on the walls can further be stimulated by modifying the plasma composition (Hooda et al. 2010; Wu et al. 2010; Zimmermann et al. 2011). An etching process that requires an even higher vacuum is ion milling. This is essentially a physical process in which plasma generated noble gas ions remove surface atoms through sputtering (Simchi et al. 2009). Some disadvantages include low throughput and a poor selectivity. Advantages however include the broad variety of materials that can be etched due to the non-chemical nature of the process and the good anisotropy, thus being mostly used for micromachining (Thornell and Johansson 1998).

I.3.5 Other lithographical techniques

Many other patterning methods have been developed. They are referenced to as lithographical methods although not all of them use the pattern formation process outlined above. In the following, some of these methods will be illustrated.

Imprint lithography

NanoImprint lithography (NIL) is a relatively young technique, being proposed in 1995 by (Chou et al. 1995, 1996a, b). It is an imprint process that allows replication of patterns from a solid, non-deformable mould into a layer of soft material and it is illustrated in **Figure I.3.9**. The deformable material is either a polymer that is heated to above its glass transition temperature in the imprint step and then solidified via cooling or the soft layer can be a monomer whose polymerization can be either heat- or light-mediated. In the latter case, the stamp, or at least some regions of the stamp, needs to be transparent to the wavelength used to initiate polymerization (Jang et al.

2010). The patterns can then either be used as an etch mask or the compressed material can be removed via etching. The main advantage of NIL is that it is a high throughput technique that allows sub-micron patterning with low cost. The limiting process is the fabrication of the mould which relies on direct-write lithographical methods. A recent development of NIL technology is the substrate conformal imprint lithography (SCIL) where a PDMS flexible stamp is used to imprint features into a resist or sol-gel film (Ji et al. 2010; Verschuuren and Sprang 2007). This technology allows nano-patterning of large areas being immune to surface flatness variations.

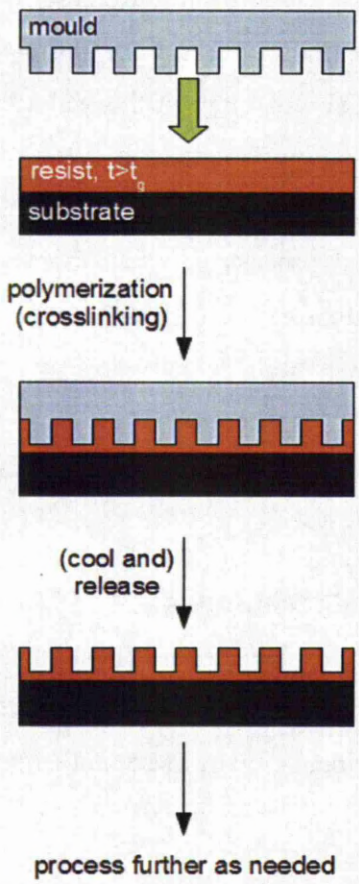

Figure I.3.9. General principle of imprint lithography

Soft lithography – microcontact printing

Soft lithography is a collection of techniques for micro- and nano-fabrication using moulds to replicate patterns in generally soft materials (Xia and Whitesides 1998). In its most used form, micro-contact printing (μCP), first proposed in 1994 (Wilbur et al. 1994), involves the replication of topographical features into a flexible layer (typically PDMS) using a solid, non-deformable mould. The stamp is then exposed

to a solution containing reagents or (bio)molecules that will be deposited on the surface of the substrate. The stamp is then pressed against the surface of the substrate and patterning is achieved by transfer of the relevant molecules from the stamp. The process is outlined in **Figure I.3.10**. The extent of the contact between recessed areas on the stamp and the surface (if any) depends on the geometrical parameters of the stamp and the pressure applied (Sharp et al. 2004). Applications of soft lithography can be very broad, ranging from patterning surfaces with etch-protective layers (Duan et al. 2010) to directed growth of nanowires (Kang et al. 2011) and to patterning of biomolecules for various applications (Chang et al. 2011).

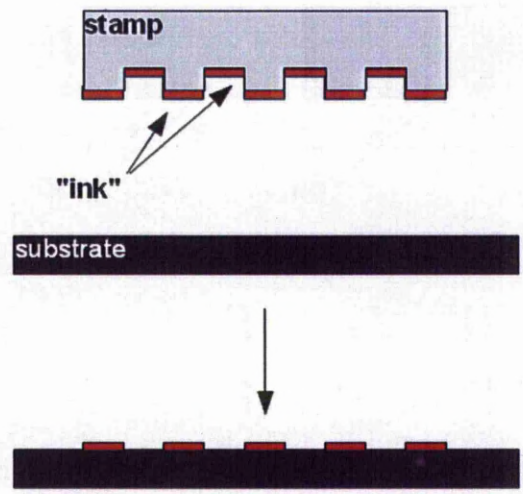

Figure I.3.10. μ-CP chemical patterning procedure. A flexible stamp is loaded with the "ink" which is then transferred to the substrate in a spatially controlled manner by contacting the stamp and the substrate

Colloidal lithography

This type of lithography use particles that are in the micron and sub-micron range and their (self)assembly phenomenon to create complex patterns. The particles used (metal, polymeric, ceramic) effectively act as deposition or etch masks. Colloidal lithography is not a new technique, being first proposed in the 1980's (Deckman and Dunsmuir 1982; Fischer and Zingsheim 1981) under the name of "natural lithography". The simplest structures that can be fabricated are vertical pillars by selective etching of areas not protected by nanoparticles (Chen et al. 2012a) but complex geometries can be achieved as demonstrated by (Miyamoto et al. 2012; Satriano et al. 2012), extensively reviewed here (Yang et al. 2006). The main advantage of colloidal lithography is the ability to create complex geometries without the requirement of fabricating an expensive photomask.

Scanning probe lithography

Scanning probe lithography involves the use of a scanning probe microscope infrastructure to pattern surfaces (Wouters and Schubert 2004). The patterning can take place either through the deposition of reagents from a liquid phase (much like writing with a fountain pen), termed Dip Pen Nanolithography (DPN) (Piner et al. 1999; Wu et al. 2011), mechanically deforming the surface (nano-scratching) (Tseng 2011), modifying the surface through interaction with light (using a near field scanning technique) (Liu et al. 2011; ul Haq et al. 2010), or locally oxidizing the surface by applying a voltage between the probe and the surface (Wouters et al. 2009). These techniques are capable of nanometre resolution but, unfortunately, suffer because of the sequential nature of the process leading to low throughput; attempts have been made at making the process parallel but they are currently at research level (Despont et al. 2000).

I.3.6 Summary

The aim of this sub-section was to provide a brief overview of the basic steps in micro- and nano-fabrication, with an emphasis on optical lithography as the main tool in the fabrication of semiconductor devices and associated processes. Three main areas were identified: thin film deposition techniques, optical lithography and pattern transfer. In the discussion about the lithographic process, the mechanism of image formation using negative and positive photoresists respectively was illustrated with examples. Alternative lithographic methods that are somewhat more accessible to non-specialized laboratories, while admittedly, less standardized, were also introduced. The concept of chemical patterning rather than topographical patterning was also mentioned in the context of μCP.

II. Part II: Structured, fluorescence interference based substrates for biorecognition devices

II.1 Chapter 1: Proof of concept

II.1.1 Introduction

The possibility of using micro- and z-nano-structured solid substrates to passively amplify fluorescence was first investigated using a fluorescent dye with excitation and emission wavelength similar to those of Cy5, a commonly used fluorescent label in microarray technology (together with its blue sister, Cy3). The surface of the substrates was first derivatised with amine groups and the fluorescent dye, in the form of an amine-reactive NHS-derivative was grafted onto the surface. The substrates were imaged in a laser scanning confocal microscope and the resulting fluorescent micrographs were processed using a purposely devised algorithm to give meaningful quantities that were further used to asses the performance of the substrates.

II.1.2 Materials and methods

II.1.2.1 Reagents and buffer solutions

Bovine serum albumin (BSA) and (3-aminopropyl)triethoxysilane (APTES) were purchased from Sigma Aldrich. DyLight 649 (N-hydroxysuccinimidyl functionalized dye) was purchased from Thermo Scientific. Solutions: PBS: 15 mM sodium phosphate, 0.15 M NaCl, pH 7.4. Bicarbonate buffer: 0.1 M sodium bicarbonate, pH 8.2. Wash buffer 1: bicarbonate buffer containing 10% ethanol; Wash buffer 2: PBS containing 0.05 % tween 20.

II.1.2.2 Substrate fabrication

Silicon wafers (4 in. diameter) have been subjected to a pre-deposition short sputter etch with Argon ions. A number of wafers have been covered with a 100 nm thick Platinum layer following the deposition of a 10 nm thick Titanium adhesion layer. Subsequently, silicon dioxide layers with thicknesses of 20, 40, 60, 80 and 100 nm, respectively, were deposited onto all the wafers, i.e., both presenting base silicon and platinum surfaces. All sputter deposition processes were carried out using a Veeco Nexus 800 sputter deposition tool. Next, a 1.5 μm thick HPR504 resist layer was

spun onto the wafers, soft-baked at 95°C for 2 minutes and exposed on an ASML i-line stepper using a standard "lines and spaces" test reticule. After the development of the resist in TMAOH developer, these patterns have been used as a mask in a CHF_3 plasma for etching the SiO2 down to the basal layer (with a 10% over-etch). This was followed by a short high pressure oxygen/nitrogen plasma treatment in order to 'open up' the resist residues (removal of 'teflon' type deposits resulting from the fluoromethane plasma treatment) for the subsequent wet-chemical resist removal. Finally, the structures were subjected to an optical quality check and pattern height was measured using an α-step profilometer.

Aminosilanisation and fluorescent dye attachment

The surface of the substrates was modified first with (3-aminopropyl)triethoxysilane (APTES) and the NHS-ester derivative of DyLight 649 (Thermo Fisher Scientific) fluorescent dye was surther grafted onto the surface.

Fluorescence imaging and image analysis

Fluorescence micrographs were obtained using a Zeiss Observer confocal microscope equipped with a Zeiss LSM 510 laser scanning module.

The images, in their original format, were processed using the freely available ImageJ package (Rasband 1997-2011) together with the LSM Reader[10] and the LSM Toolbox[11] plug-ins. The extracted parameters, i.e., surface area; signal mean and median intensity; and raw signal intensity; were processed further using the commercially available software Origin (Origin Lab, Northampton, MA, USA). The SNR, defined as the mean fluorescence intensity rationed to the background fluorescence standard deviation (Schena 2003a), signal/pillar and signal/unit area versus pillar height and footprint were quantified.

TOF-SIMS analysis

TOF-SIMS measurements were performed using an Ion-Tof IV instrument, using 25 keV Bi^+ primary ions, in both positive and negative mode. The mass resolution ΔM/M is larger than 6000 for masses above ~20.

[10] http://rsbweb.nih.gov/ij/plugins/lsm-reader.html
[11] http://imagejdocu.tudor.lu/Members/ppirrotte/lsmtoolbox

II.1.3 Experimental

II.1.3.1 Substrate fabrication

The choice of materials for the substrates was dictated by both physical and chemical properties but this point will be discussed latter. One of the underlying ideas was to be able to compare between pillars resting on a material with identical chemical properties with ones resting on a material with chemical properties sufficiently different so as to enable the appearance of chemical contrast between the pillars and the surrounding area. This is part of a wider research effort currently united under the name of "orthogonal assembly" which aims at controlling the spatial assembly properties of molecules through the use of surface chemistry (Giuntini et al. 2012). On the substrates in question, it appeared that a good choice of material combination to satisfy the chemical contrast condition would be SiO_2 pillars on a platinum layer; of course, the combination of materials is dictated by other factors like, for instance, the adhesion between materials and their inertness. The fabrication process as illustrated in **Figure II.1.1** includes two critical steps: reactive ion etching (RIE), which is an etching procedure that uses ions in a plasma phase to remove material from a surface, and a plasma ashing step to remove residues left behind after the RIE process.

The RIE step is used to transfer the pattern from the exposed and cured photoresist to the SiO2 layer but, in the process, it modifies the surface chemistry with fluorocarbon type groups that need to be removed via plasma ashing. Unfortunately, because the plasma ashing is carried out at low gas pressure, the process does not seem to be 100% efficient and this has manifested itself by the appearance of patchiness when these surfaces were derivatized with the fluorescent label. This has imposed the use of an additional cleaning step, either a liquid – RCA clean – or a dry one – UV-ozone exposure – resulting in a homegeneisation of the surface chemistry and wiping out the chemical contrast; this will be detailed in the section concerning the surface derivatization of the substrates.

Another set of substrates comprising lenticular shaped quartz structures on silicon were fabricated through a proprietary, low selectivity RIE process (see **Figure II.1.11** for a schematic cross-section).

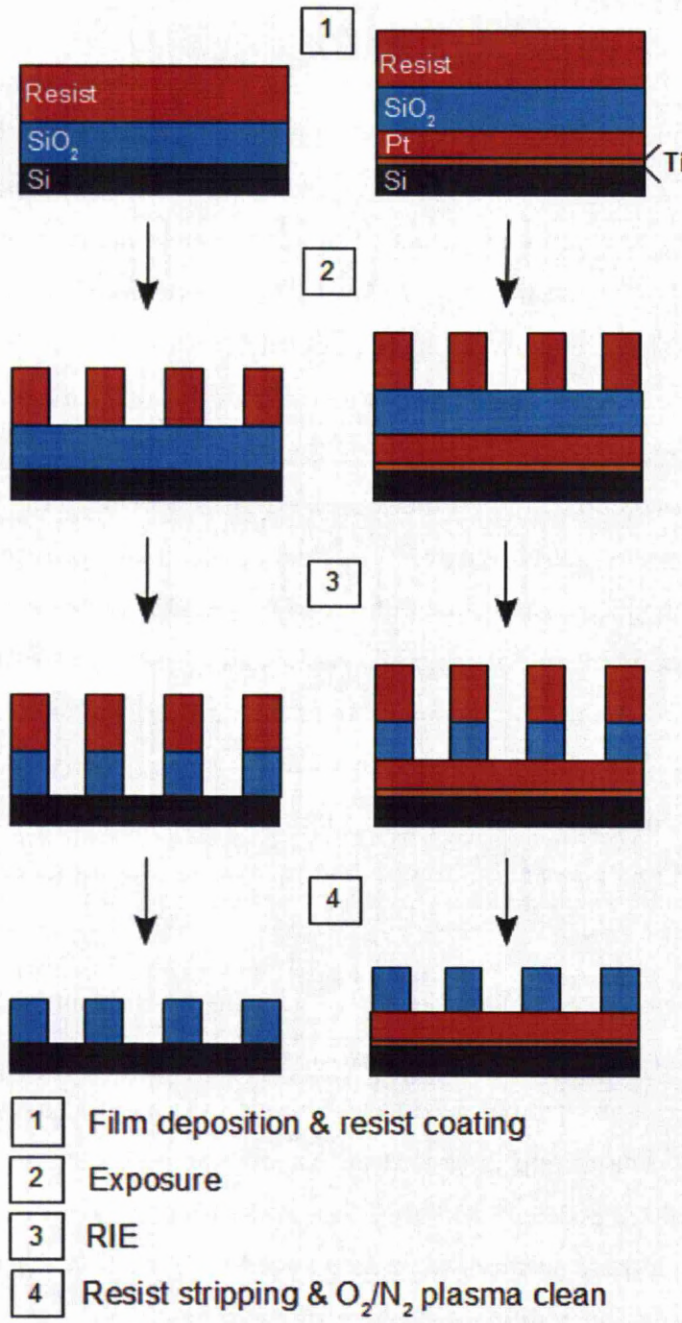

Figure II.1.1. Fabrication of pillar arrays with a silicon reflector (left) and a platinum reflector (right) respectively. Drawing is not to scale.

II.1.3.2 Aminosilanisation and fluorescent dye attachment

As previously mentioned, an additional cleaning step was deemed necessary before the substrates could be functionalized with amine and fluorescent dye. The initial cleaning procedure, an RCA cleaning was first employed. RCA cleaning is a two step wet process comprising an initial 5 minute wash in a 1:1:5 NH_4OH:H_2O_2:water

solution followed by a second 5 minute wash in a 1:1:6 $HCl:H_2O_2$:water solution; both washes are carried out at 70°C with a water washing step in between the basic and the acidic washes. The alkaline wash lightly etches away silicon oxide and, by doing this, it removes particle contaminants from the surface. The acid wash helps in removing any metal contaminant from the oxide surface. No sonication was used to avoid the pillars detaching, especially in the case of a platinum basal layer. Unfortunately, even though this cleaning technique provides a homogeneous surface, chemistry-wise, its side-effect is the removal of a few nanometres from the silicon oxide pillars. This adversely affects the performance of the substrates given that the reflector – fluorophore distance will deviate from the intended one. Another consequence is that substrates cannot be reused. A different procedure, free of the shortcomings highlighted above, is UV-ozone cleaning. It is based on the formation of ozone, reactive O3 molecular species, using the 185 nm emission of a 254 nm Hg vapour lamp which attacks organic molecular fragments generated by photons emitted at 254 nm cleaving the intramolecular bonds of organic molecules (BioForce-Nano). The advantages are the lack of etching action which conserves the height of the pillars while the fact that the process is dry results in a shortened and less hazardous process.

Surface cleaning is followed by functionalization with amine groups using the aminosilane reagent APTES. Silanization is a process of derivatizing a surface that displays hydroxyl groups with a class of reagents that are substituted derivatives of silanes with a general formula R_nSiX_{4-n}, where R is a non-hydrolizable group and X is a hydrolysable group, most commonly an alkoxy one. Silanisation is a versatile tool in surface chemistry owing to the great variety of chemical groups that can substitute a hydrogen atom and also the extent of the substitution making it a great tool for surface modification. The mechanism of silanization starts with hydrolysis of the alkoxy group with the elimination of the corresponding alcohol. These approach surface hydroxyl groups forming hydrogen bonds which, upon curing at a moderate temperature, results in the formation of covalent Si-O-Si bonds through a water elimination reaction (Pividori and Alegret 2005). The process is schematically represented in **Figure II.1.2**. Polymerization of multiple hydroxyl-silane molecules is possible if humidity is not properly controlled (Brzoska et al. 1994).

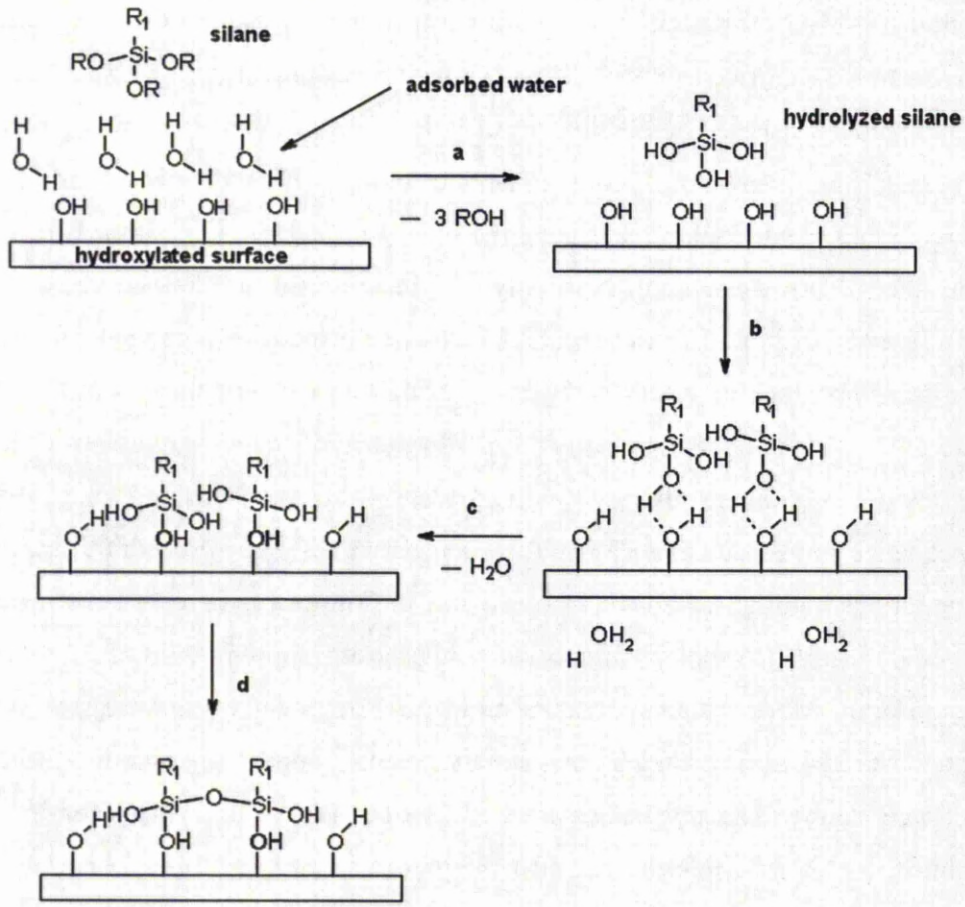

Figure II.1.2. Formation of silane layers on substrates displaying surface hydroxyl groups. Hydrolysis of the alkoxy groups takes place due to surface adsorbed water molecules (accompanied by alcohol elimination, a). The hydrolysed silane molecules are kept at the surface of the solid via hydrogen bonding (b). Surface reaction of the silane with the surface hydroxyl groups leads to covalent bonding and water elimination (c). Annealing promotes crosslinking with water elimination (d). Adapted with permission from (Brzoska et al. 1994). Copyright (1994) American Chemical Society.

Aminosilanization of the pillared substrates was carried out in solution with a mixture containing absolute ethanol, 4.25 M acetic acid in water and APTES in a ratio of 95:3:2, on a rocker plate and at room temperature for 2 hours; at the end of the reaction time, the substrates were washed 4 times in ethanol and cured by placing them in an oven at 110 °C for 45 minutes.

The attachment of the fluorescent dye to the aminated surface was carried out using an N-hydroxysuccinimide (NHS)-ester based chemistry. NHS-ester chemistry is commonly used in applications involving labelling of biomolecules and conjugate synthesis. It is based on the reactivity of NHS-esters towards amines at alkaline pH. The reaction takes place through nucleophilic attack of the amine to the carbonyl carbon atom of the ester which leads to the departure of the NHS group and the

formation of an amide bond as shown in **Figure II.1.3**. The nucleophilic attack is favoured at alkaline pH but, unfortunately, the hydrolysis of the ester is also promoted at this pH, leading to decreased coupling efficiency (Hermanson 1996). The efficiency of the coupling reaction can however be increased by increasing the amount of available amine in solution while maintaining a low temperature; also, higher NHS-ester concentrations promotes hydrolysis.

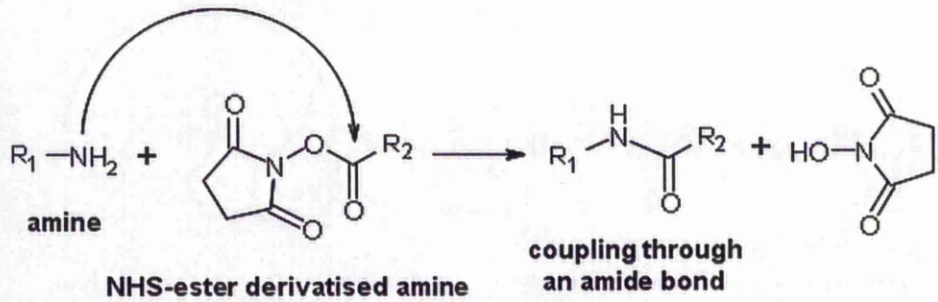

Figure II.1.3. Amide bond formation between an amine and a NHS-ester derivatized molecule.

Fluorescent dye attachment was carried out from a solution containing 10 μM DyLight 649 NHS-ester (excitation 649 nm, emission 673 nm); aminosilanized substrates were slow-tilt rotated at room temperature for 4 hours with the dye and were subsequently washed once for 5 min in wash buffer 1 and 3 times for 5 min in wash buffer 2 before being dried in a nitrogen flow. The process is outlined in **Figure II.1.4**.

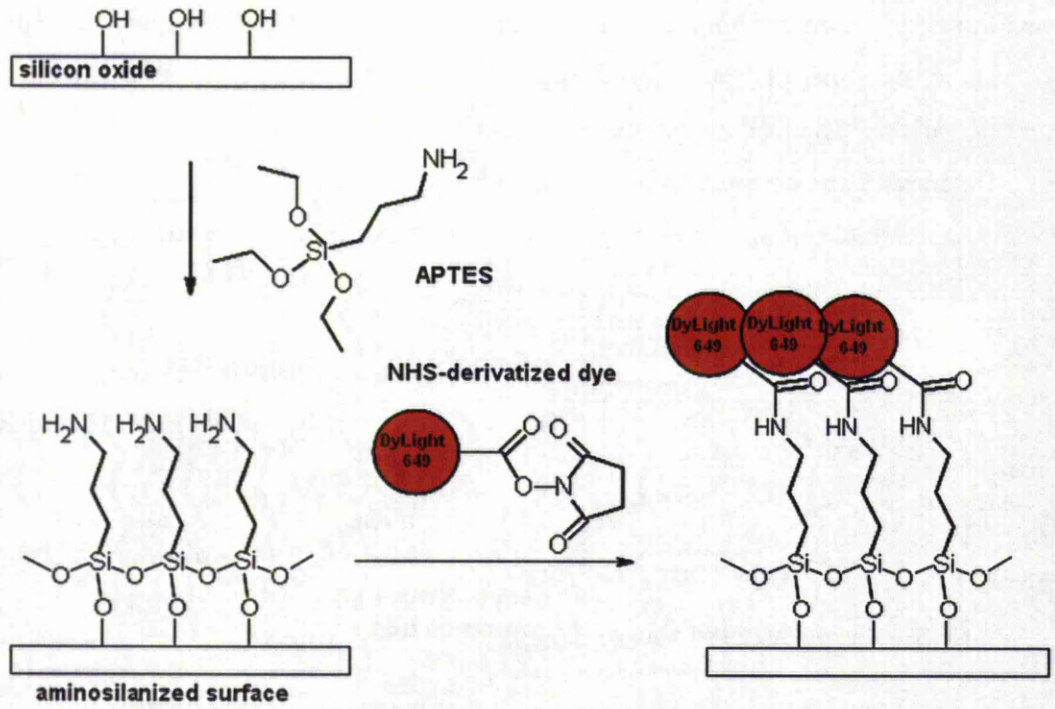

Figure II.1.4. Direct attachment of NHS-derivatized fluorescent probe onto aminosilanized surfaces

II.1.3.3 Fluorescence imaging and image processing

After fluorescent labelling, all samples were imaged with a Zeiss Observer confocal microscope equipped with a Zeiss LSM 510 laser scanning module. Excitation was achieved using the 633nm HeNe laser line and the emission was collected using a 650nm long pass filter. A low laser power was used for excitation to avoid the photobleaching of the fluorophores. The 100x dry objective yielded a field of view of approximately 65 x 65 μm and a lateral resolution of approximately 150 nm. The pinhole size was automatically optimized by the control software to yield the minimum optical slice thickness of 2μm for the combination of objective numerical aperture (NA=0.9) and emission wavelength. The detector gain was also optimized to eliminate saturated pixels.

Fluorescence micrographs were analysed as supplied by the imaging system using the freely available microscopy processing software ImageJ with the plugins mentioned before. The procedure starts with the application of a mean filter to remove the random noise followed by a band-pass filter. This helps in removing shading artefacts and levels the background insures a better foundation for following steps. Further, the image is thresholded (dividing the component pixels into two classes based on their gray value) and binarized. At this stage, the edges of the

features in each image can be detected and the edge map can be transferred to the original image. The process is outlined in **Figure II.1.5**. It is important therefore to stress the fact that the transformations mentioned here are only carried out to extract a good edge map and are not applied to the actual image that needs to be measured. All the features in the field of view (bright red squares in figure **Figure II.1.5**) are contained in the edge map, i.e. the entire collection of features in a field of view makes up the foreground while the remaining (dark) area makes up the background.

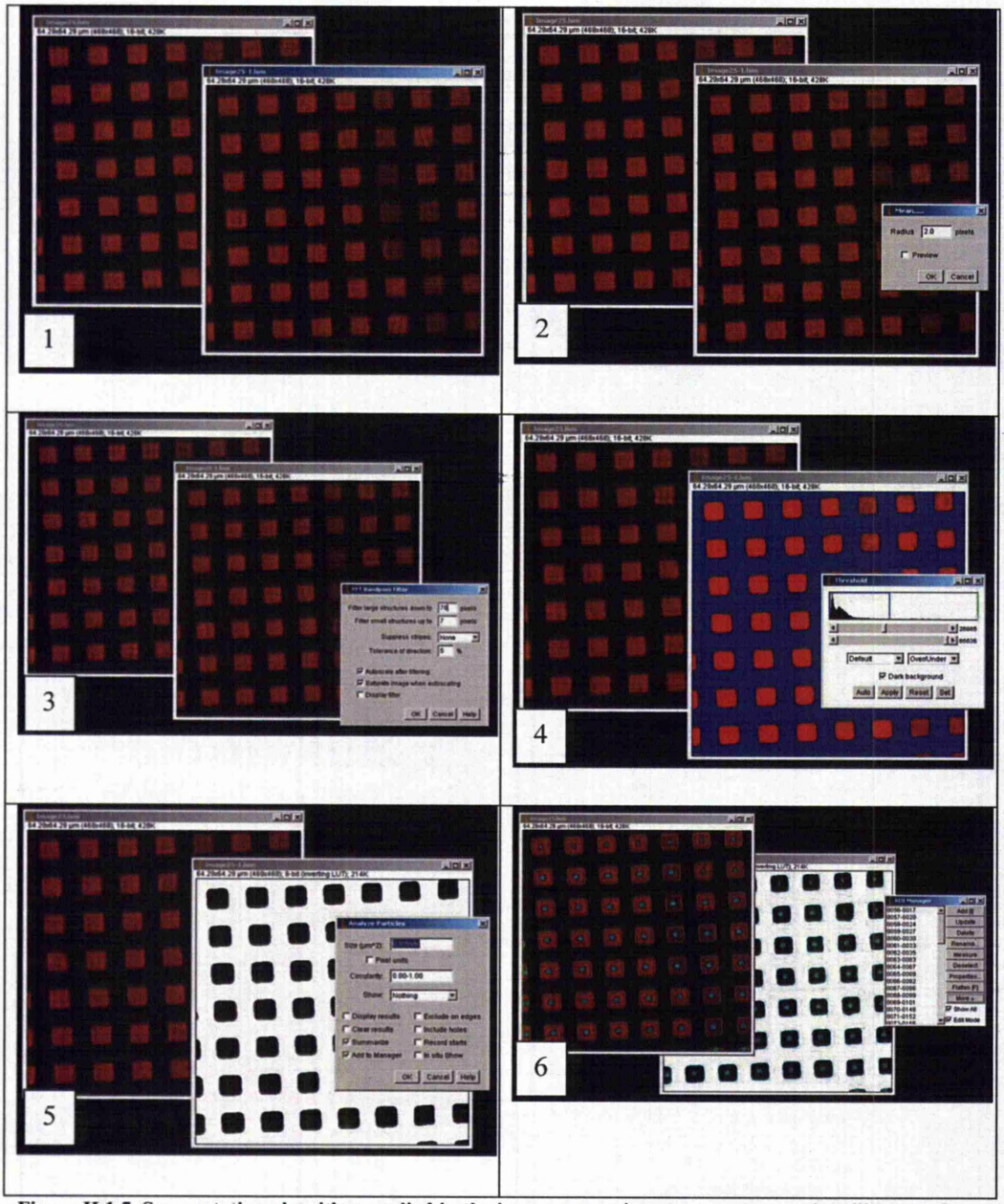

Figure II.1.5. Segmentation algorithm applied in the image processing step to separate the pillar tops from the surrounding area: (1) an image containing the features (bright red squares) is duplicated and (2) a median filter is applied to smooth the pixel to pixel transition. A bandpass filter (3) is applied to correct for non-uniform illumination and to enhance the separation between foreground and background. (4) each image is then thresholded (a pixel value is chosen so that all pixels whose gray value is lower than the reference value become saturated black while those whose values are above that threshold are become saturated white) resulting in a binary image (5). From the binary image, using the built-in particle analyser, an edge map is created which is then applied on top of the original image (6). The edge map is represents the boundary between foreground and background (blue spots are text labels).

The numerical processing and graphing were carried out using the commercially available software package Origin Lab. The computed quantities were defined as follows:

Mean fluorescence intensity - is obtained as an average gray value of all foreground pixels

Mean background intensity - is obtained as an average gray value of all the pixels making up the background

Background standard deviation - is the standard deviation of the mean background gray value

Signal-to-noise ratio

Signal to noise ratio is given by

$$SNR = \frac{Mean_{Foreground} - Mean_{Background}}{SD_{Background}}$$

where the $Mean_{Foreground}$ is the mean fluorescence intensity, the $Mean_{Background}$ is the mean background intensity and the $SD_{Background}$ is the background standard deviation (Redkar et al. 2006). SNR is a measure of how well can a real signal be discriminated from the accompanying noise or, in other words, it expresses the certainty with which one can ascribe a certain response from a measuring system to a real perturbation determined by the input rather than a random behaviour that is only due to chance; an extensive treatise on the subject can be found in the literature, e.g. (Danzer 2007). Usually, and depending on the number of samples, a SNR value of 3 is sufficient for a detection event to be characterized by a confidence level of 0.01 (Janiga et al. 2008; Walter et al. 2010) and commercial microarray manufacturers commonly report SNR values in the hundreds.

Fluorescence per pillar – is given by the sum of the gray values of all the pixels contained in the foreground multiplied by the total foreground area and divided by the pillar footprint

Fluorescence per unit area – is given by the sum of the gray values of all the pixels contained in the foreground divided by the total foreground area

II.1.4 Results and discussion

The fluorescence micrographs of the substrates after surface immobilization of the fluorescent dye reveal some interesting features. Firstly, a high contrast between the

tops of the pillars and the area surrounding them became visible. Secondly, the magnitude of this contrast seemed to increase with the pillar height, from no contrast at all for pillar heights of 0 and 20 nm to a high contrast for the 100 nm high pillars. Thirdly, pillars resting on a platinum layer are brighter that those on the silicon layer (**Figure II.1.6**). It is interesting to note at this point that the contrast can be either a result of the fluorescent light coming from the pillar tops being amplified, or the fluorescence arising from the area around the pillars being suppressed, or both of these situations might concurrently contribute to the observed behaviour. A number of hypotheses were considered to explain the height and material modulated amplification – suppression effects.

The possibility that contrast arises as a result of the capability of a confocal imaging system to filter out light not coming from the focal plane was explored and rejected (see **Figure II.1.14** and discussion). A second explanation, also based on optical effects, relied on the possibility that the silicon oxide structures together with the reflecting layer (silicon or platinum) would create the conditions for the existence of standing waves, this explanation being compatible with both the height and the material modulated amplification (see **II.1.4.1 Optical interference effects** and **Figure II.1.7**). A third possible explanation that was considered was that there is simply no fluorophore around the pillars (due to either surface chemistry spatial distribution or the wettability of the surface) and therefore the spatial distribution of fluorescence would be a surface chemistry map (see **Table II-3** and discussion). This last hypothesis does not however account for the height modulation of the fluorescence signal.

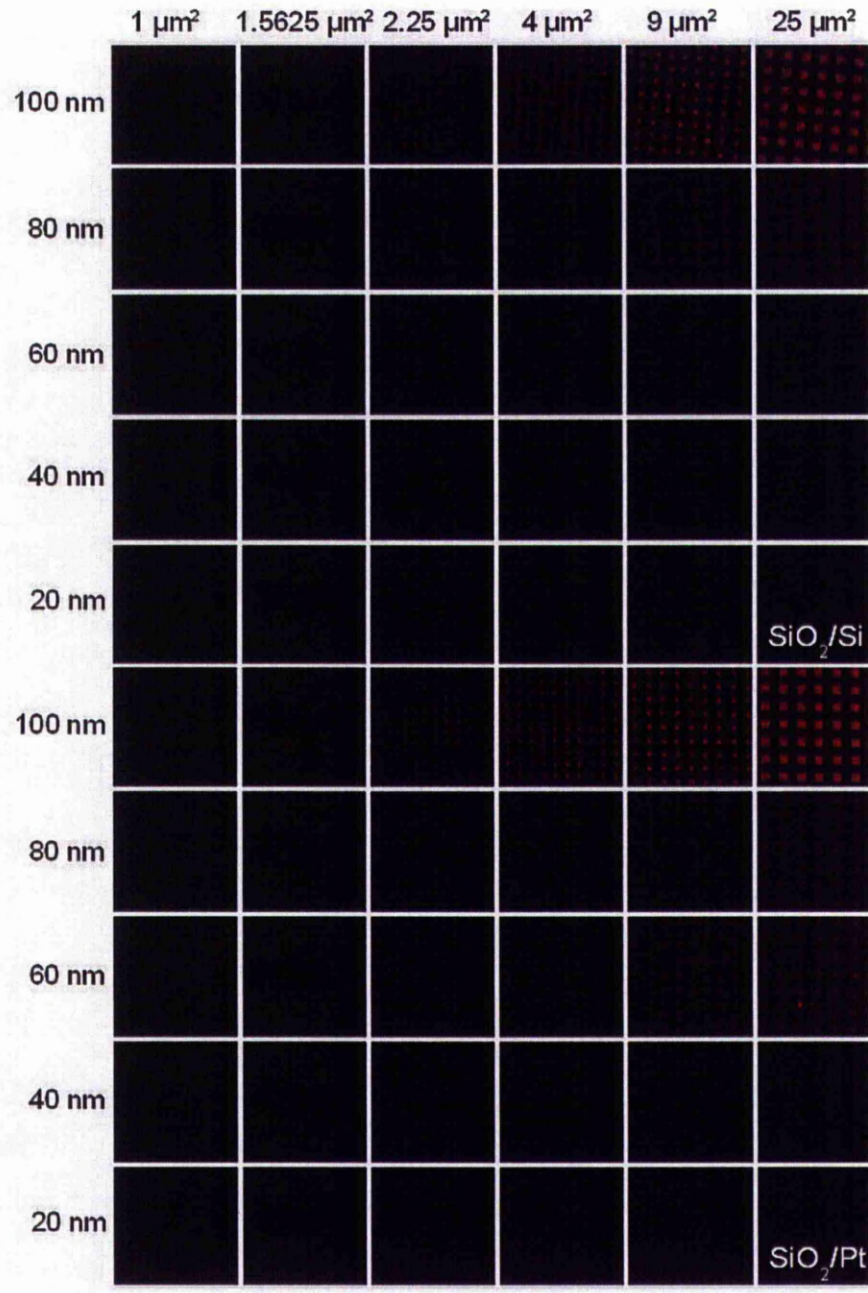

Figure II.1.6. Variation of fluorescence intensity with pillar height and the influence of pillar footprint. The cases for the two reflector are presented (Si - top panel and Pt - bottom panel)

II.1.4.1 Optical interference effects and data fitting

The relative phase difference between two or more waves is given by the relative optical path length difference, where the optical path length is given by the product between geometrical path length and the refraction index of the medium that the light traverses. For a beam of light A

$$A = A_0 \sin(kx - \omega t) \tag{2}$$

where k is the wavenumber, ω is the angular velocity, t is the time coordinate and x is the spatial coordinate. The phase is given by the term between brackets

$$\phi_A = kx - \omega t \tag{3}$$

For a second beam B with the source displaced by a quantity d and passing through a medium with a refractive index n

$$B = B_0 \sin[k(x - nd) - \omega t] \tag{4}$$

The phase is

$$\phi_B = k(x - nd) - \omega t \tag{5}$$

and the relative phase difference between beams A and B is

$$\phi_A - \phi_B = knd \tag{6}$$

Because the wavenumber k is given by

$$k = \frac{2\pi}{\lambda} \tag{7}$$

where λ is the wavelength, then the relative phase difference becomes

$$\phi_A - \phi_B = \frac{2\pi}{\lambda} nd \tag{8}$$

and the condition for maximum constructive interference is achieved when the phase difference is a multiple integer of 2π (or one wavelength) while maximum destructive interference is achieved at a phase difference that is an odd multiple of π (or, in terms of optical path difference, half a wavelength).

When a fluorophore is placed in the vicinity, i.e., nanometres to micrometres away from a reflector, as illustrated in **Figure II.1.7 A** and it is excited with light of an appropriate wavelength, so as to induce fluorescent emission, some of the excitation light is reflected back by the reflective layer and interferes with the incoming (direct) beam, thus leading to the formation of standing waves; the same is valid for the light emitted by the fluorophore. Consequently, for precisely chosen optical paths differences, the amplitude of the resulting wave becomes very large, and an amplification of the fluorescent emission is observed.

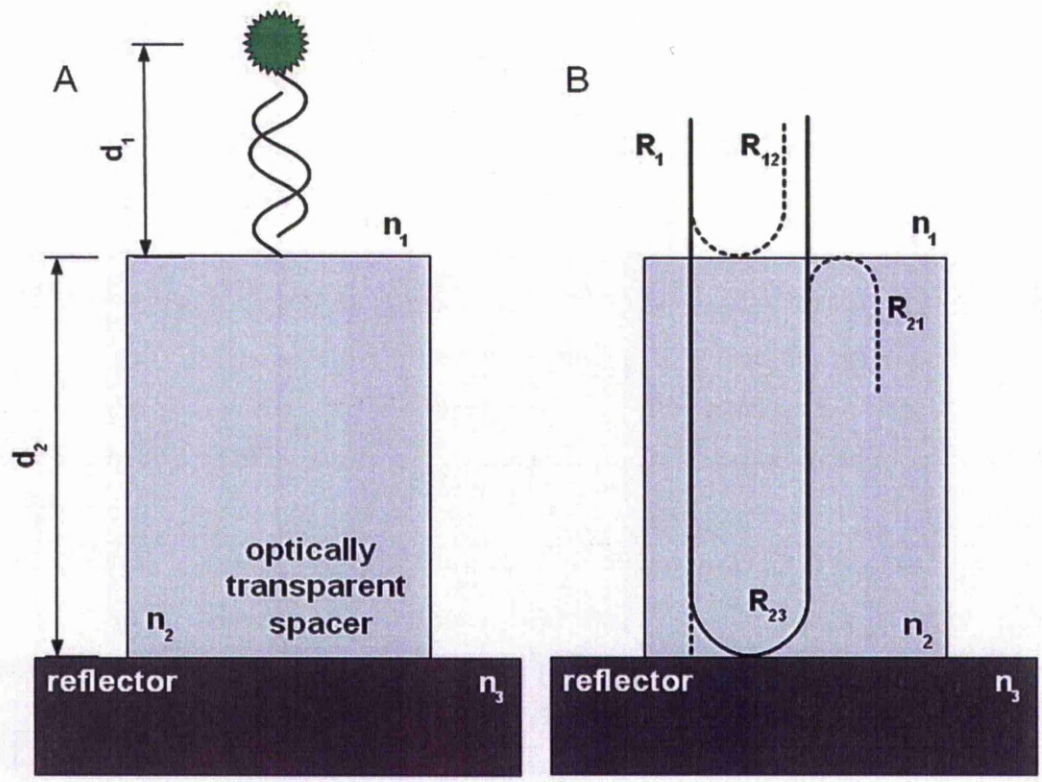

Figure II.1.7. Schematic representation of the optical set-up. (A) The fluorophore is placed in a medium characterized by the refractive index n_1 at a distance d_2 from a spacer of height d_2 characterized by a refractive index n_2 (d_1 is much smaller than d_2). (B) The light undergoes multiple reflections as is passes traverses the interfaces of the three media.

As light traverses the media characterized by refractive indices n_1, $_2$ and $_3$, some of it is transmitted and some is reflected. For simplicity, only incident light normal to the surface is considered. The amount of reflected light is given by the reflectivity coefficient according to the Fresnel equations:

$$R_s = \left| \frac{n_1 \cos\theta_i - n_2 \sqrt{1-(\frac{n_1}{n_2}\sin\theta_i)^2}}{n_1 \cos\theta_i + n_2 \sqrt{1-(\frac{n_1}{n_2}\sin\theta_i)^2}} \right|^2 \quad (9)$$

and

$$R_p = \left| \frac{n_1 \sqrt{1-(\frac{n_1}{n_2}\sin\theta_i)^2} - n_2 \cos\theta_i}{n_1 \sqrt{1-(\frac{n_1}{n_2}\sin\theta_i)^2} + n_2 \cos\theta_i} \right|^2 \quad (10)$$

for *s* and *p*-polarized light respectively.

For non-polarized light, the reflectivity coefficient is given by

$$R = \frac{R_s + R_p}{2} \tag{11}$$

For light at normal incidence, this becomes

$$R = \left|\frac{n_1 - n_2}{n_1 + n_2}\right|^2 \tag{12}$$

Substituting the refractive indices[12] for air and quartz, it can be seen that the reflection coefficient at the air-quartz interface is very small (~0.03) which in turn means that, in **Figure II.1.7 B**, R_{12}=R_{21}~0.03. Further, the reflectivity coefficients at the quartz –silicon and – platinum respectively are 0.21 and 0.57 respectively. It follows that on can use a simplified model that takes into account the interference between the direct (R_1) and reflected (R_{23}) waves. The same is valid for the emission light with some qualifications (see **I.2.2 One possible answer to the research question: structured, fluorescence interference-based substrates**). Reflectivity coefficients are shown in **Table II-1**.

Table II-1. Tabulated values of the reflectivity coefficients at the interfaces between the three media

Reflectivity coefficient	λ_{ex}	λ_{em}
Air – SiO_2 interface	0.03	0.03
Si – SiO_2 interface	0.21	0.2
Pt – SiO_2 interface	0.57	0.58

Having simplified the optical model, one can calculate the phase difference between the direct and the reflected beams

$$\phi_{ex} = \frac{2\pi}{\lambda} 2(n_1 d_1 + n_2 d_2) \tag{13}$$

And since d_1 is much smaller than d_2, the $n_1 d_1$ term can be discarded. Further, since the separation distance d_2 is the elevation height of the fluorophore above the reflector and is determined by the thickness of the silicon oxide layer, d_2 will be written as h_{SiO2}. The relative phase difference then becomes

$$\phi_{ex} = \frac{4\pi}{\lambda} n_{SiO_2} h_{SiO_2} \tag{14}$$

Or, in the case of emitted light

[12] from refractiveindex.info

$$\phi_{em} = \frac{4\pi}{\lambda} n_{SiO_2} h_{SiO_2} \quad (15)$$

As shown in **Figure I.1.4**, while the excitation light is monochromatic, the emitted light is spread over a range of wavelengths, in the form of a band. The model discussed below will take into account only the maximum emission wavelength, for simplicity.

The physical and mathematical framework of the process has been reported as a purely optical phenomenon (Brandstatter et al. 1988). This was confirmed by using a monolayer of fluorescent molecules on silicon oxide terraces (Lambacher and Fromherz 1996), showing that a model involving an energy transfer phenomenon, i.e., quenching, is not necessary to describe the phenomenon. Based on this, a microscopy technique (fluorescence interference contrast microscopy - FLIC) capable of accurately measuring nanometer scale distances on the z-axis has emerged and has been successfully applied in various experiments involving the study of the cellular membrane (Braun and Fromherz 1997), lipid layers (Ajo-Franklin et al. 2005; Crane et al. 2005; Kiessling and Tamm 2003) and even molecular motors (Kerssemakers et al. 2006). An inverse approach, in which immobilization at specific distances from a reflecting layer can be employed to improve the detection of fluorescently labelled biological analytes has also been proposed (Fernandez 2009b). A somehow similar behaviour was observed when hybridization occurs on a substrate comprising of a gold layer and variable thickness polymeric rulers (Chi et al. 2008) and this was assigned to quenching and surface plasmon effects.

The reflective surface material for the modulation of fluorescence is either silicon, or platinum. The spacers between the reflecting surface and the fluorophores are the SiO_2 pillars, which are essentially transparent to incoming light, especially at such a small thickness (pillar heights of 20-100 nm). The modulation of the intensity of the emission light is achieved by varying the separation between the fluorophore and the reflective surface. For the experimental set-up used here, an intensity maximum is obtained for pillars slightly taller than 100 nm. **Equation 16** represents a simplified mathematical formalism of the modulation of florescence by the distance to a reflecting surface described elsewhere (Parthasarathy and Groves 2004):

$$F_{exp} \propto F_0 + F\left[(1-r_{ex})^2 + 4r_{ex}sin^2\left(\frac{2\pi}{\lambda_{ex}}nd\right)\right]\left[(1-r_{em})^2 + 4r_{em}sin^2\left(\frac{2\pi}{\lambda_{ex}}nd\right)\right] \quad (16)$$

where F_{exp} is the observed fluorescence intensity; F_o is the residual fluorescence at the surface (zero height) λ_{ex} and λ_{em} are the excitation and emission wavelengths, respectively; n is the index of refraction of the medium that light passes through; h is the reflector-fluorophore distance and r_{ex} and r_{em} are reflection coefficients of the reflector material at the excitation and emission wavelengths respectively. Further, terms with unknown magnitudes like angles of incidence of the excitation and emission light, fluorophore orientation and light polarization were all included under the umbrella of a proportionality factor F.

The curve described by **eq. 16** was fitted on experimentally obtained fluorescence values as shown in **Figure II.1.8**. The residual fluorescence term F_0, obtained as an average of the fluorescence signal in between the pillars for both the silicon and the platinum reflector layer substrates, was used to supply a starting value and then allowed to fluctuate slightly. The proportionality factor F was allowed to fluctuate.

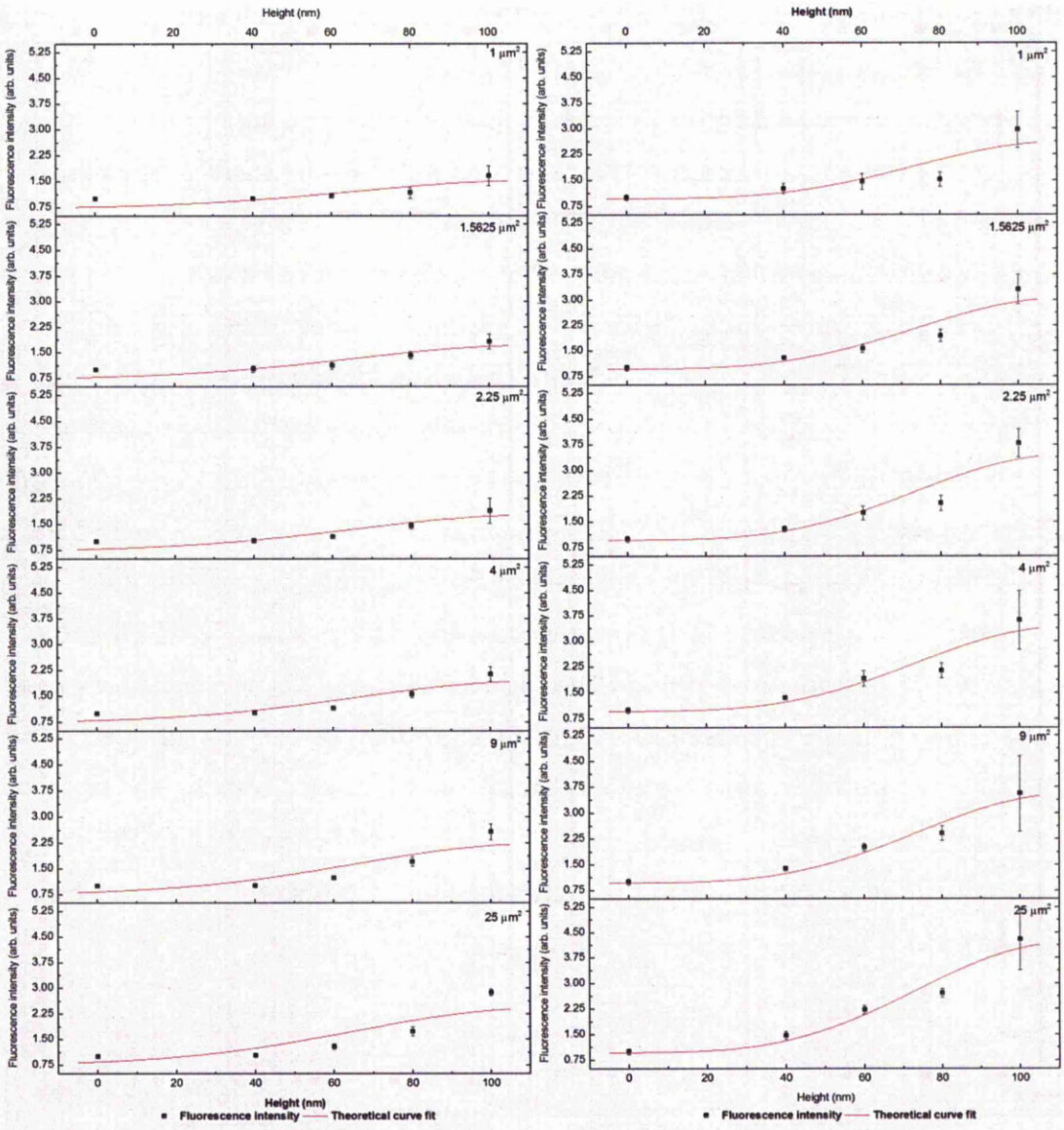

Figure II.1.8. Experimental fluorescence intensity values obtained on the silicon (left) and platinum (right) versus pillar height; a theoretical curve obtained from equation 16 Error! Reference source not found.**was fitted on these points (red line) for different pillar footprints**

The goodness of fit parameters are tabulated in **Table II-2**.

Table II-2. Tabulated goodness of fit parameters for the fitting procedure illustrated in Figure II.1.8

Goodness of fit parameter	SiO_2/Si	SiO_2/Pt
R	0.89534	0.95385
R-Square (COD)	0.80163	0.90983
Adj. R-Square	0.74988	0.88631

The necessity of introducing a shape dependency arose from the fact that a difference in fluorescence amplification for pillars with identical heights but different footprint surface area was observed. This can be explained by considering that a digital image is actually an array of elements called pixels with finite dimensions determined by the resolution of the imaging system. Because of this, the pixels making up the edge of a certain feature will always carry with them an amount of uncertainty in terms of gray value. When measuring the signal originating from that feature, the effect of the edge pixels on the integrated signal will depend on the ratio of perimeter pixels to total pixels. It is thus obvious that, for smaller features, pillars in this case, the contribution of the edge pixels will be far more important than for larger pillars (the edge pixels to total pixels ratio varies from 0.11 for the largest 5 x 5 μm2 pillars to 0.55 for 1 x 1 μm^2 pillars). Another explanation could be related to the limitations of the lithographic process. It is reasonable to assume that the shape definition is lost as the size of the feature goes down. Consequently, the square features become rounded when their (lateral) size decreases. This can also affect the image analysis algorithm because a square shape is implied. Based on this consideration, an allometric function describes the proportionality factor versus footprint dependency. A logarithmic dependence versus the pillar footprint can also be used as shown in **Figure II.1.9**.

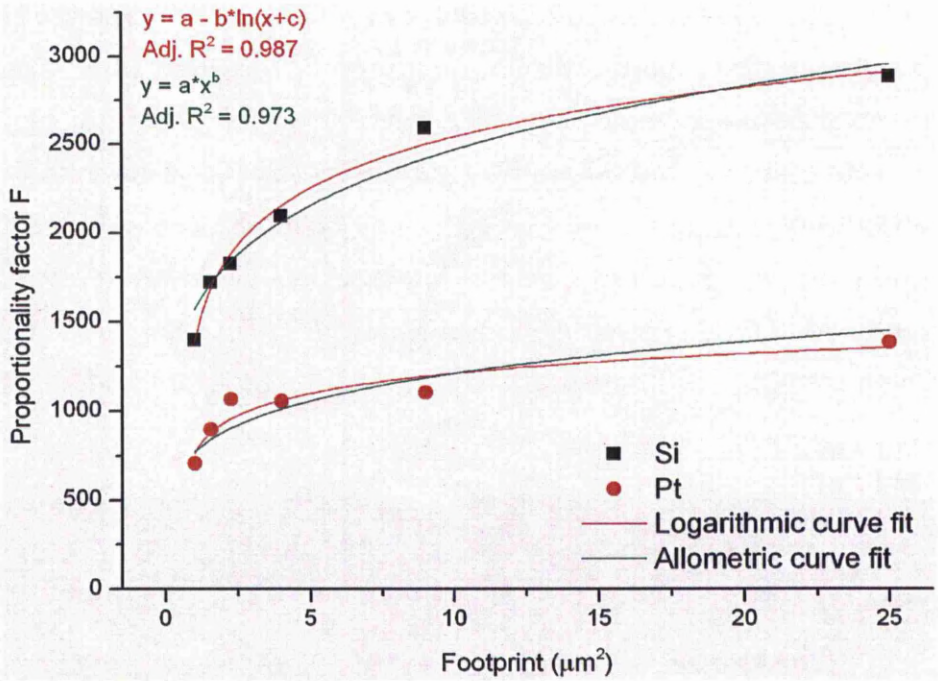

Figure II.1.9. Dependence of the proportionality factor *F* (from equation 16Error! Reference source not found.**) on the pillar footprint**

The proportionality factor versus pillar footprint could in principle be described by a number of mathematical relationships. In this particular case, two dependency laws, allometric and logarithmic respectively, are illustrated in **Figure II.1.9**. Fitting the two curves on the experimental data points results in two coefficients of determination corrected for the difference in the number of free parameters. The values of the adjusted coefficients of determination are very close together so there is no reason to choose one model over the other (not based on the adj. R^2 anyway). Moreover, the relevancy of the dependency law is only limited to emphasizing the technical limitations of both the fabrication and/or image analysis procedure.

II.1.4.2 Use of lenticular structures for testing the formation of standing waves

The validity of the standing wave based explanation was also tested using two arrays of quartz micro-lenses fabricated on top of a silicon basal layer. The geometry of the two arrays, illustrated in **Figure II.1.10** and **Figure II.1.11**, was originally quoted by the manufacturer as comprising 430 nm high quartz microlenses on a silicon layer and 440 nm high quartz microlenses on a 60 nm quartz layer respectively, resting on a silicon layer. These structures allowed us to test the interference based phenomenon hypothesis ourselves by first making a set of predictions about the way

they affect fluorescent light emitted by a fluorophore placed on their surface and then comparing these predictions with the experimental outcome (the fluorophore attachment procedure was the same as the one described previously in **II.1.3.2 Aminosilanisation and fluorescent dye attachment**). In practice however, based on the quoted heights, the results were inconsistent. The inconsistencies however were resolved by measuring the real height of the structures by means of atomic force microscopy (AFM): 360 nm high microlenses on silicon and 385 nm high microlenses on a 60 nm thick silicon oxide, as illustrated below in **Figure II.1.10, bottom**.

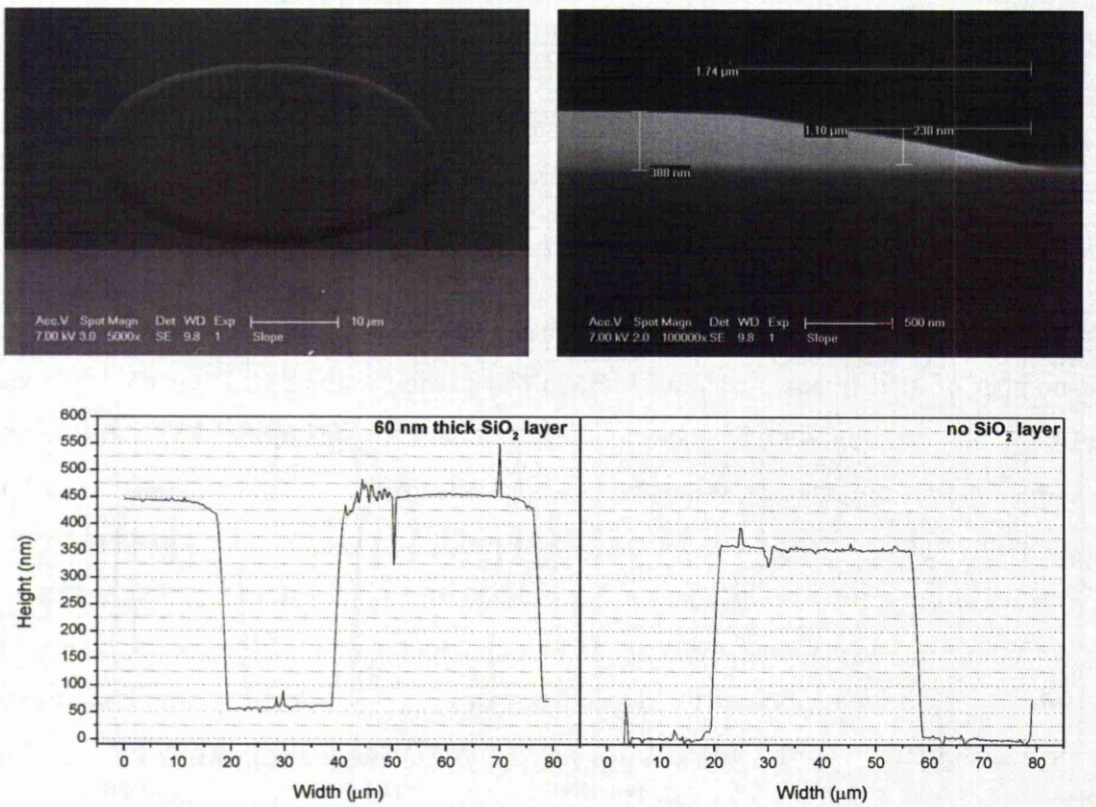

Figure II.1.10. SEM (top row), optical micrograph (bottom left) and AFM topographic profile (bottom) of the test quartz micro-lenses (with a 60 nm quartz layer at the bottom – left, and lacking this layer - right)

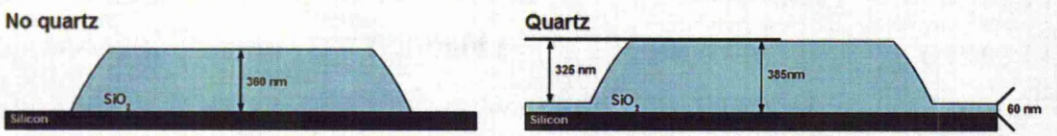

Figure II.1.11. Cross-section profiles of the two types of test quartz micro-lenses (no quartz on the left and 60 nm quartz layer on the right)

The projected behaviour of the two arrays, as predicted by the law defined in **eq. 1**, was as follows: the test substrate comprising 360 nm high quartz microlenses on "bare" silicon (where "bare" denotes the existence of a native silicon oxide film only) would be seen under a fluorescent microscope as an array of filled circles on a dark background and displaying a pair of brightly coloured rings around the rim. The test patterns comprising 390 nm high quartz microlenses and a 60 nm thick quartz layer separating them from the silicon layer should appear as low brightness circles surrounded by a pair of bright rings on a moderately bright background.

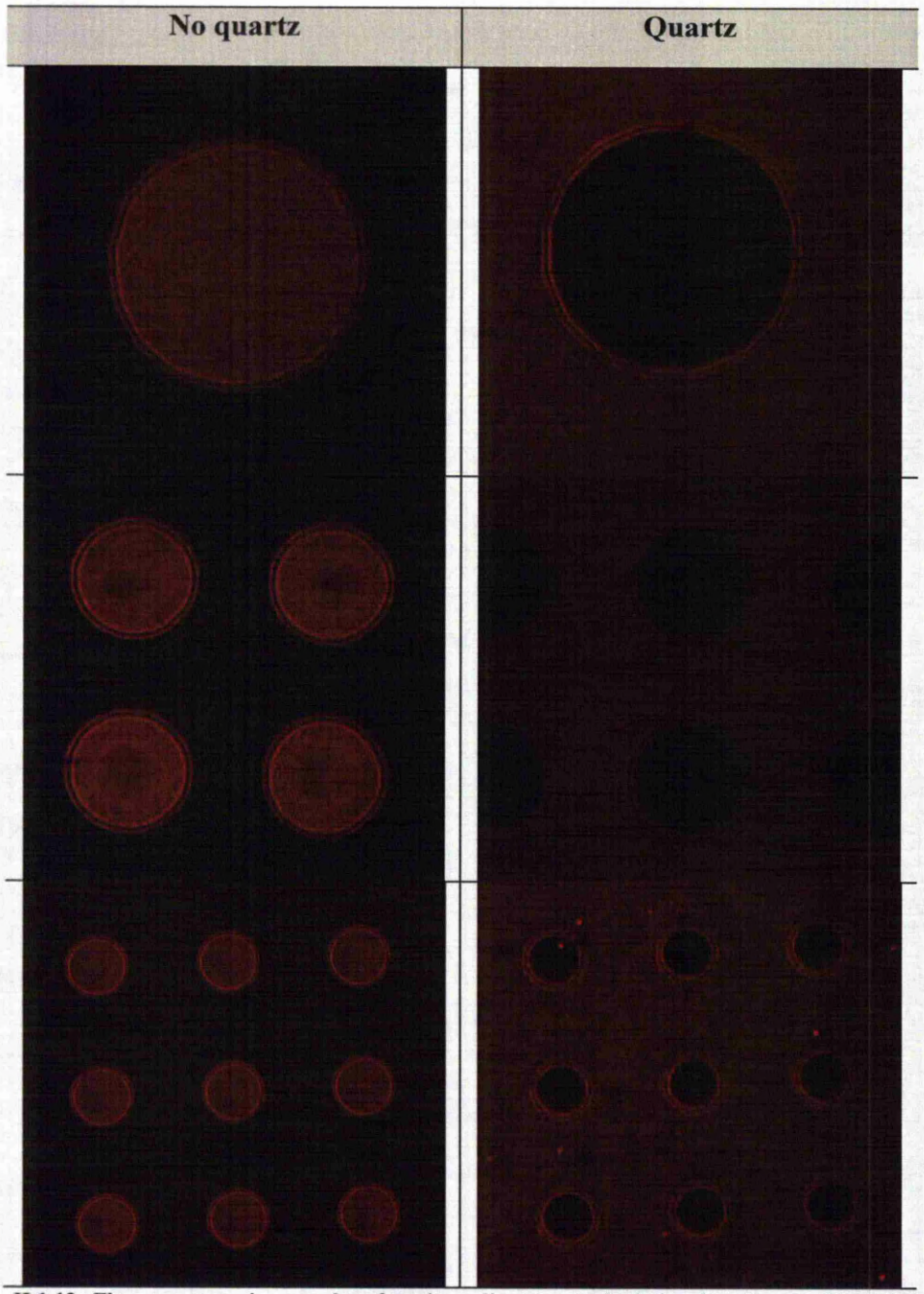

Figure II.1.12. Fluorescence micrographs of various diameter and pitch micro-lenses. The left column contains fluorescence micrographs of devices without a 60 nm oxide layer while the ones with a 60 nm oxide layer are depicted on the right. The area around the structures is in the first instance dark, as the amplitude of the electric field is set to zero at the reflector surface (though in practice, a thin oxide layer is always present and the amplitude will not be zero due to imperfect reflection). When a 60 nm oxide layer is present (right), the elevation of the fluorophore diminishes the suppression of its emission. Excitation light is 633 nm and emission is collected above 650 nm.

The fluorescence micrographs of the test microlenses shown in **Figure II.1.12** indeed confirm the behaviour predicted by **eq. 1**. The background is dark as a result of destructive interference at the silicon surface while, at 60 nm away from the reflector, there is a moderate amount of fluorescence. The slope of the side walls is able to accommodate two amplification cycles as initially predicted. The plateaus of

the 360 nm high quartz structures are only moderately bright while the plateaus of the 385 nm high structures, having an additional 60 nm thick layer of silicon oxide, appear as dark areas where the interference is destructive (**Figure II.1.13, top left**).

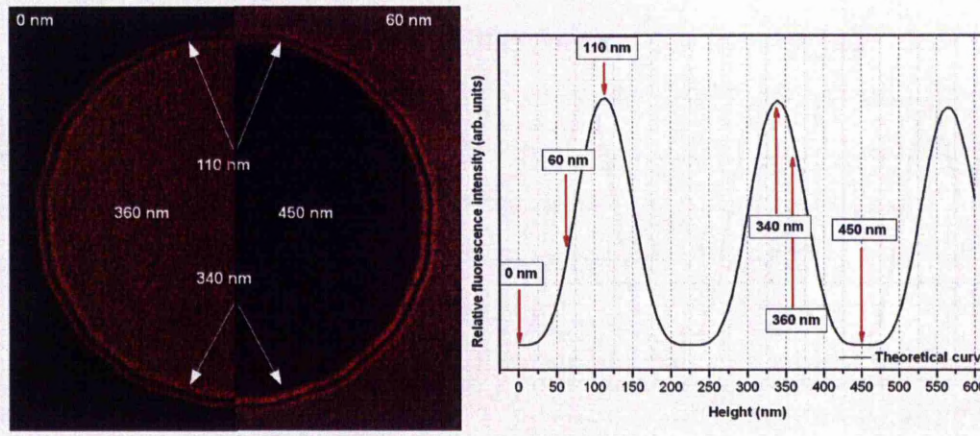

Figure II.1.13. Fluorescence micrograph showing a comparison between the two types of lenticular structures, obtained by joining half of each structure (from 40 µm diameter structures, top left). Theoretical fluorescence intensity profile versus separation distance (from equation 1, using monochromatic excitation at 633 nm and monochromatic emission at 670 nm, right)

The position fluorescence intensity distribution on and around the lenticular structures shown in **Figure II.1.13, top right** can be correlated with the theoretical shape of the curve predicted using **eq. 1** but only to a qualitative extent due to errors in overlaying the topographic and fluorescence micrographs. Also, the existence of a sloping side wall resulting in complex refraction, reflection and interference patterns, especially for the emitted light, makes the geometrical modelling of such structures quite difficult and absolute comparisons impossible at this time.

II.1.4.3 Supplementary investigations

Optical slicing as a source of contrast

As stated previously, one of the hypotheses considered initially (in addition to the standing wave model and the chemical contrast) was that the experimental results, that is the appearance of local contrast between pillar tops and the basal plane, were just an artefact arising from the use of a confocal imaging system. In non-confocal microscope, light collected from the specimen contains light from the objects situated in the focal plane contaminated with light from above and below the focal plane and, when doing fluorescence imaging. This adversely affects the quality of the information that can be extracted from the micrographs. In confocal microscopy however, through the use of a pinhole with controllable diameter, light coming from

outside the focal plane (which is, technically, a focal volume) is filtered off, a process known as optical slicing (**Figure I.1.5**). Considering a point source of light, the axial intensity profile can be modelled as a Gaussian curve and with the width parameter *FWHM (*full width at half maximum/height*)* giving the thickness of the optical slice. Based on the experimental set-up, a 100x magnification dry lens with a numerical aperture NA=0.90 and the pinhole diameter optimization (i.e. the optimal trade off between axial resolution and sensitivity) resulting in an optical slice thickness of 2 μm, a Gaussian curve with this parameter can be constructed as illustrated in **Figure II.1.14, left**. As mentioned earlier (**I.1.4 Detection**), the pinhole diameter and the objective NA mainly determine the optical slice thickness but there is a limit to which the pinhole diameter can be decreased as it adversely affects the imaging sensitivity. The centre of this Gaussian curve, x_c, gives the axial position of the focal plane and an arbitrary amplitude A can be chosen. There are two limiting cases for the position/value of x_c: the first one corresponds to focusing on the area around the pillars and gives an x_c value of 0; the second one corresponds to focusing on the tops of the pillars, giving a value for x_c of +100 nm on the z-axis (obviously, focusing is based on maximizing brightness of a certain area and this is affected by the users perception so there is some error associated with the process but the two limiting cases should account for that). From the two Gaussian curves obtained in this way (**Figure II.1.14, right**), one can easily extract the difference between two points located in focal planes placed at an axial distance of 100 nm from one another and show that the difference in amplitude is very small. It follows that a 100 nm axial distance is not enough to assign the differences in intensity between pillar tops and the silicon and platinum layers respectively observed on the substrates comprising 100 nm high pillars to optical slicing. Rejection of light resulting in local contrast would become important only in the case of extremely thin optical slices, somewhere in the order of a few hundred nanometres, a figure that is very difficult to attain, if at all possible.

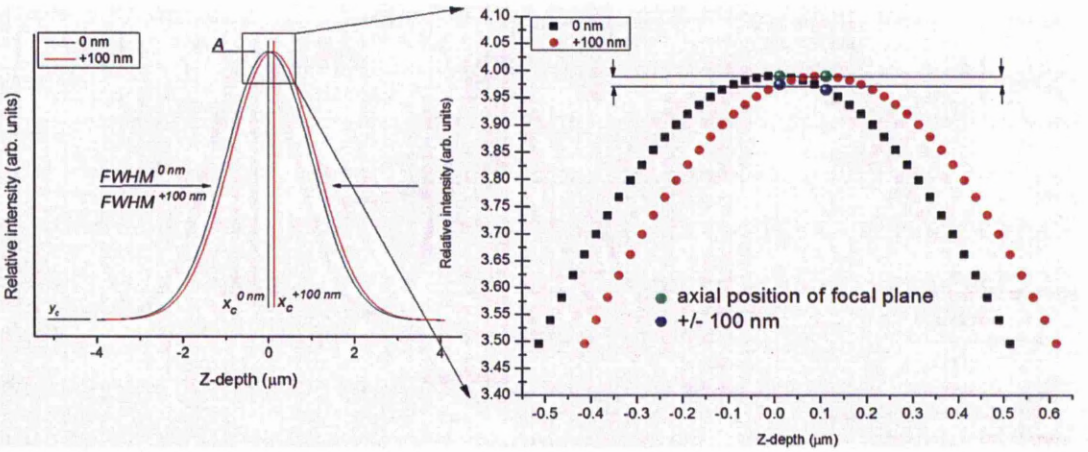

Figure II.1.14. Theoretical axial intensity profile through a confocal system using a lens with NA=0.90 (left) and exploded view of the top region of the curves (right). The two curves correspond to different locations of the focal plane, on the pillar tops (red) and on the area outside the pillars respectively (black).

Chemical contrast

Chemical contrast can be another source of fluorescence contrast. It was mentioned previously that the choice of silicon oxide material on platinum was dictated both by chemical compatibility and the ability to supply a chemical contrast, among others. While investigating the possible source of the fluorescence contrast, one of the first hypotheses that were considered was that the chemistry of the reflecting layer is different than that of the pillars. Indeed, it is reasonable to assume this when the reflector is platinum and the pillar is made of silicon oxide but it seems less obvious that the same might be valid for the silicon – silicon oxide pair. The same contrast, albeit with a lower amplitude, is observed both on the silicon and the platinum containing substrates. If chemical contrast would be the source, an explanation as to why this is happening might be found in the fabrication process. One of the steps involves transferring the pattern from the resist to the silicon oxide layer and this is achieved with the help of reactive fluoromethane that becomes ionized and etches away the silicon oxide while leaving behind fluorocarbon residues. In theory, these residues should be removed in the subsequent plasma ashing step (O_2/N_2 plasma treatment) but preliminary experiments revealed that the removal was not complete, as demonstrated by the streaky appearance of the surfaces after the grafting of the fluorescent dye. As this inhomogeneous surface is unacceptable for the purpose, a wet and dry cleaning processes were applied which led to a homogeneous surface chemistry while at the same time excluding the possibility of chemical contrast. On the platinum substrates however, chemical contrast seemed to be a very likely

scenario that would offer a satisfactory explanation for the fluorescence contrast, in conjunction with the micro/nano-structure-induced interference phenomenon. A static-SIMS analysis reveals however the presence of mass signals associated to the existence of platinum oxide on the surface; this can be explained by the possibility that the platinum oxide layer is not continuous but "patchy" so the aminosilanization reaction takes place only where surface hydroxyl groups are available. The SSIMS analysis also reveals the existence of mass signals associated to silane type molecular fragments as shown in **Table II-3**. This unfortunately confirms yet again that the envisaged chemical contrast was wiped out during the actual fabrication and pre-surface modification cleaning procedure. Moreover, if the platinum oxide layer is indeed discontinuous, this has the potential to adversely affect the performance of the device in terms of SNR due to the possible increase in the background standard deviation (see discussion on SNR and discussion on the design of new structured microarray substrates based on interference).

Table II-3. Relative abundance of different molecular fragments as obtained through ToF-SIMS analysis of the surface of the platinum containing substrates, at different chemical treatment stages

Ion	Mass	Bare platinum	+ APTES	+ DyLight 649
Si	27.973	3481	643753	306713
$SiCH_3$	42.9964	5246	549816	33036
SiO	43.9649	1868	3670	7350
SiHO	44.9744	3239	36860	90673
SiC_2H_6	58.0186	3159	40637	564
SiC_2H_7	59.031	11343	46765	472
SiC_3H_9	73.0427	37908	125411	418
Si_2CH_3O	86.9631	2606	13747	447
PtO	210.9583	8865	412	540

II.1.4.4 Signal-to-noise ratio

Probably the most important, or at least the most visible, quality metric in microarrays is the SNR (or its inverse, the coefficient of variation) is generally a measure of how well can a certain signal be separated from the background noise or, in other words, what is the confidence level with which the detection process has

yielded a true signal rather than just a random variation in background noise. In the field of microarray data analysis, the calculation of the SNR for a certain feature involves subtracting the mean background fluorescence value from the mean fluorescence value of the feature of interest and then dividing this by the standard deviation of the background (by background we understand the area around one foreground feature). It is obvious then that there are three ways of improving the SNR: increasing the feature average intensity, decreasing the background fluorescence and decreasing the variation in background fluorescence. For microarrays, traditionally relying on fluorescence detection, increasing the fluorescence intensity can be achieved in a number of ways. Common methods are improving the hybridization yield, increasing the spatial density of fluorescently labelled molecules, employing fluorescent labels with high quantum yields while using engineered substrates (with reflecting layers, optical coatings etc.) that make use of optical phenomena to enhance the signal has been explored commercially. The other two terms involved in the calculation of the SNR are both background related. The actual background fluorescence can be minimized by using non- or low-fluorescence materials or mitigating the problem of non-specific adsorption. But it is not the actual background fluorescence level that affects the magnitude of the SNR the most, it is the uniformity of the background; in other words, one can live with an elevated background fluorescence level as long as its mean value has a low dispersion (using the standard deviation SD as a measure of dispersion). That is why the surface of a microarray substrate has to be chemically homogeneous, free of imperfections and perfectly levelled. However, while it is easy to find materials that, on their own, do meet the enumerated criterions, putting them together to form an advanced substrate can be a challenge as trade-offs in performance become necessary due to technical limitations related to material compatibility and processing technologies.

In the case of structured substrates under investigation, the area of the pillar top constitutes the area of interest or foreground, similar to the spots in classical microarrays. The relationship between the florescence intensity in this area and the fluorescence intensity around the pillars (background) can be straightforwardly correlated through the SNR parameter. Further, the components necessary for the calculation of the SNR will be discussed separately.

The fluorescence intensity of the foreground is the average gray value of the foreground. It is obvious that this value will increase with the height of the pillars, as can be seen in **Figure II.1.15, top**, in the way predicted by the FLIC curve. It can also be seen that the average fluorescence intensity increases in a way that resembles a logarithmic or allometric curve with the increase in pillar footprint (**Figure II.1.15, bottom**).

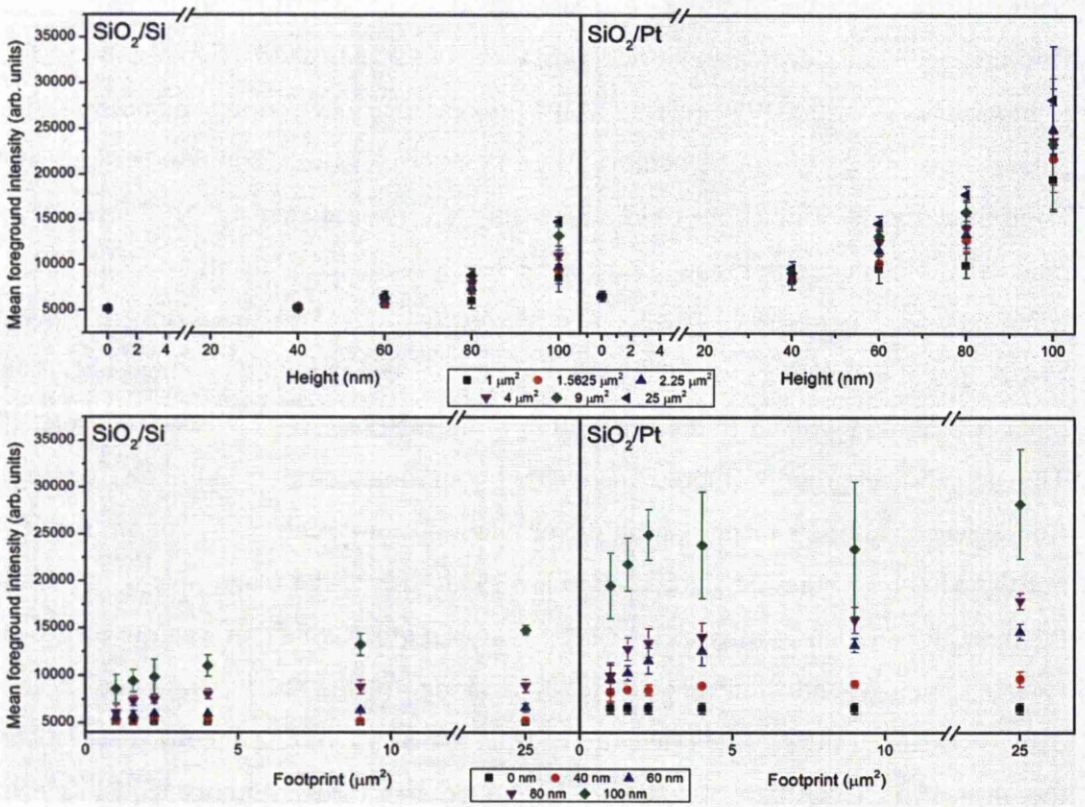

Figure II.1.15. Mean foreground intensity versus pillar height (top) and footprint (bottom) respectively (silicon reflector on the left, platinum reflector on the right)

This shape can be attributed to the ratio of edge (i.e. perimeter) to total pixels and the way this ratio changes with the total number of pixels (see discussion in **II.1.4.1 Optical interference effects and data fitting**). One can also see that the values of the fluorescence intensity depend on the reflector material and this can be attributed to the difference in reflectivity between silicon and platinum at the excitation and emission wavelengths, as shown previously in the data fitting section.

Background intensity measured on silicon and platinum respectively was subtracted from the foreground average intensity to eliminate the contribution of the residual fluorescence yielding the background-corrected foreground average fluorescence

intensity. The theory predicts that the intensity at the reflector surface should be zero; obviously, there is no "zero height" due to the presence of an oxide layer on both materials and the silane has a defined but small length. This does not however explain the level of fluorescence arising from the background since the short fluorophore to reflector distance should lead to the formation of destructive interference, as seen in **Figure II.1.16, top**. Moreover, the background fluorescence on the silicon substrate appears to mildly increase with the pillar height i.e. with the foreground intensity level suggesting that this fluorescence is a form of stray, diffuse light coming from the amplified fluorophore emission. The background fluorescence on the platinum layer is higher than that recorded on the silicon layer and it seems to be independent from the pillar height. With regards to pillar footprint, there seems to be no dependence whatsoever between background fluorescence and pillar footprint which suggests that, at least in the case of silicon, the background is contaminated with "stray" fluorescence (**Figure II.1.16, bottom**). The higher intensity levels measured on the platinum layer can probably be considered a "side-effect" of the higher reflectivity of the metal. A source of uncertainty is related to the instrumentation used for these measurements, i.e. a confocal microscope rather than a microarray scanner. Image acquisition optimization in a microarray scanner is done by optimizing the PMT (photomultiplier tube) voltage while monitoring the distribution of pixel values so that the entire dynamic range is used. In contrast, as microscopes are more complex, there are multiple detector settings available: master gain (increases the detector sensitivity much like the PMT mentioned above), digital gain (amplifies the signal from the detector), and digital offset (which changes the "zero" value of the detector). Consequently, the optimization routine is less straightforward and leads to much noisier images.

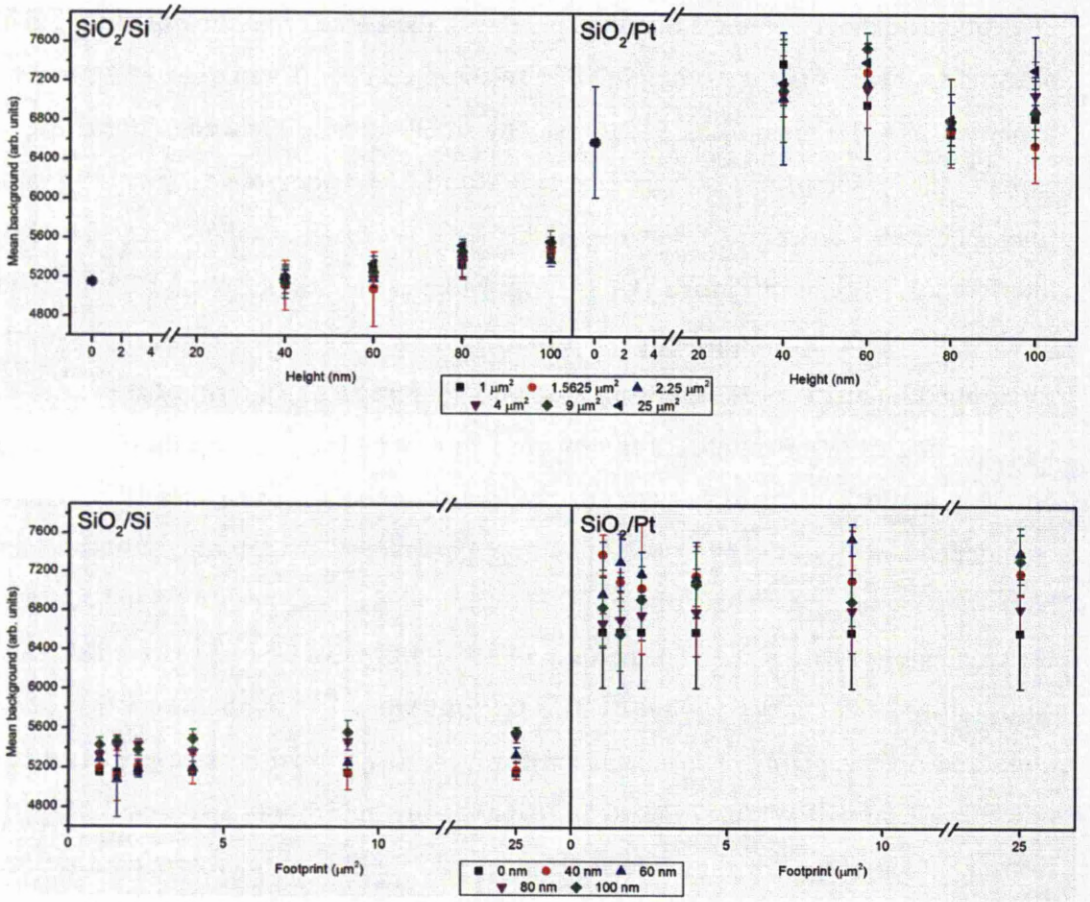

Figure II.1.16. Mean background intensity versus pillar height (top) and footprint (bottom) respectively (silicon reflector on the left, platinum reflector on the right)

The uniformity of the background is the third component influencing the SNR; as mentioned above, uniformity is more important than the actual average fluorescence level since it is the fraction denominator. With regards to its dependence on pillar height, which is illustrated in **Figure II.1.17, top**, on both silicon and platinum, there is a doubling of the dispersion of the pixel gray values from the lower to the highest pillar heights. Again, the difference between silicon and platinum is quite dramatic, with the highest level of SD measured on silicon being equal to the minimum SD measured on platinum. With regards to pillar footprint (**Figure II.1.17, bottom**), the apparent shape of this dependence (especially for the platinum reflector) indicates a possible correlation with stray fluorescence since background dispersion is elevated at higher pillar heights.

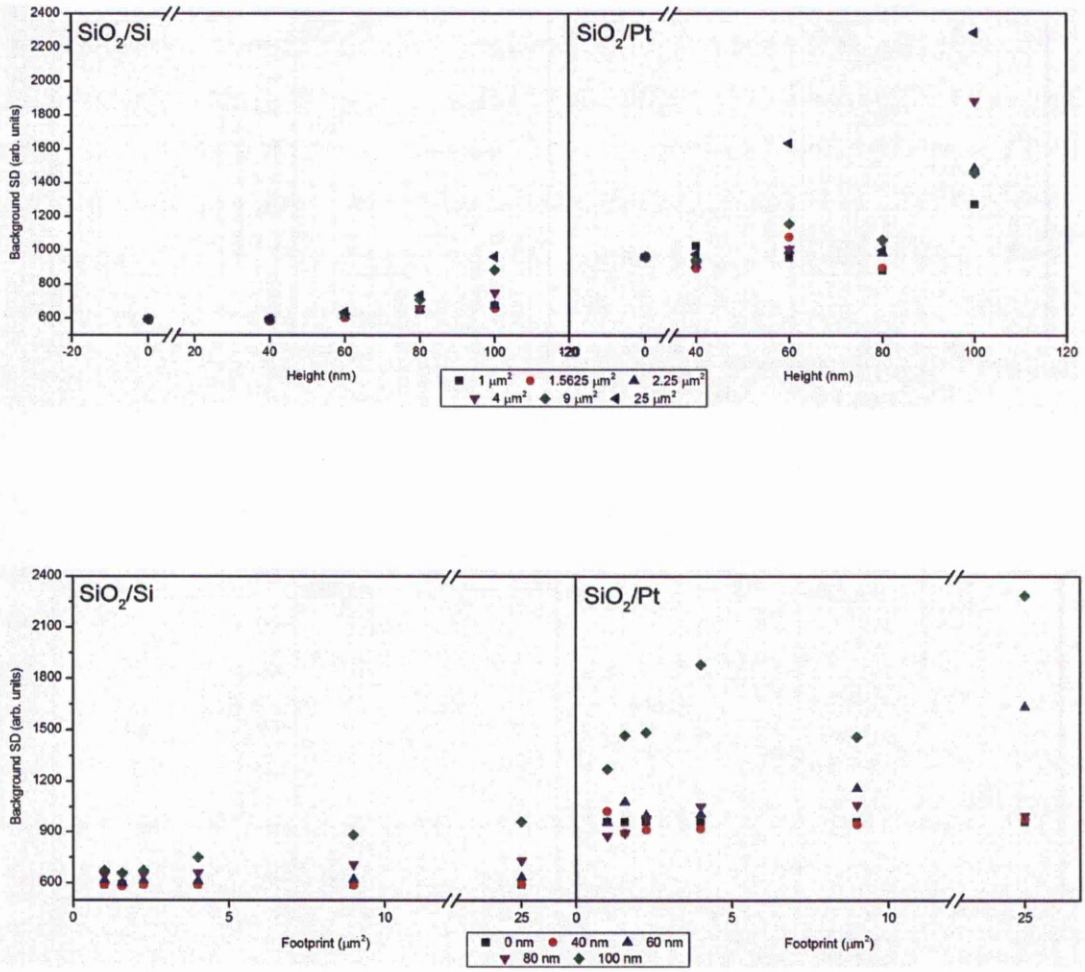

Figure II.1.17. Background uniformity (SD) versus pillar height (top) and footprint (bottom) respectively (silicon reflector on the left, platinum reflector on the right)

Having measured fluorescence levels of the foreground and background together with the dispersion of the background fluorescence, one can now calculate the SNR and plot it against pillar height and pillar footprint, as shown in **Figure II.1.8 top** and **bottom** respectively. It was shown that the average foreground intensity increases with the height of the pillars due to the amplification effect that is modulated by the thickness of the dielectric layer. At the same time, the average background intensity only slightly increases with pillar height and footprint in the case of the silicon reflector while remaining constant on the platinum substrate, i.e. independent from the pillar height and footprint. The background SD again increases with height and footprint of the pillars but with different rates. The resulting SNR increases with pillar height, which is expected because the foreground intensity increases while the

background intensity remains almost constant despite the increase in background SD shown in **Figure II.1.8, top**. The same is valid for the dependence between SNR and pillar footprint, where the SNR increases in what appears to be a logarithmic rate because the foreground and background SD increase in the same way, albeit from different levels, while the background intensity does not appear to be affected by the increase in the projection area of the pillars as can be seen in **Figure II.1.8, bottom**). It thus follows that using structured substrates capable of inducing formation of standing waves can effectively create a fluorescence contrast on a surface that is entirely functionalized with a fluorophore and puts the SNR values measured here in a different perspective.

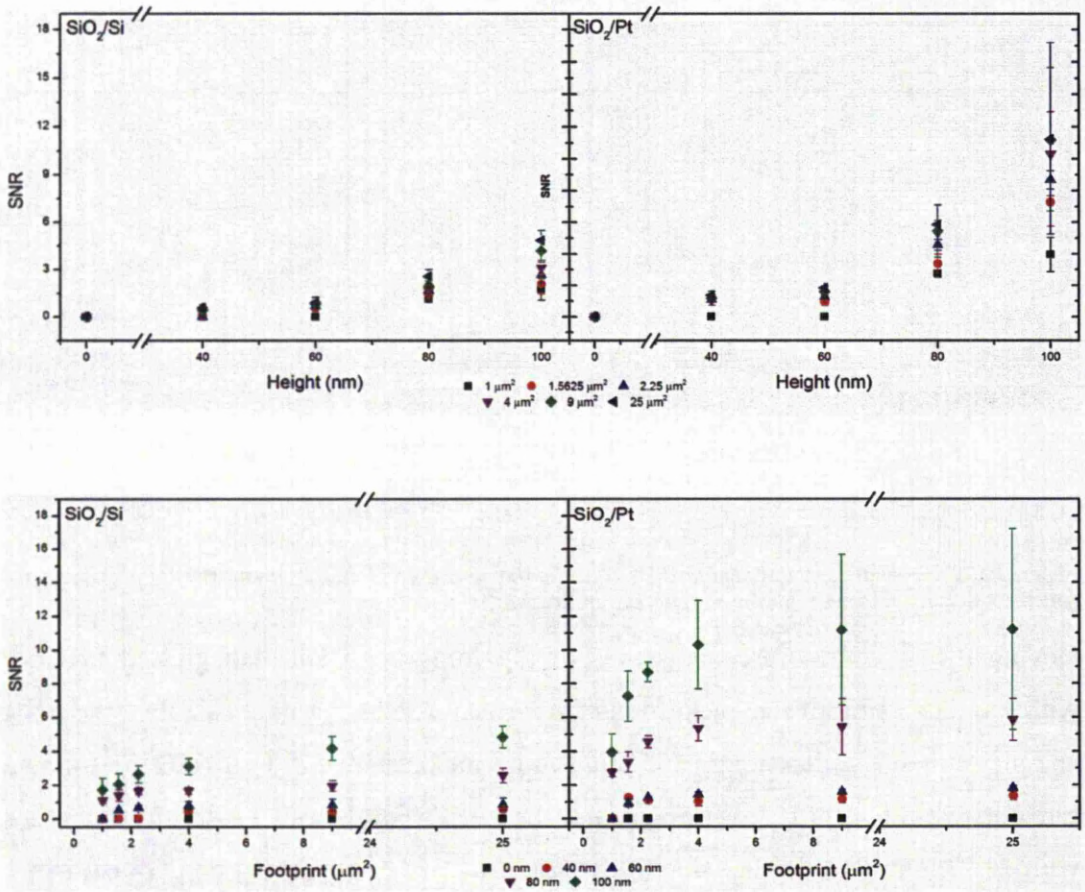

Figure II.1.18. SNR versus pillar height (top) and footprint (bottom) respectively (silicon reflector on the left, platinum reflector on the right)

Total fluorescence per pillar and total fluorescence per unit area

An interesting aspect is revealed when comparing the integrated fluorescence per pillar and the integrated fluorescence per unit area. The integrated fluorescence per pillar (**Figure II.1.19**), which is the sum of the pixel gray values belonging to one

pillar, increase linearly, as expected, with the footprint of the pillar which also increases linearly (**Figure II.1.19, top**); the same is valid for integrated pillar fluorescence as a function of pillar height, obviously due to the interference induced amplification and following the same increase law that governs the variation of fluorescence with height of the dielectric layer (**Figure II.1.19, bottom**).

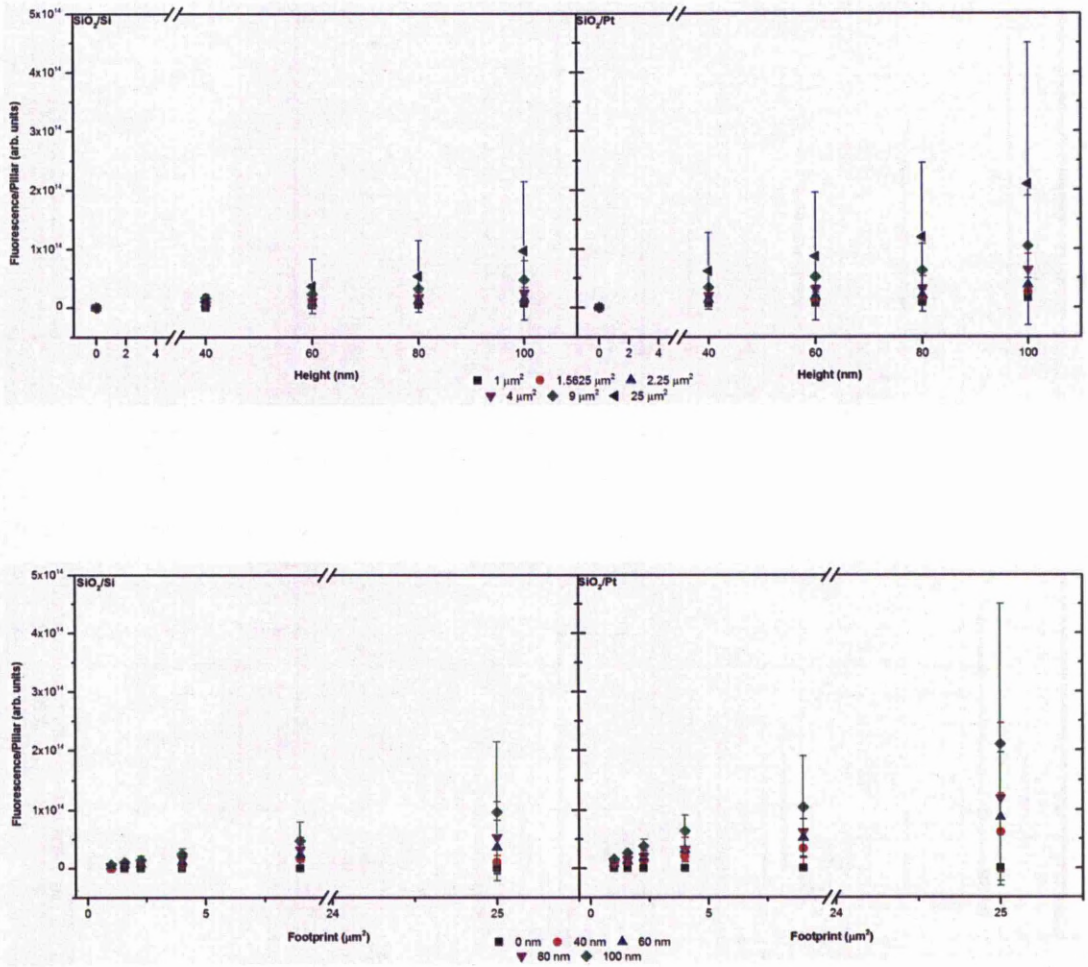

Figure II.1.19. Integrated fluorescence per pillar versus pillar height (top) and footprint (bottom) respectively (silicon reflector on the left, platinum reflector on the right)

Normalization of these values by the surface area of each pillar yields however an unexpected result (**Figure II.1.20**). The evolution of the integrated fluorescence per unit area with pillar height is again linear but at a more in depth look, it appears that, comparatively, the fluorescence per unit area corresponding to the small area pillars is amplified more than the one arising from the large area pillars (**Figure II.1.20, top**). This can be made more visible by plotting the total fluorescence per unit area

versus the pillar footprint (**Figure II.1.20, bottom**). Indeed, this confirms that the fluorescence per unit area acquired from smaller footprint pillars is higher than that collected from the larger pillars. This behaviour is observed on both silicon and platinum substrates but, while the decrease appears as almost linear in the case of silicon. The evolution of this quantity with pillar footprint displays an absolute maximum in the region around 2.25 μm^2.

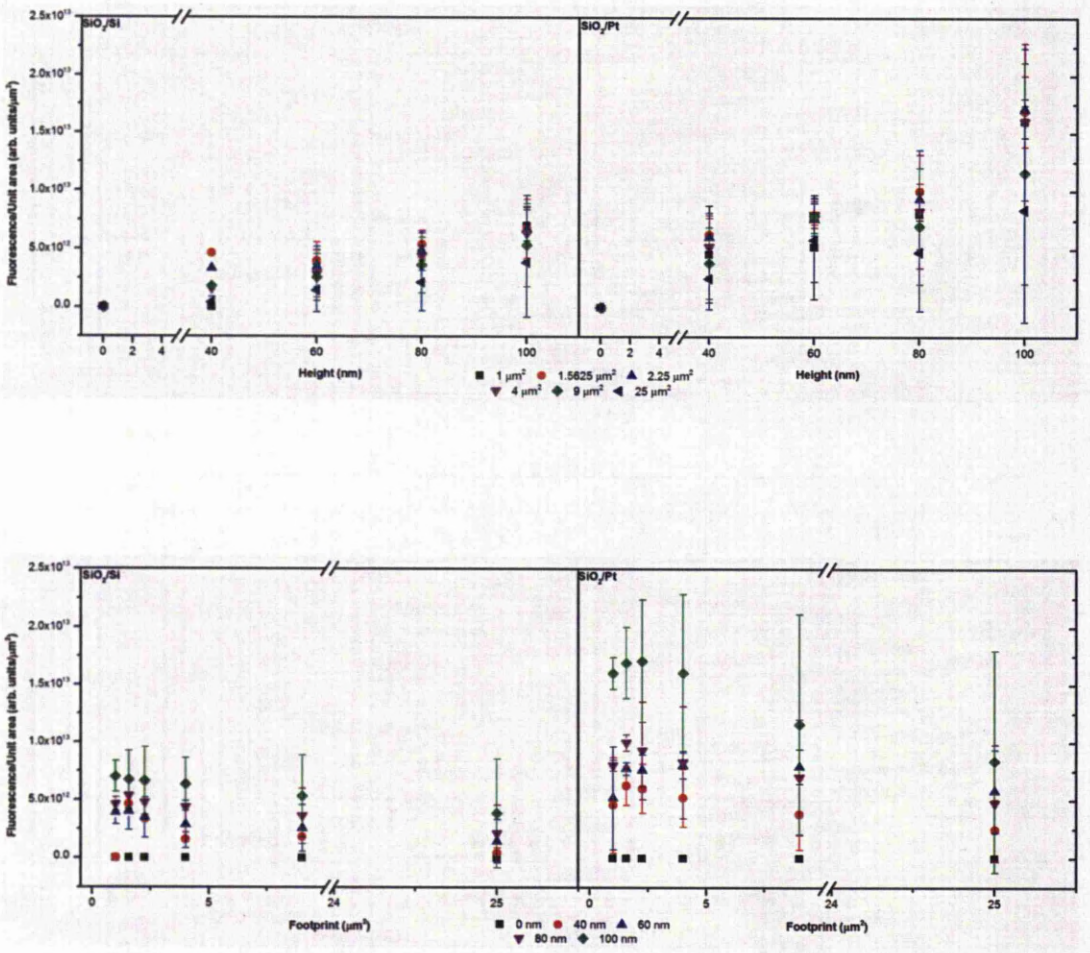

Figure II.1.20. Integrated fluorescence per unit area versus pillar height (top) and footprint (bottom) respectively (silicon reflector on the left, platinum reflector on the right)

The fabrication of a novel type of substrate with a design that is applicable and has potential to improve microarray devices using optical fluorescence detection was presented, together with the preliminary evaluation of their performance characteristics. These substrates are fabricated using standard micro-lithographic techniques and using materials that are common for the microelectronic industry.

The concept of the design is based on amplification of fluorescence emitted from certain geometrically defined areas while suppressing the fluorescence emitted from anywhere outside those areas. The amplification is the result of constructive interference while suppression is achieved by maximizing destructive interference; the formation of interference is induced by using a reflective bottom layer and an optically transparent dielectric layer that acts as spacer between the fluorescent molecule and the reflecting layer. The height of the spacers is carefully chosen based mainly on the excitation and emission wavelengths of the fluorophore and the resulting fluorescence intensity profiles are shown in **Figure II.1.21**.

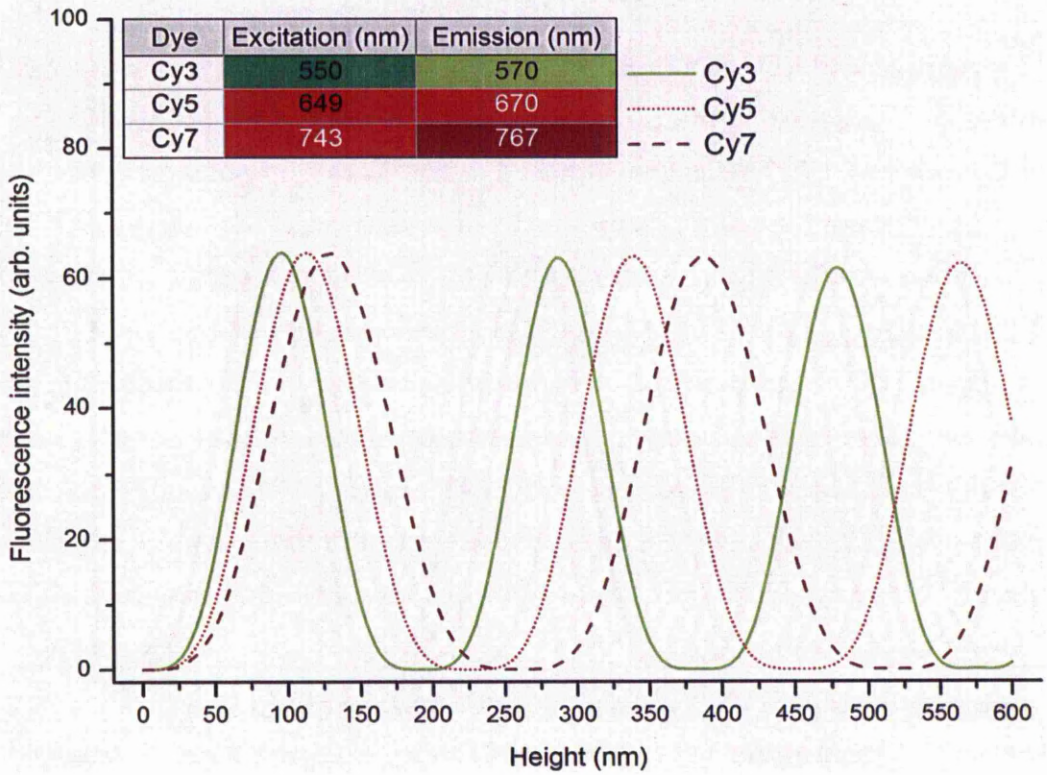

Figure II.1.21. Theoretical fluorescence amplification profile versus fluor - reflector separation distance (silicon oxide layer thickness, n=1.46) for different commercial cyanine fluorophores using eq. 16 (with their characteristic excitation and emission wavelengths shown in the figure legend and considered monochromatic).

The curves plotted in **Figure II.1.21** were obtained using eq. 1, i.e. considering an ideal process with perfect reflection and monochromatic excitation and emission light. One can see the lateral shift of curves when the excitation and emission wavelengths respectively are increased.

II.1.4.5 Comparison with classical substrates

A classical microarray experiment is generally carried out on most commonly low fluorescence glass slides but silicon chips are also available (e.g. GeneChip from Affymetrix). The experiment consists of grafting a known DNA sequence onto the surface of the slide at specific locations forming a defined array and then exposing the slide to a solution containing the fluorescently labelled unknown sequence. After hybridization, the fluorescent emission from each spot is measured which is a measure of the extent of hybridization. A variety of parameters related to the spot are then calculated and used to categorise the data collected and interpret the collected data in terms of reliability. One of these metrics is the SNR.

As mentioned earlier, in the field of microarray assays, the commonly accepted definition of the SNR is the background-corrected mean foreground fluorescence intensity divided by the background SD. For the purpose of putting our results in context, a short discussion about the three components that are used in this calculation is warranted. The presence of background fluorescence can be assigned to multiple factors. One cause is the autofluorescence of the substrate itself and this problem can be mitigated by using high quality glass. The surface treatment that the slides are subjected to may also cause unwanted fluorescence: the surface of the slides needs to be able to bind the known sequence and this means that certain chemical groups that might exhibit a certain level of autofluorescence have to be present. But maybe the most troublesome is the background fluorescence due to the non-specific adsorption of analyte molecules. Regardless of the source of background fluorescence, its presence is detrimental and the goal is to minimize it. As stated earlier, the amount of fluorescence coming from outside the features is not critical as long as its dispersion is narrow; unfortunately, this is not generally the case. It has been demonstrated that, for example, when the gain of the detector (PMT voltage) is increased to obtain a better signal from the spots, after a certain level, the noise increases faster than the actual signal does. That is to say that trying to amplify the signal by raising the gain leads to a deterioration of the quality of that signal. There is also the problem of airborne contaminants that might adhere to the slide during the experimental steps and that may contribute to a large dispersion of the background noise. For these reasons we argue that a substrate architecture that not

only amplifies the signal but also suppresses the background noise has a good potential for important improvement to currently available devices.

Fluorescence signal arising from the binding sites, the so called "spots" or "features" is due to the presence of fluorescently labelled target molecules in the spatial domain defining the spot. For the purpose of detection and quantification, one aims at increasing this fluorescence intensity and this can be achieved in several ways: increasing the hybridization yield, increasing the amount of labelled molecule by increasing the surface area (using 3D networks), or using branched linkers, e.g. dendrimers. There are also other means of boosting the fluorescence independent on the amount of fluorophore present. These methods generally rely on improving the reflectivity and selectivity for certain wavelengths through the use of alloys with high optical reflectivity, specialty optical coatings much like dichroic filters or mirrors, methods relying on interference and methods exploiting the plasmon effect of noble metals.

Regarding the SNR, there are some aspects that require clarifications. The first one is of technical nature because the use of a confocal microscope (Zeiss Observer Z1 with LSM 510 laser scanning module) rather than a dedicated microarray scanner has some disadvantages: firstly, there is no dedicated calibration and optimization procedure and secondly, a confocal microscope offers the possibility to change detector parameters to improve image quality. Unfortunately, the image quality optimization procedure for the instrument used in these studies is based on the assumption that pixel saturation is unwanted, which is generally true because saturation means loss of information; in this context however, one cannot tell what the background level really is and there is no absolute zero available to eliminate what is called the "detector offset". This has the unfortunate effect of adding background signal where it might actually not exist. A second aspect that needs to be clarified is the caution one should use to compare the SNR values reported here with those reported in literature and by microarray slide manufacturers. In a microarray experiment, the probe molecules are placed at specific location on the surface of the slide by mechanical means, be it ink-jetting, micro-spotting or others, and then the entire slide is exposed to the fluorescently tagged target. Therefore, the only mechanism through which the target can adhere to the area that has not been functionalized with probe material is through non-specific adsorption. The scope of

the experiments presented here is different and that is why the experimental conditions, and consequently, the interpretation of the results should be different. The architecture proposed aims at improving the signal characteristics on microarray slides using two approaches: amplifying the signal arising from the foreground while removing fluorescence from outside the detection domains. For this reason, the entire surface of the test slides was modified with a fluorescent dye rather than only small domains on that surface. This allows us to test not only whether fluorescence is amplified but also if fluorescence suppression can be achieved on the same slide and within a very small range, i.e. fluorescence confinement. It follows that, if integrated onto a classical slide, a surface geometry like the one described so far should be capable of eliminating at least the background noise that is the result of either non-specific binding or due to autofluorescence.

II.1.4.6 Implications for spot detection and quantification

One of the most important advantages of microarray technology is that it allows for a huge number of experiments to be performed simultaneously on a substrate the size of a microscope slide or even smaller. This in turn translates into high throughput but at the cost of having to process large amounts of data. Of course, this advantage can easily be overridden by the sheer amount of time needed to process the data manually; this is the reason why research into better algorithms for unsupervised spot detection is on-going. With respect to the detection process, the importance of a spot's shape, dimension and position is critical to the feature extraction and integration of the signal coming from spot area simply because algorithms designed to perform these tasks rely on assumptions about the structure of the spot. To put it more clearly, it is easier to detect objects with simple shapes and known dimensions in a regular array than irregular ones with only approximate dimensions and, consequently, the integration and signal statistics is more robust. Along these lines, we argue that using a physical (solid) spot geometry-inducing element, i.e. the structures comprising the substrate, whose dimensions are tightly controlled through the use of photolithographic fabrication methods with their inherent stability, can improve the reliability of detection/quantification in microarray type bio-assay experiments in two ways: feature extraction with increased robustness and increased statistic confidence owing to the fact that pixels values are included/rejected in the computation of spot metrics with higher confidence.

According to (Bozinov and Rahnenfuhrer 2002), the difficulties associated with the correct automated segmentation of microarray spots can be classified into four categories: unknown and variable spot diameter, irregular (and unknown) shape, high values of the background sometimes accompanied by low values of the foreground, and artefacts caused by contamination or low surface quality. To understand better how these problems identified by the aforementioned authors affect the spot detection and quantification process, we will first look at the general segmentation methods implemented in microarray analysis software.

The first step in the analysis of a microarray experiment is the gridding procedure that divides the image into small, usually square areas that contain one spot and a certain portion of background around that spot called target areas or grid cells. While this process presents some difficulties, it is beyond the scope of this discussion and will not be treated here. However, it is important to know that the quality of the gridding process has the potential to affect the following analysis steps. The next stage, once a target area corresponding to each spot has been assigned is assigning pixels to the actual spot or to the background in an automated, robust and error free manner, which is not a trivial matter in the real world due to deviations from the ideal behaviour (irregular shape, irregular and even unknown size, variable position). The methods employed so far for automated separation can be divided into three classes: spatial based, intensity based and hybrid methods (Petrov et al. 2002). A description of these procedures can be found in (Bajcsy 2006); a brief overview of the methods together with the way they are affected by spot size, shape and location uncertainty is highlighted here.

Spatial based algorithms involve the superposition of two concentric circles on the spot and assigning foreground status to the pixels falling inside the smallest circle while the pixels falling outside the larger circle are considered to be part of the background (pixels contained between the two circles are disregarded). However, this procedure would give satisfying results if gridding would not be affected by variations in spot position and, furthermore, because the actual size of the spot is unknown, it is susceptible to errors. Moreover, because the shape of the spot might display deviations from the template shape (be that circular, square etc.), the algorithm might end up including background pixels into the foreground or the other way around.

Intensity based algorithms can be further divided into segmentation and clustering, the difference being that segmentation assigns pixels to two contiguous groups, i.e. the pixels need to be connected, while in clustering based algorithms, the necessity for contiguousness is not enforced. In a clustering-based algorithm, a threshold value is calculated and used to assign foreground and background pixels. This border value is calculated based on the cell size and the estimated theoretical diameter of the spot; because the percentage of spot pixels in the total number of pixels is required, the shape of the spot plays an important role as well. Once the ratio between spot pixels and total pixels is known and the pixel intensity values are arranged in a descending order, the fraction corresponding to that ratio containing the brightest pixels is attributed to the foreground. The segmentation based approach can be implemented in at least two ways: seeding and watershed. In the seeding approach, a number of random pixels belonging to the spot area are chosen and the algorithm joins together pixels with similar values to form a continuous area (the seeds can be planted in an area outside the spot as well). The watershed method uses morphological operators to filter out pixel groups that deviate from a certain shape and size. This method also assumes a certain spot shape and size.

Hybrid methods are based on combinations of the two previously described classes, in an attempt to retain the advantages specific to each of them. For instance, intensity based segmentation yields a contiguous region whose contour can be fitted on a predefined shape (a circle) and, if this fitted circle differs to a defined extent from the spatial template, the spot is discarded as invalid. The problem with this approach is that it relies on template with pre-assumed dimensions. Another approach uses the Mann-Whitney statistical test applied on two populations drawn from the background and (lowest intensity) foreground respectively. The foreground original pixels are replaced by pixels that have not been previously selected until a difference in median population intensity is found with a statistical significance of at least 0.05. The pixels that passed the median difference test then constitute the foreground. Of course, the choice of where the foreground pixels are selected from is again based on a spatial template. An algorithm based on trimming the pixels with values that are regarded as outliers, both from the background and the foreground also exists. This method is also affected by the quality of the gridding process (spot location) and spot dimension.

The conclusion that can be drawn from the above is that, although different algorithms are affected to different extents by uncertainties related to the spot location, dimension and shape, a substrate architecture that would force the spot to take a certain known shape and size, and would confine the spot to a precise position relative to its neighbours could only be beneficial to microarray data extraction by improving the gridding process and allowing it to be performed independently of human intervention while eliminating the need to rely on spatial templates.

II.1.5 Summary and conclusions

A fluorophore was used to probe the fluorescence modulation capability of microfabricated structured substrates. A fluorophore was mounted on the surface of substrates comprising a silicon and platinum reflector respectively and silicon oxide pillars of various footprints. It was found that the height of the pillars, ranging from 20 to 100 nm, effectively modulates the fluorescence emission and, moreover, that fluorescence is suppressed for "zero" height pillars. It was also shown that fluorescence amplification is higher for a platinum layer than for the silicon one. An optical model that is commonly used in fluorescence contrast microscopy was successfully applied. The model predicts the formation of standing waves when light that excites a fluorophore near a reflecting surface gets reflected and interferes with the direct wave, the same being valid for the emission light. The fluorophore-reflector distance modulates the amplification of fluorescence, the pillars effectively acting as spacers by positioning the fluorophore at a specific distance from the reflector; by using a reflector material with good reflectance (e.g. platinum rather than silicon) the amplification factor can be increased.

An immediate possible application to microarray devices is envisaged, with direct effect on the signal-to-noise ratio of these devices. For this reason, the SNR was measured after modification of the surface with the fluorophore. It was found that a high contrast between chemically identical areas can be obtained and this contrast has a purely geometrically-induced optical source. Another finding concerns the amount of fluorescence per unit area (of pillar terrace); interestingly, it appears that the integrated emission from smaller footprint pillars is higher than that of larger footprint pillars and this aspect warrants further in depth investigation.

Potential improvements for microarray technology are not limit to increased SNR. Another critical aspect in microarrays is correct identification and quantification of signal levels arising from one feature and this can only be achieved if the features are correctly identified, i.e. the process of assigning segments of a grid cell to the foreground and background respectively. A discussion on how uncertainties related to the shape, position and size of a feature might affect the performance of current algorithms employed in spot detection and amplification was included.

II.2 Chapter 2: Hybridization based detection of an oligonucleotide sequence

II.2.1 Introduction

This section is an account of the experimental results obtained using the substrates described previously to detect the presence of a single stranded DNA sequence through hybridization. It was demonstrated previously that structured layered substrates comprising a reflecting layer and an optically transparent dielectric layer structured in the shape of 100 nm high pillars with a square footprint of values ranging from 1 to 25 μm^2 is capable of selectively amplifying fluorescent signal over the structures while suppressing it where the silicon oxide layer is not present. The experimental procedure includes chemically modifying the surface of the substrate and render it able to covalently bind a thiol-modified ssDNA sequence as depicted in **Figure II.2.1** and then exposing it to solutions of varying concentration of a complementary DNA strand tagged with a fluorescent label (Cy5). A glass microscope slide is modified in the same way to act as a control and a benchmark for the experimental procedure. The substrates are imaged and processed as described previously and the evolution of the SNR versus target concentration is plotted. Target hybridization is quantified using spectrofluorimetry. The results are then explained in terms of surface chemistry and imaging equipment and differences from a classical microarray image are highlighted. The existence of stray fluorescence on untreated substrates is also discussed and a possible explanation is offered together with a discussion on the retarding effect of silicon oxide on this extrinsic fluorescence.

Also contained in this section is a description of hybridization experiment carried out on binary SiO_2-TiO_2 pillars. Titanium oxide is used to improve adhesion between silicon oxide and platinum. The effect of integrating titanium oxide in the composition of the pillars is unexpected; while the theoretical effect of the new type of dielectric layer suggests a preservation of the amplification, in reality the effect is inverse. A possible explanation is offered.

This chapter will also highlight some unforeseen problems and offers a motivation for the decisions made and applied regarding the practical choices made further and presented in the following chapter in relation to the substrate layout, surface chemistry and instrumentation.

II.2.2 Materials and methods

II.2.2.1 Reagents and buffers

Bovine serum albumin (BSA),3- aminopropyl triethoxysilane (APTES), acetic acid, dithiothreitol (DTT) and N-succinimidyl 3-(2-pyridyldithio)-propionate (SPDP) were from Sigma along with sodium phosphate, sodium bicarbonate and sodium chloride used to prepare buffers. Buffers: PBS - 15 mM sodium phosphate, 0.15 M NaCl, pH 7.4; bicarbonate buffer - 0.1 M sodium bicarbonate, pH 8.2; wash buffer 1:bicarbonate buffer containing 10% ethanol; wash buffer 2: PBS containing 0.05 % tween20. Oligonucleotides (probe sequence 5'-CCT-CAA-AGA-GAG-AGA-AGA-AGA-AA-3' with a C6 thiol derivatization at the 5' end and target sequence 5-TTT-CTT-CTT-CTC-TCT-CTT-TGA-GG-3' with a Cy5 derivatization at the 5' end) were purchased from Eurogentec (Belgium). Ammonium hydroxide, hydrochloric acid and hydrogen peroxide used for wet chemical etch of substrates prior to use were purchased from Sigma while a Millipore MilliQ system was used to supply the purified and de-ionized water. PD-10 desalting columns from Amersham were used. Silicone 16 cell dividers were from GraceBiolabs (USA).

II.2.2.2 Substrate fabrication

Silicon oxide structures were patterned on silicon and platinum coated silicon substrates using a procedure described in the previous chapter. The bi-component pillars were fabricated on a platinum reflector only following the same procedure but intercalating a titanium dioxide layer between the metal layer and the silicon oxide one.

II.2.2.3 Surface modification, target hybridization and spectrofluorimetric analysis

Amine functionality was introduced on the surface of the test structures using the aminosilane APTES. After silane temperature-induced crosslinking, a heterobifunctional crosslinker N-succinimidyl-3-(2-pyridyldithio)propionate (SPDP) was conjugated to the amine groups. The thiolated probe was reduced using DTT, purified through gel chromatography and then attached to the surface.

Target hybridization

Prior to hybridization of the target sequence, the surface was blocked against nonspecific adsorption with BSA-Tween20 solution in PBS. Hybridization was

performed overnight at room temperature using a range of target concentrations, from 1 to 0.0156 μM.

Spectrofluorimetry

Spectrofluorimetry was employed to measure the target concentration after the hybridization using a Perkin Elmer LB50S equipment; quantification was based on a calibration curve constructed using the fluorescently labelled oligonucleotide.

Contact angle measurements

Water contact angles were measured using a contact angle meter from Kruss. Water contact angle evolution was monitored on glass and the structured substrates for each step of the chemical surface modification procedure.

Imaging, data extraction and analysis

Imaging and image processing as well as numerical data processing were performed in manner similar to the one described in the previous chapter.

II.2.3 Experimental

II.2.3.1 Surface modification

Surface modification procedure and oligonucleotide attachment is illustrated in **Figure II.2.1**. Prior to the derivatization procedure, substrates comprising approximately 1 cm^2 pieces of silicon comprising around 20% structured surface, together with glass microscope slide controls, were first cleaned using the wet chemical etch procedure (RCA clean) described before. Because during the wet method, the height of the pillars decreases, a dry UV-ozone cleaning method was employed, as described previously. Substrates prepared in this way were stored in a desiccator for the time between cleaning and derivatization.

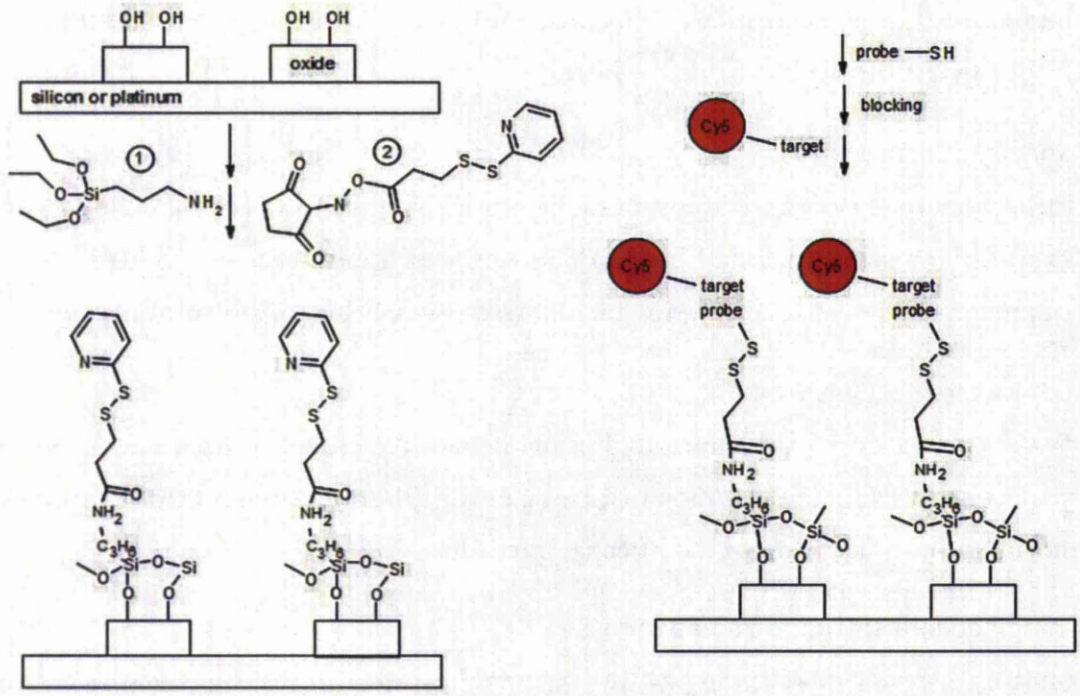

Figure II.2.1. Surface functionalization procedure and oligonucleotide target detection through hybridization. The silicon oxide pillars (displaying hydroxyl groups) are first derivatized with an aminosilane (1) then a bi-functional (amine-reactive NHS-ester functionality at one end and thiol-reactive pyridyl di-thio at the other) crosslinker (2) is reacted to the surface. The result of this process is a surface that now displays sulphide-reactive groups. A thiol-derivatized capture probe (labelled probe-SH) is attached to the surface via the thiol-reactive surface groups. The surface is then blocked against non-specific adsorption with BSA and hybridization with a complementary fluorescently labelled oligonucleotide (target-Cy5) is carried out.

Silicon oxide surfaces were aminosilanized by exposing them to a solution consisting of ethanol (absolute), 4.25 M acetic acid solution in water and APTES in a ratio of 95:3:2 by volumes for 2 hours followed by three ethanol washes, drying under a light nitrogen flow and finally baking them in an oven for 45 minutes at 110°C to allow for the silane to crosslink on the surface.

A freshly prepared SPDP stock solution (66 mM in dry dimethylformamide) was used to prepare 20 mL SPDP solution in bicarbonate buffer by adding dropwise and under stirring 600 µL SPDP stock solution to 19.4 mL bicarbonate buffer; as a hetero-bifunctional crosslinker, SPDP is expected to react with the surface amine groups through its NHS-ester end and yield pyridyl-dithio groups on the surface (Carlsson et al. 1978) and depicted schematically in **Figure II.2.2**. This is achieved by submerging the substrates in the SPDP solution for 4 hours on a rocking-plate mixer. Removal of unreacted SPDP is carried out by subjecting the substrates to three 5 minutes washes on the same rocking plate mixer, the first wash being performed in bicarbonate buffer containing 10% ethanol and the following two being

performed in bicarbonate buffer only. The substrates were then dried in a gentle stream of nitrogen.

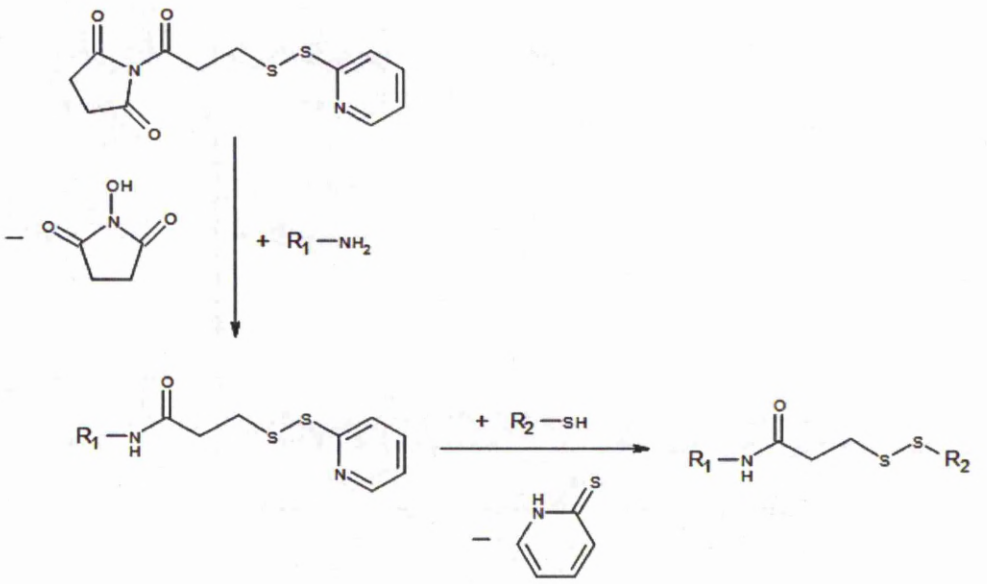

Figure II.2.2. Amine-thiol coupling mediated by hetero-bifunctional crosslinker SPDP. SPDP displays two functionalities, one is amine-reactive (the NHS-ester) and one is thiol-reactive (the pyridyl dithio group). At appropriate pH, the NHS-ester end reacts with an amine (R_1-NH_2) releasing N-hydroxysuccinimide. Further, a reaction with a thiol compound leads to the cleavage of the disulfide bond and realease on pyridylthione (which can be used to quantify the extent of the reaction via UV-Vis spectroscopy).

Thiolated probe attachment was carried out after a reduction step. Because thiols tend to dimerize, the thiolated oligonucleotide probes were reduced with a 1.5 mM DTT solution in bicarbonate buffer. A volume of water containing 8 micro-moles probe oligonucleotide was diluted to 1 mL with DTT to reach a final DTT concentration of 1.5 mM and left to react for 2 hours under mixing at room temperature. The reduced probe and excess DTT were passed through a PD-10 desalting column (see characteristic chromatogram in **Figure II.2.3**) and the appropriate 2 mL fraction was collected and diluted 10-fold with bicarbonate buffer, vigorously stirred, divided into two equal volumes and applied to the substrates. The substrates were incubated overnight at room temperature on a rocking plate mixer. Silicone dividers with a capacity of 150 µL/cell were used for the glass microscope slide controls. All substrates were subsequently washed 3 times, each wash 5 minutes long, in bicarbonate buffer and dried.

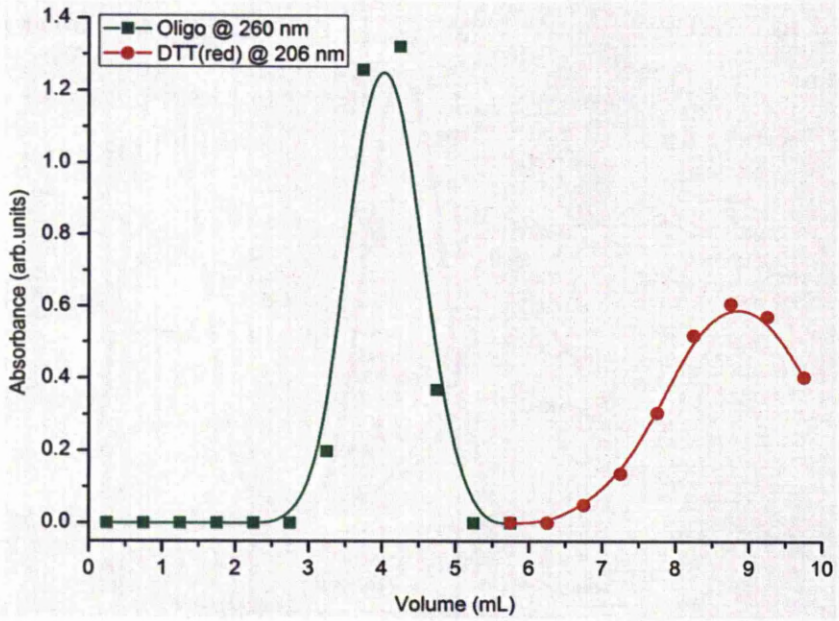

Figure II.2.3. Size exclusion chromatogram showing the purification of the reduced probe oligonucleotide from the reducing agent (DTT)

II.2.3.2 Hybridization

Prior to hybridization, a surface blocking step was carried out as follows: a solution containing BSA, 5 mg/mL, and tween 20, 0.05% by volumes, in PBS, pH 7.4 was prepared and added to the substrates; after 2 hours on the rocking-plate mixer at room temperature, excess detergent was washed off with three batches of PBS and blown dried. Subsequently, surface bound probes were hybridized with the corresponding oligonucleotide sequence at dilutions ranging from 1000nM to 15.625nM in steps of two-fold dilution (7 oligonucleotide concentrations) by exposing the substrates (1 cm^2) to 700µL target solution in PBS and leaving them overnight, under mixing on a rocking-plate mixer, at room temperature. The controls consisting of glass microscope slides were hybridized using the same silicon dividers and the target was applied manually to the surface using 500 nL printing pins; humidity was maintained by placing the slides in a polystyrene cell culture plate containing a few filter papers wetted with PBS at the bottom. Three Tween 20 0.05% by volume in PBS washes were carried out to eliminate unbound target and drying was done in a gentle stream of nitrogen. For binary TiO2-SiO2 pillars, seven concentrations (serial two-fold dilutions starting from 0.7 µM) were used

II.2.3.3 Spectrofluorimetry

The hybridization solution corresponding to each target concentration was retained and spectrofluorimetry was employed to measure the target concentration after the hybridization. Calibration curves shown in **Figure II.2.4** were constructed using the Cy5-labelled oligonucleotide and a blank; three repeats were measured and determinations of unknown concentrations were made for each of the three curves then the results were averaged.

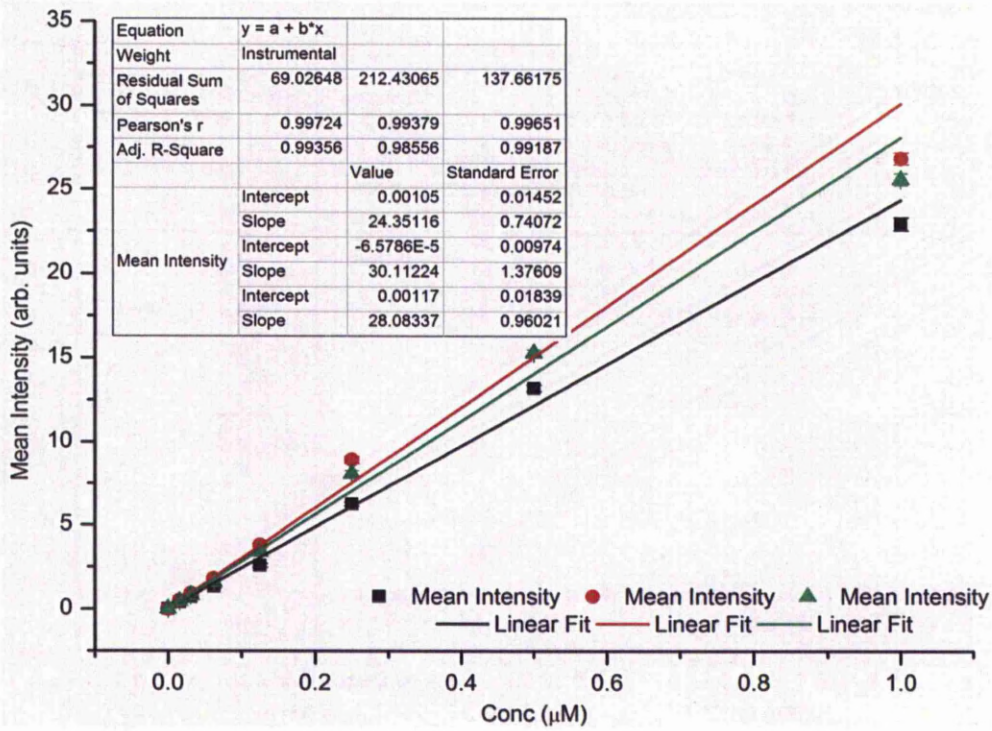

Figure II.2.4. Fluorescence calibration curve for fluorimetric assays of target consumption

To check whether a hybridization reaction really does take place, the hybridization solutions were assayed by means of fluorescence spectrometry. The target consumption curves obtained in this way are shown in **Figure II.2.5**. These measurements were also carried out to investigate the possible effect that UV-ozone treatment might have on the surface capacity to bind the target. To derive an approximate surface loading, after hybridization, the hybridization solution is spectrofluorimetrically assayed and the target concentration is measured using the calibration curve in Figure II.2.4. The values obtained in this way are subtracted from the initial (known) concentration. These values are plotted against the initial target concentration, yielding the curve in **Figure II.2.5**.

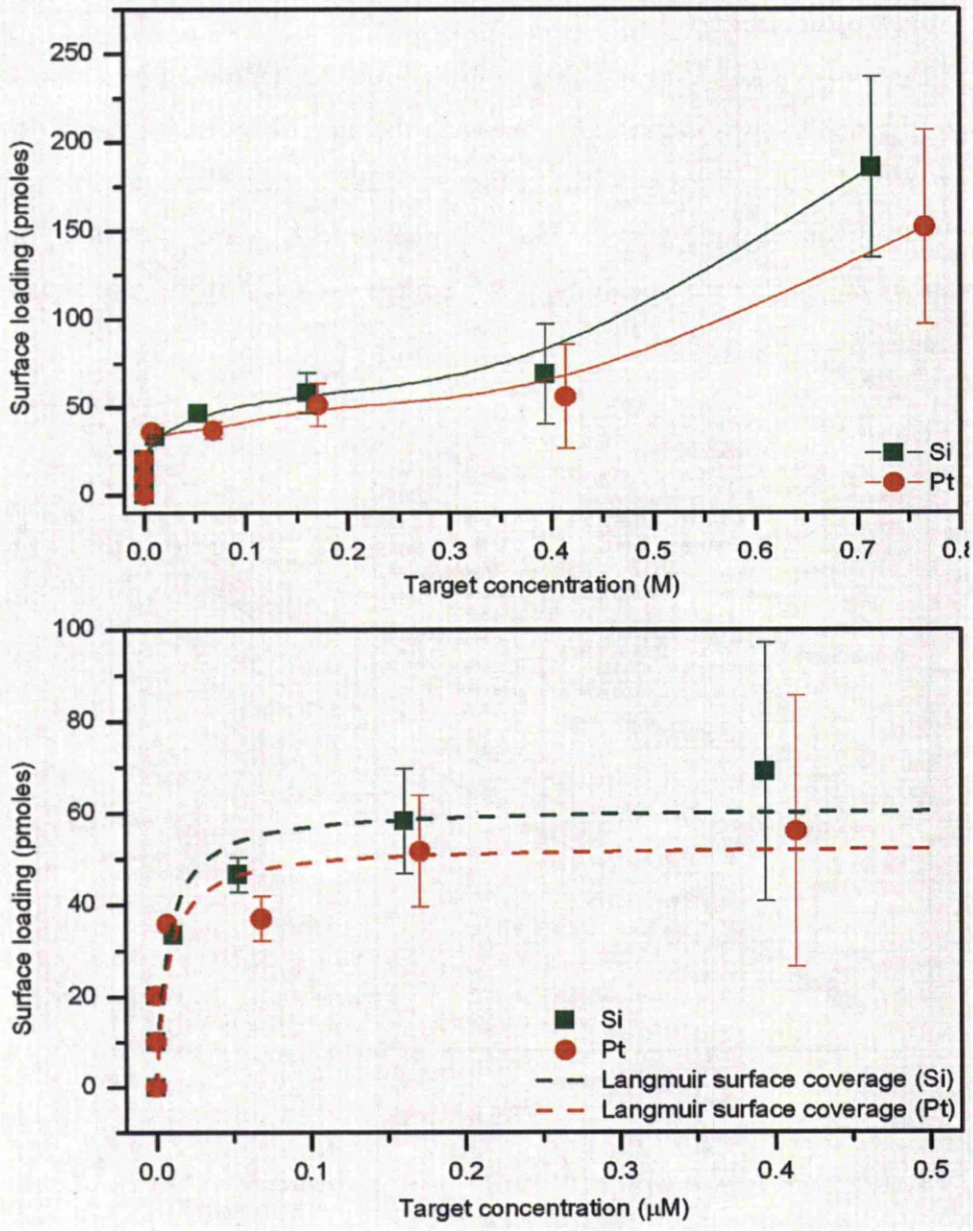

Figure II.2.5. Target hybridization for different target concentrations, monitored through fluorescence spectroscopy. Top: plot of surface coverage versus equilibrium target concentration, showing two different regimes with an inflexion point at around 0.25 μM. Bottom: the region of the curve that shows Langmuir like behaviour is fitted with the Langmuir isotherm equation

II.2.3.4 Hybridization experiments on SiO_2/Si and SiO_2/Pt substrates

The amplification obtained in the hybridization experiments was smaller than expected on the mono-component silicon oxide pillars, both on silicon and platinum. Surprisingly, the results obtained on bi-component pillars were the inverse of what was expected, with the substrates showing a contrast reversal.

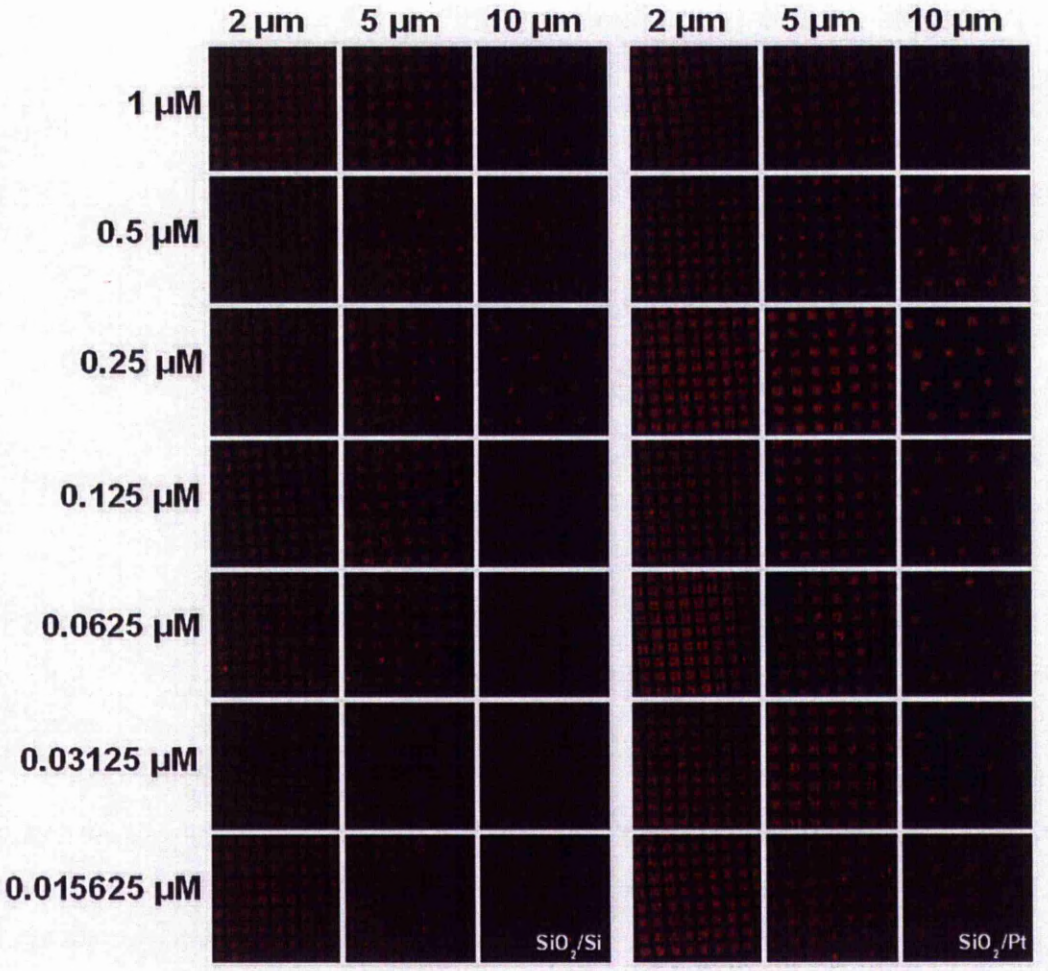

Figure II.2.6. Fluorescence micrographs after target detection on silicon (left) and platinum (right) reflector respectively. Experiments are carried out on 100 nm high microterraces with a 2, 5 and 10 µm pitch respectively (shown on the top row)

II.2.3.5 Signal-to-noise ratio

Each sample was imaged using the equipment and parameters described previously. After image and numerical processing, the SNR was calculated. The results were not as expected by comparison to previous data, as illustrated in **Figure II.2.6** and **Figure II.2.7**. The low local contrast, as can be assessed visually and also numerically through the magnitude of the SNR, is very low. The values of the SNR are very far from what was measured when a fluorophore was used. In an attempt to find the cause for the relatively lower contrast, and hypothesizing that the low lowered local contrast might be caused by unintended etching of the silicon oxide pillars by the basic ammonium hydroxide during the RCA cleaning procedure, a shift towards UV-ozone based photochemical dry cleaning was adopted.

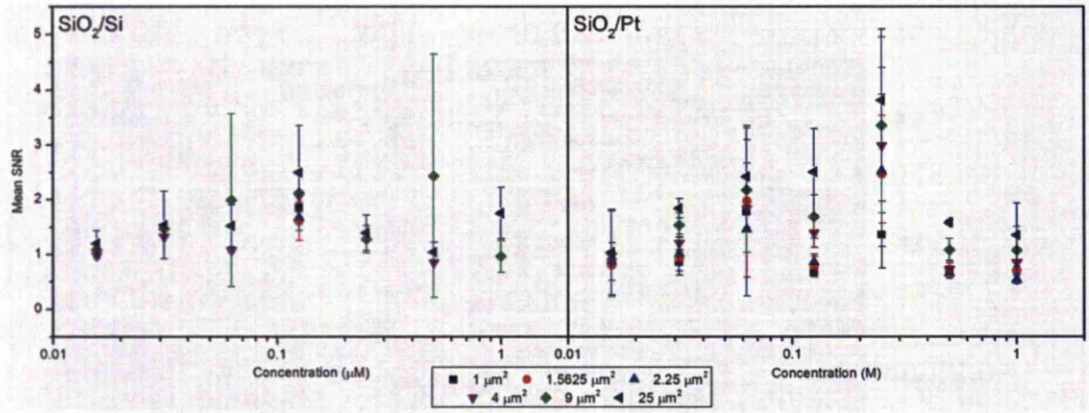

Figure II.2.7. Signal-to-noise ratio as a function of target concentration

II.2.3.6 Glass substrates

Another control/troubleshooting method consisted of carrying out identical hybridization experiments on bare glass microscope slides to make sure that the results observed on the mono- and bi-component substrates respectively are not the result of any flawed chemical treatment. **Figure II.2.8** he figure depicts a fluorescence micrograph acquired using a microarray scanner (GenePix 4000B) at the Cy5 (635 nm) excitation wavelength. The grid is due to the silicone divider used to create low volume cells. In each cell, the capture probe is printed twice (two features per cell). The two columns are identical in terms of experimental conditions.

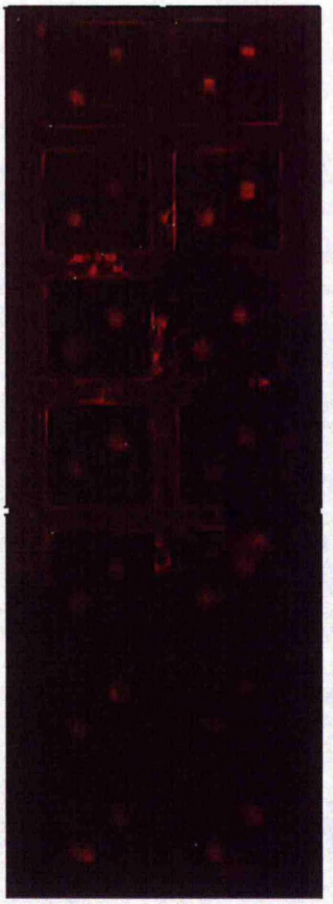

Figure II.2.8. Fluorescence micrograph showing a control hybridization experiment carried out on a simple glass slide (target concentration increases from bottom to top and are the same as those used for hybridization experiments on structured substrates; each row consists of two cells with identical target concentrations)

II.2.3.7 Residual fluorescence

Controls consisting of the silanized substrates were also imaged revealing an unexpected relationship between the fluorescence of the pillars and that of the surrounding area after silanization only. Interestingly, in the absence of a fluorophore, the silicon oxide (pillars) appears to partially suppress the background fluorescence. This is illustrated in **Figure II.2.9** where fluorescence micrographs of substrates comprising silicon oxide pillars on silicon and platinum respectively are shown (two pillar periodicities are shown, 2 and 10 μm pitch respectively). After silanization it is expected that the silane film will exhibit a slight autofluorescence and that the amount of autofluorescence will be higher on platinum than on silicon due to the difference in reflectivity. Additionally, it can be seen in that the pillars are

darker than the surrounding area suggesting a slight absorption by the silicon oxide layer.

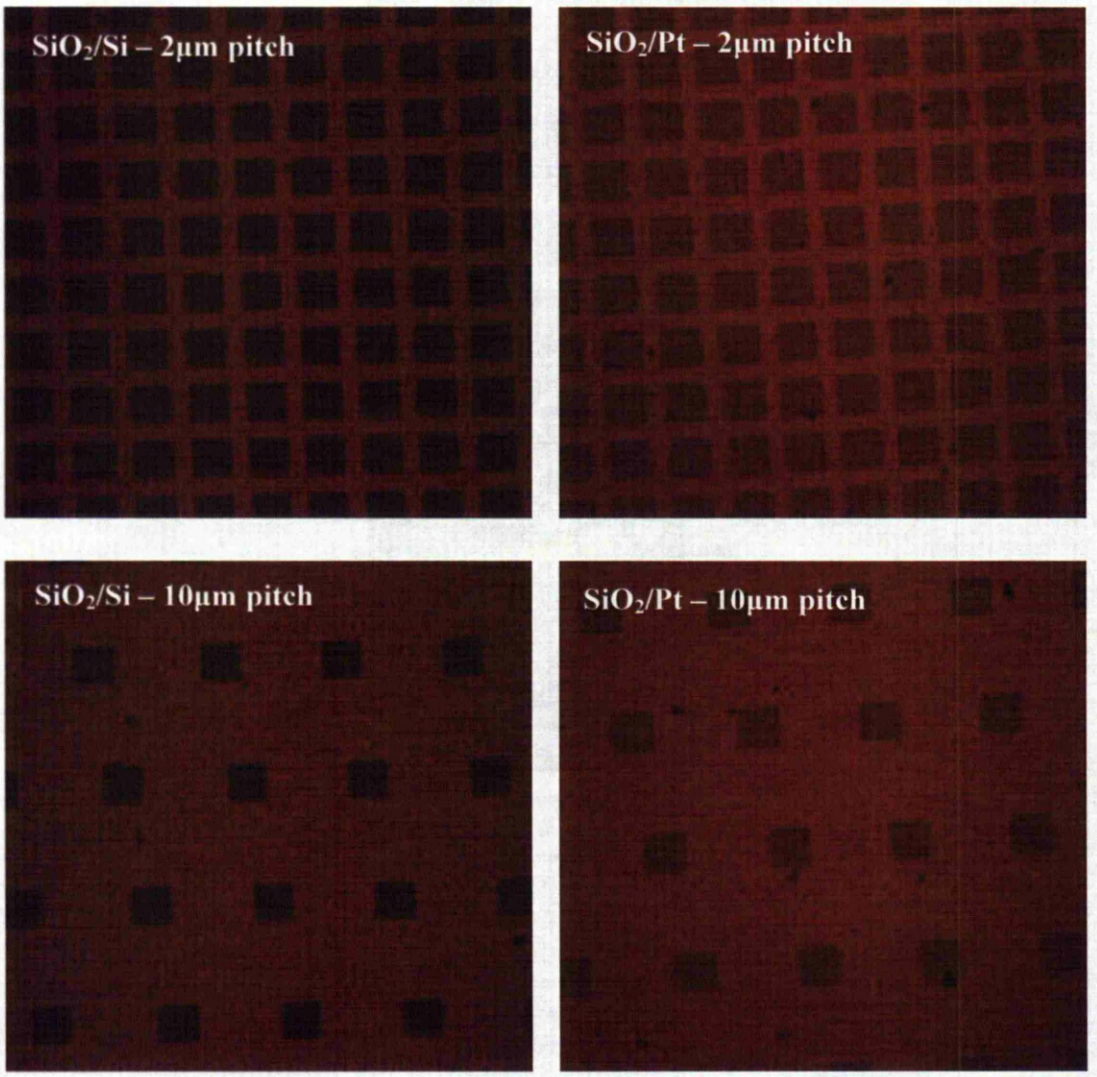

Figure II.2.9. Fluorescence micrographs of 2 µm and 10 µm pitch respectively pillars on silicon and platinum after silanization showing fluorescence suppression by the 100 nm high silicon oxide pillars. Note the contrast reversal as compared to Figure II.1.6

II.2.3.8 Hybridization experiments on $TiO_2/SiO_2/Pt$ substrates

The same procedures were applied on substrates comprising bi-component SiO_2 – TiO_2 pillars on platinum, where the height of the microterrace is 100 nm and the height fraction corresponding to the silicon oxide is 80% (20 nm thick TiO_2 layer between the reflector and a 80 nm thick SiO_2 layer). Surprisingly and contrary the theoretical model (see **II.2.3.4 Hybridization experiments on SiO2/Si and SiO2/Pt substrates**), no significant, i.e. above background, fluorescence level could be detected as shown in **Figure II.2.10**.

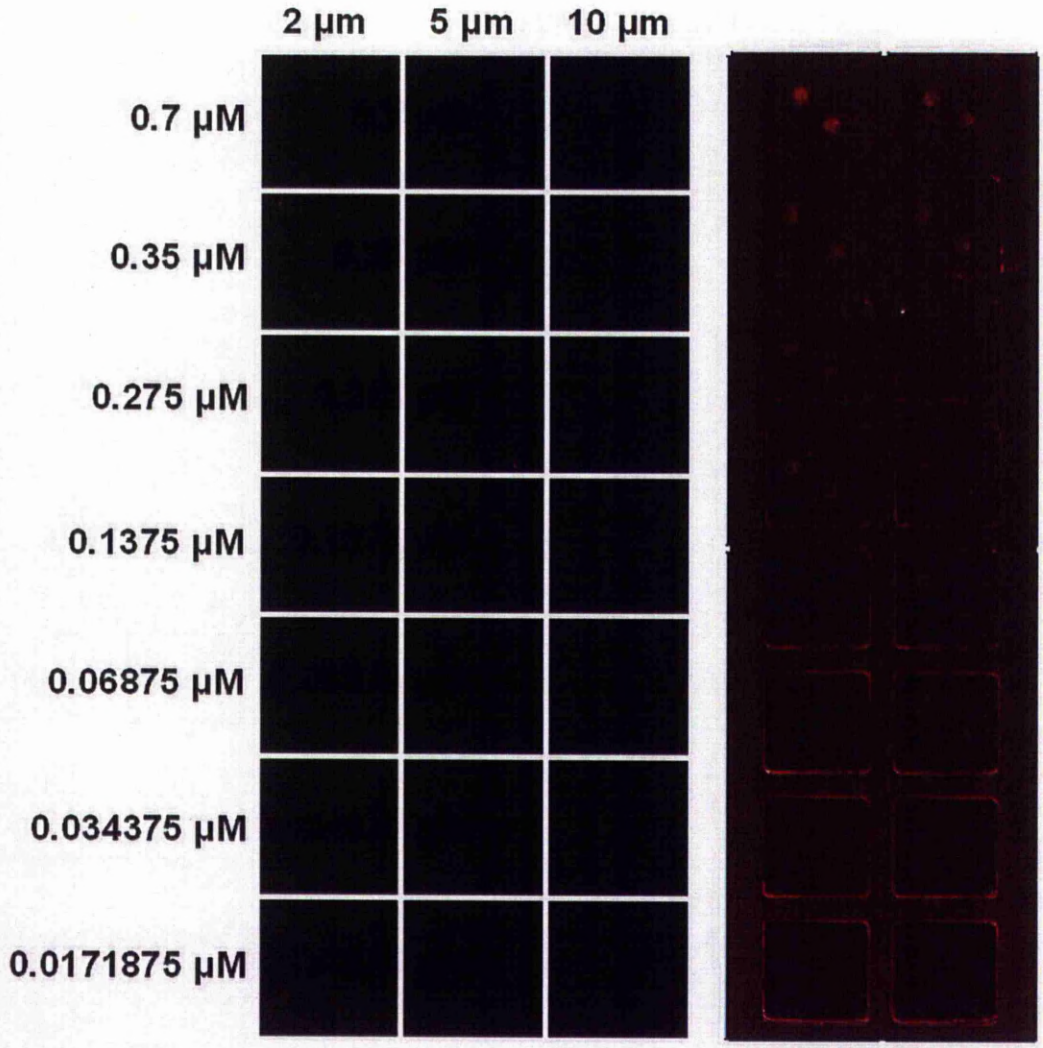

Figure II.2.10. Fluorescence micrographs illustrating negative hybridization results on bi-component TiO_2 containing pillars on platinum (left) and the same experiments carried out on glass (right). For the bi-component pillars, 25 μm^2 microterraces are depicted and the pitch increases from left to right (2, 5 and 10 µm)

II.2.3.9 Contact angle measurements

A surface chemistry difference between substrates comprising mono- and bi-component pillars was investigated as a possible cause of the results shown in **Figure II.2.10**, i.e. suppression of fluorescence on the bi-component pillars. This was achieved via water contact angle measurements at each processing stage. The contact angles measured for the six chemical treatment stages for substrates comprising mono-component pillars on silicon and platinum respectively, and bi-component pillars on platinum are illustrated in **Figure II.2.11**.

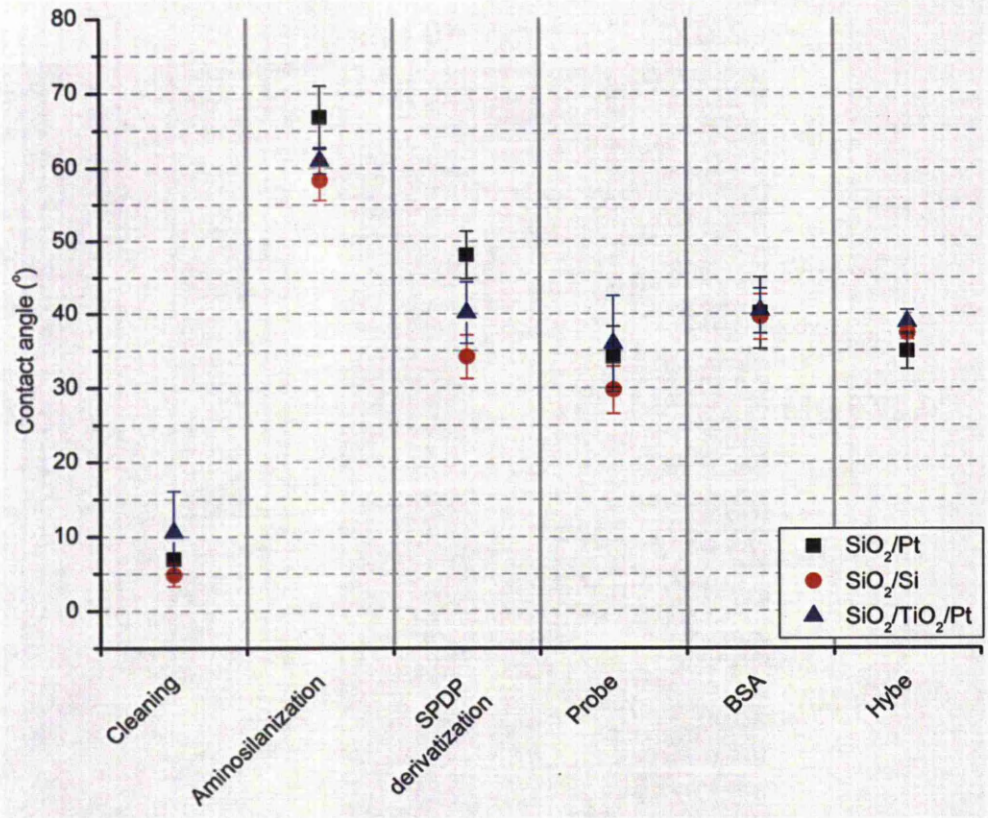

Figure II.2.11. Water contact angle evolution from a UV-ozone cleaned substrate to hybridization for the three substrate layer set-up

No significant differences in water contact angle can be seen in **Figure II.2.11** through the course of the surface modification, oligonucleotide printing and hybridization procedure. This indicates that the surfaces of the three substrates (mono-component silicon oxide pillars on silicon and platinum respectively and bi-component SiO_2-TiO_2 pillars) are chemically equivalent.

II.2.4 Results and discussion

II.2.4.1 Hybridization-based detection of avian flu virus on mono-component SiO_2 pillars on silicon and platinum

It was previously determined that, for Cy5 or a similar fluorophore, a pillar height of 100 nm is capable of inducing the amplification of fluorescence emission. Thus, substrates comprising arrays of pillars 100 nm in height were chosen for use in hybridization experiments, particularly in the detection of the avian flue virus strand. The SNR values (not shown) were found to be lower than the SNR values obtained using a direct attachment procedure of a fluorophore to the surface. Nevertheless, SNR levels of up to 3 are achieved and the difference in fluorescence intensity

between foreground and background is 3-fold. An explanation for this discrepancy is proposed in the following paragraphs.

The first possible explanation considered was the possibility of a fault in the surface modification procedure, including the hybridization step. The use of a control proved to be useful since this procedure consists of multiple steps and troubleshooting each step would be a time-consuming process requiring highly specialized equipment suitable for surface analysis. The control did not appear to be plagued by any major faults suggesting that there is no obvious fault in the chemical derivatization and hybridization processes.

A second possible reason for a low SNR when the detection of the avian flu virus was attempted was thought to be the improper surface cleaning. For this reason, the substrates were cleaned thoroughly, this time using a dry UV-ozone procedure and the experiments were repeated on the newly cleaned slide; unfortunately, the new results proved to be slightly poorer than those obtained previously. This means that the reason for the smaller amplification observed, as compared to the one achieved previously, is not surface cleanliness related.

In an attempt to monitor the depletion of target from the liquid to show that the target is indeed being hybridized to the surface, fluorescence assays of the target solutions were carried out after hybridization and measured fluorescence intensities were converted to concentrations using the purposely built calibration curve (**Figure II.2.4**). Knowing the initial and final target concentration allows the estimation of the surface target loading as a function of equilibrium solution target concentration (**Figure II.2.5**). The values are only rough estimates because the unreacted target cannot be quantitatively recovered and, as can be seen from the shape of the curve, there are reasons to believe that two adsorption processes occur sequentially. The first phase consists of target hybridization to surface bound probe molecules and the second step probably involves non-specific adsorption. The first segment of the curve was treated like an absorption process that is well described by the Langmuir isotherm (Nelson et al. 2001) below

$$\Gamma = \Gamma_{max} \frac{K \times c}{1 - K \times c} \tag{17}$$

where Γ is the equilibrium surface coverage, Γ_{max} is the maximum surface coverage, K is the equilibrium constant and c is the equilibrium target concentration. The second regime of the curve is indicative of a non-specific adsorption process and was not the subject of the Langmuir curve fitting (Figure II.2.5). The fitting procedure is used to extract the maximum coverage parameter and the equilibrium constant with reasonable accuracy, given the qualitative rather than quantitative nature of the experiment. Thus, maximum coverage values of around 60 and 50 pmoles respectively for silicon and platinum were obtained, which is in good agreement with the theoretical value of 50 pmoles per cm^2 (Dufva 2005) (and given that the substrates used were not cut down to an accurate size). Similarly, the value for the equilibrium constant, which was treated as a global parameter between the two fittings (i.e. the two reflector materials) was found to be 1.3×10^8 M^{-1}, reasonably close to the value of 1.8×10^7 M^{-1} given by (Nelson et al. 2001) for 20 mer oligonucleotides. Further, for the UV-ozone cleaned substrates, the coverage value for the silicon reflector remained unchanged while the adsorption measured on the platinum reflector increased slightly to match that on silicon. This supports the "patchy" oxide layer theory brought forward previously. Moreover, it follows that, since the adsorption behaviour on silicon is unchanged, the dry photochemical treatment does not adversely affect the native surface chemistry.

Another issue that deserves consideration is the problem of residual/stray fluorescence, which seems to be quite high for the bare substrate itself, both for silicon and platinum reflectors. There is also an interesting observation that can be made about the dielectric layer and the effect that it might have on the stray fluorescence. First of all, one can notice that the level of fluorescence measured on the bare substrates is elevated. That is to say that there is a strong possibility that an important contribution to the levels measured after hybridization is due to the substrate. The results yielded by the numerical processing are illustrated in **Figure II.2.12**. The fluorescence intensity is illustrated as the histogram of the distribution of the (binned) fluorescence intensity values. Mean fluorescence intensity and standard deviation is also shown in the same figure.

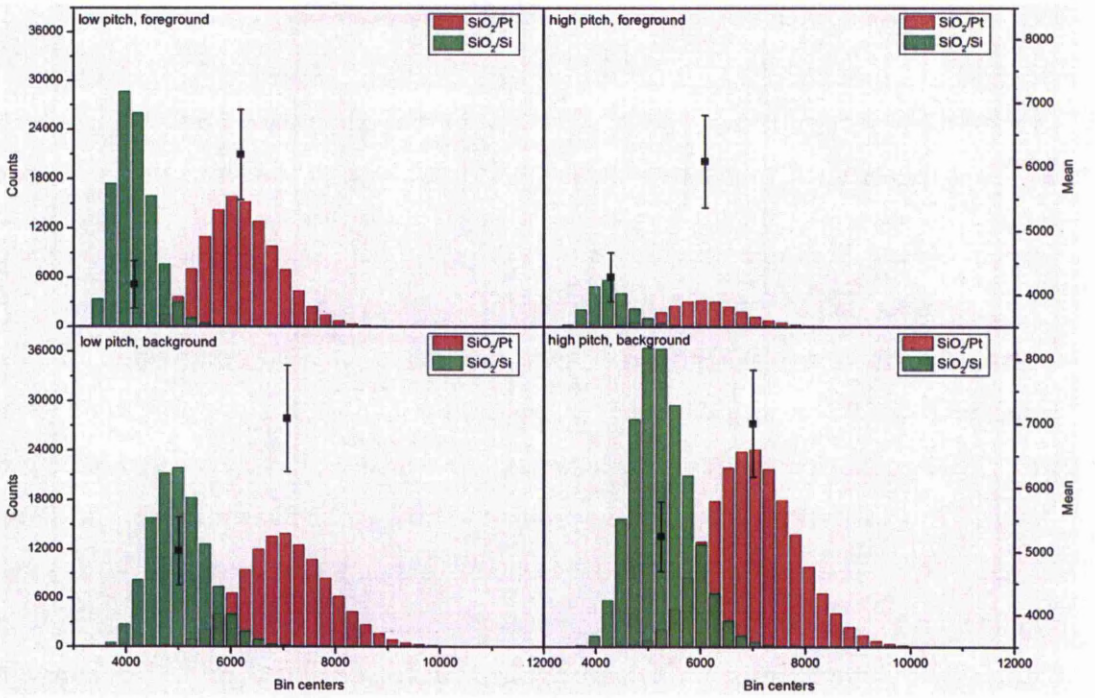

Figure II.2.12. Fluorescence distribution (left axis) and mean intensity (right axis) in the foreground (tops of the pillars) and background (area between the pillars) for differently pitched features (2 µm and 10 µm respectively, corresponding to micrographs from figure Figure II.2.9).

Two types of substrates were taken under discussion, one comprising pillars with a periodicity of 2 µm (low pitch) and the second one comprising pillars at a 10 µm (high pitch) distance from one another and the distribution, mean intensity and dispersion were calculated for both foreground and background. At first glance, one can see that the mean fluorescence value for both foreground and background is always higher for substrates using platinum as a reflector than for the ones using silicon. Moreover, the standard deviation around this mean intensity value is also higher for the platinum than for the silicon reflector. These observations are expected based on both previous experiments (having been discussed earlier, see **Figure II.1.15** and **Figure II.1.17**) and considering the reflectivity values of the two materials, i.e. the reflectivity at the .platinum surface is more than twice as high as that at the silicon surface.

First of all, it is known that, for glass substrates in general, the source of background fluorescence (autofluorescence) is impurities present in the glass matrix. However these substrates are fabricated on high purity silicon through deposition of high purity metals and silicon oxide, therefore only a low level of fluorescence can be expected to arise in the form of intrinsic fluorescence. It follows then that most of the

measured fluorescence has an extrinsic source as probably some of the reflected excitation light is leaking through the dichroic mirror. The fact that the background level on the silicon reflector is lower than that measured on the platinum one (due to the lower reflectivity of the latter versus the former) supports this hypothesis.

Secondly, the fluorescence intensity on the pillars can also yield valuable information in the context of the future improved design of such substrates. The measured levels are smaller than what is registered in the background, for both reflector materials, in all cases; and it appears that silicon oxide has a suppressing effect on the reflected fluorescence accounting for a stray fluorescence correction of about 10 to 15%. This has two implications: the first one is related to the calculation of the SNR, more specifically the background correction, and secondly, the possible exploitation of this effect in a future improved substrate. Generally, it is considered that the background across a microarray slide or at least inside a grid cell is constant. This means that, in the absence of a fluorophore, the area that would be occupied by the spot would display the same fluorescence intensity distribution as the area outside this perimeter. However in such a case as the one presented here, this is clearly not true and the existence of a structure with suppressing effect on the fluorescence results in an under-estimation of the background-corrected intensity value. This is not to say that the signal arising from a "real" spot is underestimated, but that the background correction, while still correct from the viewpoint of feature "visibility", yields a value that is lower than what would normally be expected. At the same time, the fact that a layer of silicon is able to provide a certain degree of suppression can be used to ones advantage, as it can purposely be used to "seal" the area around an amplification zone and suppress the stray fluorescence component.

II.2.4.2 Hybridization-based detection of avian flu virus onbi-component SiO_2-TiO_2 pillars

A second set of experiments was performed on substrates comprising two-oxide pillars. Titanium oxide was chosen due to its ability to improve adhesion between platinum and silicon oxide and it was first thought of as an improvement of the current architecture. This quality of titanium oxide stems from the property of titanium to display various valences through the film (which is generally described by a TiO_x formula), being able to promote the adhesion between two incompatible crystalline materials (Vogt et al. 1994). A fluorescence intensity profile versus pillar

height for a titanium dioxide pillar on platinum would be similar to the profile obtained for silicon oxide pillars on platinum but some differences would be expected. One difference, arising from the high refractive index of titanium dioxide, is the lateral shift of the intensity peaks to smaller fluorophore-reflector distances (a higher refractive index means the same optical path length is obtained at smaller separation distances). The periodicity of the curve would also be smaller. Also, the amplitude of the two curves would be different. The reason for this is that reflection at the air – dielectric and dielectric reflector interfaces respectively would differ (see **Table II-1** and **Table** II-4). Firstly, the reflection coefficient at the silicon oxide – platinum is larger than the reflection coefficient at titanium dioxide – platinum interface. It follows then that the intensity peaks will have higher amplitudes when quartz pillars are used. Further, the reflection coefficient at the air – quartz interface is small enough to be disregarded. The same is not valid for the air – titanium dioxide interface where the reflection coefficient is quite high (around 0.2). This means that an additional beam with undergoing a phase change of π radians will also interfere with incident beam, decreasing the measured fluorescence intensity. Nevertheless, the shape of the fluorescence intensity versus separation distance curve is broadly conserved.

For binary pillars, a theoretical amplification profile can be predicted using **eq. 16**, after making the necessary changes to account for additional optical paths and reflections where the optical path length component considers the two refractive indices and the proportion of each material in the total height. This set-up is illustrated in **Figure II.2.13**. Obviously, the location of the amplification maxima is dependent on both the height (which is maintained constant, at 100 nm) and the composition of the pillars. An analytical treatment of the system must start from the calculation of the reflection coefficients at the three interfaces (silicon oxide-air, silicon oxide-titanium oxide and titanium oxide-platinum) (using Fresnel equations) as shown previously (**II.1.4.1 Optical interference effects and data fitting**). The reflection coefficients are tabulated in **Table II-4**.

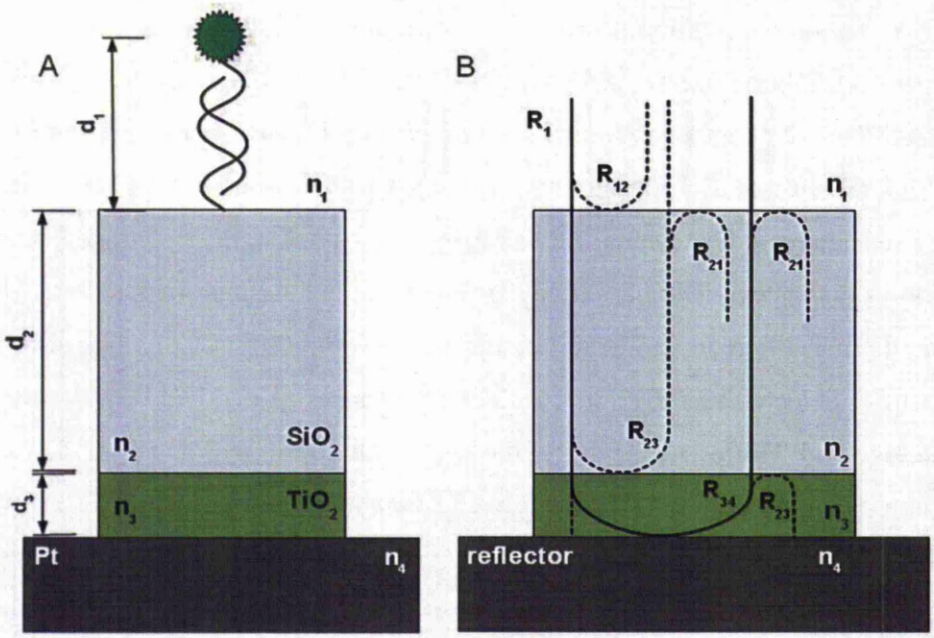

Figure II.2.13. Optical set-up for bi-component pillars comprising a TiO_2 adhesion layer (A) and the multiple beam system inside the pillar (B).

In **Figure II.2.13 A**, the distance between the fluorophore and the surface of the pillar is d_1 and can be considered negligible by comparison to the height of the entire pillar (the height of the silicon oxide segment, d_2, plus that of the titanium oxide, d_3). In **Figure II.2.13 B**, the three interfaces between media characterized by refractive indices n_1 (air), n_2 (SiO_2), n_3 (TiO_2) and n_4 (Pt) respectively give rise to multiple reflection instances.

Table II-4. Tabulated values of the reflectivity coefficients at the excitation and emission wavelengths respectively for the interfaces illustrated in Figure II.2.13

Reflectivity coefficient	λ_{ex}	λ_{em}
Air – SiO_2 interface	0.03	0.03
SiO_2 – TiO_2 interface	0.107	0.104
TiO_2 – Pt interface	0. 395	0.406

The set-up shown in Figure II.2.13 is very similar to that comprising silicon oxide only, the main difference stemming from the appearance of an extra interface (silicon oxide-titanium oxide) and from the very high refractive index of the titanium oxide. From the reflectivity values presented **Table II-4**, one can observe that there are two interfaces where significant reflection occurs, the one between the dielectrics and the one between the metal and the dielectric. The optical interference phenomenon can

be modelled considering the reflection at the dielectric boundary (R_{23}) or in a simplified manner, disregarding it. This would result in two models, a two-beam and a three-beam interference model respectively. The two-beam interference model is very similar to that used for the mono-component pillar, with only a correction of the optical path length being required. Both models will be analysed below.

II.2.4.2.1 Two-beam interference

The two-beam interference will disregard the reflection at the silicon oxide-titanium oxide as its magnitude is not very high (~0.105 as shown in **Table II-4.** Tabulated values of the reflectivity coefficients at the excitation and emission wavelengths respectively for the interfaces illustrated in Figure II.2.13). Thus, one has to calculate the optical path for a two-beam system and make the necessary adjustments in a generalized **eq. 1** (Parthasarathy and Groves 2004) the fluorescence intensity modulation is given by

$$F_{exp} \propto \left[(1 - r_{34}^{ex})^2 + 4r_{34}^{ex} sin^2\left(\frac{2\pi}{\lambda_{ex}}(n_2 d_2 + n_3 d_3)\right)\right]\left[(1 - r_{34}^{em})^2 + 4r_{34}^{em} sin^2\left(\frac{2\pi}{\lambda_{em}}(n_2 d_2 + n_3 d_3)\right)\right] \quad (18)$$

where r_{34}^{ex} and r_{34}^{em} are the reflection coefficients at the dielectric-reflector interface at the excitation and emission wavelengths (λ_{em} and λ_{ex} respectively).

Further, if the intensity profile for a bi-component, SiO_2-TiO_2 pillar, 100 nm in height, is required as a function of height fraction, the fraction of the pillar's height occupied by TiO_2 can be written as

$$d_3 = 100 - d_2$$

so the observed fluorescence becomes

$$F_{exp} \propto \left[(1 - r_{34}^{ex})^2 + 4r_{34}^{ex} sin^2\left(\frac{2\pi}{\lambda_{ex}}(n_2 d_2 + n_3(100 - d_2))\right)\right]\left[(1 - r_{34}^{em})^2 + 4r_{34}^{em} sin^2\left(\frac{2\pi}{\lambda_{em}}(n_2 d_2 + n_3(100 - d_2))\right)\right] \quad (19)$$

This equation can be used to calculate the optimum TiO_2-SiO_2 proportion in a 100 nm high bi-component pillar. The entire derivation is available in **IV.1 Two beam interference model** in the **Appendix**.

II.2.4.2.2 Three-beam interference

A slightly more rigorous model can be constructed taking into account the non-zero reflectivity at the silicon oxide-titanium oxide interface which introduces a third beam. The derivation leading to **equation 20** below is available in **IV.2 Three beam interference model** in the **Appendix**.

$$
\begin{aligned}
F_{exp} \propto P_{ex}P_{em} \propto \Bigg[& [(1-r_{23}^{ex})^2 - r_{34}^{ex}(1-r_{23}^{ex})^2]^2 + 2r_{23}^{ex}r_{34}^{ex}(1-r_{23}^{ex})^2 \\
& + 4r_{23}^{ex}\sin^2\left(\frac{2\pi n_2 d_2}{\lambda_{ex}}\right) + 4r_{34}^{ex}(1-r_{23}^{ex})^2\sin^2\left(\frac{2\pi(n_2d_2+n_3d_3)}{\lambda_{ex}}\right) \\
& - 4r_{23}^{ex}r_{34}^{ex}(1-r_{23}^{ex})^2\sin^2\left(\frac{2\pi n_3 d_3}{\lambda_{ex}}\right)\Bigg]\Bigg[[(1-r_{23}^{em})^2 - r_{34}^{em}(1-r_{23}^{em})^2]^2 \\
& + 2r_{23}^{em}r_{34}^{em}(1-r_{23}^{em})^2 + 4r_{23}^{em}\sin^2\left(\frac{2\pi n_2 d_2}{\lambda_{em}}\right) \\
& + 4r_{34}^{em}(1-r_{23}^{em})^2\sin^2\left(\frac{2\pi(n_2d_2+n_3d_3)}{\lambda_{em}}\right) \\
& - 4r_{23}^{em}r_{34}^{em}(1-r_{23}^{em})^2\sin^2\left(\frac{2\pi n_3 d_3}{\lambda_{em}}\right)\Bigg]
\end{aligned}
\tag{20}
$$

where r_{23}^{ex}, r_{34}^{ex} and r_{23}^{em}, r_{34}^{em} are the reflection coefficients at the dielectric – dielectric and dielectric-reflector interface respectively at the excitation and emission wavelengths (λ_{em} and λ_{ex} respectively).

Further, if the intensity profile for a bi-component, SiO_2-TiO_2 pillar, 100 nm in height, is required as a function of height fraction, the fraction of the pillar's height occupied by TiO_2 can be written as

$$d_3 = 100 - d_2$$

so the observed fluorescence becomes

$$F_{exp} \propto P_{ex}P_{em} \propto \Big[[(1-r_{23}^{ex})^2 - r_{34}^{ex}(1-r_{23}^{ex})^2]^2 + 2r_{23}^{ex}r_{34}^{ex}(1-r_{23}^{ex})^2 + 4r_{23}^{ex}\sin^2\left(\frac{2\pi n_2 d_2}{\lambda_{ex}}\right) + 4r_{34}^{ex}(1-r_{23}^{ex})^2\sin^2\left(\frac{2\pi(n_2 d_2 + n_3(100-d_2))}{\lambda_{ex}}\right) - 4r_{23}^{ex}r_{34}^{ex}(1-r_{23}^{ex})^2\sin^2\left(\frac{2\pi n_3(100-d_2)}{\lambda_{ex}}\right)\Big]\Big[[(1-r_{23}^{em})^2 - r_{34}^{em}(1-r_{23}^{em})^2]^2 + 2r_{23}^{em}r_{34}^{em}(1-r_{23}^{em})^2 + 4r_{23}^{em}\sin^2\left(\frac{2\pi n_2 d_2}{\lambda_{em}}\right) + 4r_{34}^{em}(1-r_{23}^{em})^2\sin^2\left(\frac{2\pi(n_2 d_2 + n_3(100-d_2))}{\lambda_{em}}\right) - 4r_{23}^{em}r_{34}^{em}(1-r_{23}^{em})^2\sin^2\left(\frac{2\pi n_3(100-d_2)}{\lambda_{em}}\right)\Big] \tag{21}$$

Using **eq. 19** and **21**, two curves describing the modulation of fluorescence intensity for binary pillars, 100 nm in height, by the fraction of the pillar height occupied by titanium dioxide can be obtained as depicted in **Figure II.2.14**.

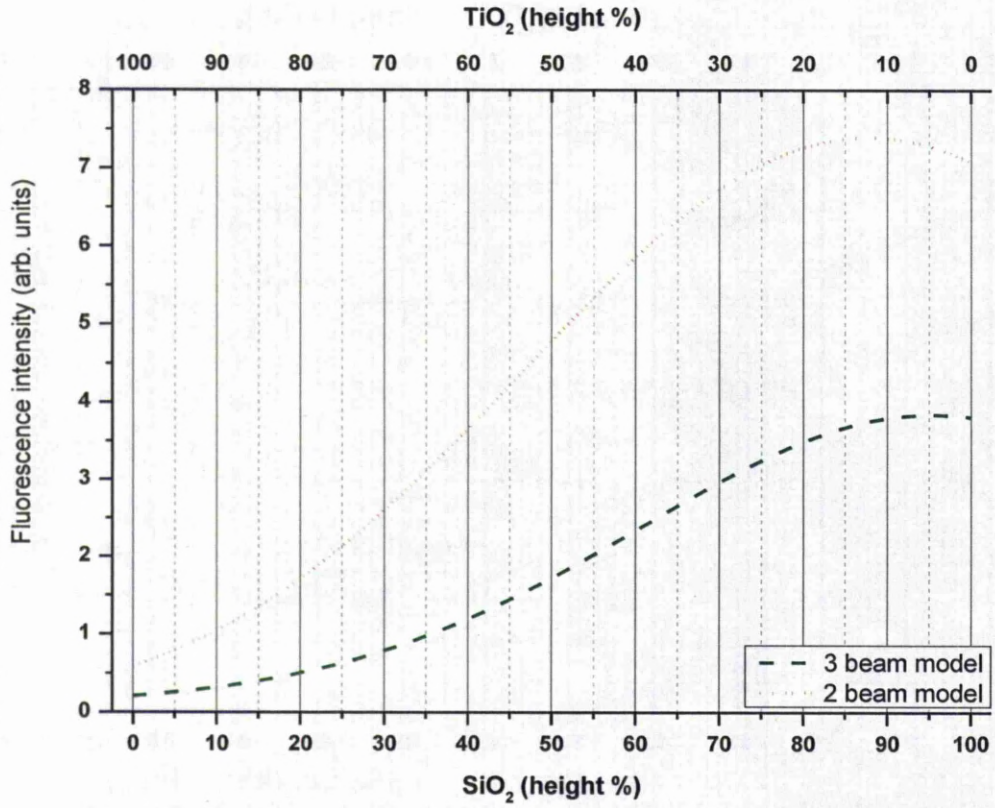

Figure II.2.14. Fluorescence intensity profile on binary SiO_2-TiO_2 pillars as a function of height fraction using a two beam and a three beam interference model (considering monochromatic excitation at 633 nm and emission at 670 nm respectively)

The two models shown above are very similar in terms of the position of the intensity peak. The intensity amplitude obtained using the three beam model is lower than that obtained using the two beam model but this is expected since the efficiency of the metal reflector is lower. From **Figure II.2.14** one can select a titanium oxide height fraction of 20% (i.e. 20 nm titanium dioxide under a 80 nm high silicon oxide layer) and expect that a fluorescence enhancement would still occur, albeit with a lower intensity. In reality however, the predicted value for the ratio between the thicknesses of the two component oxides did not result in the expected intensity profile but, rather unexpectedly, a suppression of fluorescence on the pillars was recorded as can be seen in **Figure II.2.15** where representative fluorescence intensity distributions on the pillars and between the pillars are shown.

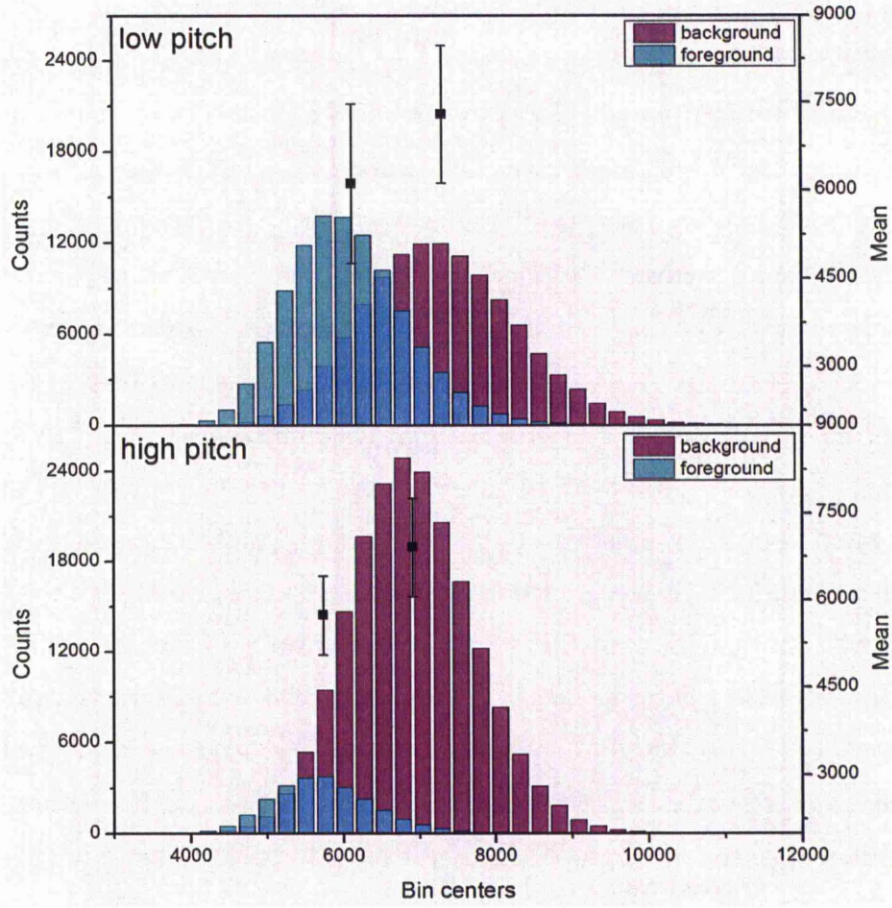

Figure II.2.15. Fluorescence intensity distribution (left axis) and mean (right axis) showing the extent of fluorescence suppression through intercalation of the 20 nm titanium oxide layer between silicon and platinum for a pillar pitch of 2 and 10 µm respectively

This unexpected behaviour might be due to chemical or optical sources and this is what needs to be studied further. In order to eliminate any fault regarding the chemical modification procedure, including bad reagents, the experiments (repeated three times) were carried out in parallel, using a glass microscope slide as control. Imaging the control slides in a microarray scanner did not reveal any abnormalities so we conclude that the lack of fluorescence on the binary pillars is not due to any faults in the chemical treatment. Further, it is reasoned that the suppression of fluorescence on the binary pillars, as opposed to amplification on the mono-component ones, can be caused by some unknown difference between the surface chemistries of the two types of substrates. To explore this avenue, we measured the water contact angle on silicon oxide on silicon and platinum respectively and bi-component pillars after each surface modification step but no significant differences were found, as expected. These results suggest that the reason for this opposite behaviour should be of optical nature.

Titanium dioxide is a very versatile material, being used extensively in the dye and pigments industry due to its bright white colour and in health-care in sun-screens and other products. It is also used in specialty surface coatings (optical coatings) and it is now emerging as promising material for photocatalysis and solar cell technology. One of the most striking features of titanium dioxide is its unusually high refractive index, with values between 2.5 and 2.9, among the highest known. Although commonly referred to as a dioxide, the formula that better describes the real Ti:O ratio is TiO_{2-x}, the actual ratio being determined by the presence and type of defects, which is in turn determined by the oxygen availability during, in this case, the deposition process. It is known that, generally, the properties of deposited thin films are different from the properties of the bulk material and that, even for identical deposition conditions, the actual deposition equipment can also affect the properties of the film. For titanium oxide films, for instance, a study of their optical properties as a function of deposition technique is available, revealing discrepancies between both films deposited using different techniques on one hand and different between films deposited by different research teams using the same method (Bennett et al. 1989). There are also contributions discussing the influence of deposition parameters in ion-beam sputtering deposition processes which was used to fabricate the pillars. Thus, the oxygen partial pressure seems to affect the refractive index, extinction coefficient and even surface roughness of the deposited films.

The refractive index of a thin, 20 nm thick slice of titanium oxide under a 80 nm thick layer of silicon oxide should not, at least in theory, affect dramaticcaly the amplification profile. The evolution of the amplification profile for 100 nm high bi-component pillars with a TiO_2:SiO_2 ratio of 20:80 as a function of the refractive index of the bottom layer can be theoretically modelled and a curve of fluorescence intensity versus refractive index can be obtained as shown in **Figure II.2.16**. The resulting curve shows that only a moderate loss in amplification, about 40%, should be measured when the refractive index is swept between 2 and 3. This drop however would not explain the measured values, which indicated rather a complete suppression. This, in turn, means that even though departure of the refractive index value from the average is expected, it would not explain the results.

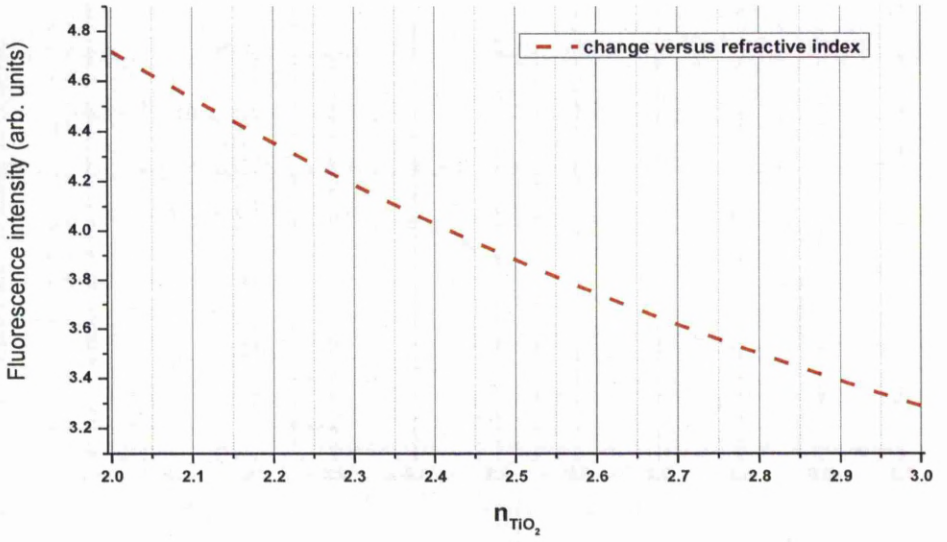

Figure II.2.16. Theoretical effect of the titanium oxide refractive index on the overall amplification for a bilayer consisting of 80% silicon oxide and 20% titanium oxide (monochromatic excitation at 633 nm and emission at 670 nm were considered)

There are two other scenarios that might be able to explain the lack of fluorescence as measured on the pillars. One envisaged phenomenon would involve either a refractive index continuous gradient along the vertical axis of the layer or the existence of "pockets" or "slices" of material with different values for the refractive index resulting in a complex optical system with multiple refraction effects. Another possible explanation is the existence of a non-transparent interface at the $TiO_2 - SiO_2$ boundary. Unfortunately, at this point, these suppositions cannot be substantiated by experimental evidence.

II.2.5 Summary and conclusions

Previous experimental results obtained on pillar substrates using a fluorescent molecule yielded promising results demonstrating that fluorescence can be amplified and suppressed by changing the surface geometry and suggesting a possible application in microarray technology. The substrates described in the previous section were tested in the detection of a specific ssDNA sequence in a manner similar to some extent to the way a microarray experiment is carried out. The surface was chemically modified, first with amino groups, then, using a hetero-bifunctional linker that introduces a cleavable disulfide group. Finally, a surface bound ssDNA sequence was attached to the surface. Such a surface can then be exposed to a solution containing the fluorescently labelled target sequence and the fluorescence can be measured. SNR, an important metric in signal processing in general, and

specifically, in microarray technology was calculated for different target concentrations. The same experiments were performed on similar substrates comprising stacked titanium oxide – silicon oxide pillars; the introduction of titanium oxide was dictated by the need to improve the adhesion between silicon oxide and the metal reflector with possible affect on the ability to reuse the substrates after a simple cleaning procedure.

The hybridization-based detection experiments carried out on the mono-component pillars yielded mixed results. Firstly, the results confirmed, both visually and numerically the behaviour predicted by fluorophore experiments; quantitatively however, the magnitude of the expected contrast was smaller than anticipated based on previous experimental results and modelling. These differences were assigned to the existence of various limiting factors that are not related to the optical phenomena: multiple chemical steps with proceeding with different efficiencies (i.e. surface chemical activation) and the inability to exactly match the conditions of a microarray experiment (e.g. probe distribution). The existence of background, residual fluorescence was also investigated on these substrates. It was found that pristine substrates exhibit a quite high level of fluorescence, but this was assigned mostly to the imaging equipment used; it was also found that silicon dioxide covered area exhibit a lower fluorescence level introducing the possibility of using such layers to suppress low level background fluorescence.

Additionally, detection of a DNA sequence was carried out on substrates comprising a platinum reflector and bi-component stacked TiO_2 – SiO_2 pillars. Theoretical prediction made based on the optical model indicated that, for 100 nm high pillars, a 20:80 height ratio between titanium and silicon dioxide would provide the least amount of perturbation to the optical system. Unexpectedly, the titanium oxide appeared to suppress the fluorescence to a level comparable to the one measured on pristine silicon oxide on platinum; although some hypotheses to explain this behaviour were proposed, the lack of experimental data to back them up suggests that a future, ellipsometric, investigation is necessary.

The results presented here prompted a re-evaluation of the surface attachment procedure and a switch towards a more robust epoxide based attachment chemistry. Also, the need to use a dedicated, field-specific instrumentation became clear.

II.3 Chapter 3: Prototype substrates for fluorescence detection based biorecognition devices

II.3.1 Introduction

Previously, a new fluorescence-based bio-recognition device architecture comprising z-nano structures in the form of pillars was introduced. These substrates are based on the enhancement and suppression of fluorescence over defined areas of a reflector, and due to the use of micro-fabricated structures, these areas are well defined, with known size and shape. Some problems (or sub-optimality) encountered before was addressed through newly designed substrates geared more closely towards practical applicability. Such issues were related to dimension of substrates, delivery of the capture probe and the use of a dedicated microarray scanner.

The new design followed a set of pre-set criteria. The size of the substrates was chosen to be compatible with standard sizes accepted by microarray scanners and also to accommodate silicone dividers. Another design idea was to integrate two controls, flat areas where the oxide thickness creates constructive and destructive interference respectively. These controls mimic the two horizontal planes found on the structured areas. Another aspect was related to the technically correct manner in which SNR calculation can be done. To this end, the substrates were designed to offer two more background contribution estimations. Lastly, an inverted architecture comprising nano-wells (as opposed to the nano-pillars) was implemented.

Another change with respect to previous experiments was the surface and consequently the attachment chemistry. The epoxide based chemistry was chosen because it offers a much simplified procedure by minimizing the number of steps and increasing reliability. A surface chemistry optimization was deemed necessary and this was achieved employing a number or techniques: water contact angle measurements, scanning probe and optical fluorescence microscopy.

Finally, an objective assessment of the new prototypes' performance was carried out by comparing their performance with that of two commercial slides, one using a similar but more complex fluorescence enhancement technology.

A short description of the work carried out towards the goals stated above and reported in the following paragraphs. Two types of substrate architecture were

designed and fabricated. The two approaches consisted on patterning nano-pillars and nano-wells respectively on a reflector surface (silicon and platinum). The theoretical grounds that the designs are based on are extensively discussed. Briefly, each substrate comprised three regions: the active region with pillars or well patterned onto it and two controls. The two controls consist of a flat and continuous oxide films whose thickness promotes fluorescence enhancement and suppression respectively. A new epoxide based surface chemistry was adopted since the one presented in the previous chapter proved to be unreliable. The introduction of surface epoxy groups on the surface of the substrates was done via liquid phase deposition and this required first optimizing the deposition conditions. Monitoring the variation of surface properties with the change in deposition conditions was achieved via water contact angle measurements and atomic force microscopy. Optimal surface chemistry in terms of surface binding capacity was determined by using a fluorescently labelled probe able to bind to the surface epoxy groups via it's native free epoxy-reactive chemical groups.

After determining the optimal deposition conditions, the performance new substrates was tested by carrying out fluorescence based bio-recognition experiments in a manner similar to that used in microarrays using two figures of merit. The signal-to-noise ratio was assessed to evaluate their fluorescence enhancement and confinement properties and the uniformity of the features was assessed by measuring the percent standard deviation. For comparison purposes, commercial slides were included to provide a more complete picture of performance levels. The results showed that the prototype slides are comparable or better in performance than commercial slides.

II.3.2 Materials and methods

II.3.2.1 Buffers and reagents

De-ionized water used throughout the experimental stages was obtained via a Millipore water purification system. The following reagents were purchased from Sigma Aldrich and were of analytical grade or better: acetone, 2-propanol, ethanol amine, bovine serum albumin (BSA), betaine, di-sodium phosphate, sodium chloride, Tris base, Triton X-100, sodium dodecyl sulfate (SDS), sodium citrate saline (SSC) powder, hydrochloric acid, potassium chloride. The epoxy-silane 3-glicidoxypropyl

triethoxysilane (GPTES) was purchased from Fluorochem (Hadfield, UK). Synthetic oligonucleotides with the probe and target sequence respectively 5' CCTCAAAGAGAGAGAAGAAGAAA 3', with a C6 amine modifier at the 5' end, and 5' TTTCTTCTTCTCTCTCTTTGAGG 3', with a Cy5 modification at the 5' end, were purchased from Eurogentec (Seraing, Belgium).

Commercial substrates

Nexterion E and HiSens E epoxy coated slides were purchased from Schott AG (Mainz, Germany).

Microscopy and imaging. Contact angle measurement

Optical fluorescence microscopy was carried out using a Leica DM LB2 up-right microscope (Leica Microsystems, UK) equipped with a 2.5 x magnification lens and a Cy5 filter set, a Hg lamp and a Spot RT Slider camera (Diagnostic Instruments, Michigan, USA).

Test substrates were imaged on a GenePix 4000A Microarray Scanner (Axon/Molecular Devices, Sunnyvale, California, USA).

Atomic force microscopy imaging was carried out using a CP-II atomic force microscope (Veeco, Santa Barbara, California, USA) equipped with a large area scanner. Tapping mode scanning was employed using silicon probes attached to cantilevers with a typical force constant of 40 N/m and a typical resonance frequency of 300 kHz (Budget Sensors, Windsor Scientific, UK).

Contact angle measurements were carried out using a Kruss Drop Shape Analysis System DSA 10 Mk2.

Dry-cleaning

Surface adsorbates decontamination was carried out in a Bioforce Nano UV-ozone chamber (Bioforce Nanosciences, Ames, Iowa, USA).

Image and numerical processing

Image processing was carried out using the freely available image processing suite ImageJ (NIH, USA) (Rasband 1997-2011). Scanning probe microscopy images were processed using WSxM scanning probe microscopy analysis package from Nanotec

Electronica, Spain (Horcas et al. 2007). Numerical processing was done using Origin Lab (Northampton, MA, USA).

II.3.2.2 Microfabricated substrate architecture and layout

Substrates were fabricated on 4 inch silicon wafers, in pairs of two standard microscope-slide sized slides per wafer. Four types of slides were fabricated, each test slide containing an active area covering one vertical half of the slide, and two control areas covering each one vertical quarter of the slide. The two control areas are complementary to the active area in that one of the controls consists of the flat, unstructured counterpart of the active area, that is, a continuous dielectric layer with the thickness equal to that of the pillars or inverted pillars respectively, in the active area. The second control is a negative type of control, with a thickness of the dielectric layer that leads to maximum suppression of the fluorescence. The layout and architecture of the four types of substrates is illustrated in **Figure II.3.1** and **Figure II.3.2** and **Table II-5** below.

Table II-5. Summary of substrate composition

Type	Reflector	Pillar height (nm)	Control 1 (flat)	Control 2 (flat)
Pillars	Si	110	native oxide	110 nm SiO_2/Si
Pillars	Pt	110	native oxide	110 nm SiO_2/Pt
Inverted pillars	Si	-110/220*	220 nm SiO_2/Si	110 nm SiO_2/Si
Inverted pillars	Pt	-110/220*	220 nm SiO_2/Pt	110 nm SiO_2/Pt

*220 nm thick SiO2 layer with inverted pillars (110 nm deep micro-wells)

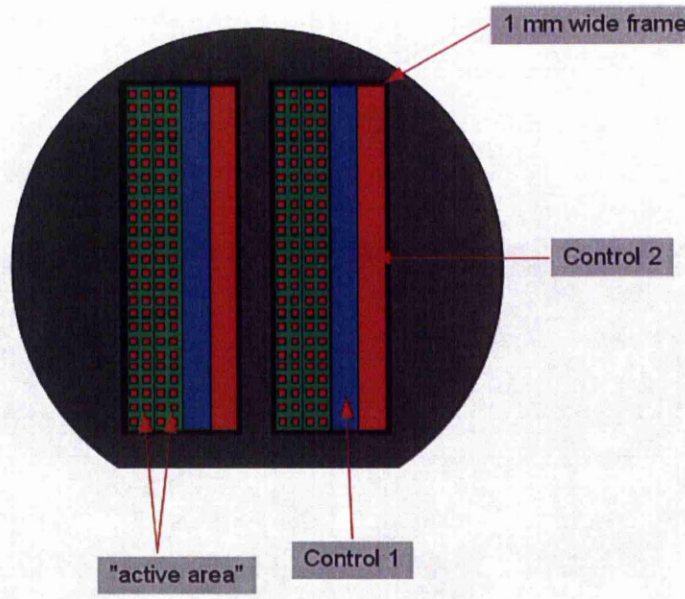

Figure II.3.1. Substrate diagram within a 4' silicon wafer

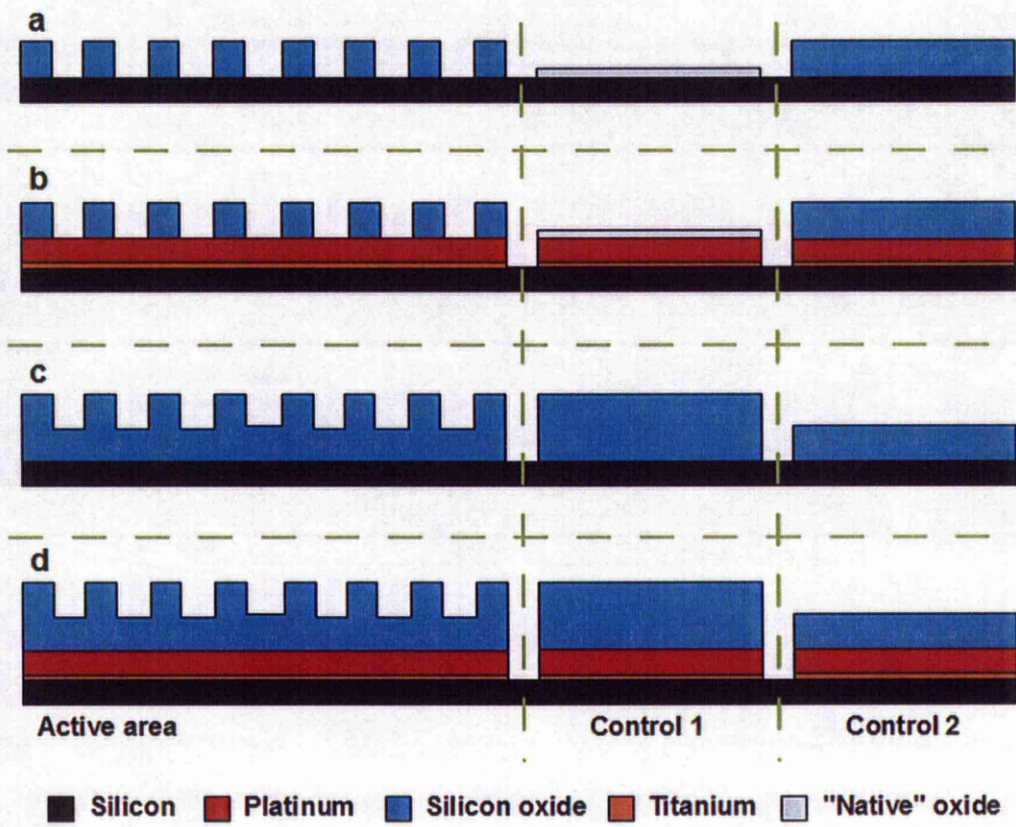

Figure II.3.2. Cross-section profile for the four substrates architectures showing the active structured areas on the left and the two types of controls on the right. (a) nano-pillars on silicon, (b) nano-pillars on platinum, (c) nano-wells on silicon and (d) nano-wells on platinum

Pillar footprint was chosen so that each pillar will comprise a sufficient number of pixels using the 5 μm maximum resolution of the microarray scanner. Thus, each

pillar is 30 x 30 μm in footprint giving 36 pixels per pillar (**Figure II.3.3**). The pitch between the pillars was chosen at 25 μm resulting in a 5 pixel separation between the pillars. As mentioned earlier, each slide is 23 x 73 mm with a 1 mm frame surrounding the slide.

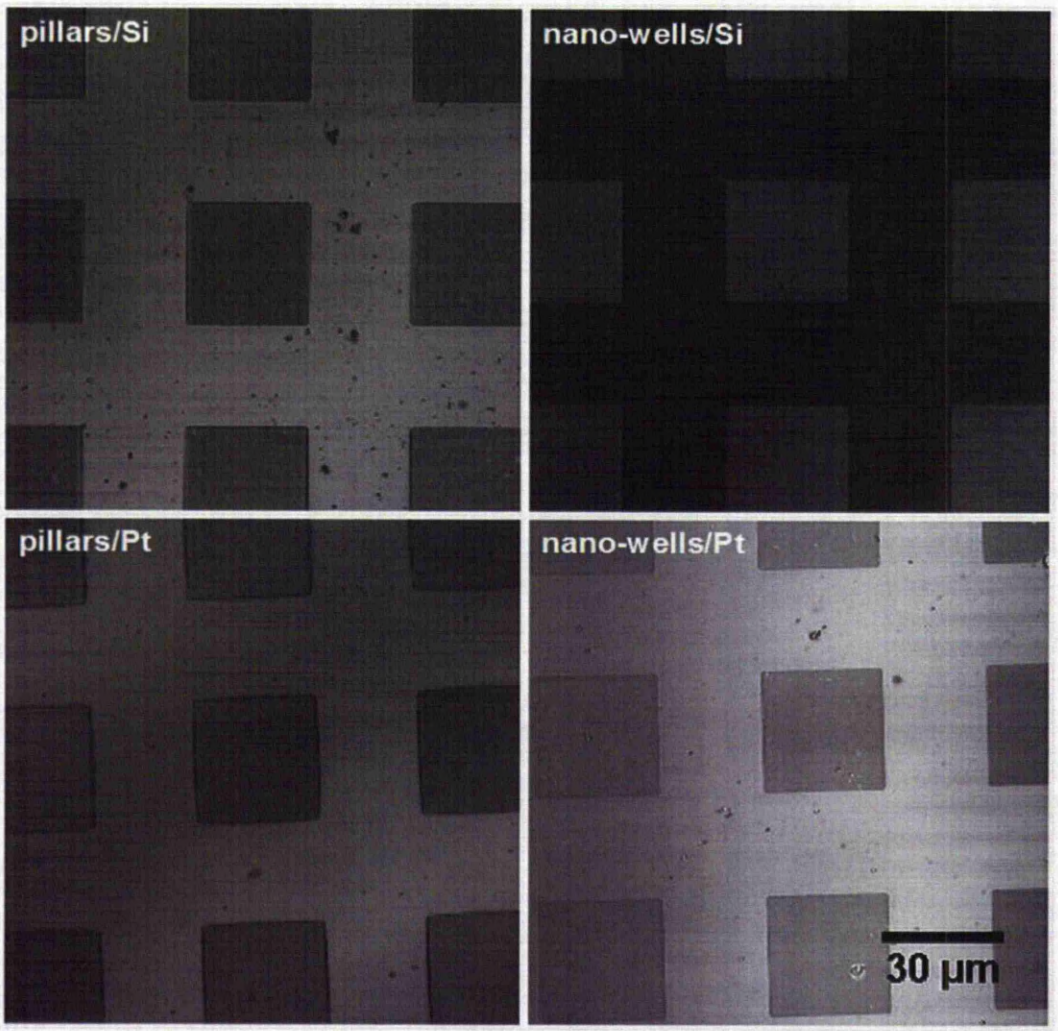

Figure II.3.3. Optical micrographs of structured areas on the four types of substrates

II.3.2.3 Substrate fabrication

The procedures described in Part 2 – Chapter 1 (**II.1.2.2 Substrate fabrication**) were employed for the fabrication of these substrates. The procedure is shown schematically in **Figure II.3.4** for silicon oxide pillars on silicon (A) and platinum (B) respectively and silicon oxide nano-wells on silicon (C) and platinum respectively. The only difference from the procedure previously reported is that for nano-wells, an incomplete RIE is performed (i.e. RIE is stopped before the underlayer is reached).

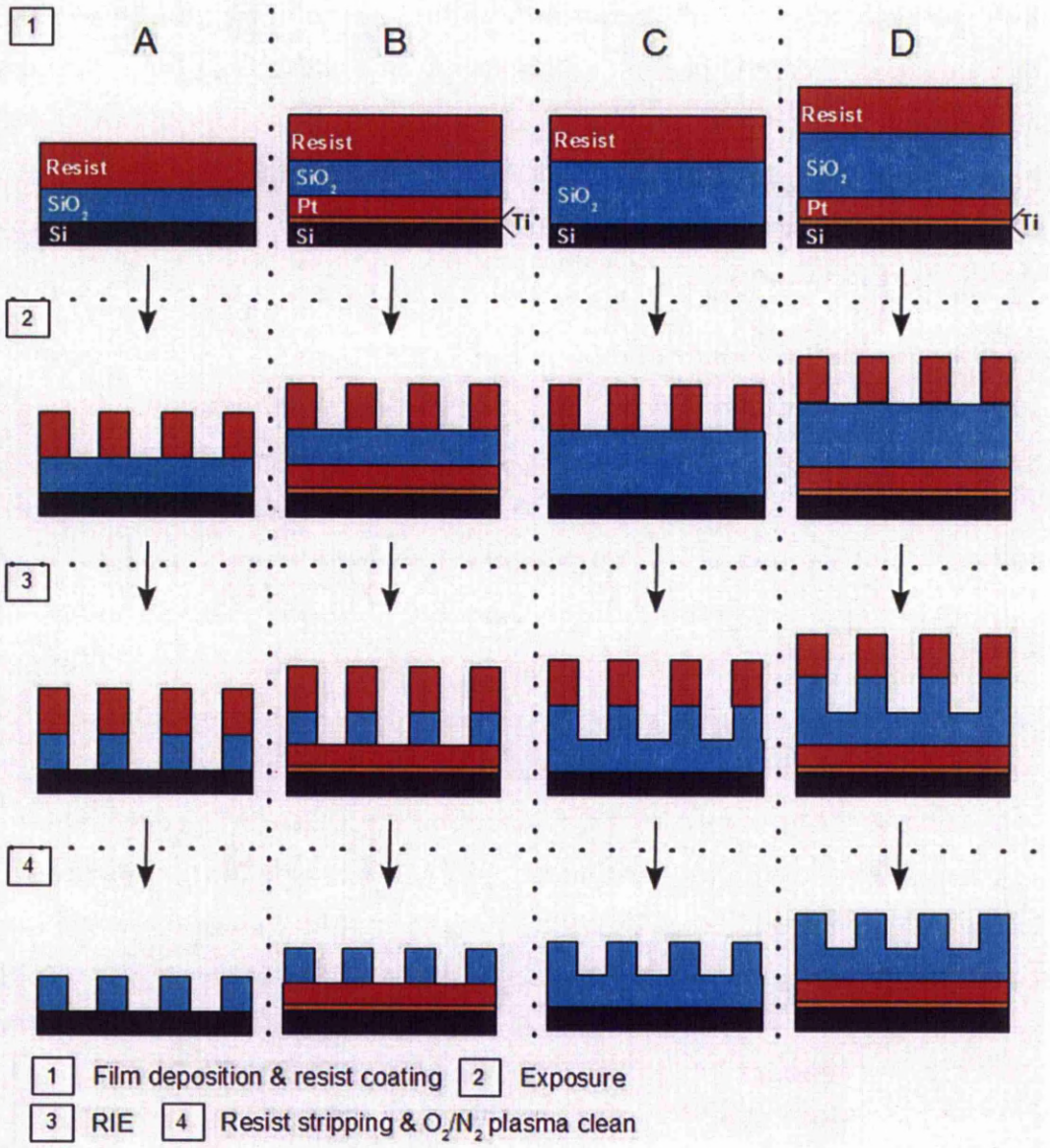

Figure II.3.4. Schematic substrate fabrication procedure

II.3.3 Experimental

II.3.3.1 Substrate coating optimization

The optimal GPTES in toluene concentration was chosen after preliminary experiments. Glass substrates were silanised with different GPTES concentrations and the surface hydrophilicity and topography were monitored throughout the entire process. Fluorescence intensity as a function of initial silane concentration was also measured using a Cy5-labelled BSA probe molecule. No *a priori* knowledge of expected surface characteristics exists, other than maximization of the binding capacity and obtaining good surface chemistry coverage. There is no target surface

hydrophobicity that needs to be reached and there are no roughness characteristics that are known from the beginning. But the set of results arising from a range of analysis techniques can be correlated to give a clear picture of not only what are the optimal values but also why these values are optimal. Further, for instance, water contact angle measurements can be used as a quality control metric for reproducibly fabricating the substrates.

Fluorescence based optimization

Fluorescence probing of the silane film with respect to binding capacity versus initial silane concentration was also measured. This was first attempted using a DyLight 649 modified oligonucleotide but the binding was found to be almost inexistent. DyLight 649-BSA was successfully used in these experiments. Optimization was carried out for 5 ranges of concentrations: 0.1, 0.25, 0.5, 1.0, 2.0 and 4.0 % respectively GPTES in toluene, by volume. A control was also included. Thus, the water contact angle of 6 glass slides was measured before and after a 60 minute UV-ozone cleaning procedure. Afterwards, the slides were immersed in the 3 mL toluene solutions containing from 0 to 4% GPTES and incubated for 2 hours. After the reaction, the slides were rinsed in toluene and dried in a gentle flow of nitrogen, then annealed in a convection oven at 120 ^{o}C for 1 hour. After cooling down, the water contact angle was measured and the surface topography was measured. Also, the surface chemistry was probed using fluorescently labelled BSA (DyLight 649-BSA provided by dr. Robert Wilson).

Solutions containing DyLight 649-BSA, 13 μM protein concentration and 18.1 μM dye concentration, in water containing 100 mg/L NaN_3 were diluted 10 times in PBS 0.1 M, pH = 9.0, containing 1.5 M NaCl. 2 μL volumes of this solution were spotted onto the functionalized glass substrates using a micro-pipette. The slides were then incubated overnight (16 hours) in a humidity chamber. Briefly, the humidity chamber consisted of a glass dessicator containing 1.5 L water and 0.5 kg of commercial table salt (NaCl) (Obrien 1948). The humidity chamber was left to equilibrate for 10 hours prior to use. After the expiration of the incubation time, the substrates were washed once, for 15 minutes, in water containing 0.05% Tween 20, and twice (15 minutes each) in de-ionized water; drying was done under a stream of nitrogen.

Water contact angle-based optimization

The static contact angle was measured multiple times using multiple methods on each substrate and a mean contact angle was calculated. There were two factors that were found to affect the quality of the measurements: evaporation and droplet deposition. Inconsistent results were first obtained when a 0.5 μL droplet was used and this was attributed to evaporation of the liquid. The droplet volume was changed to 2 μL as a consequence and the results improved. The droplets were deposited carefully, maintaining the smallest possible distance between the pipette tip and the substrate to avoid droplet spreading due to impact. The expected behaviour is that, as a silane monolayer forms, the contact angle will increase up to a value corresponding to complete mono-layer surface coverage. After this value is reached, formation of silane aggregates on top of the monolayer through non-specific interaction would induce a change to either smaller or higher values of the contact angle or a change in the slope with which the contact angle increases.

Atomic force microscopy-based optimization

In parallel, the topography of the surfaces was monitored throughout the silanization process. The surfaces were scanned in tapping mode before cleaning, after UV-ozone treatment and after silanization. The surface roughness was measured and the surface morphology was assessed.

Atomic force microscopy is a branch of scanning probe microscopy (SPM), a collection of techniques that allow surface imaging with high resolution by using a probe that is scanned across the surface to be measured. In AFM, an atomically sharp probe, generally of pyramidal shape (radius of curvature in the range of nanometres to tens of nanometres) is mounted on a cantilever. The principle of operation is based on monitoring the probe's deflection by shining a laser onto it and reflecting the laser light onto a position-sensitive photo-detector (PSPD). The voltage on the PSPD is then transformed into the relevant signal (height, lateral force, magnetic force etc.). The simplest operation mode is contact mode with constant force. In this mode, the probe is brought into contact with the surface and the force that the probe exerts on the surface is maintained constant. This means that, when the probe is scanned across the surface (most commonly, the sample to be measured is placed on a piezoelectric stage and the sample is scanned under the probe rather than the probe being scanned over a fixed sample) and it encounters topography changes, the distance between the

two needs to be corrected in real time. This is achieved through the use of a feedback loop that monitors the cantilever's deflection as the topography changes and adjusts the probe to sample separation distance. This imaging mode, although simple, is characterized by drawbacks such as sample and probe damage, difficult if not impossible to scan soft or sticky samples, artefacts to name but a few. A more advanced imaging mode, the so called tapping mode has been developed that alleviates these issues. The difference between a topographical and a phase scan is illustrated in **Figure II.3.5**.

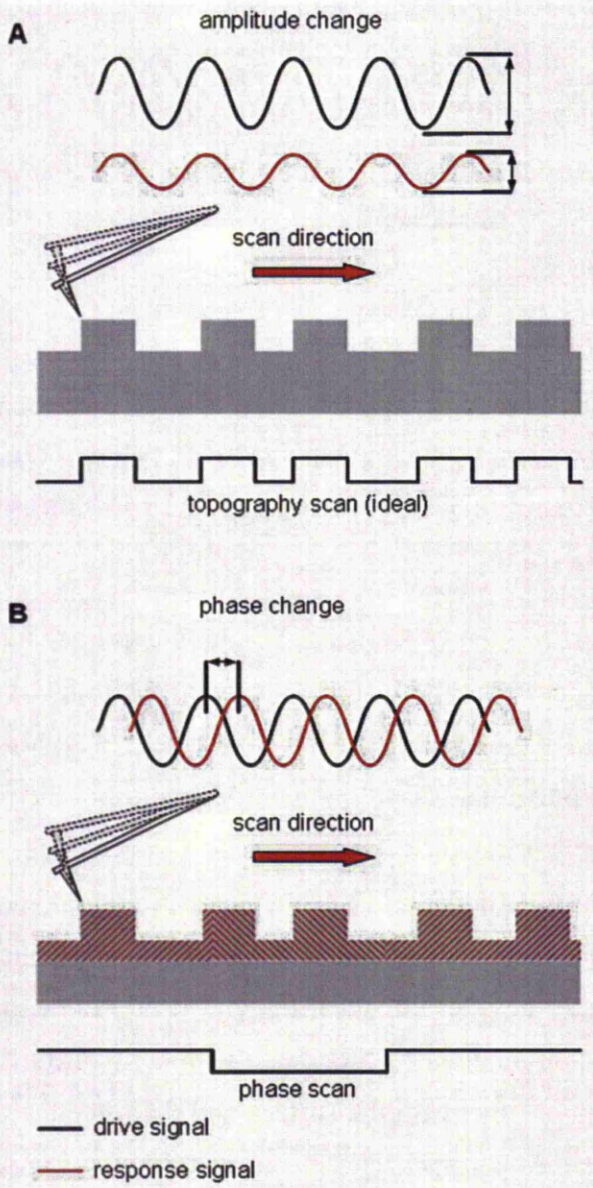

Figure II.3.5. Topographical contrast (A) and phase contrast (B) formation in tapping mode AFM

In tapping mode imaging, part of the dynamic or oscillating probe techniques, the probe is made to oscillate at or near to its resonance frequency by means of a piezoelectric element. The amplitude of the oscillation is in the order of a few tens of nanometres. In free space, that is at a sufficiently large probe-sample distance where no interaction between the two occurs, is driven by the current that is fed to the piezoelectric element. As the probe is brought closer to the sample, it will briefly come into contact with the surface, gently tapping it (hence, the name). Two advantages of tapping mode imaging over contact mode imaging arise from this: because the contact time is only a very brief one, the forces between the two contacting elements are minimized leading to low sample and probe damaging and to low interference from the layer of adsorbates on the sample surface (water vapours, other contaminants). As illustrated in **Figure II.3.5 A**, imaging is based on monitoring the response oscillation amplitude versus the drive oscillation amplitude, as the amplitude of the oscillation once the probe engages the surface changes (decreases). This is due to small range forces acting on the probe. As the oscillation amplitude is kept constant, the probe-sample separation distance needs to be continuously adjusted. An extension of tapping mode imaging, called phase imaging or phase contrast, is illustrated in figure B. As the probe engages the surface, it is not only the amplitude oscillation that changes but also the phase of the oscillation, with respect to the drive oscillation phase. The magnitude of the phase lag provides another signal that can be used for mapping some physical properties of the sample surface like elasticity, adhesion, compliance. Unfortunately, the resulting phase lag contains all the convolved information about the surface physical properties so interpretation of the images is not straightforward (although it can be done by employing other scanning probe techniques like force-distance curves, friction force microscopy and so on). Nevertheless, phase imaging can provide information that is effectively inaccessible through "standard" means especially since phase imaging does not require a dedicated set-up and is performed simultaneously with topography imaging.

II.3.3.2 Substrate processing

To protect the integrity of the patterns and the chemical characteristics of the surface and to avoid particulate contamination during transportation, the substrates were coated in a layer of resist. Removal of the resist layer was carried out via acetone

rinsing, four rinses with 300 mL acetone per 4 microfabricated and one control glass slide to remove the bulk of the resist, and UV-ozone exposure for two hours. Water contact angle was measured before and after protective resist stripping. The same cleaning procedure was applied to the glass microscope slides and the water contact angle was also measured.

II.3.3.3 Substrate chemical activation

Surface chemical fabrication of the microfabricated and plane glass slides was carried out by introducing epoxy groups on their surface using 2% GPTES in toluene. A Coplin jar was rinsed in water and ethanol then dried in an oven at 120 °C for 2 hours. Prior to silanization, the recipient was washed with toluene for 30 minutes. At the same time, the substrates were again exposed to UV-ozone for 30 minutes to ensure a clean and active surface. Silanization was carried out in 300 mL toluene containing 2% GPTES by volume (4 microfabricated and one glass slide). After silanization, the slides were washed three times in 300 mL toluene and dried in a stream of nitrogen. Annealing of the silane layer was done at 120 °C for 2 hours. After natural cooling of the substrates, the water contact angle was measured and compared to the one measured on the epoxy-coated commercial slides.

II.3.3.4 Capture probe printing

Printing of the capture probes was carried out following the protocol recommended for the printing of the Schott slides. The lyophilized 5'-amine modified oligonucleotide with the sequence 5' CCTCAAAGAGAGAGAAGAAGAAA 3' was reconstituted in Millipore de-ionized water to give a final concentration of 333.3 µM. This stock solution was used to prepare a 10 µM probe concentration in PBS buffer 0.1M, pH = 9.0, containing 0.15 M NaCl and 1.5 M betaine. Printing was carried out using a manual printer with 0.5 µL capacity split head printing pins. The printed substrates were then incubated for two hours in a high humidity chamber and then one hour at 60 °C in polystyrene culture dishes whose bottom was previously lined with filter paper and wetted with a saturated NaCl solution. Removal of the unbound probes was carried out in 4 rinsing steps. An initial rinse was carried out for 5 minutes in a 0.1% Triton X-100 aqueous solution. The second washing step consisted of two 2 minutes washes in a 1 mM HCl solution. The third stage was a 10 minutes wash in a 10 mM KCl solution and finally, the last step was a 1 minute wash

in de-ionized water. All washes were carried out using a sufficiently large volume of liquid, following the protocol guidelines (min. 250 mL per 5 slides)

Surface blocking was carried out using a solution containing 50 mM ethanolamine and 0.01% SDS in 0.1 M Tris buffer, pH = 9.0. The slides were incubated for 15 minutes in the blocking solution (a minimum of 100 mL blocking solution per 5 slides), on a water bath at 50 ^{o}C. The slides were then rinsed in de-ionized water for 1 minute.

II.3.3.5 Hybridization

Multiple target concentrations were used in hybridization experiments. The target sequence used was a 5'-Cy5 modified synthetic oligonucleotide (Eurogentec, Seraing, Belgium) corresponding to the avian flue virus (5' TTTCTTCTTCTCTCTCTTTGAGG 3'). Before hybridization experiments, 64-well silicone dividers (Grace Biolabs, Bend, Oregon, USA) were affixed to the substrates, where each well had a capacity of 22.05 μL. The lyophilized powder was reconstituted in 893 μL de-ionized water to yield a 100 μM target stock. The hybridization was carried out using solutions containing different target concentrations. The hybridization solutions were prepared so the hybridization buffer (4 x SSC buffer containing 0.1 % SDS) content in the final solution would exceed 90% and target concentration was varied from 1 to 16.4 x 10^{-11} μM in five-fold dilutions. A 10 μL volume of target was delivered to each well and the slides were incubated overnight (16 hours) at room temperature in a high humidity chamber.

Post hybridization washes were performed to remove non-specifically bound target molecules. All washes were carried out for 10 minutes. The first wash was done in 2 x SSC buffer containing 0.2% SDS. The second wash was done in 2 x SSC buffer and the third one in 0.2 x SSC buffer. After washing, the slides were dried in a gentle stream of nitrogen. The probe immobilization and target capture process is summarized in **Figure II.3.6**.

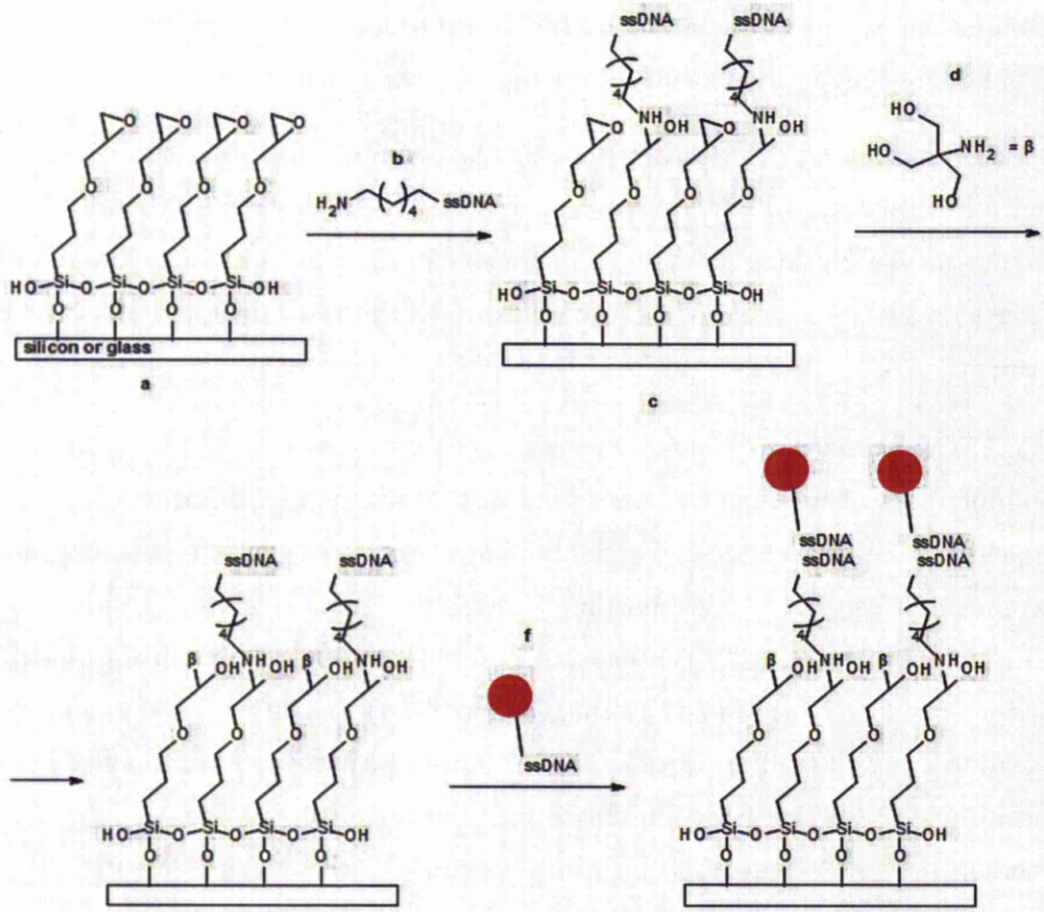

Figure II.3.6. Surface chemical activation with epoxy groups, probe attachment, blocking of residual active groups and hybridization. A substrate displaying surface hydroxyl (such as silicon or glass) which were derivatized to introduce surface epoxide groups (a) is used to array amine-derivatized oligonucleotides (b) through an epoxide ring opening reaction (c). Further, the areas containing the epoxide surface functionality are blocked using Tris buffer solution (d). Hybridization of the surface bound probe to the appropriate fluorescently labelled target (f) is then carried out.

II.3.3.6 Fluorescence measurements

After hybridization, the slides were scanned in a GenePix 4100A Microarray Scanner using the Cy5 laser line (635 nm) and the PMT gain setting was optimized for each slide. The slides were scanned twice, the first time using a scanner resolution of 40 μm/pixel and the second time using the minimum possible pixel size of 5 μm/pixel.

II.3.3.7 Image processing

Images were processed using ImageJ and IrfanView, and numerical processing was performed using Origin Lab (Northampton, MA, USA). The original format supplied by the GenePix 6.0 software comprises multiple TIFF images with a 16 bit colour coding. Read-out of the multi-page TIFF files was done in IrfanView which unfortunately only supports 8 bit colour encoding.

Processing in ImageJ was done starting from the 8 bit images. The first step consists of thresholding the image via the Otsu algorithm. This thresholding procedure is commonly used in microarray data extraction (Rueda and Rezaeian 2011) and it is based on dividing a sample into two populations with minimal intra-population variability. The result of the thresholding process is a binary image that can then supply the spot boundary information as shown in **Figure II.3.7**. This information is superimposed on the initial image and both the spot and its surrounding can be quantified in terms of both intensity (mean gray level and standard deviation), and shape and size (circularity, area). Further calculations are performed using OriginLab.

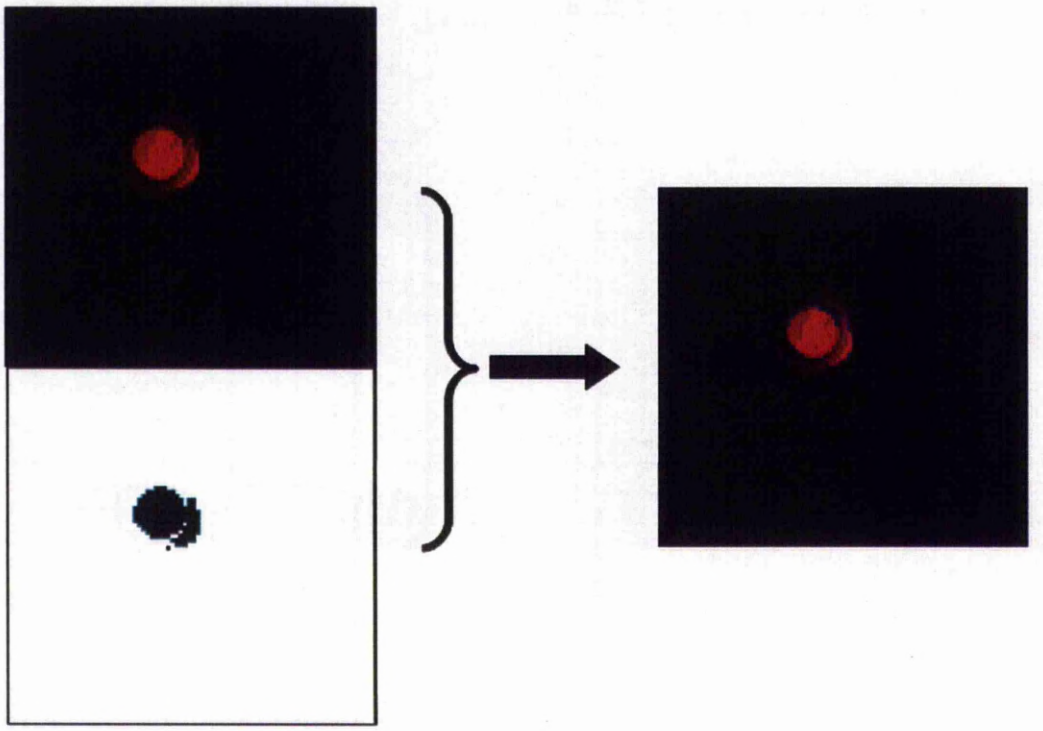

Figure II.3.7. Feature segmentation for features printed on flat areas. A typical spot printed on a flat area is depicted in the top left fluorescence micrograph. The result of applying the Otsu algorithm is shown at the bottom left of the figure. Using the particle analysis tool in ImageJ, one can detect the edges of the spot and apply locate the boundaries of the initial spot (right).

A very similar procedure is applied to the "spots" measured on the structured surfaces. The spot area, that is, the area containing the "sub-spots" is identified using the Otsu thresholding. A 3 x 3 array of squares, each of them 6 x 6 pixels (30 x 30 μm) at a 5 pixel (25 μm) pitch is superimposed on 9 sub-spots. This array determines the boundaries of the sub-spots. The mean intensity and the standard deviation of the sub-spots can be determined. For the area outside the sub-spots, the selection is

enlarged by 1 pixel and then inverted. Another way to determine the "real" background is to use the same selection for the sub-spots, the 9 x 9 array, but measured in an area that is well away from that being determined via Otsu thresholding as illustrated in **Figure II.3.8**.

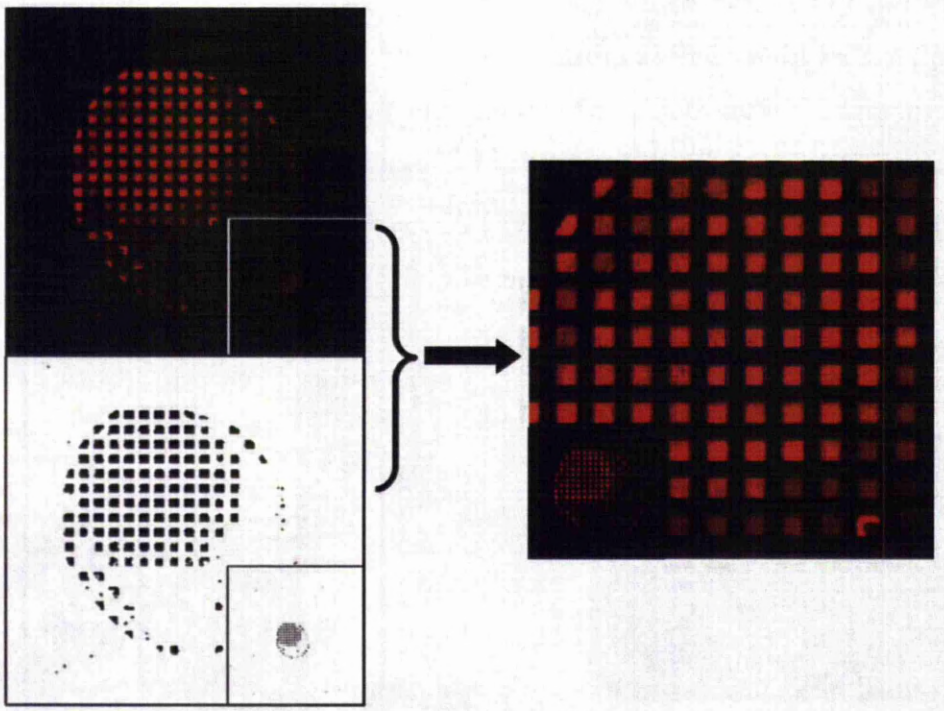

Figure II.3.8. Feature segmentation for features printed on structured areas. The top right fluorescence micrograph shows a typical printed spot (zoomed out in inset). At the bottom left, the resulting binary image after application of the Otsu algorithm is shown. It can be seen that some features of the original image were rejected by the algorithm. On the right, a 3 x 3 cell array is used to analyse a collection of sub-spots.

Data normalization, in particular the SNR, is carried out using the spot circularity and the spot average surface area as normalization elements. Obviously, this is not applicable to the spots on structured surfaces, since their size and shape is already known.

II.3.4 Results and discussion

II.3.4.1 Silane coating optimization

The optimization of the film deposition conditions was carried out since a multitude of recipes is available in literature. A common trait for these methods is the use of toluene to dissolve the epoxy silane. They differ by the silane concentration (between 0.1 and 2%), deposition time (between 10 minutes and 10 hours), annealing temperature and additives used. A moderately long deposition time of two hours was

chosen and no additives were used here. Also, the annealing temperature was set at 120 °C so the only parameter that was varied was the initial silane content, from 0.1 to 4%. Also, the aim is to obtain a silane film whose quality is comparable to that on commercial substrates (silane coating is generally applied of the commercial from vapour state due to better film characteristics).

The contact angle of water on the epoxy-silanized glass substrates was measured. The procedure included both an "as received" glass substrate, a UV-ozone cleaned one without a silane film, a control consisting of UV-ozone cleaned glass exposed to bare toluene and six glass substrates that were cleaned and then exposed to solutions of GPTES in toluene with GPTES concentration of 0.1, 0.2, 0.5, 1.0, 2.0 and 4.0% respectively, by volume. The evolution of the water contact angle is illustrated in **Table II-6** and **Figure II.3.9**.

Table II-6. Contact angle (CA) measured on glass substrates that have been subjected to different chemical treatments

Glass substrate treatment	CA
as received	17.72±1.66
UV-ozone cleaned	could not measure
0% GPTES	37.66±0.28
0.1% GPTES	38.09±1.09
0.2% GPTES	37.93±0.41
0.5% GPTES	42.27±0.34
1.0% GPTES	49.27±0.28
2.0% GPTES	50.23±1.54
4.0% GPTES	45.33±0.42

The contact angle measured on the "as received" glass was 17.72±1.66° and this was attributed to surface contamination since, once the surface was dry-cleaned, the contact angle dropped to a value so small that could not be measured. The control surface that was treated with clean toluene displayed an elevated contact angle even though the substrates were heated to 120 °C for one hour after the liquid phase deposition. This high contact angle was attributed to the physisorption of toluene onto the glass surface. The surfaces that were treated with GPTES in toluene initially

appeared to be immune to low GPTES concentrations, then a steep increase in contact angle was measured, from 42 to 50° respectively, for GPTES concentrations between 0.5 and 2.0% respectively. These findings appear to be in agreement with the data published (Luzinov et al. 2000), albeit their experiments were performed with the methoxy homologue of GPTES. Unfortunately, the authors do not report a contact angle value for a control surface treated with only toluene. Rather surprisingly, for a 4% GPTES concentration, the contact angle seems to drop to 45°. One possible cause might be the formation of polymerized silane aggregates that contribute to the increase of the surface roughness which, in turn, leads to a increase in the wettability of the glass surface.

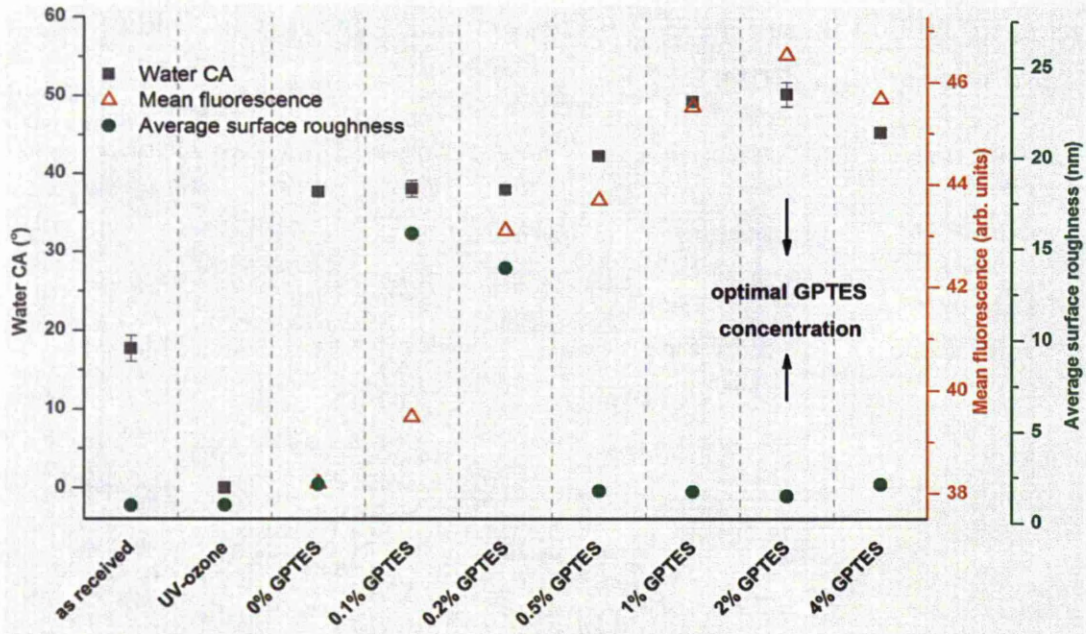

Figure II.3.9. Water contact angle (grey squares), fluorescence intensity after fluorescent BSA attachment (orange triangles) and average surface roughness (green circles) for glass substrates that received different chemical treatment

Figure II.3.9 also illustrates the evolution of the fluorescence emission as a function of GPTES initial concentration using a Cy5-labelled BSA as a fluorescent probe. The silanization process endows the surface of the substrates with epoxide functional groups. The epoxide group is of extreme importance in synthetic chemistry as, due to its strained nature, it is susceptible to opening by various functional compounds. In the realm of conjugation chemistry, biomolecules often display at least one of the following free groups: thiol, amine or hydroxyl. These three groups can open epoxide rings with the formation of covalent bonds and the reactivity of epoxides to

these groups is modulated, among others, by the pH. Thus, thiols are the most reactive towards epoxide ring opening, the reaction proceeding at neutral to slightly basic pH; amines react at slightly elevated pH values, upwards of 8.5 pH units; and hydroxyl groups require a very basic pH, over 12 units, to open the epoxide ring (Hermanson 1996).

The fluorescent probe can be chosen to be either a fluorescent dye or a fluorescently labelled (bio)molecule. For practical reasons, the fluorescently labelled biomolecule route was chosen. The first attempt was carried out with a Cy5-labelled oligonucleotide with no extra modifications. The reasoning behind this was that, although there are no modifications apart from the fluorescent dye, the free amines on the nucleic bases will provide the anchoring points to the surface epoxide groups. Although there is an abundance of literature (and even claims by microarray slide manufacturers) suggesting that these amine groups make viable candidates for epoxide ring opening reaction, they were found to be unreactive in practice, even though the printing concentration was 10 μM. The resulting spots proved to be difficult if not impossible to quantify.

As a result of the lack of reactivity of nucleic base amines towards epoxide opening, the use of Cy5-labelled BSA was considered, as BSA has both free amine (Habeeb 1966) and one thiol (Oblak et al. 2004) group. The advantage of using BSA stems from the existence of free chemical groups on the protein that can react with epoxides. But there are some disadvantages as well. First of all, the size of the molecule means that its footprint will be larger than that of a DNA strand. Consequently it is highly probable that free surface epoxide groups will be effectively blocked from reacting. Arising from the molecular footprint issue, a moderate labelling degree would lead to a lower fluorescence than what could be expected from the attachment of a "slender" molecule like DNA. In other words, in theory, for a 1:1 labelling ratio, using a labelled oligonucleotide would yield a 1:1 fluor to surface epoxide ratio while a 1:1 labelling degree of the BSA molecule would possibly yield a sub-unity ratio of fluors to surface epoxide groups. For instance, the labelling degree for the Cy5-BSA conjugate used in the optimization study, the labelling degree was 1.4 dye molecules per BSA molecule. Another disadvantage of using BSA, or probably any protein for that matter, is the lack of specificity. Due to its low cost, BSA is commonly used as a surface blocking agent,

i.e. blocking a surface against non-specific binding (as used in microarray technology). This is because proteins in general (another example from microarray industry is casein from milk) have a variety of surface groups on their surface and this makes them prone to adsorption to virtually any surface (unless they have been specially treated against protein adsorption). So, in a sense, a protein surface is a combinatorial surface that is able to adsorb onto virtually any solid surface due to a combination between protein size and surface chemistry. Despite these apparent drawbacks, the purpose of the experiment is to comparatively asses the binding capacity of the epoxy-silane layer and to choose the best silanization conditions. In this respect, it was found that fluorescence emission increases and the water contact angle both follow an increasing trend with respect to the initial silane concentration. Also, the emission on the control substrate is not zero due to the non-specific adsorption discussed previously. Additionally, it was found that a maximum fluorescence intensity is measured on the substrates corresponding to an initial silane concentration of 2% and that for an initial silane concentration of 4%, the fluorescence intensity decreases. This last finding is useful in that it can confirm that the decreased contact angle is not a measurement artefact.

A third methodology employed for the determination of the optimal liquid phase deposition of the epoxy-silane was atomic force microscopy (AFM). As with the contact angle and fluorescence intensity, AFM characterization of the surfaces was carried out before and after each stage of the glass substrate surface chemical activation. The topography and phase scans shown in **Figure II.3.10** and **Figure II.3.11** were acquired on 20 x 20 μm areas and then analysed in WSxM and Origin Lab. WSxM was used to remove the stage movement induced bow of the surface by fitting and then subtracting a plane from the image. The same software was used for average surface roughness and RMS roughness determination. The height distribution of the surfaces, characterized by both the mean (and the standard deviation) and the median (and interquartile distance) were measured using Origin Lab.

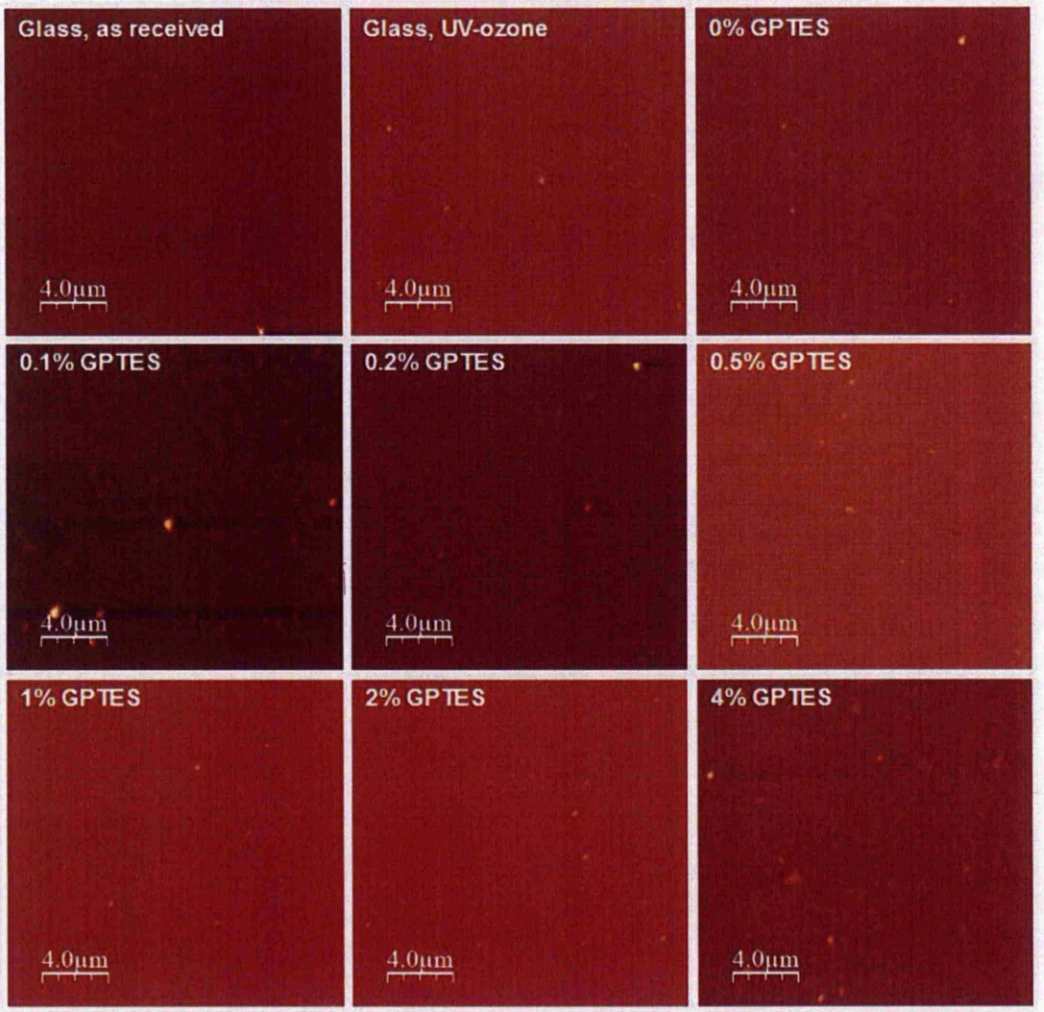

Figure II.3.10. AFM topography scans of the glass substrates

A visual assessment of the topography scans does not reveal very obvious trends and can prove to be misleading. However, one can observe that the bare glass surface, both the "as received" one and the UV-ozone treated one, as well as the one that has only been exposed to GPTES-free toluene is quite flat and lacks surface features. Additionally, increasing the GPTES concentration results in the formation of small, granular structures. At the highest GPTES concentration used, i.e. 4%, there is a somewhat noticeable change in the morphology of the surface elements, from a granular to a less defined, "blobby" shape.

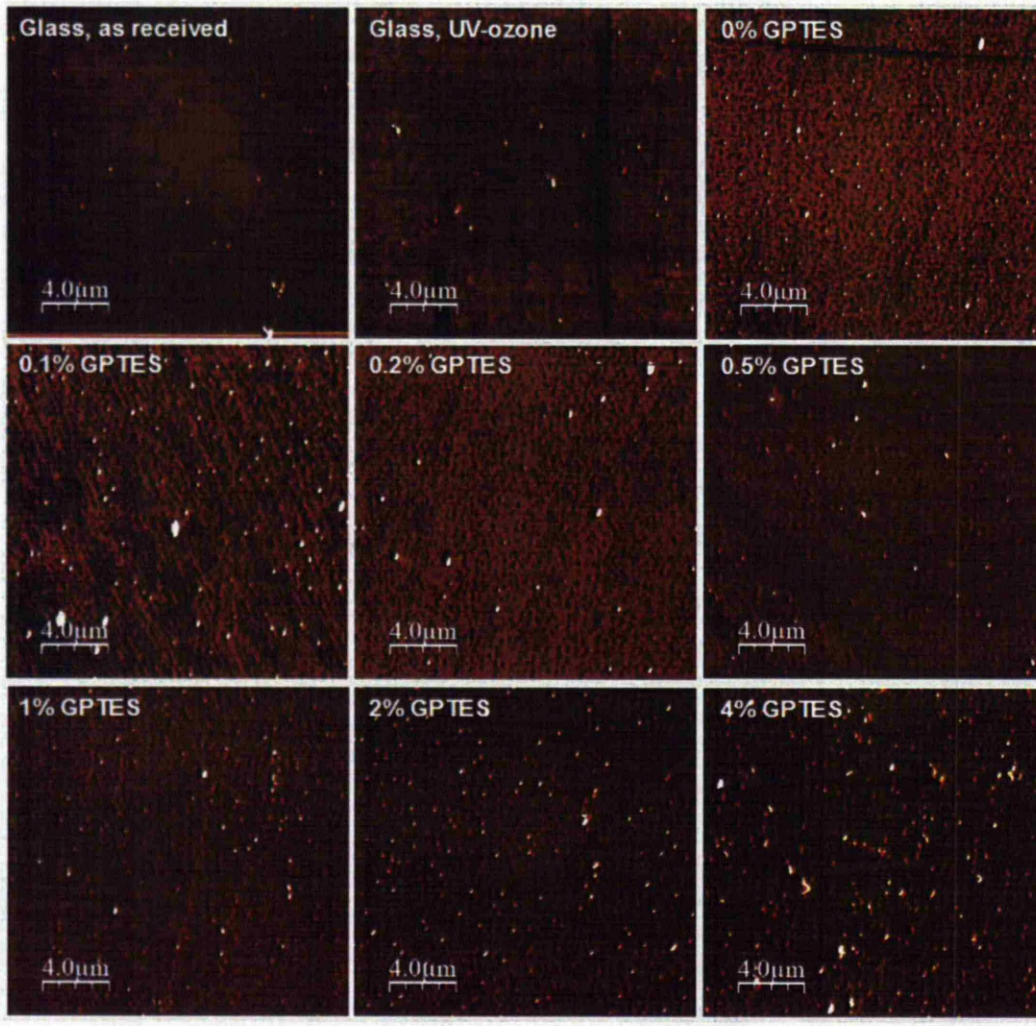

Figure II.3.11. AFM phase scans of test glass substrates for different surface treatments

The motivation for using phase contrast phase imaging in conjunction with tapping mode imaging is two-folded. The simplest reason for doing so is that, since phase information can be acquired at the same time with topography data at no extra cost (time or otherwise). The second reason is that phase imaging can offer a wealth of information about the physical properties of the surface. Consequently, phase information can help discriminate between layers with different properties that could otherwise not be differentiated. The phase scans associated to the topography scans presented previously are shown in **Figure II.3.11**. Phase information is difficult to interpret due to the mixed nature of the properties that give rise to the actual phase contrast. In this particular case, one would expect phase contrast arising from the softness of the organic silane film or, rather more probable, different adhesion between the probe and the glass and silane film respectively. The images appear to

display a faint contrast. The magnitude and distribution of the contrast can be further explored through numerical analysis.

Due to the possible erroneous nature of interpreting AFM images by visual means, numerical analysis was also considered. Thus, from the topographical scans, the average surface roughness, given by the mean of the absolute distance between every point on the surface and a plane that is placed at the mean height of the surface, and the RMS roughness, calculated as the square root of the variance of the mean surface roughness, were calculated using WSxM and plotted as a function of surface treatment and are shown in **Figure II.3.12, top**. Additionally, the mean phase (with its standard deviation used for error bars) and the median phase (accompanied by its interquartile distance as error bars) were plotted and are shown in **Figure II.3.12, bottom**. From the variation of the average and RMS roughness throughout the process, one can see that a relatively small roughness is measured on the glass before and after dry-cleaning. The same can be observed for the toluene treated (i.e. 0% GPTES) glass surface. Also, the presence of topographical elements (like surface roughness) that might affect the measured contact angle cannot be detected so the value of the water contact angle is attributed, again, to the presence of surface contaminants and their removal respectively. It can also be seen that the roughness parameters increase sharply when the GPTES concentration is low but then start to go down as the concentration of the silane increases. Low values of the surface roughness parameters are measured for an initial silane concentration of 1 and 2% respectively and then a slight increase trend seems to appear. This can be explained as follows: at first, the surface is topographically homogeneous so the roughness parameters are low; the addition of the silane slowly promotes the formation of islands of silane, increasing the roughness. The contact angle does not increase sharply at this time because the surface coverage is not enough to affect the water contact angle. It is enough however to contribute to the roughness. As the silane film starts to cover more of the surface, the roughness decreases to a level that is comparable to that measured before chemical treatment, when the surface topography was homogeneous. A further increase in the silane concentration might result in the formation of additional layers, probably less organized ones since the surface silanol groups are now shielded from the adsorbing molecules, and this leads to a slight increase in the surface inhomogeneity.

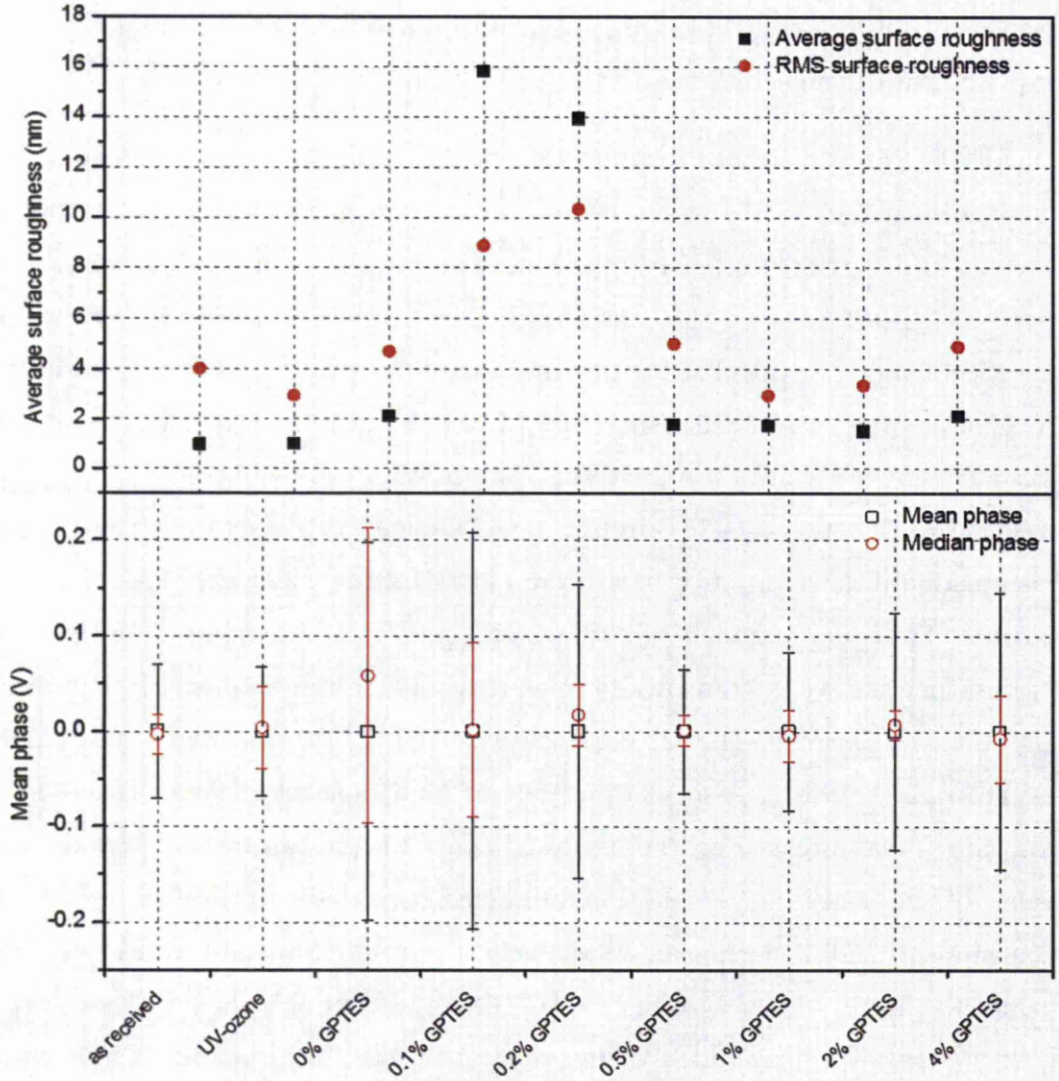

Figure II.3.12. Surface parameters numerical analysis. Average surface roughness (black squares) and RMS surface roughness (red circles) measured from the topography (top) and mean (hollow black squares) and median phase (hollow red circles) measured from the phase scans (bottom)

The mean phase distribution is less information rich due to its centring around the 0 V value (phase lag is normally measured in degrees but due to instrumental constraints, only the values recorded on the detector are available and they are given in volts). Median phase distribution however offers slightly better information. The trend of the median phase lag is generally preserved with the same unusually high value for the toluene treated control. The median then decreases with the increase in GPTES concentration then, at 1%, it starts to creep up slowly. This increase is very shallow but the increase in the interquartile distance is more pronounced, suggesting that, while the median value is not affected by the increase in GPTES concentration, its dispersion is wider, probably due to the appearance of an additional phase. This

can be correlated with the appearance of morphologically different surface features in the topography scan at 4% GPTES concentration. The high dispersion of both the mean and median phase and the elevated value of the median phase at the 0% GPTES concentration (toluene treatment only) is unexpected and cannot be assigned to a specific cause at the moment (it is also of little practical relevance).

While assigning the source of the phase lag correctly is difficult (as phase contrast can be the result of a mix of surface properties – adhesion, elasticity), in the region of higher than unity silane concentrations, the data is consistent with what the topographical data suggests, that is the minimum dispersion is achieved for 2% GPTES and an increase in the dispersion occurs at 4% silane concentration.

The sequence of analysis techniques used thus far, i.e. water contact angle measurements, topography and phase contrast imaging and fluorescence imaging, summarized in **Figure II.3.9**, suggest that the best "recipe" for the epoxy-silane film deposition, based on a deposition time of two hours and a one hour annealing time at 120 °C, is based on a 2% GPTES initial concentration. However, the standard silanization procedure suitable for a commercial process would probably be based on vapour phase deposition.

II.3.4.2 Microfabricated substrates layout

The architecture of the microfabricated slides differs from that of the substrates used previously in both layout and layer structure (**Chapters II.1.** and **II.2.**). At this time, an attempt at a working prototype was made i.e. substrate with standard commercial microarray dimensions, compatible with microarray scanners. Additionally, the relevant controls (see **Table II-5** and **Figure II.3.1** and **Figure II.3.2**) were included on the same slide so that the direct and relevant comparisons can be made, i.e. if the active and the control areas are on the same slide, then direct comparison would be less prone to error than if the active and control areas were on different slides. But the evolution in the design of the previous test substrates does not reside only in the integration of the features and control areas on a substrate that is compatible with current microarray technology. An important addition has been made in that the original pillars have been complemented by the inclusion of an anti-symmetric architecture comprising inverted pillars (or nano-wells).

The nano-well (inverted nano-pillar) structure has been implemented for several reasons. One of them is that it constitutes a different route towards obtaining the same result in terms of optical enhancement/suppression. The nano-wells are etched into a silicon oxide film with a thickness that has been chosen to provide maximum destructive interference for Cy5 fluorophores (as shown in **Chapter II.1.**). Thus, the silicon oxide layer will act as a spacer between the fluor and the reflector, be that silicon or platinum, and will provide the necessary separation distance for suppressed fluorescence. There is also an additional benefit: as shown previously, the "stray fluorescence", that is, fluorescence coming from the reflector plane, is partially suppressed by a 100 nm layer of silicon oxide (see **II.2.3.7 Residual fluorescence**) probably due to the slightly imperfect transmittance through the oxide layer. The second optical set-up is similar but not identical to the first one comprising pillars. The reflector - fluorophore separation distance remains unchanged so the fluorescence enhancement is expected to be the same as can be seen from **Figure II.3.13** where the two architectures are schematically depicted side by side. Additionally, outside the pillars and wells respectively, the optical set-up leads to suppression via interference and the suppression degree should be the same. An advantage of nano-wells over the nano-pillars arises from the imperfect transmittance through the silicon oxide and the extent of the attenuation is expected to increase in strength for a silicon oxide layer that is thicker.

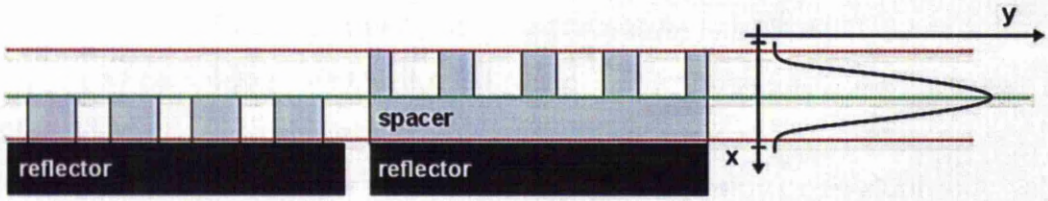

Figure II.3.13. The optical set-ups corresponding to the two architectures (nano-pillars and nano-wells respectively). When the fluorophore is placed in a plane represented by the green dotted line, its fluorescence emission is enhanced while the opposite will happen when the fluorophore is placed in the plane described by the red dotted line. A theoretical fluorescence profile is shown on the right, with fluorophore – reflector separation distance on the x-axis and fluorescence intensity on the y-axis.

A third reason for the use of the nano-well set-up arises from practical considerations. Surface cleanliness is essential for any surface chemistry modification process. Contaminants removal, whether they are the result of physisorption from the environment or simply residues from protective resist layers (as is the case here), can be either a wet or a dry process. Previously the influence of the wet chemical cleaning (RCA), which is based (partly) on etching, along with its

incompatibility with silicon oxide structures, was discussed. As an alternative, dry cleaning through UV-ozone exposure was used. While etching of the silicon oxide is no longer a problem in the case of photochemical treatment, the build-up of oxide can pose as one. Build-up of oxide as a result of UV-ozone exposure, especially its thickness, depends on the material (Kern 1993). While it is true that a silicon oxide layer only a few nanometres thick is formed on silicon (Fink et al. 2009), there are no studies about platinum behaviour. Moreover, a characterization of oxide film formation would entail complex investigations (e.g. ellipsometric) that are outside the scope of the present investigation. A simple way to overcome these problems is to use an "insulating" oxide film whose thickness will remain constant during the cleaning process (as active oxygen species would not be able to travel through the oxide to reach the base material, at room temperature at least). The film therefore insulates the underlying layer from the oxidizing action of the UV/ozone treatment. The fact that the thickness of this film remains constant is critical to the conservation of the optical properties of the slide. Furthermore, the oxide film surface should, in theory, be regenerated through the same photochemical treatment, contributing to the potential reusability of the substrate. This is an important aspect as the cost of microarray substrates cannot be neglected.

II.3.4.3 Substrate chemical activation

The microfabricated substrates and a glass control were chemically activated with surface epoxy groups through silanization. The process was monitored through contact angle measurements before and after each stage of the chemical activation procedure.

Water contact angle was measured on the micro-fabricated substrates (as shown in **Figure II.3.14** and **Figure II.3.15**).as a control method for good surface derivatization based on the values measured during the optimization procedure (**Table II-6**). In **Figure II.3.14** (with the active and control areas respectively in separate panels), the contact angle evolution during the process was compared for the four different substrates. Some general trends are obvious: before the resist stripping steps, the contact angle is high, around or above 70°, which is expected since photoresists are hydrophobic. The variability in contact angle at this stage is however inexplicable since the resist should well cover the surfaces. Further, after the acetone resist strip, the contact angle decreases moderately and a clean surface is only

available after a dry treatment. After the UV-ozone treatment (dry resist stripping), a pronounced tendency of water to spread was noticed so the contact angles could not be measured; it was reasonably assumed that they were below 5^{o} and this value was used for plotting purposes. The UV-ozone stripping appears to affect the surfaces in a similar manner, showing that a clean surface of most probably oxidic nature is reached after two hours photo-chemical treatment. After silanization, a water contact angle in the low 50^{o} is obtained, as expected from previous experiments. The substrates comprising nano-pillars on a platinum film stand out through the elevated contact angle, as shown in **Figure II.3.14** for all the three types of surface geometry (the two continuous film controls and the nano-pillar geometry). While this might be explained for the nano-pillars on platinum and the bare platinum surface respectively (Control 1), the elevated contact angle is an indicative of a certain degree of chemical heterogeneity that complements the ordered surface topography (Yoshimitsu et al. 2002). The reason for the over 70^{o} contact angle on the Control 2 surface is not very obvious, despite being sealed by a 110 nm thick silicon oxide layer.

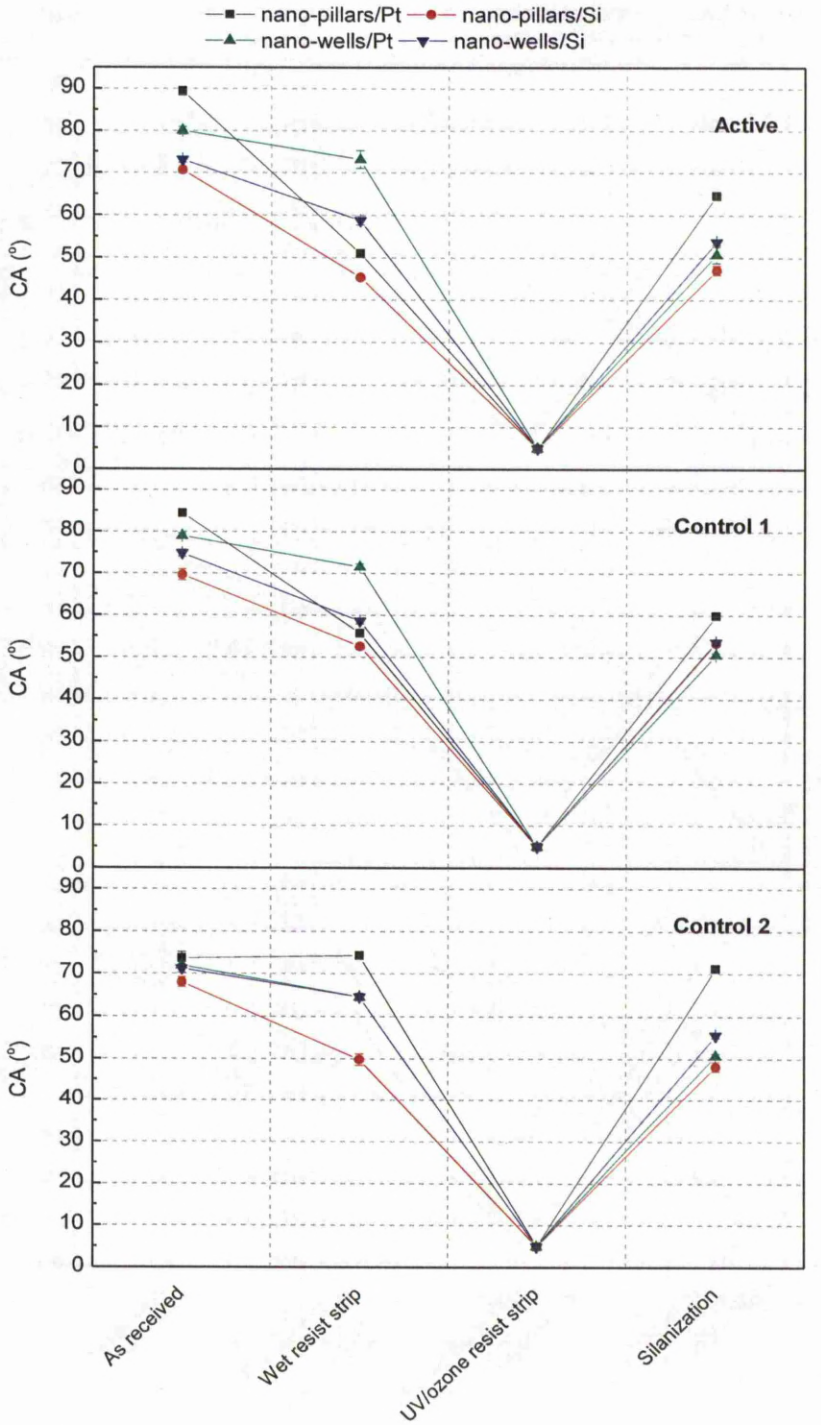

Figure II.3.14. Water contact angle measured on the micro-fabricated substrates as a function of surface treatment; the legend denotes the substrate type (Figure II.3.2) and the title in each panel denotes the region on each substrate

The contact angle variation with processing stage was also plotted to illustrate a comparison between different surface geometries on the same slide, that is, to compare primarily the active and control areas from the same (microfabricated) slide and is available in **Figure II.3.15**. Again, a general trend exists and the data

correlates well both intra and in between slides. The substrates comprising a silicon reflector, and the substrate where the platinum reflector is sealed by a thick layer of silicon oxide (nano-wells on platinum **Figure II.3.2 b**) appear to be more consistent, with less dispersed water contact angle values. The substrate comprising the platinum reflector and no insulating oxide layer (nano-pillars on platinum) retains the unexplained behaviour in terms of contact angle value dispersion for the silanised surface (top left panel, **Figure II.3.15**), and, additionally, these values (**Figure II.3.15, top left**) are consistently higher than those of the other substrates. Again, while an increased hydrophobicity on the silicon oxide nano-pillar covered platinum surface might be expected (for instance, an effect of the pillars compounded by some surface property of the Pt), the controls surfaces should not be affected (as these are simply flat areas). This does not seem to be the case since the contact angle on the Control 1 surface is smaller than that of the active surface (but still high) while that of the Control 2 surface is higher, both in absolute terms and relative to that measured on the structured active surface.

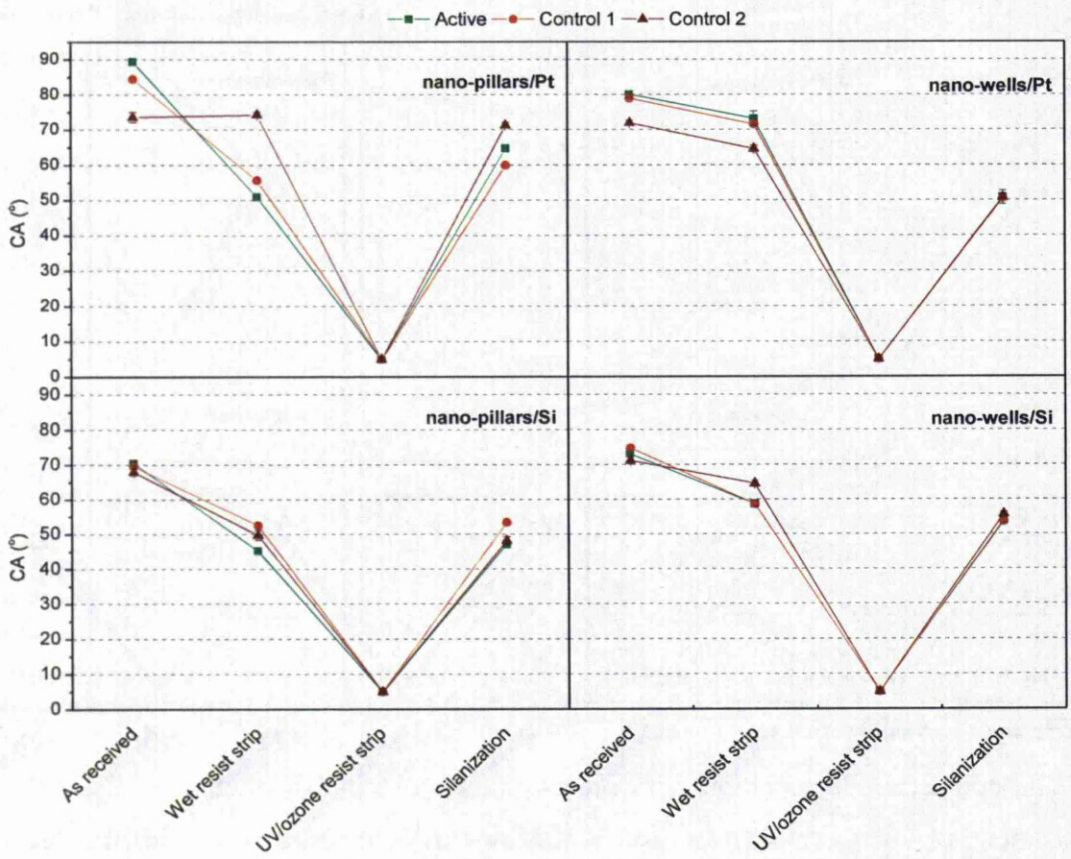

Figure II.3.15. Water contact angle measured on micro-fabricated substrates versus surface treatment; each panel contains contact angle values from the three regions of the same substrate

Contact angles of water on the commercial Nexterion E and Nexterion HiSense E slides from Schott were also measured and are available in **Table II-7**. The results of these measurements show that the surface of the commercial slides is slightly more hydrophilic than the surfaces of the in-house silanized substrates (values in **Table II-6 last row** versus values in **Table II-7**). The reason for this is not clear, as it can arise from two sources. One potential reason for a decreased water contact angle can be related to the density of the surface epoxy groups. Indeed, as it was shown previously, exposing a substrate to different concentrations of silanizing agent can result in differences in water contact angle and this can be attributed to the surface silane density. Also, the chemical structure of the epoxy-silanization reagent might play a role in the hydrophilic character of the surface. That is to say that in-house silanised substrates were surface activated with one specific silane (i.e. GPTES) but an epoxy-silane with a different chemical structure could have been used for the commercial slides. Regardless of the reason(s), the increased surface hydrophilicity appears to affect the liquid transfer process (printing) as will be shown later in this chapter.

Table II-7. Water contact angle measured on commercial substrates

Slide	Water contact angle (°)
Nexterion E	41.38±0.54
Nexterion HiSense E	40.88±0.79

II.3.4.4 Microarray-type experiments

The testing of the new substrates was carried out in a comparative, relative way, versus the commercially available ones, rather than in absolute terms. One reason why relative testing was chosen is that microarray experiments are very complex, their performance being linked to a variety of factors: probe printing density, probe concentration, probe delivery, printing solution, incubation time, temperature and humidity control, post-printing washing, surface blocking and the list can continue (not to mention the initial surface chemistry optimization which, although attempted here, was done in a brief manner). Therefore, assessment of absolute performance is difficult and tedious and it is outside the scope of this contribution.

Figure II.3.16 shows fluorescent micrographs (as obtained via a Genepix 4000B microarray scanner) of the seven substrates that were initially considered: in-house

functionalized microarray grade glass, the two types of epoxy-slides from Schott and the four types of microfabricated substrates, as described previously in **Figure II.3.2.** All substrates present a fluorescent grid-like structure due to the residual adhesive from the silicone dividers but this does not interfere with the analysis in any way. Further, the dividers partition the surface of the slides into 64 equal areas, divided further into sixteen columns and four rows. The target concentration was varied along across rows, from 1 μM to 1.164 fM (decreasing from left to right in **Figure II.3.16**). Along a column, the target concentration was kept constant, i.e. the four rows are replicates of each other. Out of the three commercial substrates, the HiSense slide is clearly the best performing one, with a visibly less intense background and more consistent spot shape, followed by the Nexterion E, while the in-house silanised slide is clearly outperformed. As a result, the two commercial products from Schott were retained for further analysis.

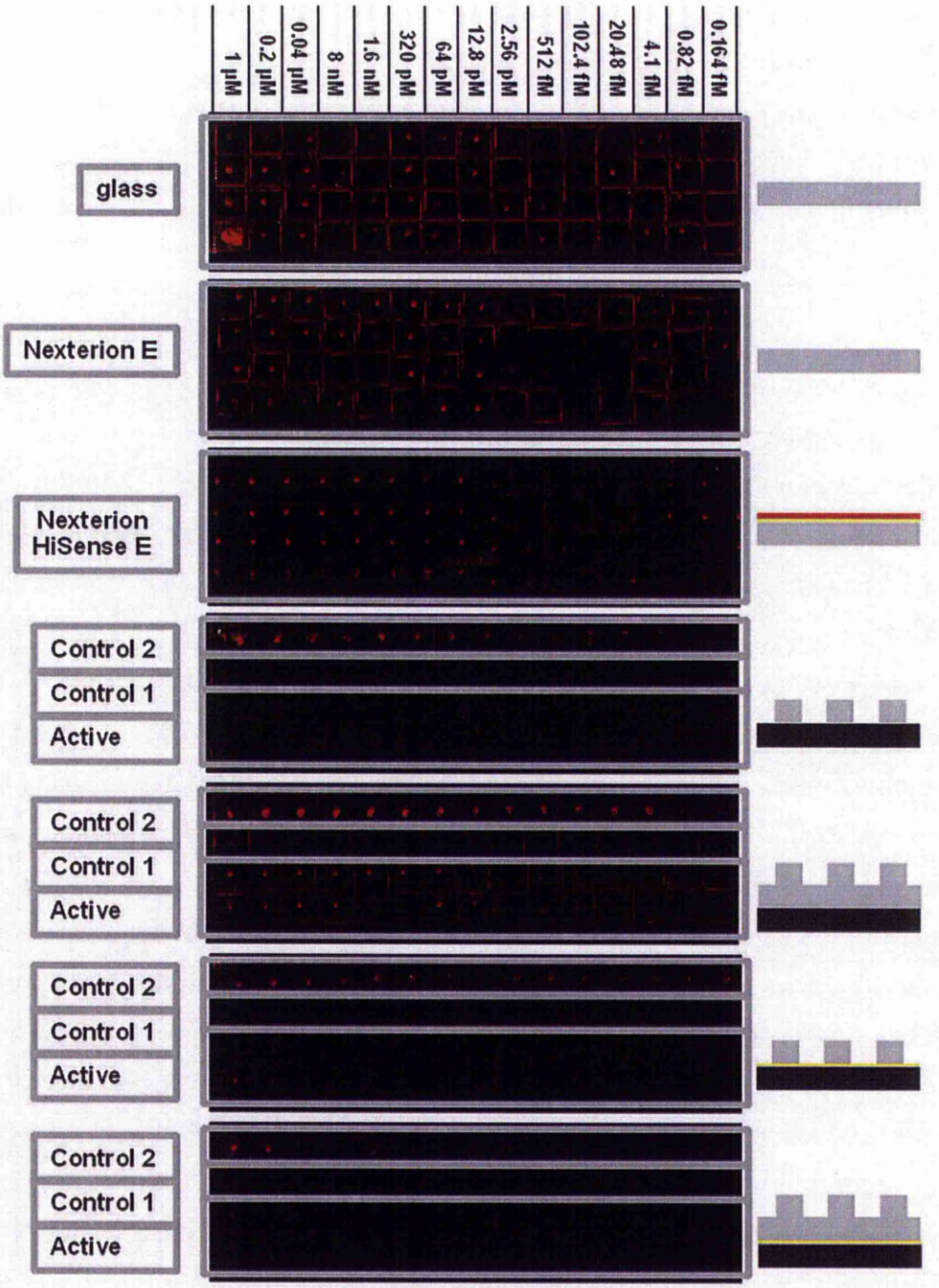

Figure II.3.16. Fluorescence micrographs showing hybridization of the different substrates under test and the corresponding geometries of their active regions (gray signifies optically transparent medium, orange signifies metal reflector and dark grey is used for silicon). Every red dot represents fluorescent emission from the target after hybridization to the surface-bound capture probe. Target concentration is shown at the top

The microfabricated substrates are partitioned into three domains: the structured bottom half, the first control ("zero" height) surface occupying a quarter of the slide area in the middle and finally the second control at the top comprising an oxide film with a thickness sufficient for providing close to maximum amplification (as

illustrated in **Figure II.3.2**). A direct visual comparison between the two commercial epoxy-slides and the two control surfaces on the micro-fabricated slides is available in **Figure II.3.17** and **Figure II.3.18** and together with a target concentration scale on the left hand side. The strips corresponding to each commercial substrate were obtained by cropping one spot area from each column, based on a visual quality assessment.

Firstly, the flat areas on the micro-fabricated slides can be compared to the commercial slides from Schott as shown in **Figure II.3.17**. The flat areas, as described earlier, consist of an oxide film whose thickness is chosen so that it leads to the formation of destructive interference (silicon native oxide next to the silicon oxide pillars on silicon and 220 nm thick oxide next to the nano-wells on silicon, native platinum oxide next to the nano-pillars on platinum and 220 nm thick silicon oxide next to the nano-wells on platinum). The other type of flat area can be considered as the "continuous" film version of the structured surfaces (conversely, the structured films can be considered "discontinuous" films). These films provide maximum enhancement. Comparing the performance of the latter to that on the commercial slides, the most striking difference lies in the spot morphology rather than in the intensity of the features. Naturally, since the features were printed manually, some degree of irregularity is expected but this should be (and is) visible on the commercial slides as well. To illustrate this, one can see double-printed features, where the pin has moved slightly on the surface (appearing as a round relatively well defined spot inside an irregular pattern) or the appearance of two intersecting circles with a relatively low fluorescence while the result of this intersection is brightly fluorescent. This is most certainly due to the manual printing. An encouraging aspect is that the micro-structures were not damaged though after contact with the printing pins. Apart from this, an obvious reason for the lowered regularity of the printed features can be assigned to the liquid delivery process.

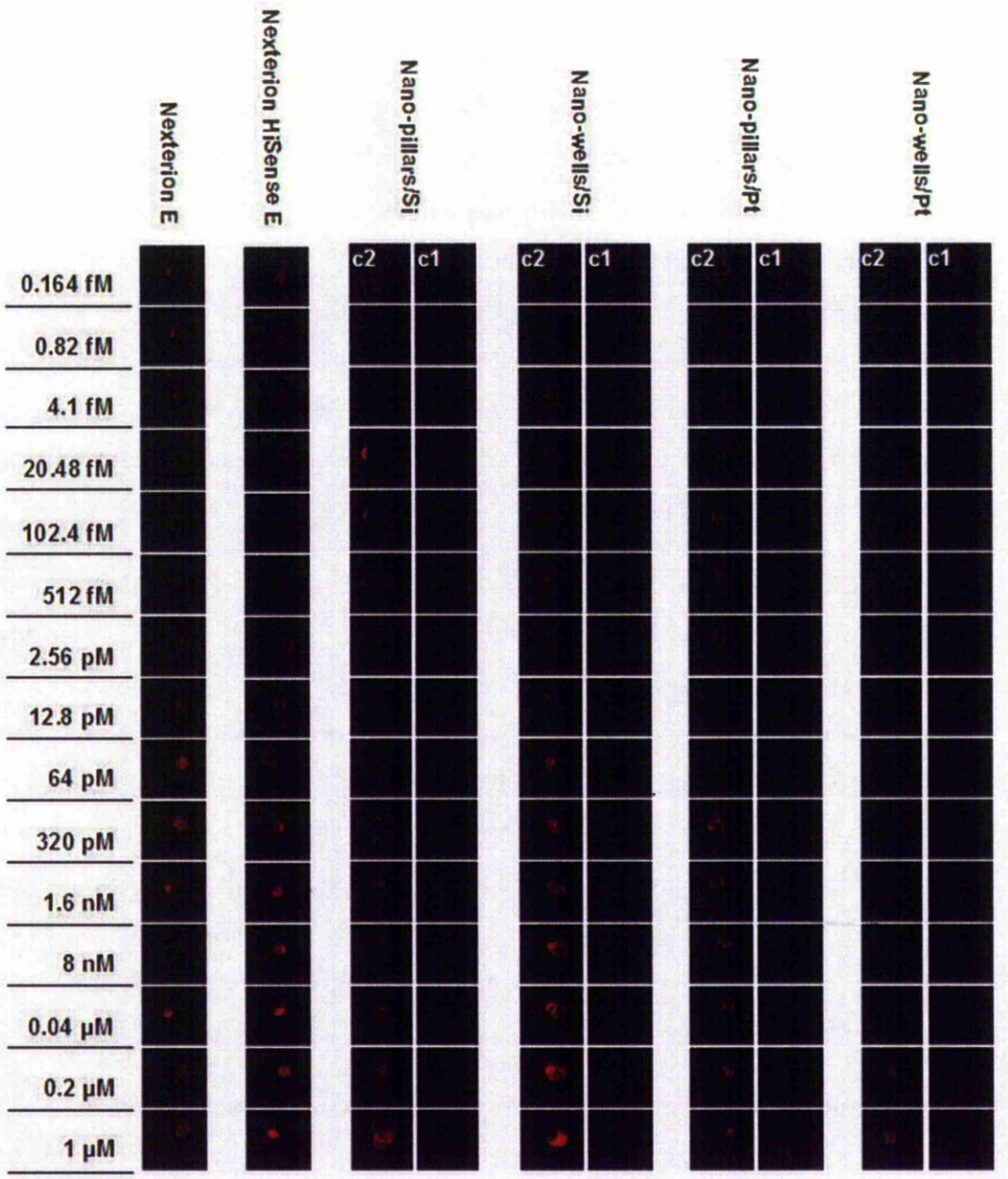

Figure II.3.17. Detail of features (fluorescence micrographs) analysed on flat (Control 1 - c1 and Control 2 - c2 respectively) substrates (spots on commercial slides are shown for comparison

With a split-tip pin configuration, the liquid is absorbed into the reservoir through capillarity. The liquid is held inside the reservoir due to a balance between gravity on the one hand and cohesive (inside the liquid) and adhesive (between the liquid and the walls) forces on the other. When the pin is brought into contact with the surface, considering that inertia does not play a role (i.e. that the pin does not travel at relatively high velocity and experiences a sudden stop) liquid transfer occurs when the sum between adhesive forces between the liquid and the surface to be printed and the weight of the liquid (gravitational force) will be higher than the sum of the

cohesive and adhesive forces experienced by the liquid inside the reservoir. The adhesion between the printing solution (buffered aqueous solution, therefore hydrophilic) and the surface is better for the commercial slides than for the microfabricated ones, as illustrated by the difference in water contact angle between the two types of slides (see Table **II-6** and **Table II-7**). As mentioned earlier, this difference cannot be pin-pointed as it can arise from differences in the silanization process (time, silane concentration, whether performed in a liquid or gas phase and so on) or even the structure of the silane itself. In terms of fluorescence intensity, the microfabricated slides seem to display comparable levels, with the silicon reflector based slides appearing to be the best options. However, the actual performance can only be estimated from the results of the numerical processing.

Another interesting aspect that can be extracted from figure **Figure II.3.17** is the appearance of low intensity fluorescent features on the Control 1 area (220 nm thick silicon oxide) on the substrate comprising nano-wells. The oxide thickness in this area was chosen to provide (close to) maximum destructive interference and consequently, no fluorescent features should be visible. In this particular case however, such features are visible (**Figure II.3.17**) and this can be attributed to errors in the fabrication process leading to a film thickness that deviates slightly from the theoretical one. It is not very clear whether the difference between the theoretical and practical oxide thicknesses is constant or the height varies but the first scenario seems more plausible.

Further, morphology of the spots printed on the structured ("active") areas on the microfabricated slides is compared to that of spots printed on the commercial slides as depicted in **Figure II.3.18**. Visually, the features printed on the active areas within the microfabricated slides appear to be very irregular in terms of morphology by comparison to the ones printed on the commercial slides. This can be attributed to less optimal liquid transfer, as was the case with the flat continuous control surface described previously and furthermore likely affected by the surface topography.

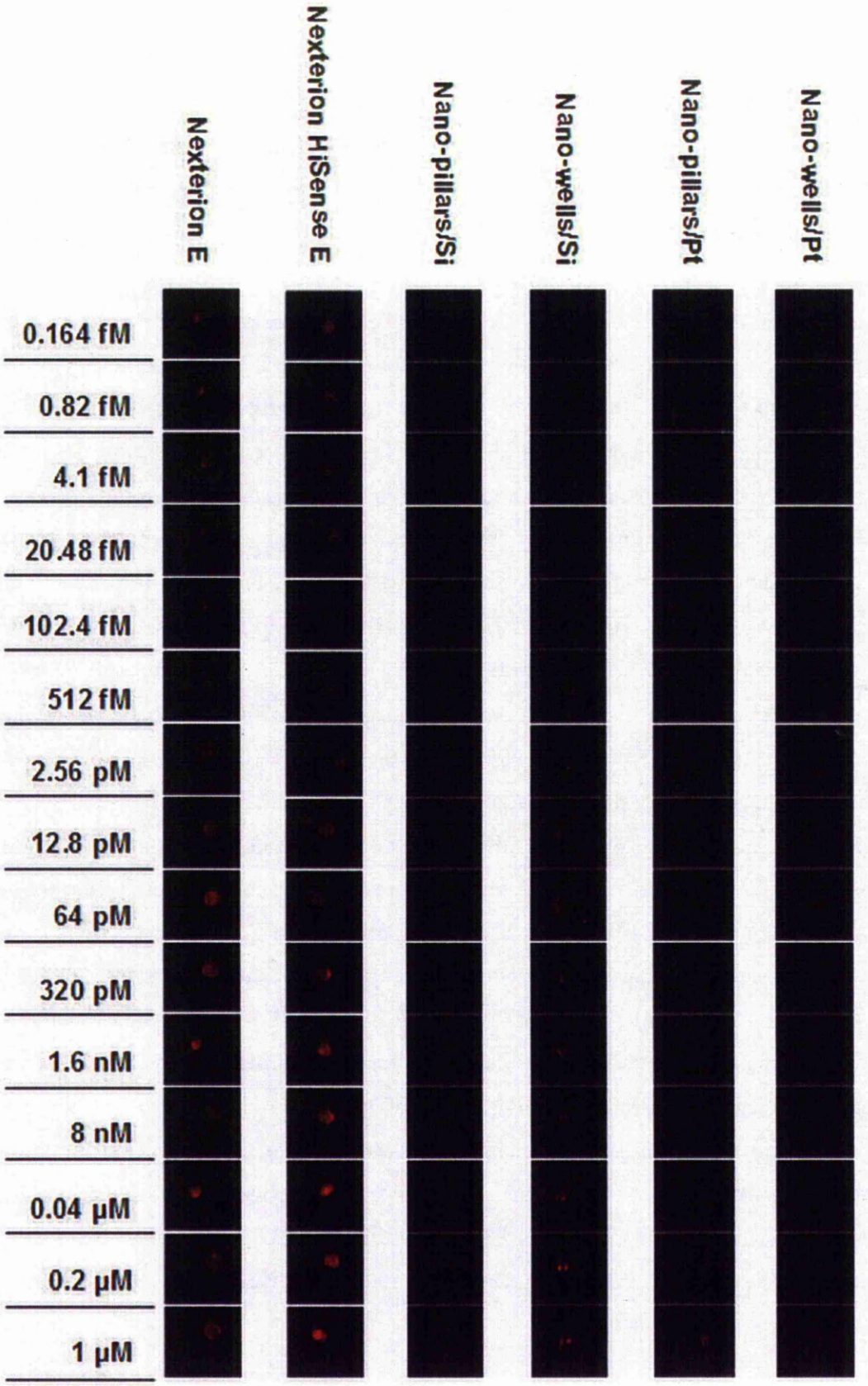

Figure II.3.18. Detail of features (fluorescence micrographs) analysed on structured substrates (spots on commercial slides are shown for comparison)

II.3.4.5 Image processing

The procedure that was used to extract the quality data was described in the experimental section but deserves a more in depth description. The procedure applied for the spots printed on the flat substrates was simple, based on a simple thresholding to separate the region of interest into foreground, i.e. the spot, and background. For the structured substrates however, the same type of thresholding was applied initially to ensure minimal-biased identification of the area where the sub-spots are. Further, a selection comprising a 3 x 3 array of 6 x 6 pixels is superimposed on a set of 9 sub-spots. The selection is enlarged by one pixel, as shown in **Figure II.3.19**, and then reversed to obtain the local background. The reason for the one pixel dilation of the selection is the elimination of edge pixels which carry a certain degree of uncertainty. Unfortunately, the appearance of this area of uncertainty was not foreseen when designing the slides so data skewing due the edge pixels was eliminated by discarding the one pixel-wide area around each sub-spot (the method is commonly used in microarray data analysis; see discussion about segmentation and quantification in **I.1.5 Spot quality metrics** and **Comparison with classical substrates**; also, see the discussion about the variation of the proportion of edge pixels in **II.1.4.1 Optical interference effects and data fitting**). Nevertheless, future design will take this into account a necessary changes will be made. Because reference was made to previously described work, one can notice that the algorithm used here differs slightly from the one used previously in that bandpass filtering was not used (see **II.1.3.3 Fluorescence imaging and image processing**). The reason is that previously, images were acquired using a confocal microscope which is particularly sensitive to variations in sample tilt. These variations lead to uneven thresholding across the sample and they can be eliminated by correcting for background intensity variations. For non-confocal instruments, this is not necessary since they acquire light from a much thicker volume. Also, some practical limitations played a role here: the sample size, the need to use double-sided adhesive tape etc. For SNR measurements, another measurement for the background was also used but this will be detailed in the section discussing the SNR.

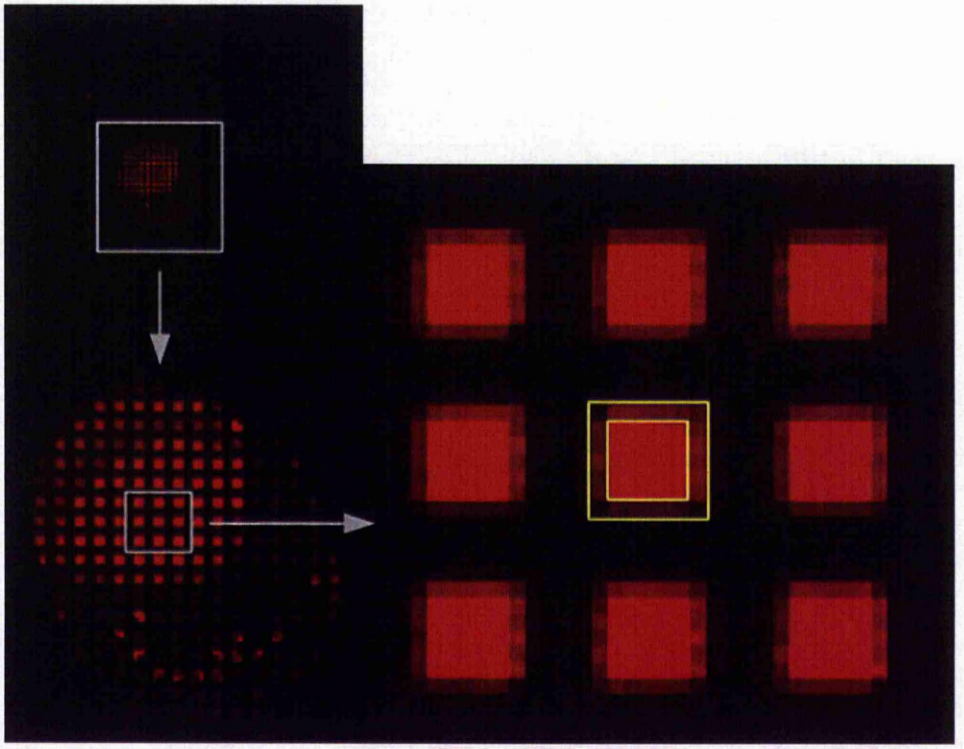

Figure II.3.19. Typical spot printed on structured area (top left) and detail (bottom left) together with a selection array (right) showing the area of uncertainty around one sub-spot (between yellow boundaries)

Because the choice of where to place the 3 x 3 array is left to the human element, at least at this stage there might appear that the data is biased (in the future, an automated procedure will hopefully be developed). Therefore, additional qualifications are warranted. Firstly, the determination of the area where the sub-spots are located is done without human interference. Moreover, the same algorithm is applied to the features printed on the flat control areas and the commercial slides. So the choice of where to place the selection array is limited to an area identified in a manner which limits human interference.

Secondly, within the area identified via thresholding, square sub-spots exist on the boundary. These sub-spots are excluded through human decision but again this does not mean that the process is biased. One of the concepts supporting the slide design is based on the idea that, when it comes to automated segmentation, the algorithm used needs to accurately identify objects which, unfortunately, display a certain degree of shape and size variation. Since this process needs to be automated to fully exploit the advantages brought by multiplexing, human intervention is not a viable option. The substrate architecture proposed here addresses this issue by "forcing" spots (sub-spots here) to take a standard (known) shape and (known) size, based on

the principle that it is computationally less complex to automatically identify features whose size and shape are known *a priori*. Within this framework, it is only natural that sub-spots with shapes different from the expected one (square) are excluded (although, at this stage, the process is manual).

Thirdly, only a set of sub-spots is chosen and not all the sub-spots that qualify through their shape and size and this could also be interpreted as a human bias. There are a number of reasons for this. The simplest one is related to time constraints and/or the lack of automation. Another reason is that these slides were designed to offer the possibility of "recovering" what would seem like a sub-par spot. In current microarray technology spots are assigned quality scores based on various descriptors (Wang et al. 2001). These scores are then used to eliminate or minimize variability in a process called normalization. The confidence that is placed in the information resulting from a certain spot can therefore decrease as a result and, moreover, data can be discarded altogether because of low spot quality. The approach presented here would allow for the "recovery" of bad spots by dividing them into smaller elements that are, individually, less likely to suffer from the shortcomings of the whole.

Finally, the use of an array-type selection aims to reduce human bias. An arbitrary number of sub-spots form the selection. The choice of number is not important, as long as it delivers a statistically sufficient number of pixels (9 sub-spots x 30 pixels/sub-spot = 270 pixels in this case). The number of pixels per spot deemed statistically acceptable in the microarray literature caries between a minimum of 25 (Dufva 2005) or, generally, a pixels size of a tenth of the spot diameter (Schena 2003b). The important aspect however is that the sub-spots are linked inside the array selection. That is, even if the positioning of the selection is biased with regards to one or two sub-spots (and even this assessment is on a visual basis), the array contains 9 elements and it is therefore difficult if not impossible to purposely choose the best ones, let alone all of them fitting in the array.

II.3.4.6 Spot uniformity

Measures used to quantify the data resulting from each spot (whether mean, median, mode etc.) do not offer any information about the spatial intensity distribution inside the spot. Moreover, non-uniform spots can lead to data quality degradation and consequently low confidence and even to "legitimate" spots being completely

discarded in the process of data normalization. This process aims to account for and eliminate differences between data from different spots, leaving only the ones that can be correlated to the extent of the bio-molecular recognition. One of the normalizing elements is the spot intensity uniformity and, following the route proposed by (Moran-Mirabal et al. 2007), is the percentage standard deviation (PSD), given by the percent ratio of intra-spot standard deviation to intra-spot mean intensity. This figure of merit was used as a measure of uniformity. First the PSD of the spots printed on the flat, continuous areas that provide maximum constructive interference was measured together with the PSD of the spots printed on the commercial slides. The two are plotted alongside in **Figure II.3.20** to make comparison easier.

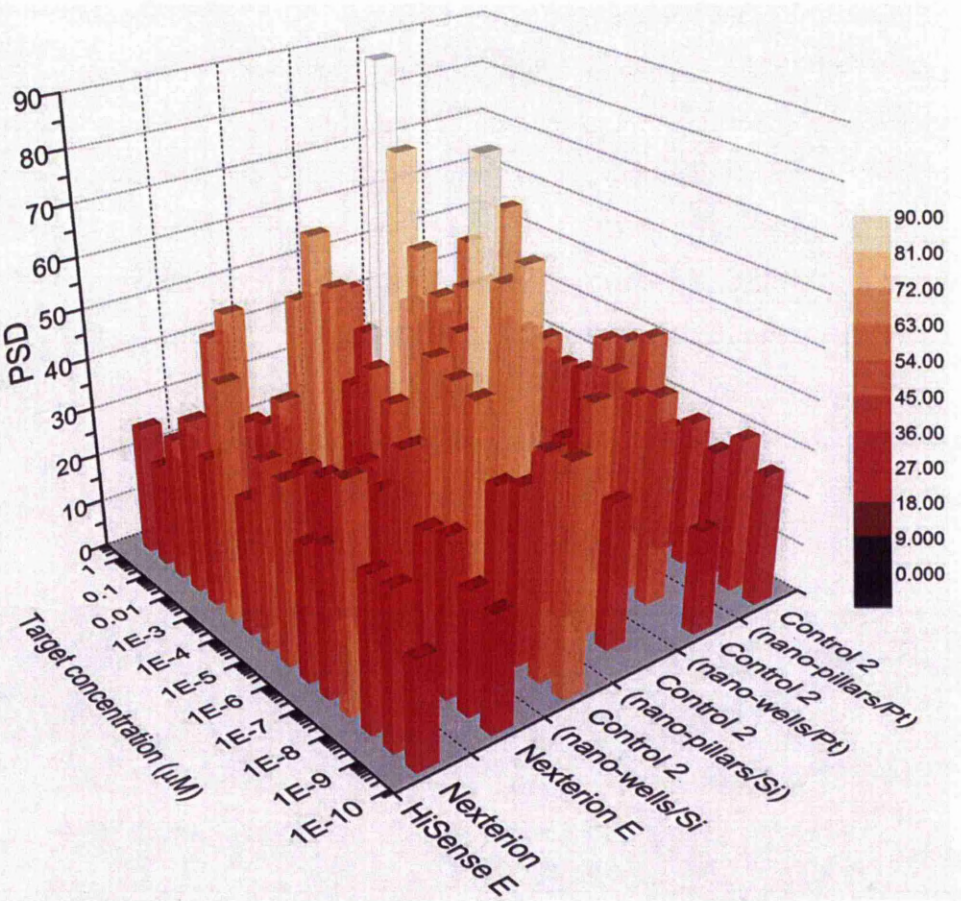

Figure II.3.20. Intra-feature uniformity versus target concentration for spots printed on flat continuous areas as compared to spots printed on commercial substrates

It can be seen that the uniformity measured on the flat control 2 areas (**Figure II.3.20**) are either similar or higher than those measured on the commercial slides. Given the water contact angles measured previously and the other elements that have

potential to influence liquid transfer that have been discussed earlier, this result is expected. The values of the PSD on the flat areas of the micro-fabricated slides are higher but comparable to those measured on the commercial slides.

Further, the PSD measured on the structured substrates show a marked improvement relative to the standard, commercial slides. To illustrate this, in **Figure II.3.21**, spots that were printed on the commercial slide with an optical coating and the four structured substrates respectively are shown in false colour. This allows for a better visualization of the fluorescence distribution inside each spot. Also, the spots are shown before and after the application of the Otsu thresholding algorithm. From this perspective, one can clearly see that the algorithm is "fooled" by the wide dispersion of fluorescence intensity values in the case of the spot printed on the commercial slide. This results in the spot being truncated. On the structured slides, this truncation takes place only when a nano-well/Si architecture was used. At the same time, it is easily discernible that the spot printed on the substrate based on this architecture is actually the result of double contact between the pin and the substrate. It can therefore be treated as an artefact. However, even in this case, the fluorescence dispersion inside the area identified by thresholding is lower than that inside the spot printed on the commercial substrate. On the other three substrates (i.e. the ones comprising nano-pillars/Si, nano-pillars/Pt and nano-wells/Pt respectively) there are two main characteristics easily discernible: high intra-spot uniformity and poor circularity. An explanation for the latter has been supplied previously as being a result of manual printing coupled with a possible reduced wetting effect.

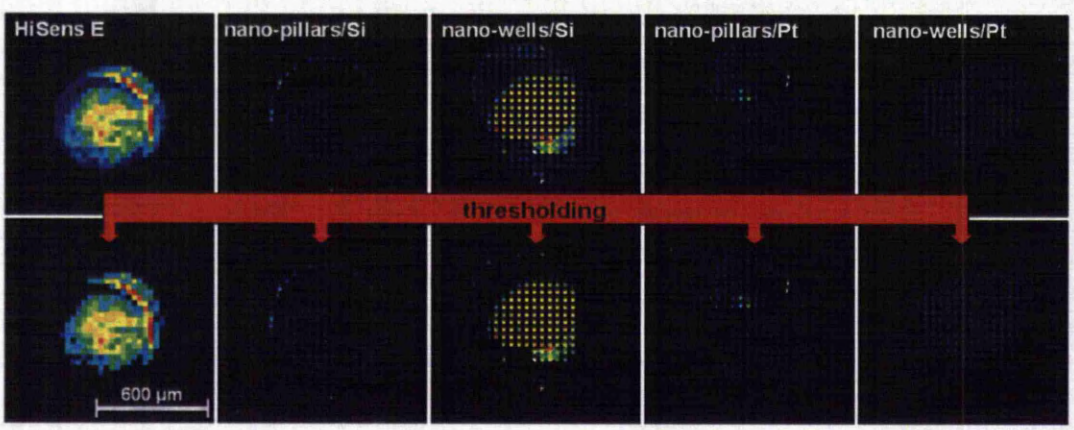

Figure II.3.21. False colour figure showing spots printed on structured substrates along one spot printed on a Schott Nexterion HiSens E. The native spots are shown on the top row and the result of the Otsu thresholding algorithm. The false colour helps to illustrate the differences in fluorescence intensity uniformity (the target concentration is 1.6 nM)

Generally, the sub-spot arrays generated by the structured substrates outperform the commercial slides in terms of uniformity. A comparison that conveys this is the one shown in **Figure II.3.22**. The values of the PSD are illustrated using colour-mapped bars. The lower PSD values are characteristic of the spots printed on structured substrates. The differences in PSD between the structured and commercial substrates are not massive and the significance of these differences is analysed in the following.

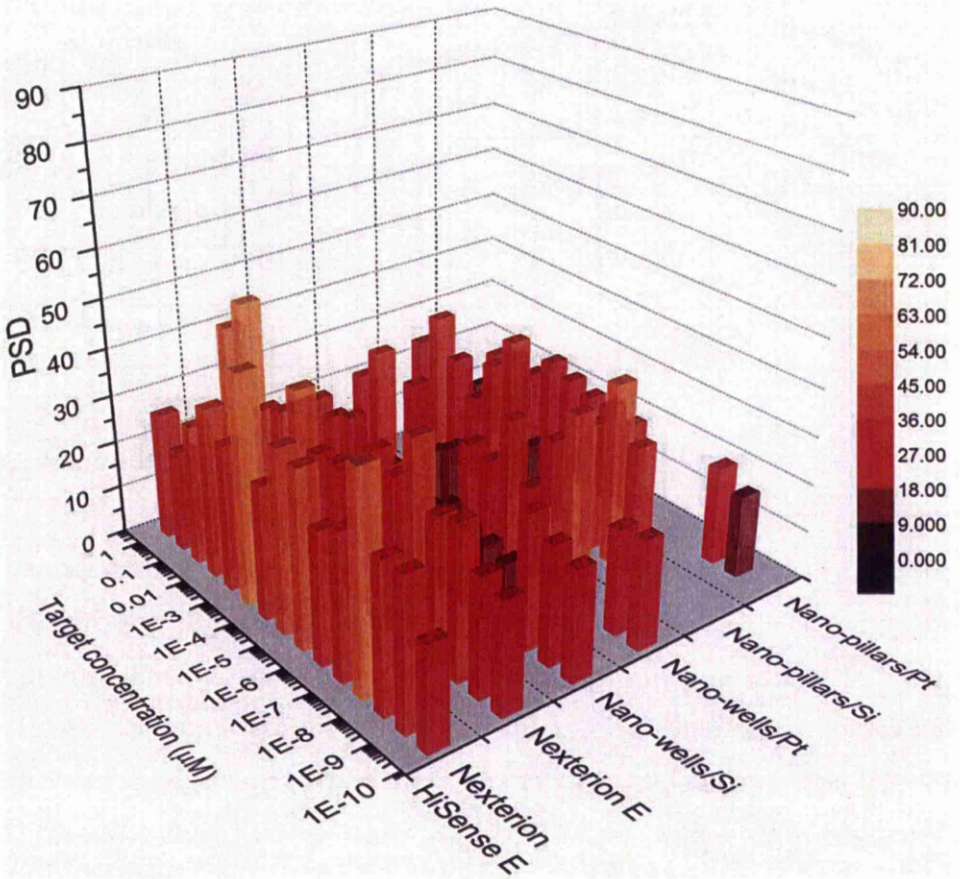

Figure II.3.22. Intra-feature uniformity versus target concentration for spots printed on structured areas as compared to spots printed on commercial substrates

For a better, more adequate comparison, the uniformities measured on both the structured and the continuous control areas on the microfabricated substrates were sequentially paired with those measured on the commercial slides and a paired t-test was used to asses whether the differences are significant and whether the performance of the structured substrates is actually better than that of the commercial slides. The results are shown in in **Table II-8.** . The same null hypothesis was chosen for both comparisons, that is, the PSD values are not different between the microfabricated substrates and the commercial slides. The alternate hypothesis for

the comparison between continuous films and commercial slides was that a difference exists while for the structured substrates, that the PSD's are smaller than those measured on the commercial slides.

Table II-8. Results of paired t-tests performed between the PSD measured on the different test substrates and the PSD measured on the different structured substrates and that measured on the commercial slides

SiO_2/Si		SiO_2/Pt			
nano-pillars	**nano-wells**	**nano-pillars**	**nano-wells**		
x	<	<	=	**nano-pillars**	**SiO_2/Si**
>	x	=	>	**nano-wells**	
>	=	x	>	**nano-pillars**	**SiO_2/Pt**
=	<	<	x	**nano-wells**	
<	<	<	<	**Nexterion E**	
<	<	<	<	**Nexterion HiSense E**	

The results of the t-test confirm the initial findings that structured substrates do significantly improve the uniformity while the uniformity of spots printed on the control areas is comparable or lower than that of the spots printed on commercial slides tested. The exact mechanism that leads to improved uniformity on the structured substrates is, in the absence of experimental proof, a matter of speculation. However, a possible contribution to this can stem from the simple fact that, because what would be a regular spot now consists of an array of smaller areas, variability on small ranges is less pronounced. Another possible explanation would be the mitigation of drying effects through the formation of micro-droplets, each resting on a single pillar or inside an individual micro-well and allowing thus independent droplet to droplet behaviour through micro-confinement. Another important aspect is related to the ability to isolate "bad spots" in the first place, thanks to the known size and shape, and disregard their contribution (for instance, edge sub-spots that were incompletely wetted by the liquid). A further enhancement in performance is foreseen by better matching the structure size with the scan resolution to eliminate the effect of edge pixels.

II.3.4.7 Signal-to-noise ratio

Signal to noise ratio (SNR) is a measure of how well a signal can be de-convoluted, or separated from the accompanying background noise. A minimum value of 3 is generally used as a benchmark for confidently detecting a certain signal. The theory and calculation of the SNR were discussed previously. Also previously, we used the SNR as a measure of local contrast rather than its classical meaning due to the fact that our estimation of SNR was taking into account the local background, that is, the immediate vicinity of the structures. Technically speaking, this is not correct, as the use of the area outside the spot as an estimate for the so-called background, in theory, no longer accurately represents the behaviour of the surface in the absence of the capture probe. The concept of SNR and the ability to estimate it is based on the assumption that background contribution can be extracted from the vicinity of the spot, where no capture probe has been attached, since one never knows a priori what constitutes signal and what constitutes noise.

For the structured substrates, this SNR concept is less clear, since it is obvious that the local background is possibly artificially lowered due to optical interference effects. On the other hand, having shown previously that the presence of an oxide film leads to a decrease in fluorescence, probably due to non-unity transmittance, would also misrepresent the true background contribution. This is why the SNR was calculated in three different ways, with the background component being extracted from the local vicinity of the structures, from the actual structures but outside the printed area and finally from the continuous film "control 2" areas.

First, the SNR was calculated considering the local background. These values were plotted alongside those measured on commercial slides to benchmark the measurements and are illustrated in **Figure II.3.23**; for comparison purposes, the SNR of spots printed on the "control 2" areas were plotted in the same way in **Figure II.3.24**.

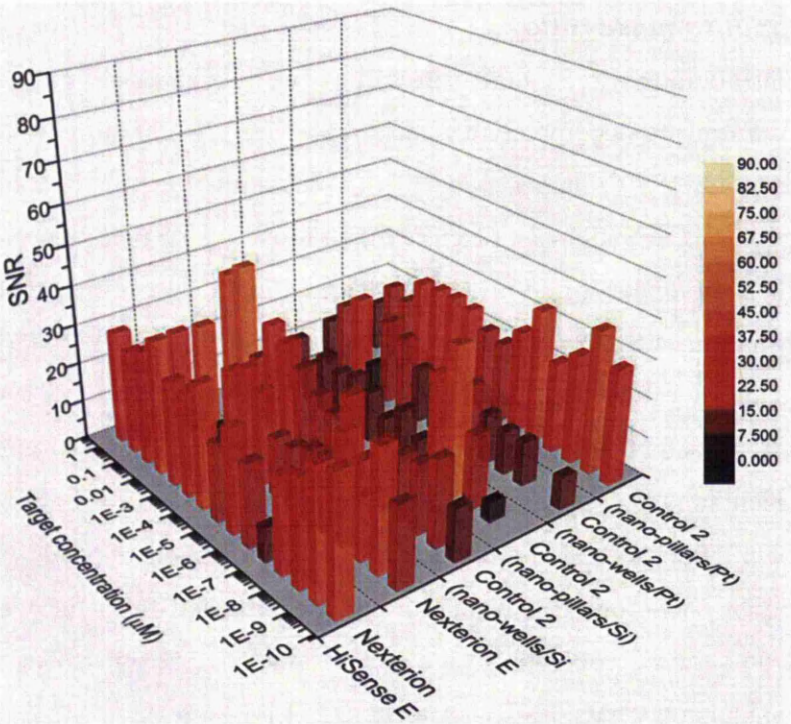

Figure II.3.23. SNR as a function of target concentration for the four substrate architecture, for spots printed on flat areas and commercial substrates as comparison

The comparisons show that for the spots printed on flat areas, the SNR is lower but comparable to that of spots printed on commercial substrates (**Figure II.3.23**).

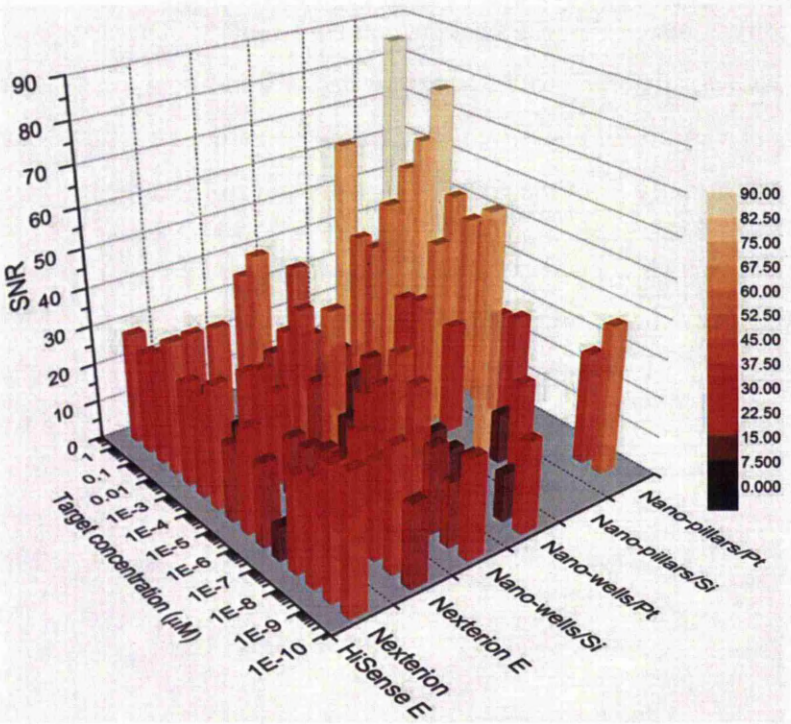

Figure II.3.24. SNR plotted against target concentration for spots printed on the structured areas of the substrates and spots printed on commercial slides as a benchmark

The same can be said about the features printed on structured substrates, when the differences in favour of the commercial slides blur out, with the structured substrates even taking the lead as can be seen in **Figure II.3.24**. The relationship between these values can be further analysed using t-test (as was done when the PSD values were compared). The results are illustrated in **Table II-9**. The analysis shows allows for comparison both between the SNR values obtained on structured substrates and those obtained on the commercial ones and also comparison between the structured substrates themselves. The comparison between structured and commercial flat substrates shows that the test prototypes are, on the whole, comparable to the commercial slides. It can be seen that, for instance, the nano-well on Pt architecture is not as well performing as the others but finding an explanation for this would require levels of fabrication accuracy that were not attainable for these prototypes. Also, differences in SNR are evident between the four structured architectures. Again, to correctly assign these differences to substrate characteristics (e.g. wetting, reflectivity), one would need to make sure that the geometrical parameters are perfectly identical. In the case of these prototypes, there is slight variation in parameters such as, for instance, the film thickness or film thickness uniformity so the source of the observed differences in performance cannot be correctly attributed at this time.

Table II-9. Results of paired t-tests performed between the SNR measured on the different test substrates and the SNR measured on the different structured substrates and that measured on the commercial slides

SiO_2/Si		SiO_2/Pt			
nano-pillars	**nano-wells**	**nano-pillars**	**nano-wells**		
x	<	=	<	**nano-pillars**	**SiO_2/Si**
>	x	>	=	**nano-wells**	
=	<	x	<	**nano-pillars**	**SiO_2/Pt**
>	>	>	x	**nano-wells**	
>	>	>	<	**Nexterion E**	
>	=	>	<	**Nexterion HiSense E**	

To gain some insight into the workings of the SNR and whether calculating the SNR using the local background under- or over-estimates the "true" value, alternate SNR's were extracted using as an estimate for background contribution the background from the corresponding spots printed on the "control 2" areas and the intensity and standard deviation measured over a 3 x 3 array of pillars and wells from outside the area where the capture probe was printed, respectively. A very similar method of printing "blank" spots has been proposed previously for microarrays printed on flat substrates to better estimate the background and, consequently, the SNR (Cagnazzo et al. 2006). The results are plotted in **Figure II.3.25**.

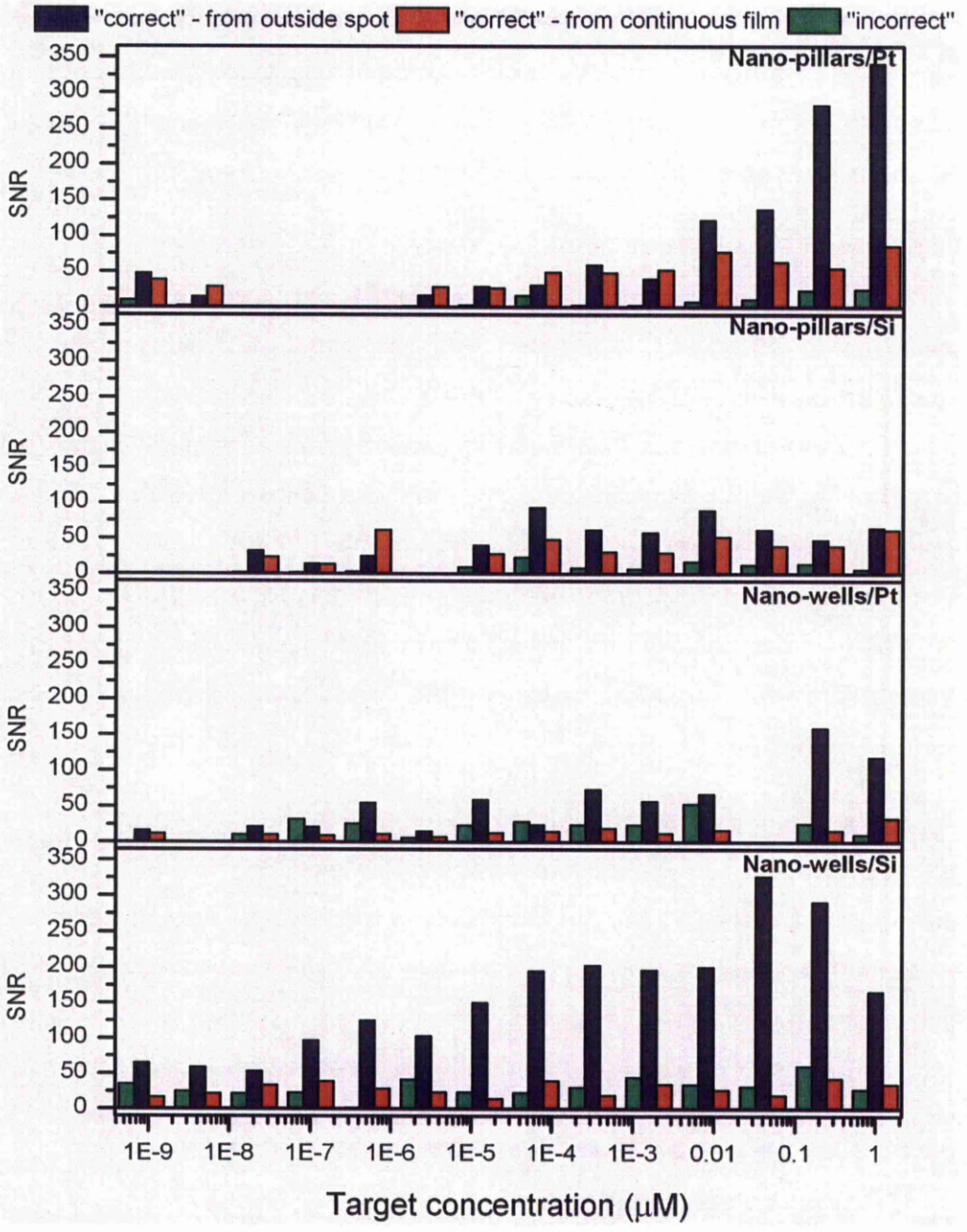

Figure II.3.25. SNR as a function of target concentration for the four different substrate architectures. The SNR is calculated for three different background contributions

As it can be seen in **Figure II.3.25**, the three ways of calculating the SNR yield quite different results. The highest, by far, SNR is obtained if one uses the intensity and standard deviation value acquired over 9 structuring elements that, while belonging to the same vicinity, are located outside the area where the capture probe has been printed. Using as an estimate for background contribution the local background and the background measured on the complementary flat surface respectively does appear to produce more similar results. The differences between SNR's calculated

using the three methods are significant but the solution to this problem is not yet accessible. Nevertheless, using the local background to calculate the SNR purely as a measure of contrast, i.e. how well features stand out and, consequently, a measure of fluorescence confinement.

II.3.5 Summary and conclusions

Four prototype slides were designed, fabricated and tested for their potential application as substrates for multiplexed bio-recognition devices using fluorescent detection. The design of the prototypes was based on the results of experiments reported in chapters **1** and **2** of **part II**, both in terms of surface chemistry and geometry. The aim was to fabricate a slide that was compatible with existing read-out technology. The procedure included optimization of the surface chemistry by screening a series of deposition conditions. The prototypes were tested by carrying out DNA hybridization experiments and analysing the results with respects to intra-spot uniformity (as measured using the PSD) and fluorescence confinement (as measured through the SNR).

The design of the new slides included the integration of three types of areas onto each of them: 50% of the slide area comprises a structured silicon oxide film with either pillars or wells; 25 % of the substrate area comprises a "zero"-thickness native oxide; the remaining area of the slide is covered by another control comprising a thick silicon oxide layer. The structured area is the active area which is the main element of focus. To make up the optical system described in the previous chapters, two similar but non-equivalent, complementary architectures were pursued: pillars and wells. The control areas, covering the other half of each substrate mimic the structure of the neighbouring active area. Thus, the areas called Control 1 induce the formation of destructive interference and the ones called Control 2 induce the formation of constructive interference. The oxide film covering the control areas is flat and continuous.

Preliminary experiments aimed at optimizing the surface chemical activation procedure with epoxy groups using water contact angle measurements, atomic force microscopy in both topographical and phase contrast and fluorescence measurements using fluorescently labelled BSA as a fluorescent probe. Liquid phase deposition was optimized in terms of initial silane concentration which was found to be best at 2%

for a deposition time of 2 hours. The chemical processing was applied to the micro-fabricated slides.

Two figures of merit were used to characterize the performance of the substrates as compared to commercial substrates (one made of special grade glass and the other integrating a special optical layer): uniformity of printed spots and signal-to-noise ratio. It was found that the structured substrates outperform the flat ones, making possible the recovery of information from the so-called "bad spots", i.e. spots that deviate from ideal shape and area. Further, the data shows that there is a marked improvement in uniformity when features are printed on structured surfaces. We hypothesize that there are added benefits stemming from the fixed size and shape of subs-spots which could potentially improve the automated detection process and its outcomes.

With respect to SNR, things proved to be less clear. Previously, SNR was calculated using the local background to account for background contribution. But with structured substrates that suppress and enhance light, SNR calculation is not straightforward. One of the ideas behind the slide design is that it offers the possibility of exploring various background contribution extraction methods. The resulting SNR's proved to be very different, the only reasonable conclusion being that the SNR as it was originally calculated is most probably under-estimating the true SNR. Nevertheless, the SNR can be used to characterize local contrast and consequently, the ease with which features would reliably be automatically detected.

III. Concluding remarks and future perspectives

A hybrid approach towards bio-recognition, fluorescence based detection, solid devices, i.e. microarray substrates, was presented. Optical interference and departure from substrate planarity were combined to provide a substrate that addresses issues related to spot morphology and, by extension, it is expected to positively impact data extraction and quality. Additionally the proposed substrate designs were found to be comparable or better than commercially available, state of the art, slides. Further, a brief description of the potential development directions of the new architectures will be given.

Obtaining reproducible and morphology controlled features in bio-array format is of critically affects the quality of the information extracted from such experiments. The ability to control/determine the size and shape of a printed feature *a priori* would relieve to a great extent the dependence on computationally intensive software tools to perform image recognition and data correction (normalization). Unfortunately, the way in which a droplet behaves when deposited on a surface (i.e. the wetting and evaporation behaviour) is determined by surface and liquid properties. Thus, it is difficult to develop a strategy that would efficiently cater to essentially a very broad range of surface chemistries and liquid properties combinations. A way to obtain controlled and pre-determined morphologies and sizes would be to essentially trap/confine the liquid droplet to a certain area using either physical or chemical barriers or both. With physical barriers, one would control the spreading behaviour of the droplet but not the evaporation regime. Also, physical barriers would require very good positional control, requiring semiconductor fabrication accuracy levels. With chemical confinement one could in principle trap liquid droplets using hydrophobicity barriers. But it is foreseeable that the efficiency of such barriers would depend on the physical properties of the liquid that needs to be confined. This is clearly not a universal solution. A different approach is proposed in this work and it relies on fluorescence confinement.

As fluorescence is the main read-out method in bio-recognition based arrays, it is essentially the fluorescence emission that needs to confined to a region with controlled morphology. Contrary to liquid confinement, fluorescence emission (light) can be easily confined by making use of interference effects. Structures that promote

the formation of standing waves can be patterned on solid surfaces with relative ease using standard photolithography tools. If light is directed towards a reflecting surface, standing waves will form. If a light emitting molecule (a fluorophore) is placed in the vicinity of such a reflecting surface, its distance from the surface will modulate the intensity of the light emitted by the said molecule since the standing wave comprises intensity maxima and minima. To confine the fluorescence therefore is equivalent to:

i. keeping the fluorophore at a distance from the reflector where an intensity maximum is formed in the region where fluorescence is wanted
ii. and keeping the fluorophore at a distance from the reflector where an intensity minimum is formed in the region where fluorescence is unwanted.

The feasibility of this approach was investigated in this work. The first approach consisted of using a simple fluorophore attached to surfaces comprising silicon oxide pillars patterned on silicon and platinum reflectors respectively. Secondly, detection of a DNA sequence through hybridization was investigated on these substrates. Finally, prototype substrates were designed to be compatible with standard microarray scanners.

The first test was carried out on substrates comprising silicon oxide micro-pillars of various (0-100 nm) heights patterned on silicon and platinum respectively. A fluorescent probe was grafted onto the surface of the substrates and the variation of fluorescence intensity versus pillars height was shown to be consistent with a standing wave model. Fluorescence confinement was evaluated using SNR as a measure of local contrast. As expected, the confinement became more pronounced as the pillar height approached the value predicted theoretically for maximum enhancement. Also, it was found that the variation in SNR for pillars of identical height but with different footprints. This was assigned to limitations of the patterning process and possibly limited robustness of the image processing algorithm.

The second series of tests involved the hybridization based detection of a fluorescently labelled DNA strand from solution in a procedure similar to that used in microarray experiments. The results were disappointing in that a very low SNR

could be measured (results were also plagued by lack of consistency). This was attributed to the use of a multi-step, sub-optimal surface modification chemistry.

Finally, based on what was learned from the work undertaken thus far, a set of prototype slides was designed, fabricated and tested. They were specifically engineered to be compatible with standard microarray scanners (and microarray technology in general e.g. arrayers). The prototypes were fabricated on silicon and platinum respectively and comprise three different regions (longitudinally): an active area covering half of the slide and two equally sized control areas covering the other half of the slide. The two control areas were flat oxide films whose thickness would allow for the fluorophore to stand at a distance from the reflector that would suppress and enhance fluorescence respectively. Two architectures were chosen for the active areas: silicon nano-pillars and nano-wells respectively. The two architectures are optically very similar, with the nano-well architecture providing some important advantages over its nano-pillar based counterpart:

i. for the nano-well architecture, the reflector surface was insulated by a silicon oxide layer that would shield the reflector surface from oxide build-up during the cleaning process and thus maintain the optical properties of the system constant and
ii. as a consequence of this, the slides would become re-usable by regenerating the surface chemistry after use using quick and non-hazardous photochemical dry cleaning.

The surface chemistry of the substrates was optimized for best loading capacity and the substrates were then tested in hybridization based detection experiments using a printed oligonucleotide and a fluorescently labelled DNA sequence. Two figures of merit were used for performance assessment of the prototypes: signal to noise ratio and intra-feature uniformity. The performance of the prototypes was compared to that of commercial slides. From this perspective, it was found that:

i. in terms of signal to noise ratio, the prototypes were comparable to the commercial substrates;
ii. the performance of the prototypes could be improved with more accurate control of the deposition/patterning process;

iii. the structured surfaces consistently improve the fluorescence distribution inside the feature.

The proposed novel approach involving the use of a micro-structured surface (a departure from the classical microarray technology standards in terms of substrate properties) by confining the fluorescence to regions with defined and known geometric properties was shown to have the potential to allow for the control of feature morphology. Further intra-feature uniformity was shown to be positively affected by the said micro-structures. These factors critically affect the operational aspects of microarray technology. Most importantly, this was achieved without imposing a technology shift i.e. fluorescence detection and compatibility with standard microarray scanners and arrayers. Another benefit is the possibility of chemically regenerating the surfaces and then reusing them and thus reducing costs The proposed technology can however be improved along several direction, as outlined below.

One important factor for judging the feasibility of introducing new technologies is to do with costs. In this particular case, since compatibility to commonly used printing or imaging equipment is assured, the actual cost of the devices is the deciding factor. Classical semiconductor photolithography techniques are expensive (even when economies of scale are possible, the margins are extremely small). To this end, one can argue the hybrid devices shown here could be too expensive to warrant their adoption. One way of addressing this problem is by switching to non-classical lithographical techniques such as imprint lithography. This would require the use of photolithography once, for the fabrication of the imprint mould, while device fabrication would be based on replication using the mould. Such a process would only consist of depositing a sol-gel material onto a solid substrate, e.g. silicon, and simply stamping it with the right mould (either solid or elastomeric one, e.g. SCIL). Regarding the solid substrate, it is worth mentioning that part of the cost of a commercial microarray slide is going towards the cost of ultra-flat and ultra-low autofluorescence glass. In a hybrid architecture like the one presented here, the problem of fluorescence, and, by consequence, its price, would be eliminated. This is because only the characteristics of the reflector and spacer layer are affecting the performance of the substrate. Another beneficial consequence that arises is the ability to move towards different, cheaper, substrate materials like plastics (polymers like

PMMA, polycarbonate). Polymer films have good planarity and can be easily metallised while the use of lasers makes high precision processing possible. Finally, an issue that has been discussed previously but deserves emphasis in relation to the cost-effectiveness of the hybrid substrates is their recyclability. The possibility of re-using the substrates after only short dry photochemical cleaning run is very appealing and it is made possible by the nature of the materials used (this is in contrast to the parylene lift-off substrates that require a repetition of the lithography step to re-pattern the substrate).

The implications of a structured substrate go beyond cost related issues into the operational dimension of such a device. From this perspective, an impact on surface chemical patterning can be envisaged. Thus, a μCP-derived method could be easily applied to the hybrid substrates. In classical μCP, the chemical patterning arises from the structuring of the stamp, so any change in required pattern would need a new stamp. Contrary to this, the hybrid substrates could be chemically patterned using a flat stamp as the pattern is topographic and pertains to the surface of the substrate. A similar approach could rely on simultaneous topographical and chemical patterning. This would be possible by patterning in a layer of sol-gel precursor with an "inked' elastomeric stamp.

IV. Appendix

IV.1 Two beam interference model

The optical path length (*opl*) of the beam through the pillar is given by the sum of the optical path lengths of the beams through the two components of the pillar.

$$opl_{total} = opl_{SiO_2} + opl_{TiO_2}$$

$$opl_{SiO_2} = 2n_2d_2$$

$$opl_{TiO_2} = 2n_3d_3$$

The phase difference between the direct and the reflected beams, ϕ, is given by

$$\phi = \frac{2\pi}{\lambda} opl_{total}$$

$$= \frac{2\pi}{\lambda}(2n_2d_2 + 2n_3d_3)$$

$$= \frac{2\pi}{\lambda} 2(n_2d_2 + n_3d_3)$$

Following the approach in (Parthasarathy and Groves 2004) and starting from the condition that the electric field amplitude at the metal surface is given by

$$F \propto 1 - re^{i\phi}$$

where F is the electric field amplitude and r is the reflectivity coefficient at the metal-dielectric interface. For the excitation light, the probability of excitation is given by the square of the modulus of F_{ex}

$$F_{ex} \propto 1 - re^{i\phi}$$

$$P_{ex} \propto |F_{ex}|^2 \propto \left|1 - re^{i\phi}\right|^2$$

$$\propto \left(\sqrt{(1 - rcos\phi)^2 + (-rsin\phi)^2}\right)^2$$

$$\propto \left(\sqrt{(1-rcos\phi)^2+(-rsin\phi)^2}\right)^2$$

$$\propto 1-2rcos\phi+r^2cos^2\phi+r^2+r^2sin^2\phi$$

$$\propto 1-2rcos\phi+r^2$$

$$P_{ex} \propto 1-r(2cos\phi-r)$$

$cos\phi$ can be rewritten as $cos\ 2\phi/2$ so the expression above becomes

$$P_{ex} \propto 1-r\left[2\left(1-2sin^2\frac{\phi}{2}\right)-r\right]$$

$$\propto 1-r\left(2-4sin^2\frac{\phi}{2}-r\right)$$

$$\propto 1-2r+4rsin^2\frac{\phi}{2}+r^2$$

$$P_{ex} \propto (1-r)^2+4rsin^2\frac{\phi}{2}$$

The same is valid for the emission probability. After replacing r with the corresponding reflection coefficients at the excitation and emission wavelengths respectively (r_{em} and r_{ex} respectively) so the total observed fluorescence will be

$$F_{exp} \propto \left[(1-r_{ex})^2+4r_{ex}sin^2\left(\frac{2\pi}{\lambda_{ex}}\frac{opl_{total}}{2}\right)\right]\left[(1-r_{em})^2\right.$$
$$\left.+4r_{em}sin^2\left(\frac{2\pi}{\lambda_{em}}\frac{opl_{total}}{2}\right)\right]$$

Substituting opl_{total} gives the observed fluorescence *Fexp*

$$F_{exp} \propto \left[(1-r_{ex})^2+4r_{ex}sin^2\left(\frac{2\pi}{\lambda_{ex}}(n_2d_2+n_3d_3)\right)\right]\left[(1-r_{em})^2\right.$$
$$\left.+4r_{em}sin^2\left(\frac{2\pi}{\lambda_{em}}(n_2d_2+n_3d_3)\right)\right]$$

IV.2 Three beam interference model

The optical path length (*opl*) of the reflected beams, R_{23} and R_{34}, are given by :

$$opl_{R_{23}} = 2n_2d_2$$

$$opl_{R_{34}} = 2n_2d_2 + 2n_3d_3$$

The optical path lengths of beams R_{23} (opl_1) and R_{34} (opl_2) respectively through the pillar are given by

$$opl_1 = 2n_2d_2$$

$$opl_2 = 2n_2d_2 + 2n_3d_3$$

Optical path differences between R_1 and R_{23} (ϕ_1), and R_1 and R_{34} (ϕ_2) respectively are given by

$$\phi_1 = \frac{2\pi 2n_2d_2}{\lambda}$$

$$\phi_2 = \frac{2\pi(2n_2d_2 + 2n_3d_3)}{\lambda}$$

Following the route described by (Parthasarathy and Groves 2004), the amplitude of the electric field at the surface is given by

$$F \propto 1 - r_{23}e^{i\phi_1} - r_{34}e^{i\phi_2}$$

where F is the electric field amplitude and r is the reflectivity coefficient at the metal-dielectric interface. For the excitation light, the probability of excitation is given by the square of the modulus of F_{ex}

$$P_{ex} = |F_{ex}|^2 \propto \left|1 - r_{23}e^{i\phi_1} - r_{34}e^{i\phi_2}\right|^2$$

$$|F_{ex}|^2 \propto |1 - r_{23}\cos\phi_1 - r_{23}i\sin\phi_1 - r_{34}(1 - r_{23})^2\cos\phi_2 - r_{34}(1 - r_{23})^2 i\sin\phi_2|^2$$

After separating grouping the real and the imaginary part of the equation, one can write

$$|F_{ex}|^2 \propto [1 - r_{23}\cos\phi_1 - r_{34}(1 - r_{23})^2\cos\phi_2]^2 + [r_{23}\sin\phi_1 + r_{34}(1 - r_{23})^2\sin\phi_2]^2$$

We denote the first term with a and the second one with b and expand each of the two:

$$a = [1 - r_{23}\cos\phi_1 - r_{34}(1 - r_{23})^2\cos\phi_2]^2$$

$$a = 1 + r_{23}^2\cos^2\phi_1 + r_{34}^2(1 - r_{23})^4\cos^2\phi_2 - 2r_{23}\cos\phi_1 - 2r_{34}(1 - r_{23})^2\cos\phi_2 + 2r_{23}r_{23}(1 - r_{23})^2\cos\phi_1\cos\phi_2$$

$$b = [r_{23}\sin\phi_1 + r_{34}(1 - r_{23})^2\sin\phi_2]^2$$

$$b = r_{23}^2\sin^2\phi_1 + r_{34}^2(1 - r_{23})^4\sin^2\phi_2 + 2r_{23}r_{23}(1 - r_{23})^2\sin\phi_1\sin\phi_2$$

When adding a and b, the highlighted terms can be simplified using trigonometric identities. The sum $a + b$ becomes

$$a + b = 1 - 2r_{23}\cos\phi_1 - 2r_{34}(1 - r_{23})^2\cos\phi_2 + r_{23}^2 + r_{34}^2(1 - r_{23})^4 + 2r_{23}r_{34}(1 - r_{23})^2\cos(\phi_1 - \phi_2)$$

Further, the argument of the cosine is rewritten in terms of half angle and using the relationship between *cos(2x)* and *sin(x)* the sum becomes

$$a + b = 1 - 2r_{23}\left[1 - 2\sin^2\left(\frac{\phi_1}{2}\right)\right] - 2r_{34}(1 - r_{23})^2\left[1 - 2\sin^2\left(\frac{\phi_2}{2}\right)\right] + r_{23}^2 + r_{34}^2(1 - r_{23})^4 + 2r_{23}r_{34}(1 - r_{23})^2\left[1 - 2\sin^2\left(\frac{\phi_1 - \phi_2}{2}\right)\right]$$

$$a + b = 1 - 2r_{23} + 4r_{23}\sin^2\left(\frac{\phi_1}{2}\right) - 2r_{34}(1 - r_{23})^2 + 4r_{34}(1 - r_{23})^2\sin^2\left(\frac{\phi_2}{2}\right) + r_{23}^2 + r_{34}^2(1 - r_{23})^4 + 2r_{23}r_{34}(1 - r_{23})^2 - 4r_{23}r_{34}(1 - r_{23})^2\sin^2\left(\frac{\phi_1 - \phi_2}{2}\right)$$

The above equation can finally be rewritten as

$$a + b = [(1 - r_{23})^2 - r_{34}(1 - r_{23})^2]^2 + 2r_{23}r_{34}(1 - r_{23})^2 + 4r_{23}\sin^2\left(\frac{\phi_1}{2}\right) + 4r_{34}(1 - r_{23})^2\sin^2\left(\frac{\phi_2}{2}\right) - 4r_{23}r_{34}(1 - r_{23})^2\sin^2\left(\frac{\phi_1 - \phi_2}{2}\right)$$

It follows then that

$$P_{ex} \propto |F_{ex}|^2 \propto [(1 - r_{23})^2 - r_{34}(1 - r_{23})^2]^2 + 2r_{23}r_{34}(1 - r_{23})^2 + 4r_{23}\sin^2\left(\frac{\phi_1}{2}\right) + 4r_{34}(1 - r_{23})^2\sin^2\left(\frac{\phi_2}{2}\right) - 4r_{23}r_{34}(1 - r_{23})^2\sin^2\left(\frac{\phi_1 - \phi_2}{2}\right)$$

And the same is valid for the probability of emission, P_{em}. The observed fluorescence will be proportional to the product between P_{ex} and P_{em}. The phase difference terms will be

$$\frac{\phi_1}{2} = \frac{2\pi n_2 d_2}{\lambda}$$

$$\frac{\phi_2}{2} = \frac{2\pi(n_2 d_2 + n_3 d_3)}{\lambda}$$

$$\frac{\phi_1 - \phi_2}{2} = \frac{2\pi n_3 d_3}{\lambda}$$

Substituting the phase terms and the reflectivity coefficients at the excitation wavelength gives

$$P_{ex} \propto [(1-r_{23}^{ex})^2 - r_{34}^{ex}(1-r_{23}^{ex})^2]^2 + 2r_{23}^{ex}r_{34}^{ex}(1-r_{23}^{ex})^2 + 4r_{23}^{ex}\sin^2\left(\frac{2\pi n_2 d_2}{\lambda}\right) + 4r_{34}^{ex}(1-r_{23}^{ex})^2\sin^2\left(\frac{2\pi(n_2 d_2 + n_3 d_3)}{\lambda}\right) - 4r_{23}^{ex}r_{34}^{ex}(1-r_{23}^{ex})^2\sin^2\left(\frac{2\pi n_3 d_3}{\lambda}\right)$$

The observed fluorescence intensity, F_{exp}, is proportional to the product between the excitation and emission probability and thus given by

$$F_{exp} \propto P_{ex}P_{em} \propto \left[[(1-r_{23}^{ex})^2 - r_{34}^{ex}(1-r_{23}^{ex})^2]^2 + 2r_{23}^{ex}r_{34}^{ex}(1-r_{23}^{ex})^2 + 4r_{23}^{ex}\sin^2\left(\frac{2\pi n_2 d_2}{\lambda_{ex}}\right) + 4r_{34}^{ex}(1-r_{23}^{ex})^2\sin^2\left(\frac{2\pi(n_2 d_2 + n_3 d_3)}{\lambda_{ex}}\right) - 4r_{23}^{ex}r_{34}^{ex}(1-r_{23}^{ex})^2\sin^2\left(\frac{2\pi n_3 d_3}{\lambda_{ex}}\right)\right]\left[[(1-r_{23}^{em})^2 - r_{34}^{em}(1-r_{23}^{em})^2]^2 + 2r_{23}^{em}r_{34}^{em}(1-r_{23}^{em})^2 + 4r_{23}^{em}\sin^2\left(\frac{2\pi n_2 d_2}{\lambda_{em}}\right) + 4r_{34}^{em}(1-r_{23}^{em})^2\sin^2\left(\frac{2\pi(n_2 d_2 + n_3 d_3)}{\lambda_{em}}\right) - 4r_{23}^{em}r_{34}^{em}(1-r_{23}^{em})^2\sin^2\left(\frac{2\pi n_3 d_3}{\lambda_{em}}\right)\right]$$

V. References

Ajo-Franklin, C.M., Yoshina-Ishii, C., Boxer, S.G., 2005. Probing the structure of supported membranes and tethered oligonucleotides by fluorescence interference contrast microscopy. Langmuir 21(11), 4976-4983.

Alwine, J.C., Kemp, D.J., Stark, G.R., 1977. Method for Detection of Specific Rnas in Agarose Gels by Transfer to Diazobenzyloxymethyl-Paper and Hybridization with DNA Probes. P Natl Acad Sci USA 74(12), 5350-5354.

Austin, J., Holway, A.H., 2011. Contact Printing of Protein Microarrays 785, 379-394.

Bajcsy, P., 2004. Gridline: Automatic grid alignment in DNA microarray scans. Ieee T Image Process 13(1), 15-25.

Bajcsy, P., 2006. An overview of DNA microarray grid alignment and foreground separation approaches. Eurasip J Appl Sig P.

Balci, S., Hahn, K., Kopold, P., Kadri, A., Wege, C., Kern, K., Bittner, A.M., 2012. Electroless synthesis of 3 nm wide alloy nanowires inside Tobacco mosaic virus. Nanotechnology 23(4).

Banuls, M.J., Garcia-Pinon, F., Puchades, R., Maquieira, A., 2008. Chemical derivatization of compact disc polycarbonate surfaces for SNPs detection. Bioconjugate Chem 19(3), 665-672.

Barron, J.A., Young, H.D., Dlott, D.D., Darfler, M.M., Krizman, D.B., Ringeisen, B.R., 2005. Printing of protein microarrays via a capillary-free fluid jetting mechanism. Proteomics 5(16), 4138-4144.

Becker, H.W., 2003. Early mask making during the 1960's in Dresden. 19th European Conference on Mask Technology for Integrated Circuits and Microcomponents 5148, 6-15.

Bennett, J.M., Pelletier, E., Albrand, G., Borgogno, J.P., Lazarides, B., Carniglia, C.K., Schmell, R.A., Allen, T.H., Tuttlehart, T., Guenther, K.H., Saxer, A., 1989. Comparison of the Properties of Titanium-Dioxide Films Prepared by Various Techniques. Appl Optics 28(16), 3303-3317.

Bensebaa, F., Voicu, R., Huron, L., Ellis, T.H., Kruus, E., 1997. Kinetics of formation of long-chain n-alkanethiolate monolayers on polycrystalline gold. Langmuir 13(20), 5335-5340.

Benson, J., Boukhalfa, S., Magasinski, A., Kvit, A., Yushin, G., 2012. Chemical vapor deposition of aluminum nanowires on metal substrates for electrical energy storage applications. Acs Nano 6(1), 118-125.

BioForce-Nano, BioForce Nano UV/Ozone cleane, http://www.bioforcenano.com/index.php?id=290

Blanchard, A.P., Kaiser, R.J., Hood, L.E., 1996. High-density oligonucleotide arrays. Biosens Bioelectron 11(6-7), 687-690.

Bombera, R., Leroy, L., Livache, T., Roupioz, Y., 2012. DNA-directed capture of primary cells from a complex mixture and controlled orthogonal release monitored by SPR imaging. Biosensors and Bioelectronics 33(1), 10-16.

Borgogno, J.P., Flory, F., Roche, P., Schmitt, B., Albrand, G., Pelletier, E., Macleod, H.A., 1984. Refractive-Index and Inhomogeneity of Thin-Films. Appl Optics 23(20), 3567-3570.

Bozinov, D., Rahnenfuhrer, J., 2002. Unsupervised technique for robust target separation and analysis of DNA microarray spots through adaptive pixel clustering. Bioinformatics 18(5), 747-756.

Bradley, D.C., 2001. Chapter 7. Industrial Applications. In: Bradley, D.C. (Ed.), Alkoxo and aryloxo derivatives of metals, pp. 671-673. Academic Press, San Diego.
Brandstatter, M., Fromherz, P., Offenhausser, A., 1988. Fluorescent Dye Monolayers on Oxidized Silicon. Thin Solid Films 160(1-2), 341-346.
Braun, D., Fromherz, P., 1997. Fluorescence interference-contrast microscopy of cell adhesion on oxidized silicon. Appl Phys a-Mater 65(4-5), 341-348.
Brueggemeier, S.B., Kron, S.J., Palecek, S.P., 2004. Use of protein-acrylamide copolymer hydrogels for measuring protein concentration and activity. Anal Biochem 329(2), 180-189.
Brueggemeier, S.B., Kron, S.J., Palecek, S.P., Parker, L., Kent, S.B.H., 2009. Hydrogels for biomolecule analysis and corresponding method to analyze biomolecules. In: USPTO (Ed.), Official Gazette of the United States Patent and Trademark Office. Wisconsin Alumni Research Foundation; The University of Chicago, USA.
Brueggemeier, S.B., Wu, D., Kron, S.J., Palecek, S.P., 2005. Protein-acrylamide copolymer hydrogels for array-based detection of tyrosine kinase activity from cell lysates. Biomacromolecules 6(5), 2765-2775.
Bruning, J.H., 1997. Optical lithography - Thirty years and three orders of magnitude - The evolution of optical lithography tools. Emerging Lithographic Technologies 3048, 14-27.
Bruning, J.H., 2007. Optical Lithography... 40 years and holding - art. no. 652004. Optical Microlithography XX, Pts 1-3 6520, 52004-52004.
Brzoska, J.B., Benazouz, I., Rondelez, F., 1994. Silanization of Solid Substrates - a Step toward Reproducibility. Langmuir 10(11), 4367-4373.
Cagnazzo, M., te Pas, M.F.W., Priem, J., de Wit, A.A.C., Pool, M.H., Davoli, R., Russo, V., 2006. Comparison of prenatal muscle tissue expression profiles of two pig breeds differing in muscle characteristics. J Anim Sci 84(1), 1-10.
Caminade, A.M., Padie, C., Laurent, R., Maraval, A., Majoral, J.P., 2006. Uses of dendrimers for DNA microarrays. Sensors-Basel 6(8), 901-914.
Caminade, A.M., Turrin, C.O., Majoral, J.P., 2008. Dendrimers and DNA: Combinations of two special topologies for nanomaterials and biology. Chem-Eur J 14(25), 7422-7432.
Campbell, S.A., 2008a. Chapter 11. Etching. In: Campbell, S.A. (Ed.), Fabrication engineering at the micro and nanoscale, p. 283, 3rd ed. Oxford University Press, New York.
Campbell, S.A., 2008b. Chapter 11. Etching. In: Campbell, S.A. (Ed.), Fabrication engineering at the micro and nanoscale, p. 284, 3rd ed. Oxford University Press, New York.
Carlsson, J., Drevin, H., Axen, R., 1978. Protein Thiolation and Reversible Protein-Protein Conjugation - N-Succinimidyl 3-(2-Pyridyldithio)Propionate, a New Heterobifunctional Reagent. Biochem J 173(3), 723-737.
Carlsson, K., Aslund, N., 1987. Confocal Imaging for 3-D Digital Microscopy. Appl Optics 26(16), 3232-3238.
Carrillo, A., Gujraty, K.V., Kane, R.S., 2005. Surfaces and Substrates. In: Müller, U.R., Nicolau, D.V. (Eds.), Biological and medical physics, biomedical engineering,, p. 45. Springer, Berlin.
Chang, M.J., Pang, C.R., Liu, J., Bai, H., Deng, J., Xu, Z.G., Zhang, H.L., 2011. High spatial resolution label-free detection of antigen-antibody binding on patterned surface by imaging ellipsometry. J Colloid Interf Sci 360(2), 826-833.

Chen, J.K., Qui, J.Q., Fan, S.K., Kuo, S.W., Ko, F.H., Chu, C.W., Chang, F.C., 2012a. Using colloid lithography to fabricate silicon nanopillar arrays on silicon substrates. J Colloid Interf Sci 367, 40-48.
Chen, S., Deng, T., Wang, T., Wang, J., Li, X., Li, Q., Huang, G., 2012b. Visualization of high-throughput and label-free antibody-polypeptide binding for drug screening based on microarrays and surface plasmon resonance imaging. J Biomed Opt 17(1), 015005.
Cheng, J.Y., Wei, C.W., Hsu, K.H., Young, T.H., 2004. Direct-write laser micromachining and universal surface modification of PMMA for device development. Sensor Actuat B-Chem 99(1), 186-196.
Chi, Y.S., Byon, H.R., Lee, B.S., Kong, B., Choi, H.C., Choi, I.S., 2008. Polymeric Rulers: Distance-Dependent Emission Behaviors of Fluorophores on Flat Gold Surfaces and Bioassay Platforms Using Plasmonic Fluorescence Enhancement. Adv Funct Mater 18(21), 3395-3402.
Cho, G.H., Lee, K.H., Lee, J.O., Sohn, M.J., Lee, B., Choi, S.H., Kim, S.K., Yoon, J.B., 2010. One-chip electronic detection of DNA hybridization using precision impedance-based CMOS array sensor. Biosens Bioelectron 26(4), 1373-1379.
Chorkendorff, I., Niemantsverdriet, J.W., 2003. Chapter 5. Solid catalysts. In: Chorkendorff, I., Niemantsverdriet, J.W. (Eds.), Concepts of modern catalysis and kinetics, p. 207. Wiley-VCH, Weinheim Germany.
Chou, S.Y., Krauss, P.R., Renstrom, P.J., 1995. Imprint of Sub-25 Nm Vias and Trenches in Polymers. Appl Phys Lett 67(21), 3114-3116.
Chou, S.Y., Krauss, P.R., Renstrom, P.J., 1996a. Imprint lithography with 25-nanometer resolution. Science 272(5258), 85-87.
Chou, S.Y., Krauss, P.R., Renstrom, P.J., 1996b. Nanoimprint lithography. J Vac Sci Technol B 14(6), 4129-4133.
Clark, S.M., Hamilton, G.E., Nordmeyer, R.A., Uber, D., Cornell, E.W., Brown, N., Segraves, R., Davis, R., Albertson, D.G., Pinkel, D., 2008. High-Efficiency Microarray Printer Using Fused-Silica Capillary Tube Printing Pins. Anal Chem 80(19), 7639-7642.
Corgier, B.P., Li, F., Blum, L.J., Marquette, C.A., 2007. On-chip chemiluminescent signal enhancement using nanostructured gold-modified carbon microarrays. Langmuir 23(16), 8619-8623.
Crane, J.M., Kiessling, V., Tamm, L.K., 2005. Measuring lipid asymmetry in planar supported lipid bilayers by fluorescence interference contrast microscopy. Biophys J 88(1), 234a-234a.
Cretich, M., di Carlo, G., Longhi, R., Gotti, C., Spinella, N., Coffa, S., Galati, C., Renna, L., Chiari, M., 2009. High Sensitivity Protein Assays on Microarray Silicon Slides. Anal Chem 81(13), 5197-5203.
Danzer, K., 2007. Analytical chemistry : theoretical and metrological fundamentals. Springer, Berlin ; New York.
Dawson, E.D., Reppert, A.E., Rowlen, K.L., Kuck, L.R., 2005. Spotting optimization for oligo microarrays on aldehyde-glass. Anal Biochem 341(2), 352-360.
De Simone, D., Tenaglia, E., Piazza, P., Vaccaro, A., Bollin, M., Capetti, G., Piacentini, P., Canestrari, P., 2011. Potential applications of negative tone development in advanced lithography. Microelectron Eng 88(8), 1917-1922.
Deckman, H.W., Dunsmuir, J.H., 1982. Natural Lithography. Appl Phys Lett 41(4), 377-379.

Deegan, R.D., Bakajin, O., Dupont, T.F., Huber, G., Nagel, S.R., Witten, T.A., 1997. Capillary flow as the cause of ring stains from dried liquid drops. Nature 389(6653), 827-829.
del Campo, A., Bruce, I.J., 2005. Substrate Patterning and Activation Strategies for DNA Chip Fabrication. In: Wittmann, C., Alegret, S. (Eds.), Immobilisation of DNA on chips, p. 95. Springer, Berlin ; New York.
Deng, Y., Zhu, X.Y., Kienlen, T., Guo, A., 2006. Transport at the air/water interface is the reason for rings in protein microarrays. J Am Chem Soc 128(9), 2768-2769.
Despont, M., Brugger, J., Drechsler, U., Durig, U., Haberle, W., Lutwyche, M., Rothuizen, H., Stutz, R., Widmer, R., Binnig, G., Rohrer, H., Vettiger, P., 2000. VLSI-NEMS chip for parallel AFM data storage. Sensor Actuat a-Phys 80(2), 100-107.
Dettin, M., Muncan, N., Bugatti, A., Grezzo, F., Danesin, R., Rusnati, M., 2011. Chemoselective Surface Immobilization of Proteins through a Cleavable Peptide. Bioconjugate Chem, 110811150354027.
Didar, T.F., Foudeh, A.M., Tabrizian, M., 2012. Patterning Multiplex Protein Microarrays in a Single Microfluidic Channel. Anal Chem 84(2), 1012-1018.
Dinca, V., Farsari, M., Kafetzopoulos, D., Popescu, A., Dinescu, M., Fotakis, C., 2008. Patterning parameters for biomolecules microarrays constructed with nanosecond and femtosecond UV lasers. Thin Solid Films 516(18), 6504-6511.
Dobroiu, S., van Delft, F.C.M.J.M., van Thiel, E., Hanson, K.L., Nicolau, D.V., 2010. Laser-assisted structuring of metal-polymer bilayers for protein patterning. Microelectron Eng 87(5-8), 1190-1194.
Douvas, A.M., Petrou, P.S., Kakabakos, S.E., Misiakos, K., Argitis, P., Sarantopoulou, E., Kollia, Z., Cefalas, A.C., 2005. 157-nm laser ablation of polymeric layers for fabrication of biomolecule microarrays. Analytical and Bioanalytical Chemistry 381(5), 1027-1032.
Drăghici, S., 2003. Chapter 3. Image processing. In: Drăghici, S. (Ed.), Data analysis tools for DNA microarrays, pp. 53-55. Chapman & Hall/CRC, Boca Raton.
Duan, X.X., Zhao, Y.P., Perl, A., Berenschot, E., Reinhoudt, D.N., Huskens, J., 2010. Nanopatterning by an Integrated Process Combining Capillary Force Lithography and Microcontact Printing. Adv Funct Mater 20(4), 663-668.
Dufva, M., 2005. Fabrication of high quality microarrays. Biomol Eng 22(5-6), 173-184.
Dufva, M., 2009. Introduction to Microarray Technology. In: Dufva, M. (Ed.), DNA microarrays for biomedical research : methods and protocols, pp. 8-9. Humana Press, New York.
Dugas, V., Broutin, J., Souteyrand, E., 2005. Droplet evaporation study applied to DNA chip manufacturing. Langmuir 21(20), 9130-9136.
Elsholz, B., Nitsche, A., Achenbach, J., Ellerbrok, H., Blohm, L., Albers, J., Pauli, G., Hintsche, R., Worl, R., 2009. Electrical microarrays for highly sensitive detection of multiplex PCR products from biological agents. Biosens Bioelectron 24(6), 1737-1743.
Enrichi, F., Ricco, R., Meneghello, A., 2011. Signal enhancement in DNA microarray using dye doped silica nanoparticles: Application to Human Papilloma Virus (HPV) detection. Biosens Bioelectron 26(5), 2761-2765.
Eritja, R., 2007. Solid-phase synthesis of modified oligonucleotides. Int J Pept Res Ther 13(1-2), 53-68.

Ewis, A.A., Zhelev, Z., Bakalova, R., Fukuoka, S., Shinohara, Y., Ishikawa, M., Baba, Y., 2005. A history of microarrays in biomedicine. Expert Rev Mol Diagn 5(3), 315-328.
Fernandez-Sanchez, C., Bonilla, D., Mallen, M., de la Rica, R., Baldi, A., 2011. Electrical Readout of Protein Microarrays on Regular Glass Slides. Anal Chem 83(5), 1726-1731.
Fernandez, A., 2009a. Structures for enhanced detection of fluorescence. In: USPTO (Ed.), Official Gazette of the United States Patent and Trademark Office. Complete Genomics, Inc. , USA.
Fernandez, A., 2009b. Structures for enhanced detection of fluorescence. Complete Genomics, Inc. , USA.
Fink, C.K., Nakamura, K., Ichimura, S., Jenkins, S.J., 2009. Silicon oxidation by ozone. J Phys-Condens Mat 21(18).
Fischer, U.C., Zingsheim, H.P., 1981. Sub-Microscopic Pattern Replication with Visible-Light. J Vac Sci Technol 19(4), 881-885.
Fixe, F., 2004. Functionalization of poly(methyl methacrylate) (PMMA) as a substrate for DNA microarrays. Nucleic Acids Res 32(1), 9e-9.
Fixe, F., Dufva, M., Telleman, P., Christensen, C.B.V., 2004. Functionalization of poly(methyl methacrylate) (PMMA) as a substrate for DNA microarrays. Nucleic Acids Res 32(1).
Fodor, S.P.A., Read, J.L., Pirrung, M.C., Stryer, L., Lu, A.T., Solas, D., 1991. Light-Directed, Spatially Addressable Parallel Chemical Synthesis. Science 251(4995), 767-773.
Franssila, S., 2004a. Chapter 5. Thin-film Materials and processes. Introduction to microfabrication, pp. 50-51. J. Wiley, Chichester, West Sussex, England ; Hoboken, NJ.
Franssila, S., 2004b. Chapter 5. Thin-film Materials and Processes. Introduction to microfabrication, p. 50. J. Wiley, Chichester, West Sussex, England ; Hoboken, NJ.
Franssila, S., 2004c. Chapter 5. Thin-film Materials and Processes. Introduction to microfabrication, pp. 47-48. J. Wiley, Chichester, West Sussex, England ; Hoboken, NJ.
Gao, X.L., Gulari, E., Zhou, X.C., 2004. In situ synthesis of oligonucleotide microarrays. Biopolymers 73(5), 579-596.
Geissler, M., Roy, E., Diaz-Quijada, G.A., Galas, J.C., Veres, T., 2009. Microfluidic Patterning of Miniaturized DNA Arrays on Plastic Substrates. Acs Appl Mater Inter 1(7), 1387-1395.
George, R.A., 2006. The printing process: Tips on tips. DNA Microarrays Part A: Array Platforms and Wet-Bench Protocols 410, 121-+.
Gharaibeh, R.Z., Fodor, A.A., Gibas, C.J., 2010. Accurate Estimates of Microarray Target Concentration from a Simple Sequence-Independent Langmuir Model. Plos One 5(12).
Giuntini, F., Dumoulin, F., Daly, R., Ahsen, V., Scanlan, E.M., Lavado, A.S.P., Aylott, J.W., Rosser, G.A., Beeby, A., Boyle, R.W., 2012. Orthogonally bifunctionalised polyacrylamide nanoparticles: a support for the assembly of multifunctional nanodevices. Nanoscale 4(6), 2034-2045.
Gruber, H.J., Hahn, C.D., Kada, G., Riener, C.K., Harms, G.S., Ahrer, W., Dax, T.G., Knaus, H.G., 2000. Anomalous fluorescence enhancement of Cy3 and Cy3.5 versus anomalous fluorescence loss of Cy5 and Cy7 upon covalent linking to IgG and noncovalent binding to avidin. Bioconjugate Chem 11(5), 696-704.

Gudmundsdottir, A.V., Paul, C.E., Nitz, M., 2009. Stability studies of hydrazide and hydroxylamine-based glycoconjugates in aqueous solution. Carbohyd Res 344(3), 278-284.
Habeeb, A.F.S., 1966. Determination of Free Amino Groups in Proteins by Trinitrobenzenesulfonic Acid. Anal Biochem 14(3), 328-&.
Hartmann, M., Sjödahl, J., Stjernström, M., Redeby, J., Joos, T., Roeraade, J., 2008. Non-contact protein microarray fabrication using a procedure based on liquid bridge formation. Analytical and Bioanalytical Chemistry 393(2), 591-598.
Hekstra, D., Taussig, A.R., Magnasco, M., Naef, F., 2003. Absolute mRNA concentrations from sequence-specific calibration of oligonucleotide arrays. Nucleic Acids Res 31(7), 1962-1968.
Hermanson, G.T., 1996. The Chemistry of Reactive Groups. In: Hermanson, G.T. (Ed.), Bioconjugate techniques, p. 174. Academic Press, San Diego.
Hiratsuka, A., Fukui, H., Suzuki, Y., Muguruma, H., Sakairi, K., Matsushima, T., Maruo, Y., Yokoyama, K., 2008. Sulphur dioxide plasma modification on poly(methyl methacrylate) for fluidic devices. Current Applied Physics 8(2), 198-205.
Hof, M., 2003. Basics of Optical Spectroscopy. In: Vo-Dinh, T., Gauglitz, G. (Eds.), Handbook of spectroscopy, p. 74. Wiley-VCH, Weinheim ; Cambridge.
Holmberg, A., Blomstergren, A., Nord, O., Lukacs, M., Lundeberg, J., Uhl◆n, M., 2005. The biotin-streptavidin interaction can be reversibly broken using water at elevated temperatures. Electrophoresis 26(3), 501-510.
Hong, B.J., Oh, S.J., Youn, T.O., Kwon, S.H., Park, J.W., 2005. Nanoscale-controlled spacing provides DNA microarrays with the SNP discrimination efficiency in solution phase. Langmuir 21(10), 4257-4261.
Hooda, M.K., Wadhwa, M., Verma, S., Nayak, M.M., George, P.J., Paul, A.K., 2010. A systematic study of DRIE process for high aspect ratio microstructuring. Vacuum 84(9), 1142-1148.
Horcas, I., Fernandez, R., Gomez-Rodriguez, J.M., Colchero, J., Gomez-Herrero, J., Baro, A.M., 2007. WSXM: A software for scanning probe microscopy and a tool for nanotechnology. Rev Sci Instrum 78(1).
Hu, H., Larson, R.G., 2006. Marangoni effect reverses coffee-ring depositions. J Phys Chem B 110(14), 7090-7094.
Huang, H., Xiao, P.F., Qi, Z.T., Bu, Y., Liu, W.B., Zhou, G.H., 2009. A gel-based solid-phase amplification and its application for SNP typing and sequencing on-chip. Analyst 134(12), 2434-2440.
Hwang, S.J., Tseng, M.C., Shu, J.R., Yu, H.H., 2008. Surface modification of cyclic olefin copolymer substrate by oxygen plasma treatment. Surface & Coatings Technology 202(15), 3669-3674.
Irvine, E.J., Hernandez-Santana, A., Faulds, K., Graham, D., 2011. Fabricating protein immunoassay arrays on nitrocellulose using Dip-pen lithography techniques. Analyst 136(14), 2925-2930.
Ito, H., 1997. Chemical amplification resists: History and development within IBM. Ibm J Res Dev 41(1-2), 69-80.
Ito, H., 2007. Chemical amplification resists: Laboratory curiosity to paradigm. J Photopolym Sci Tec 20(3), 319-332.
Jang, J.H., Choi, W.S., Kim, N.J., Lee, C.H., Kim, T.Y., Park, C., Suh, S.J., 2010. Formation of aluminum tunnel pits arrayed using SU-8 masks with UV-assisted thermal imprint lithography. Microelectron Eng 87(12), 2610-2613.

Janiga, I., Mocak, J., Garaj, I., 2008. Comparison of Minimum Detectable Concentration with the IUPAC Detection Limit. Meas Sci Rev 8(5), 108-110.
Ji, R., Hornung, M., Verschuuren, M.A., van de Laar, R., van Eekelen, J., Plachetka, U., Moeller, M., Moormann, C., 2010. UV enhanced substrate conformal imprint lithography (UV-SCIL) technique for photonic crystals patterning in LED manufacturing. Microelectron Eng 87(5-8), 963-967.
Jin, Q., Rodriguez, J.A., Li, C.Z., Darici, Y., Tao, N.J., 1999. Self-assembly of aromatic thiols on Au(111). Surf Sci 425(1), 101-111.
Kang, H.W., Yeo, J., Hwang, J.O., Hong, S., Lee, P., Han, S.Y., Lee, J.H., Rho, Y.S., Kim, S.O., Ko, S.H., Sung, H.J., 2011. Simple ZnO Nanowires Patterned Growth by Microcontact Printing for High Performance Field Emission Device. J Phys Chem C 115(23), 11435-11441.
Kern, W., 1993. Ultraviolet-Ozone Cleaning of Semiconductor Surfaces. In: Kern, W. (Ed.), Handbook of semiconductor wafer cleaning technology : science, technology, and applications, p. 260. Noyes Publications, Park Ridge, N.J., U.S.A.
Kerssemakers, J., Howard, J., Hess, H., Diez, S., 2006. The distance that kinesin-1 holds its cargo from the microtubule surface measured by fluorescence interference contrast microscopy. P Natl Acad Sci USA 103(43), 15812-15817.
Kiessling, V., Tamm, L.K., 2003. Measuring distances in supported bilayers by fluorescence interference-contrast microscopy: Polymer supports and SNARE proteins. Biophys J 84(1), 408-418.
Kim, D.-N., Lee, W., Koh, W.-G., 2008. Micropatterning of proteins on the surface of three-dimensional poly(ethylene glycol) hydrogel microstructures. Anal Chim Acta 609(1), 59-65.
Kim, K.K., Hsu, A., Jia, X.T., Kim, S.M., Shi, Y.S., Hofmann, M., Nezich, D., Rodriguez-Nieva, J.F., Dresselhaus, M., Palacios, T., Kong, J., 2012. Synthesis of Monolayer Hexagonal Boron Nitride on Cu Foil Using Chemical Vapor Deposition. Nano Lett 12(1), 161-166.
Kinoshita, K., Fujimoto, K., Yakabe, T., Saito, S., Hamaguchi, Y., Kikuchi, T., Nonaka, K., Murata, S., Masuda, D., Takada, W., Funaoka, S., Arai, S., Nakanishi, H., Yokoyama, K., Fujiwara, K., Matsubara, K., 2006. Multiple primer extension by DNA polymerase on a novel plastic DNA array coated with a biocompatible polymer. Nucleic Acids Res 35(1), e3-e3.
Kivlehan, F., Paolucci, M., Brennan, D., Ragoussis, I., Galvin, P., 2012. Three-dimensional hydrogel structures as optical sensor arrays, for the detection of specific DNA sequences. Anal Biochem 421(1), 1-8.
Klein, L.C., 1991. Chapter10. Sol–Gel Coatings. In: Vossen, J.L., Kern, W. (Eds.), Thin film processes II, pp. 502-504. Academic Press, Boston.
Kwon, J.W., Kama-Bahl, S., Kim, E.S., 2006. In situ DNA synthesis on glass substrate for microarray fabrication using self-focusing acoustic transducer. Ieee T Autom Sci Eng 3(2), 152-158.
Kwon, M.J., Lee, J., Wark, A.W., Lee, H.J., 2012. Nanoparticle-Enhanced Surface Plasmon Resonance Detection of Proteins at Attomolar Concentrations: Comparing Different Nanoparticle Shapes and Sizes. Anal Chem 84(3), 1702-1707.
Laitinen, O.H., Hytönen, V.P., Nordlund, H.R., Kulomaa, M.S., 2006. Genetically engineered avidins and streptavidins. Cellular and Molecular Life Sciences 63(24), 2992-3017.
Lakowicz, J.R., 2006a. Introduction to Fluorescence. In: Lakowicz, J.R. (Ed.), Principles of fluorescence spectroscopy, p. 11, 3rd ed. Springer, New York.

Lakowicz, J.R., 2006b. Introduction to Fluorescence. In: Lakowicz, J.R. (Ed.), Principles of fluorescence spectroscopy, p. 5, 3rd ed. Springer, New York.
Lambacher, A., Fromherz, P., 1996. Fluorescence interference-contrast microscopy on oxidized silicon using a monomolecular dye layer. Appl Phys a-Mater 63(3), 207-216.
Lee, J.W., Serna, F., Nickels, J., Schmidt, C.E., 2006. Carboxylic acid-functionalized conductive polypyrrole as a bioactive platform for cell adhesion. Biomacromolecules 7(6), 1692-1695.
Lenoir, T., Giannella, E., 2006. The emergence and diffusion of DNA microarray technology. Journal of Biomedical Discovery and Collaboration 1(1), 11.
Levinson, H.J., 2005a. Chapter 3. Photoresists. In: Levinson, H.J. (Ed.), Principles of lithography, p. 59, 2nd ed. SPIE Press, Bellingham, WA.
Levinson, H.J., 2005b. Chapter 3. Photoresists. In: Levinson, H.J. (Ed.), Principles of lithography, p. 63, 2nd ed. SPIE Press, Bellingham, WA.
Li, Y.C., Wang, Z., Ou, L.M.L., Yu, H.Z., 2007. DNA detection on plastic: Surface activation protocol to convert polycarbonate substrates to biochip platforms. Anal Chem 79(2), 426-433.
Liu, Y.S., Li, C.M., Hu, W.H., Lu, Z.S., 2009. High performance protein microarrays based on glycidyl methacrylate-modified polyethylene terephthalate plastic substrate. Talanta 77(3), 1165-1171.
Liu, Z.M., ul-Haq, E., Hobbs, J.K., Leggett, G.J., Zhang, Y., Weaver, J.M.R., Roberts, C.J., 2011. Parallel scanning near-field photolithography in liquid: The Snomipede. Microelectron Eng 88(8), 2109-2112.
Loiacono, C.E.D.C.a.D.N., 1990. Chemical Functionality in Self -Assembled Monolayers: Structural and Electrochemical Properties. Langmuir 6, 682-691.
Luzinov, I., Julthongpiput, D., Liebmann-Vinson, A., Cregger, T., Foster, M.D., Tsukruk, V.V., 2000. Epoxy-terminated self-assembled monolayers: Molecular glues for polymer layers. Langmuir 16(2), 504-516.
MacDonald, C., Morrow, R., Weiss, A.S., Bilek, M.M.M., 2008. Covalent attachment of functional protein to polymer surfaces: a novel one-step dry process. Journal of the Royal Society Interface 5(23), 663-669.
Maclean, D., Baldwin, J.J., Ivanov, V.T., Kato, Y., Shaw, A., Schneider, P., Gordon, E.M., 1999. Glossary of terms used in combinatorial chemistry - (Technical Report). Pure Appl Chem 71(12), 2349-2365.
Manova, D., Gerlach, J.W., Mandl, S., 2010. Thin Film Deposition Using Energetic Ions. Materials 3(8), 4109-4141.
Marino, V., Galati, C., Arnone, C., 2008. Optimization of fluorescence enhancement for silicon-based microarrays. J Biomed Opt 13(5).
Marsden, D.M., Nicholson, R.L., Ladlow, M., Spring, D.R., 2009. 3D small-molecule microarrays. Chem Commun(46), 7107-7109.
Martel, R.R., Rounseville, M.P., Botros, I.W., Seligmann, B.E., 2005. Array Formats. In: Müller, U.R., Nicolau, D.V. (Eds.), Microarray technology and its applications, pp. xxii, 379 p. Springer, Berlin.
Martinez-Otero, A., Gonzalez-Monje, P., Maspoch, D., Hernando, J., Ruiz-Molina, D., 2011. Multiplexed arrays of chemosensors by parallel dip-pen nanolithography. Chem Commun 47(24), 6864-6866.
Matson, R.S., Rampal, J., Pentoney, S.L., Anderson, P.D., Coassin, P., 1995. Biopolymer Synthesis on Polypropylene Supports - Oligonucleotide Arrays. Anal Biochem 224(1), 110-116.

Matson, R.S., Rampal, J.B., Coassin, P.J., 1994. Biopolymer Synthesis on Polypropylene Supports .1. Oligonucleotides. Anal Biochem 217(2), 306-310.
Matteucci, M.D., Caruthers, M.H., 1981. Nucleotide Chemistry .4. Synthesis of Deoxyoligonucleotides on a Polymer Support. J Am Chem Soc 103(11), 3185-3191.
McGovern, M., Fayek, R., 2002. Advantages of Laser Confocal Microarray Scanners In: Kamberova, G.L., Shah, S.K. (Eds.), DNA Array Image Analysis: Nuts & Bolts, p. 61. DNA Press, Skippack, PA.
McHale, G., 2007. Surface free energy and microarray deposition technology. Analyst 132(3), 192-195.
McNaught, A.D., Wilkinson, A., International Union of Pure and Applied Chemistry., 1997. Compendium of chemical terminology : IUPAC recommendations, 2nd ed. Blackwell Science, Oxford.
McQuain, M.K., Seale, K., Peek, J., Levy, S., Haselton, F.R., 2003. Effects of relative humidity and buffer additives on the contact printing of microarrays by quill pins. Anal Biochem 320(2), 281-291.
Merrifield, R.B., 1963. Solid Phase Peptide Synthesis .1. Synthesis of a Tetrapeptide. J Am Chem Soc 85(14), 2149-&.
Michel, O., Ravoo, B.J., 2008. Carbohydrate Microarrays by Microcontact "Click" Chemistry. Langmuir 24(21), 12116-12118.
Minsky, M., 1961. Microscopy Apparatus. In: USPTO (Ed.), USA.
Miyake, Y., Isono, M., Sekiguchi, A., 2001. Study of Deprotection Reaction during Exposure in Chemically Amplified Resists for Lithography Simulation. J Photopolym Sci Tec 14(3), 463-467.
Miyamoto, T., Saito, S., Isobe, T., Nakajima, A., Matsushita, S., 2012. Six-rayed star-like nanostructures in prospective plasmonic devices. Chem Commun 48(11), 1668-1670.
Moorcroft, M.J., Meuleman, W.R.A., Latham, S.G., Nicholls, T.J., Egeland, R.D., Southern, E.M., 2005. In situ oligonucleotide synthesis on poly(dimethylsiloxane): a flexible substrate for microarray fabrication. Nucleic Acids Res 33(8).
Moore, G.E., 1995. Lithography and the future of Moore's law. Advances in Resist Technology and Processing Xii 2438, 2-17.
Moran-Mirabal, J.M., Tan, C.P., Orth, R.N., Williams, E.O., Craighead, H.G., Lin, D.M., 2007. Controlling microarray spot morphology with polymer liftoff arrays. Anal Chem 79(3), 1109-1114.
Nagaraj, V.J., Eaton, S., Thirstrup, D., Wiktor, P., 2008. Piezoelectric printing and probing of Lectin NanoProbeArrays for glycosylation analysis. Biochemical and Biophysical Research Communications 375(4), 526-530.
Nakata, H., Nishioka, K., Abe, H., 1980. Plasma-Etching Characteristics of Chromium Film and Its Novel Etching Mode. J Vac Sci Technol 17(6), 1351-1357.
Nelson, B.P., Grimsrud, T.E., Liles, M.R., Goodman, R.M., Corn, R.M., 2001. Surface Plasmon Resonance Imaging Measurements of DNA and RNA Hybridization Adsorption onto DNA Microarrays. Anal Chem 73(1), 1-7.
Nicolau, D.V., Ivanova, E.P., Fulga, F., Filipponi, L., Viezzoli, A., Dobroiu, S., Alekseeva, Y.V., Pham, D.K., 2010. Protein immobilisation on micro/nanostructures fabricated by laser microablation. Biosens Bioelectron 26(4), 1337-1345.
Nyamjav, D., Holz, R.C., 2010. Direct Patterning of Silanized-Biomolecules on Semiconductor Surfaces. Langmuir 26(23), 18300-18302.
Oblak, M., Prezelj, A., Pecar, S., Solmajer, T., 2004. Thiol-reactive clenbuterol analogues conjugated to bovine serum albumin. Z Naturforsch C 59(11-12), 880-886.

Obrien, F.E.M., 1948. The Control of Humidity by Saturated Salt Solutions. J Sci Instr Phys Ind 25(3), 73-76.
Ochs, M., Bidaut, G., 2002. Microarray Data Normalization. In: Kamberova, G.L., Shah, S.K. (Eds.), DNA Array Image Analysis: Nuts & Bolts, pp. 134-135. DNA Press, Skippack, PA.
Oehrlein, G.S., 1986. Reactive-Ion Etching. Phys Today 39(10), 26-33.
Offord, D.A., John, C.M., Linford, M.R., Griffin, J.H., 1994. Contact-Angle Goniometry, Ellipsometry, and Time-of-Flight Secondary-Ion Mass-Spectrometry of Gold Supported, Mixed Self-Assembled Monolayers Formed from Alkyl Mercaptans. Langmuir 10(3), 883-889.
Okoroanyanwu, U., 2010a. Chapter 7. Positive resists. Chemistry and lithography, pp. 313-314. SPIE Press, Bellingham, Wash.
Okoroanyanwu, U., 2010b. Chapter 7. Positive Resists. Chemistry and lithography, pp. 297-302. SPIE Press, Bellingham, Wash.
Okoroanyanwu, U., 2010c. Chapter 13. Optical lithography. In: Okoroanyanwu, U. (Ed.), Chemistry and lithography, p. 687. SPIE Press, Bellingham, Wash.
Pan, Z.Q., Li, Y.Q., Shan, Q., Hong, X.H., Zhou, D.R., Zhang, M.H., Chen, P., Xiao, P.F., Lu, Z.H., 2008. Fabrication of 3-D gel microarrays directly with raw polymerase chain reaction products by heat-directed polymerization. Electrophoresis 29(11), 2424-2436.
Park, J.-U., Lee, J.H., Paik, U., Lu, Y., Rogers, J.A., 2008a. Nanoscale Patterns of Oligonucleotides Formed by Electrohydrodynamic Jet Printing with Applications in Biosensing and Nanomaterials Assembly. Nano Lett 8(12), 4210-4216.
Park, J.Y., Kwon, S.H., Park, J.W., Park, S.M., 2008b. Label-free detection of DNA molecules on the dendron based self-assembled monolayer by electrochemical impedance spectroscopy. Anal Chim Acta 619(1), 37-42.
Parthasarathy, R., Groves, J.T., 2004. Optical techniques for imaging membrane topography. Cell Biochem Biophys 41(3), 391-414.
Pease, A.C., Solas, D., Sullivan, E.J., Cronin, M.T., Holmes, C.P., Fodor, S.P.A., 1994. Light-Generated Oligonucleotide Arrays for Rapid DNA-Sequence Analysis. P Natl Acad Sci USA 91(11), 5022-5026.
Peng, H., Soeller, C., Vigar, N., Kilmartin, P.A., Cannell, M.B., Bowmaker, G.A., Cooney, R.P., Travas-Sejdic, J., 2005. Label-free electrochemical DNA sensor based on functionalised conducting copolymer. Biosens Bioelectron 20(9), 1821-1828.
Petrov, A., Shah, S.K., Draghici, S., Shams, S., 2002. Microarray Image Processing and Quality Control. In: Kamberova, G.L., Shah, S.K. (Eds.), DNA Array Image Analysis: Nuts & Bolts. DNA Press, Skippack, PA.
Piner, R.D., Zhu, J., Xu, F., Hong, S.H., Mirkin, C.A., 1999. "Dip-pen" nanolithography. Science 283(5402), 661-663.
Pividori, M.I., Alegret, S., 2005. immobilization of Oligonucleotides for Biochemical Sensing by SAMs. In: Wittmann, C., Alegret, S. (Eds.), Immobilisation of DNA on chips, p. 45. Springer, Berlin ; New York.
Pool, R., Schapotschnikow, P., Vlugt, T.J.H., 2007. Solvent effects in the adsorption of alkyl thiols on gold structures: A molecular simulation study. J Phys Chem C 111(28), 10201-10212.
Preininger, C., Sauer, U., Dayteg, J., Pichler, R., 2005. Optimizing processing parameters for signal enhancement of oligonucleotide and protein arrays on ARChip Epoxy. Bioelectrochemistry 67(2), 155-162.

Qin, M., Hou, S., Wang, L., Feng, X., Wang, R., Yang, Y., Wang, C., Yu, L., Shao, B., Qiao, M., 2007. Two methods for glass surface modification and their application in protein immobilization. Colloids and Surfaces B: Biointerfaces 60(2), 243-249.
Rahman, M., Day, B.S., Cao, H., Butts, H., Norton, M.L., 2006. Ordered DNA arrays prepared via soft lithography 6370, 637012-637012-637019.
Rakickas, T., Ericsson, E.M., Ruzele, Z., Liedberg, B., Valiokas, R., 2011. Functional Hydrogel Density Patterns Fabricated by Dip-Pen Nanolithography and Photografting. Small 7(15), 2153-2157.
Rappe, Y.Y.a.A.M., 2002. Structure and energetics of alkanethiol adsorption on the Au„111... surface. J. Chem. Phys. 117(2), 825-833.
Rasband, W.S., Image J, U. S. National Institutes of Health, Bethesda, Maryland, USA, http://rsbweb.nih.gov/ij/
Redkar, R.J., Schultz, N., Scheumann, V., Burzio, L.A., Haines, D.E., Metwalli, E., Becker, O., Conzone, S.D., 2006. Signal and Sensitivity Enhancement Through Optical Interference Coating for DNA and Protein Microarray Applications. Journal of Biomolecular Technology 17(2).
Reinhardt, K.A., Kern, W., 2008. Handbook of silicon wafer cleaning technology, 2nd ed. William Andrew, Norwich, NY.
Reiser, A., 1998. The molecular mechanism of Novolak resists. J Imaging Sci Techn 42(1), 15-22.
Reiser, A., Huang, J.P., He, X., Yeh, T.F., Jha, S., Shih, H.Y., Kim, M.S., Han, Y.K., Yan, K., 2002. The molecular mechanism of novotak-diazonaphthoquinone resists. Eur Polym J 38(4), 619-629.
Reiser, A., Shih, H.Y., Yeh, T.F., Huang, J.P., 1996. Novolak-diazoquinone resists: The imaging systems of the computer chip. Angewandte Chemie-International Edition in English 35(21), 2428-2440.
Reiser, A., Yan, Z.L., Han, Y.K., Kim, M.S., 2000. Navolak-diazonaphthoquinone resists: The central role of phenolic strings. J Vac Sci Technol B 18(3), 1288-1293.
Renault, J.P., Bernard, A., Juncker, D., Michel, B., Bosshard, H.R., Delamarche, E., 2002. Fabricating microarrays of functional proteins using affinity contact printing. Angew Chem Int Edit 41(13), 2320-2323.
Reynolds, G.W., Taylor, J.W., 1999. Factors contributing to sidewall roughness in a positive-tone, chemically amplified resist exposed by x-ray lithography. J Vac Sci Technol B 17(2), 334-344.
Richards, C.I., Choi, S., Hsiang, J.C., Antoku, Y., Vosch, T., Bongiorno, A., Tzeng, Y.L., Dickson, R.M., 2008. Oligonucleotide-stabilized Ag nanocluster fluorophores. J Am Chem Soc 130(15), 5038-+.
Rickman, D.S., Herbert, C.J., Aggerbeck, L.P., 2003. Optimizing spotting solutions for increased reproducibility of cDNA microarrays. Nucleic Acids Res 31(18).
Robertson, D., 2001. Affymetrix license valid, rules court. Nat Biotechnol 19(1), 13-14.
Rodriguez-Canto, P.J., Nickel, U., Abargues, R., 2011. Understanding Acid Reaction and Diffusion in Chemically Amplified Photoresists: An Approach at the Molecular Level. J Phys Chem C 115(42), 20367-20374.
Rossnagel, S., 2002. Chapter 8. Sputtering and Sputter Deposition. In: Seshan, K. (Ed.), Handbook of thin-film deposition processes and techniques : principles, methods, equipment, and applications, p. 324, 2nd ed. Noyes Publications, Norwich, N.Y.
Rubtsova, M.Y., Ulyashova, M.M., Edelstein, M.V., Egorov, A.M., 2010. Oligonucleotide microarrays with horseradish peroxidase-based detection for the

identification of extended-spectrum beta-lactamases. Biosens Bioelectron 26(4), 1252-1260.
Rueda, L., Rezaeian, I., 2011. A fully automatic gridding method for cDNA microarray images. BMC Bioinformatics 12.
Saaem, I., Ma, K.S., Marchi, A.N., LaBean, T.H., Tian, J.D., 2010. In situ Synthesis of DNA Microarray on Functionalized Cyclic Olefin Copolymer Substrate. Acs Appl Mater Inter 2(2), 491-497.
Sarantopoulou, E., Petrou, P.S., Kollia, Z., Palles, D., Spyropoulos-Antonakakis, N., Kakabakos, S., Cefalas, A.C., 2011. Protein immobilization and detection on laser processed polystyrene surfaces. J Appl Phys 110(6).
Satriano, C., Fragala, M.E., Aleeva, Y., 2012. Ultrathin and nanostructured ZnO-based films for fluorescence biosensing applications. J Colloid Interf Sci 365(1), 90-96.
Schena, M., 2003a. Microarray analysis. Wiley-Liss, Hoboken, N.J.
Schena, M., 2003b. Microarray Detection. In: Schena, M. (Ed.), Microarray analysis, pp. 237-238. Wiley-Liss, Hoboken, NJ.
Schena, M., 2003c. Microarray manufacturing. In: Schena, M. (Ed.), Microarray Analysis, pp. 163-164. Wiley-Liss, Hoboken, NJ.
Schena, M., 2003d. Microarray Surfaces. In: Schena, M. (Ed.), Microarray analysis, pp. 95-99. Wiley-Liss, Hoboken, NJ.
Schena, M., 2003e. Preface. In: Schena, M. (Ed.), Microarray analysis, pp. ix-x. Wiley-Liss, Hoboken, NJ.
Schena, M., Shalon, D., Davis, R.W., Brown, P.O., 1995. Quantitative Monitoring of Gene-Expression Patterns with a Complementary-DNA Microarray. Science 270(5235), 467-470.
Schultz, N., Conzone, S.D., Becker, O., Haines, D., Pawlowski, E., Scheumann, V., 2011. Arrangement for fluorescence amplification. In: USPTO (Ed.), Official Gazette of the United States Patent and Trademark Office. Schott AG, USA.
Seisyan, R.P., 2011. Nanolithography in microelectronics: A review. Tech Phys+ 56(8), 1061-1073.
Seo, J., Hoffman, E.P., 2006. Probe set algorithms: is there a rational best bet? BMC Bioinformatics 7.
Sha, J., Jung, B., Thompson, M.O., Ober, C.K., Chandhok, M., Younkin, T.R., 2009. Submillisecond post-exposure bake of chemically amplified resists by CO2 laser spike annealing. J Vac Sci Technol B 27(6), 3020-3024.
Shalon, D., 1995. DNA micro arrays: A new tool for genetic analysis. Stanford University.
Sharp, K.G., Blackman, G.S., Glassmaker, N.J., Jagota, A., Hui, C.Y., 2004. Effect of stamp deformation on the quality of microcontact printing: Theory and experiment. Langmuir 20(15), 6430-6438.
Simchi, H., Raastgoo, M., Ranjbar, A., Barzekar, T., Qasempour, M., Daaraei, M., Mahmoodzadeh, E., Saani, M.H., Mohammadnejad, S., 2009. Ar(+) ion milling of InSb for manufacturing single electron devices. Infrared Phys Techn 52(4), 113-118.
Singh-Gasson, S., Green, R.D., Yue, Y.J., Nelson, C., Blattner, F., Sussman, M.R., Cerrina, F., 1999. Maskless fabrication of light-directed oligonucleotide microarrays using a digital micromirror array. Nat Biotechnol 17(10), 974-978.
Smith, J.T., Viglianti, B.L., Reichert, W.M., 2002. Spreading diagrams for the optimization of quill pin printed microarray density. Langmuir 18(16), 6289-6293.

Sobek, J., Aquino, C., Schlapbach, R., 2007. Quality Considerations and Selection of Surface Chemistry for Glass-Based DNA, Peptide, Antibody, Carbohydrate, and Small Molecule Microarrays 382, 17-31.
Southern, E.M., 1975. Detection of Specific Sequences among DNA Fragments Separated by Gel-Electrophoresis. J Mol Biol 98(3), 503-&.
Southern, E.M., Casegreen, S.C., Elder, J.K., Johnson, M., Mir, K.U., Wang, L., Williams, J.C., 1994. Arrays of Complementary Oligonucleotides for Analyzing the Hybridization Behavior of Nucleic-Acids. Nucleic Acids Res 22(8), 1368-1373.
Southern, E.M., Maskos, U., Elder, J.K., 1992. Analyzing and Comparing Nucleic-Acid Sequences by Hybridization to Arrays of Oligonucleotides - Evaluation Using Experimental-Models. Genomics 13(4), 1008-1017.
SreeHarsha, K.S., 2006. Chapter 9. Nucleation and growth of films. In: SreeHarsha, K.S. (Ed.), Principles of physical vapor deposition of thin films, pp. 685-827, 1st ed. Elsevier, Amsterdam ; Boston.
Srinivas, R.L., Chapin, S.C., Doyle, P.S., 2011. Aptamer-Functionalized Microgel Particles for Protein Detection. Anal Chem 83(23), 9138-9145.
Srivannavit, O., Gulari, M., Hua, Z.S., Gao, X.L., Zhou, X.C., Hong, A.L., Zhou, T.C., Gulari, E., 2009. Microfluidic reactor array device for massively parallel in situ synthesis of oligonucleotides. Sensor Actuat B-Chem 140(2), 473-481.
Stachowiak, T.B., Mair, D.A., Holden, T.G., Lee, L.J., Svec, F., Frechet, J.M.J., 2007. Hydrophilic surface modification of cyclic olefin copolymer microfluidic chips using sequential photografting. J Sep Sci 30(7), 1088-1093.
Stokes, G.G., 1864. On the Application of the Optical Properties of Bodies to the Detection and Discrimination of Organic Substances. Mathematical and Physical Papers 4, 249-263.
Strother, T., Hamers, R.J., Smith, L.M., 2000. Covalent attachment of oligodeoxyribonucleotides to amine-modified Si (001) surfaces. Nucleic Acids Res 28(18), 3535-3541.
Sun, Y., Perch-Nielsen, I., Dufva, M., Sabourin, D., Bang, D.D., Høgberg, J., Wolff, A., 2011. Direct immobilization of DNA probes on non-modified plastics by UV irradiation and integration in microfluidic devices for rapid bioassay. Analytical and Bioanalytical Chemistry 402(2), 741-748.
Tabakman, S.M., Lau, L., Robinson, J.T., Price, J., Sherlock, S.P., Wang, H.L., Zhang, B., Chen, Z., Tangsombatvisit, S., Jarrell, J.A., Utz, P.J., Dai, H.J., 2011. Plasmonic substrates for multiplexed protein microarrays with femtomolar sensitivity and broad dynamic range. Nat Commun 2.
Tanase, C.P., Albulescu, R., Neagu, M., 2011. Application of 3D hydrogel microarrays in molecular diagnostics: advantages and limitations. Expert Rev Mol Diagn 11(5), 461-464.
Tang, J., Xiao, P.F., 2009. Polymerizing immobilization of acrylamide-modified nucleic acids and its application. Biosens Bioelectron 24(7), 1817-1824.
Teh, W.H., Durig, U., Drechsler, U., Smith, C.G., Guntherodt, H.J., 2005. Effect of low numerical-aperture femtosecond two-photon absorption on (SU-8) resist for ultrahigh-aspect-ratio microstereolithography. J Appl Phys 97(5).
Thomas, T., Blackman, C.S., Parkin, I.P., Carmalt, C.J., 2011. Titanium arsenide films from the atmospheric pressure chemical vapour deposition of tetrakisdimethylamidotitanium and tert-butylarsine. Dalton T 40(40), 10664-10669.
Thompson, D.G., McKenna, E.O., Pitt, A., Graham, D., 2011. Microscale mesoarrays created by dip-pen nanolithography for screening of protein-protein interactions. Biosens Bioelectron 26(12), 4667-4673.

Thornell, G., Johansson, S., 1998. Microprocessing at the fingertips. J Micromech Microeng 8(4), 251-262.
Tlili, C., Jaffrezie-Renault, N.J., Martelet, C., Korri-Youssoufi, H., 2008. Direct electrochemical probing of DNA hybridization on oligonucleotide-functionalized polypyrrole. Materials Science & Engineering C-Biomimetic and Supramolecular Systems 28(5-6), 848-854.
Torres-Huerta, A.M., Dominguez-Crespo, M.A., Onofre-Bustamante, E., Flores-Vela, A., 2012. Characterization of ZrO(2) thin films deposited by MOCVD as ceramic coatings. J Mater Sci 47(5), 2300-2309.
Totzeck, M., 2012. Interferometry. In: Träger, F. (Ed.), Springer handbook of lasers and optics, p. 1269, 2nd ed. Springer, Dordrecht ; New York.
Towbin, H., Staehelin, T., Gordon, J., 1979. Electrophoretic Transfer of Proteins from Polyacrylamide Gels to Nitrocellulose Sheets - Procedure and Some Applications. P Natl Acad Sci USA 76(9), 4350-4354.
Trevisiol, E., Le Berre-Anton, V., Leclaire, J., Pratviel, G., Caminade, A.M., Majoral, J.P., Francois, J.M., Meunier, B., 2003. Dendrislides, dendrichips: a simple chemical functionalization of glass slides with phosphorus dendrimers as an effective means for the preparation of biochips. New J Chem 27(12), 1713-1719.
Tsai, J.G.F., Chen, Z., Nelson, S.F., Kim, C.-J., 2006. Selective surface treatment of micro printing pin and its performance. Appl Phys Lett 89(8), 083901.
Tseng, A.A., 2011. Removing Material Using Atomic Force Microscopy with Single- and Multiple-Tip Sources. Small 7(24), 3409-3427.
Turova, N.Y., 2002. Chapter 1. Introduction. The chemistry of metal alkoxides, p. 6. Kluwer Academic Publishers, Boston.
ul Haq, E., Liu, Z.M., Zhang, Y.A., Ahmad, S.A.A., Wong, L.S., Armes, S.P., Hobbs, J.K., Leggett, G.J., Micklefield, J., Roberts, C.J., Weaver, J.M.R., 2010. Parallel Scanning Near-Field Photolithography: The Snomipede. Nano Lett 10(11), 4375-4380.
Ulman, A., 1996. Formation and Structure of Self-Assembled Monolayers. Chem. Rev.(96), 1533-1554.
Valiokas, R., Svedhem, S., Svensson, S.C.T., Liedberg, B., 1999. Self-assembled monolayers of oligo(ethylene glycol)-terminated and amide group containing alkanethiolates on gold. Langmuir 15(10), 3390-3394.
Vandencasteele, N., Nisol, B., Viville, P., Lazzaroni, R., Castner, D.G., Reniers, F., 2008. Plasma-modified PTFE for biological applications: Correlation between protein-resistant properties and surface characteristics. Plasma Processes and Polymers 5(7), 661-671.
Verschuuren, M., Sprang, H.V., 2007. 3D Photonic structures by sol-gel imprint lithography. Printing Methods for Electronic, Photonics and Biomaterials - 2007 MRS Spring Meeting, April 9, 2007 - April 13, 2009, pp. 7-12. Materials Research Society, San Francisco, CA, United states.
Viana, A.S., Leupold, S., Montforts, F.P., Abrantes, L.M., 2005. Self-assembled monolayers of a disulphide-derivatised cobalt-porphyrin on gold. Electrochimica Acta 50(14), 2807-2813.
Vogt, K.W., Kohl, P.A., Carter, W.B., Bell, R.A., Bottomley, L.A., 1994. Characterization of Thin Titanium-Oxide Adhesion Layers on Gold - Resistivity, Morphology, and Composition. Surf Sci 301(1-3), 203-213.
Walter, J.G., Stahl, F., Reck, M., Praulich, I., Nataf, Y., Hollas, M., Pflanz, K., Melzner, D., Shoham, Y., Scheper, T., 2010. Protein microarrays: Reduced autofluorescence and improved LOD. Eng Life Sci 10(2), 103-108.

Wang, J., Song, F.Y., Zhou, F.M., 2002. Silver-enhanced imaging of DNA hybridization at DNA microarrays with scanning electrochemical microscopy. Langmuir 18(17), 6653-6658.
Wang, X., Ghosh, S., Guo, S.W., 2001. Quantitative quality control in microarray image processing and data acquisition. Nucleic Acids Res 29(15).
Wang, Y., Goh, S.H., Bi, X., Yang, K.-L., 2009. Replication of DNA submicron patterns by combining nanoimprint lithography and contact printing. J Colloid Interf Sci 333(1), 188-194.
Wasa, K., Kitabatake, M., Adachi, H., 2004a. Chapter 1. Thin Film Materials and Devices. In: Wasa, K., Kitabatake, M., Adachi, H. (Eds.), Thin film materials technology : sputtering of compound materials, pp. 6-9. William Andrew Pub.; Springer, Norwich, NY, Heidelberg.
Wasa, K., Kitabatake, M., Adachi, H., 2004b. Chapter 2. Thin Film Processes. In: Wasa, K., Kitabatake, M., Adachi, H. (Eds.), Thin film materials technology : sputtering of compound materials, pp. 17-19. William Andrew Pub.; Springer, Norwich, NY, Heidelberg.
Wasa, K., Kitabatake, M., Adachi, H., 2004c. Chapter 2. Thin film processes. In: Wasa, K., Kitabatake, M., Adachi, H. (Eds.), Thin film materials technology : sputtering of compound materials, p. 35. William Andrew Pub.; Springer, Norwich, NY, Heidelberg.
Wendeln, C., Heile, A., Arlinghaus, H.F., Ravoo, B.J., 2010. Carbohydrate Microarrays by Microcontact Printing. Langmuir 26(7), 4933-4940.
Widrig, C.A., Chung, C., Porter, M.D., 1991. The Electrochemical Desorption of N-Alkanethiol Monolayers from Polycrystalline Au and Ag Electrodes. Journal of Electroanalytical Chemistry 310(1-2), 335-359.
Wilbur, J.L., Kumar, A., Kim, E., Whitesides, G.M., 1994. Microfabrication by Microcontact Printing of Self-Assembled Monolayers. Adv Mater 6(7-8), 600-604.
Williams, K.R., Gupta, K., Wasilik, M., 2003. Etch rates for micromachining processing - Part II. J Microelectromech S 12(6), 761-778.
Williams, K.R., Muller, R.S., 1996. Etch rates for micromachining processing. J Microelectromech S 5(4), 256-269.
Willson, C.G., Dammel, R.A., Reiser, A., 1997. Photoresist materials: A historical perspective. Emerging Lithographic Technologies 3048, 28-41.
Wilson, T., 2011. Resolution and optical sectioning in the confocal microscope. J Microsc-Oxford 244(2), 113-121.
Wong, E.Y., Diamond, S.L., 2009. Advancing Microarray Assembly with Acoustic Dispensing Technology. Anal Chem 81(1), 509-514.
Wouters, D., Hoeppener, S., Schubert, U.S., 2009. Local Probe Oxidation of Self-Assembled Monolayers: Templates for the Assembly of Functional Nanostructures. Angew Chem Int Edit 48(10), 1732-1739.
Wouters, D., Schubert, U.S., 2004. Nanolithography and nanochemistry: Probe-related patterning techniques and chemical modification for nanometer-sized devices. Angew Chem Int Edit 43(19), 2480-2495.
Wu, B.Q., Kumar, A., Pamarthy, S., 2010. High aspect ratio silicon etch: A review. J Appl Phys 108(5).
Wu, C.C., Reinhoudt, D.N., Otto, C., Subramaniam, V., Velders, A.H., 2011. Strategies for Patterning Biomolecules with Dip-Pen Nanolithography. Small 7(8), 989-1002.
Wu, D., Song, L.B., Chen, K., Liu, F., 2012. Modelling and hydrostatic analysis of contact printing microarrays by quill pins. Int J Mech Sci 54(1), 206-212.

Wu, W., Wildsmith, S.E., Winkley, A.J., Yallop, R., Elcock, F.J., Bugelski, P.J., 2001. Chemometric strategies for normalisation of gene expression data obtained from cDNA microarrays. Anal Chim Acta 446(1-2), 451-466.
Xia, Y.N., Whitesides, G.M., 1998. Soft lithography. Annu Rev Mater Sci 28, 153-184.
Xiao, P.F., He, N.Y., Liu, Z.C., He, Q.G., Sun, X., Lu, Z.H., 2002. In situ synthesis of oligonucleotide arrays by using soft lithography. Nanotechnology 13(6), 756-762.
Xu, B., Lee, Y.-K., Jin, Q., Zhao, J., Ho, C.-M., 2006. Multilayer SU-8 based microdispenser for microarray assay. Sensors and Actuators A: Physical 132(2), 714-725.
Yang, S.M., Jang, S.G., Choi, D.G., Kim, S., Yu, H.K., 2006. Nanomachining by colloidal lithography. Small 2(4), 458-475.
Yeh, W.-M., Lawson, R.A., Tolbert, L.M., Henderson, C.L., 2011. The effect of drying rate on pattern collapse performance in thin film lithography, 79721Y-79721Y-79728.
Yoshimitsu, Z., Nakajima, A., Watanabe, T., Hashimoto, K., 2002. Effects of Surface Structure on the Hydrophobicity and Sliding Behavior of Water Droplets. Langmuir 18(15), 5818-5822.
Zajac, A., Song, D.S., Qian, W., Zhukov, T., 2007. Protein microarrays and quantum dot probes for early cancer detection. Colloid Surface B 58(2), 309-314.
Zammatteo, N., Girardeaux, C., Delforge, D., Pireaux, J.J., Remacle, J., 1996. Amination of polystyrene microwells: Application to the covalent grafting of DNA probes for hybridization assays. Anal Biochem 236(1), 85-94.
Zaugg, F.G., Wagner, P., 2003. Drop-on-demand printing of protein biochip arrays. Mrs Bull 28(11), 837-842.
Zhang, J., Zhou, X.C., 2011. Novel 3-dimensional dendrimer platform for glycolipid microarray. Biosens Bioelectron 28(1), 355-361.
Zhang, Y.Z., Wang, Z., Jiang, W., 2011. A sensitive fluorimetric biosensor for detection of DNA hybridization based on Fe/Au core/shell nanoparticles. Analyst 136(4), 702-707.
Zhao, Z., Peytavi, R., Diaz-Quijada, G.A., Picard, F.J., Huletsky, A., Leblanc, E., Frenette, J., Boivin, G., Veres, T., Dumoulin, M.M., Bergeron, M.G., 2008. Plastic Polymers for Efficient DNA Microarray Hybridization: Application to Microbiological Diagnostics. Journal of Clinical Microbiology 46(11), 3752-3758.
Zhu, N.N., Gao, H., Xua, Q., Lin, Y.Q., Su, L., Mao, L.Q., 2010. Sensitive impedimetric DNA biosensor with poly(amidoamine) dendrimer covalently attached onto carbon nanotube electronic transducers as the tether for surface confinement of probe DNA. Biosens Bioelectron 25(6), 1498-1503.
Zimmermann, S., Ahner, N., Blaschta, F., Schaller, M., Zimmermann, H., Rulke, H., Lang, N., Ropcke, J., Schulz, S.E., Gessner, T., 2011. Influence of the additives argon, O(2), C(4)F(8), H(2), N(2) and CO on plasma conditions and process results during the etch of SiCOH in CF(4) plasma. Microelectron Eng 88(5), 671-676.